

DISSERTATION ZUR ERLANGUNG DES DOKTORGRADES  
DER FAKULTÄT FÜR CHEMIE UND PHARMAZIE  
DER LUDWIG-MAXIMILIANS-UNIVERSITÄT MÜNCHEN

**Quantitative live-cell imaging studies on the  
biological effects of nanoparticles  
at the cellular level**

Adriano de Andrade Torrano

aus

Esteio, Brasilien

2015



### Erklärung

Diese Dissertation wurde im Sinne von §7 der Promotionsordnung vom 28. November 2011 von Herrn Prof. Dr. Christoph Bräuchle betreut.

### Eidesstattliche Versicherung

Diese Dissertation wurde eigenständig und ohne unerlaubte Hilfe bearbeitet.

München, den 15. Juni 2015

Adriano de Andrade Torrano

Dissertation eingereicht am 18.06.2015

1. Gutachter: Prof. Dr. Christoph Bräuchle
2. Gutachter: Prof. Dr. Achim Wixforth

Mündliche Prüfung am 22.07.2015



## Summary

The interaction of nanoparticles (NPs) with biological systems, such as living cells, has become one of the most stimulating areas of basic and applied science. NPs are used in a wide variety of consumer products and have been increasingly designed for nanomedical applications. Therefore, unintentional or deliberate human exposure to NPs has become inevitable. However, in spite of intensive investigations, our current knowledge about the biological impact of NPs is still incomplete. The goal of this work was to perform an interdisciplinary approach to analyze the effects of distinct NPs at cellular level. In particular, we used quantitative live-cell imaging under static and physiological flow conditions to investigate in great detail the uptake of NPs.

Live-cell imaging is commonly the method of choice to visualize uptake of NPs in real time with high spatial resolution. Although acquired image data are rich in information, outcomes of NP-cell interactions are normally evaluated by simple qualitative approaches. In the first part of this work, a highly innovative method integrating live-cell imaging with quantitative image analysis is described. Particle\_in\_Cell-3D is able to quantify the uptake of NPs into single cells in absolute numbers. Further studies presented in this thesis demonstrate the use of Particle\_in\_Cell-3D, as well as the crucial importance of quantitative live-cell imaging approaches.

Particle\_in\_Cell-3D was used to evaluate cell type-dependent uptake and cytotoxicity of the 310 nm silica NPs. After 24 hours, the absolute number of particles internalized by cancer cells derived from cervix carcinoma (HeLa) was twice as large as the number of particles taken up by human vascular endothelial cells (HUVEC). Strikingly, exposure to silica NPs for 24 h induces cell death in HUVEC but not in HeLa cells. Quantitative determination of NP uptake appears to be essential to demonstrate that nanotoxicity of materials cannot be generalized and translated from one cell type to another. In another case study, we assessed the uptake kinetics of 8 nm and 30 nm ceria NPs interacting with human microvascular endothelial cells (HMEC-1). These NPs formed agglomerates in biological medium, and particles directly contacting cells had a mean diameter of 417 nm and 316 nm, respectively. Quantitative analysis was decisive to reveal significant particle size-dependent effects. After 48 h of interaction, the number of intracellular particles was over four times higher for 316 nm agglomerates. In addition, our findings offer new insights into the “dilution” of intracellular NPs, possibly influenced by cell division and exocytosis. Titania NPs are widely used as physical barriers for UV light in sunscreens. The results of this research project shed light on mostly neglected potential cytotoxicity related to coating

composition of sunscreen titania NPs. The presence of organic shell in NPs is found to correlate with an enhanced cytotoxicity of titania NPs on HMEC-1 cells.

The most recent project focuses on platinum-decorated ceria (Pt-ceria) NPs. They resemble catalyst-derived NPs emitted by motor vehicles into the environment. Using live-cell imaging we clearly show that ~50 nm Pt-ceria NPs can rapidly penetrate cell membranes and reach the cytosol. Moreover, if properly targeted, these NPs are able to selectively accumulate in cellular organelles, like mitochondria. Interestingly, no permanent membrane disruption or any other significant adverse effects on cells were observed.

Mesoporous silica nanoparticles (MSNs) attract increasing interest in the field of gene and drug delivery due to their versatile features. Here we describe poly(amidoamine) dendron-functionalized MSNs that can successfully deliver various compounds into cells. Furthermore, quantitative uptake kinetics and cytotoxicity studies indicate a good biocompatibility of dendronized MSNs.

Static conditions represent an important shortcoming of the *in vitro* experiments on uptake of NPs by cells. This work describes a versatile microfluidic device based on streaming which is induced by surface acoustic waves. The device offers a convenient method for mimicking capillary blood flow and it can be combined with live-cell imaging. Using this approach along with Particle\_in\_Cell-3D, we demonstrated the influence of flow on the uptake of NPs. Under physiological flow conditions, NP uptake rates were significantly lower than under low shear conditions, highlighting the vital importance of fluidic environment for cellular uptake mechanisms.

On the whole, potential adverse effects on cells depend strongly on the physicochemical properties of NPs and are influenced by biological environment and experimental conditions. Taken together, the studies presented in this thesis show that quantitative live-cell imaging is a powerful method to investigate the biological effects of NPs at cellular level in great detail.

# Contents

<b>SUMMARY .....</b>	<b>V</b>
<b>1 INTRODUCTION.....</b>	<b>1</b>
<b>2 BIOLOGICAL RESPONSES TO NANOPARTICLES.....</b>	<b>5</b>
2.1 Introduction .....	5
2.2 Entry of nanoparticles into the human body .....	6
2.2.1 Uptake of nanoparticles by the lung.....	6
2.2.2 Interaction of nanoparticles with the skin .....	8
2.2.3 Uptake of nanoparticles by the gastrointestinal tract .....	9
2.3 Interaction of nanoparticles with proteins.....	10
2.4 Interaction of nanoparticles with endothelial cells.....	11
2.5 Cellular uptake mechanisms .....	11
2.5.1 Phagocytosis .....	12
2.5.2 Pinocytosis .....	13
2.5.3 Direct translocation through the cell plasma membrane .....	13
2.6 Trafficking and intracellular distribution of nanoparticles.....	14
2.7 Cytotoxic potential of nanoparticles .....	16
2.8 Conclusions .....	16
<b>3 QUANTITATIVE LIVE-CELL IMAGING .....</b>	<b>17</b>
3.1 Introduction .....	17
3.2 Principles of fluorescence .....	17
3.3 Live-cell imaging .....	19
3.4 Quantitative image analysis .....	21
<b>4 IMAGE ANALYSIS METHOD 'PARTICLE_IN_CELL-3D' .....</b>	<b>23</b>
4.1 Introduction .....	23
4.2 The Particle_in_Cell-3D ImageJ macro .....	24
4.2.1 Main features.....	25
4.2.2 Comparison to other methods.....	26
4.2.3 Routine selection .....	27
4.2.4 Input of analysis parameters .....	33
4.3 Results & Discussion.....	34
4.3.1 Cell segmentation strategy .....	34
4.3.2 Fraction of nanoparticles internalized by single cells .....	35

4.3.3	Accuracy of absolute quantification .....	36
4.4	Conclusions .....	39
<b>5</b>	<b>CELL TYPE-DEPENDENT UPTAKE KINETICS AND CYTOTOXICITY OF SILICA NANOPARTICLES .....</b>	<b>41</b>
5.1	Introduction .....	41
5.2	Results & Discussion.....	42
5.2.1	Characterization of silica nanoparticles .....	42
5.2.2	Quantification of silica nanoparticle uptake by cells .....	43
5.2.3	Cytotoxicity of silica nanoparticles .....	47
5.3	Conclusions .....	50
<b>6</b>	<b>EFFECTS OF THE PHYSICOCHEMICAL PROPERTIES ON THE CYTOTOXICITY OF SUNSCREEN TITANIA NANOPARTICLES .....</b>	<b>52</b>
6.1	Introduction .....	52
6.2	Results & Discussion.....	54
6.2.1	Characterization of titania nanoparticles .....	54
6.2.2	Cytotoxicity of titania nanoparticles .....	59
6.3	Conclusions .....	64
<b>7</b>	<b>PARTICLE SIZE-DEPENDENT UPTAKE OF CERIA NANOPARTICLES .....</b>	<b>66</b>
7.1	Introduction .....	66
7.2	Results & Discussion.....	67
7.2.1	Characterization of ceria nanoparticles .....	67
7.2.2	Quantification of ceria nanoparticle uptake by cells .....	68
7.3	Conclusions .....	70
<b>8</b>	<b>CELL MEMBRANE PENETRATION AND MITOCHONDRIAL TARGETING BY PLATINUM-DECORATED CERIA NANOPARTICLES .....</b>	<b>71</b>
8.1	Introduction .....	71
8.2	Results & Discussion.....	73
8.2.1	Characterization of platinum-decorated ceria nanoparticles .....	73
8.2.2	Cellular uptake behavior of platinum-decorated ceria nanoparticles .....	78
8.3	Conclusions .....	93
<b>9</b>	<b>ENDOSOMAL ESCAPE AND SUCCESSFUL CYTOSOLIC DRUG RELEASE OF DENDRONIZED MESOPOROUS SILICA NANOPARTICLES.....</b>	<b>94</b>
9.1	Introduction .....	94
9.2	Results and Discussion .....	96
9.2.1	Synthesis and characterization of dendronized MSNs.....	96
9.2.2	Cellular uptake kinetics and cytotoxicity studies .....	99



9.2.3	Specific receptor-mediated cell uptake .....	100
9.2.4	Endosomal escape and drug release.....	101
9.3	Conclusions .....	104
<b>10</b>	<b>A SURFACE ACOUSTIC WAVE-DRIVEN MICROFLUIDIC SYSTEM FOR NANOPARTICLE UPTAKE INVESTIGATION UNDER PHYSIOLOGICAL FLOW CONDITIONS .....</b>	<b>105</b>
10.1	Introduction .....	105
10.2	Results & Discussion.....	108
10.2.1	Microfluidic setup.....	108
10.2.2	Characterization of the flow pattern .....	109
10.2.3	Nanoparticle uptake under flow.....	110
10.3	Conclusions .....	111
<b>11</b>	<b>EXPERIMENTAL METHODS .....</b>	<b>112</b>
11.1	Methods used in Chapter 4 .....	112
11.1.1	Synthesis and preparation of nanoparticles .....	112
11.1.2	Cell culture.....	112
11.1.3	Incubation of cells with nanoparticles.....	113
11.1.4	Live-cell imaging .....	113
11.1.5	Super-resolution imaging of 100 nm nanoparticles .....	114
11.2	Methods used in Chapter 5 .....	114
11.2.1	Synthesis and characterization of silica nanoparticles .....	114
11.2.2	Cell culture.....	115
11.2.3	Incubation of cells with silica nanoparticles .....	116
11.2.4	Atomic force microscopy.....	116
11.2.5	Live-cell imaging .....	116
11.2.6	Cytotoxicity studies .....	117
11.2.7	Statistical analysis.....	117
11.3	Methods used in Chapter 6 .....	118
11.3.1	Extraction of titania nanoparticles from sunscreens.....	118
11.3.2	Characterization of titania nanoparticles .....	118
11.3.3	Cell culture.....	119
11.3.4	Cytotoxicity studies .....	119
11.3.5	Statistical analysis.....	120
11.4	Methods used in Chapter 7 .....	121
11.4.1	Synthesis and characterization of ceria nanoparticles .....	121
11.4.2	Cell culture.....	121
11.4.3	Incubation of cells with ceria nanoparticles .....	121
11.4.4	Live-cell imaging .....	122

11.4.5	Statistical analysis.....	122
11.5	Methods used in Chapter 8.....	122
11.5.1	Synthesis and characterization of platinum-decorated ceria nanoparticles.....	122
11.5.2	Cell culture.....	123
11.5.3	Incubation of cells with platinum-decorated ceria nanoparticles.....	123
11.5.4	Live-cell imaging.....	124
11.5.5	Cytotoxicity studies.....	125
11.5.6	Statistical analysis.....	125
11.6	Methods used in Chapter 9.....	126
11.6.1	Synthesis and characterization of dendronized MSNs.....	126
11.6.2	Cell culture.....	127
11.6.3	Incubation of cells with MSNs.....	127
11.6.4	Live-cell imaging.....	129
11.6.5	Cytotoxicity studies.....	129
11.7	Methods used in Chapter 10.....	129
11.7.1	Microfluidic chip.....	129
11.7.2	Flow characterization.....	130
11.7.3	Uptake experiments.....	130
	<b>BIBLIOGRAPHY.....</b>	<b>131</b>
	<b>LIST OF ABBREVIATIONS.....</b>	<b>145</b>
	<b>ACKNOWLEDGEMENTS.....</b>	<b>147</b>
	<b>LIST OF PUBLICATIONS.....</b>	<b>149</b>

# 1 Introduction

More than 1,600 consumer products introduced to the market contain nanomaterials. This is the current information in a public inventory based on data provided by manufacturers [1]. However, since manufacturers are not required to declare presence of nanomaterials in their products, the actual number on markets worldwide is probably larger than this. Nanomaterials are used in a great variety of applications, ranging from food and sunscreens to textiles and fuel additives. Due to their very small size, nanoscale materials such as nanoparticles (NPs) often display unique physical and chemical properties, creating new possibilities for technological applications. On the other hand, since NPs are of the same size scale as typical cellular components, they can surpass the natural defenses of human organism and lead to permanent cell damages.

With the increasing use of nanomaterials, accidental or intentional human exposure to engineered NPs is inevitable. Comprehensive understanding about potential health impact of NPs is therefore highly needed. Accordingly, interaction of NPs with biological systems has become a very stimulating topic in basic and applied science and engineering. In the last decade, academia, industry, and regulatory agencies have been challenged to develop advanced methods that could help to identify which features make NPs safe or toxic, as well as the underlying mechanisms of nanotoxicity. In a recent press release, the German Federal Institute for Risk Assessment (BfR) highlighted a key question: “How can the safety of nanomaterials be ensured?” [2]. Among other statements, this BfR communication points to the urgent need of reliable methods for assessment of nanomaterials with regard to their physicochemical and toxicological properties.

Having the same key question in mind, the national Priority Program SPP1313: “Biological Responses to Nanoscale Particles” was initiated by the German Research Foundation (DFG) in 2007 and operated until 2014 [3]. Within the interdisciplinary framework of the SPP1313, a research project called NPBIOMEM was started aiming its activities at the “Bioactivity and cellular uptake of distinct nanoparticles in human endothelial cells”. The results presented in this thesis were achieved in close collaboration with the groups forming the NPBIOMEM network: Prof. Dr. A. Reller (University of Augsburg; synthesis and characterization of NPs), Prof. Dr. A. Wixforth (University of Augsburg; microfluidic system and artificial cell membranes), Prof. Dr. M. F. Schneider (Boston University, USA; microfluidic system), Prof. Dr. S. W. Schneider (University of Mannheim; cytotoxicity), Prof. Dr. I. Hilger (University of Jena; cytotoxicity), and Prof. Dr. C. Bräuchle (LMU Munich; live-cell imaging). Additionally, particular results were achieved in

cooperation with the groups of Prof. Dr. T. Bein (LMU Munich; mesoporous silica NPs as drug delivery systems) and Prof. Dr. J. Michaelis (University of Ulm; super-resolution microscopy).

The main routes by which NPs may access the body are lungs, gastrointestinal tract, and skin. In all three cases NPs can reach the bloodstream, where they can interact with endothelial cells covering the inner surface of vessels. These cells play a crucial role in the process of blood flow, while changes in endothelium are often found in a number of diseases. Therefore, endothelial cell lines represent an important model system to investigate the bioactivity and cellular uptake of NPs, and they are extensively used in our studies.

The studies presented here focus on the development and application of advanced live-cell imaging techniques for visualization and quantification of NP-cell interactions. Additionally, these results are complemented by cytotoxicity assays, thus providing insights into the biological effects of NPs on cells. A new method to visualize and rapidly quantify the absolute number of NPs taken up by single cells was developed. This work describes Particle\_in\_Cell-3D, a method based on an innovative approach that integrates high resolution live-cell imaging with quantitative image analysis. Particle\_in\_Cell-3D can be applied to investigate the dose-dependent effects for the risk assessment of NPs.

NPs of different chemical composition (e.g., metals, oxides, and polymers) are synthesized in numerous distinct forms (e.g., different sizes, shapes, and coatings). Our research in the NPBIOMEM project has been concentrated on three widely produced and applied oxidic materials: silica (SiO<sub>2</sub>), titania (TiO<sub>2</sub>), and ceria (CeO<sub>2</sub>) NPs. Silica NPs have found applications in food and beverages, cleaning products, cosmetics, textiles, and sporting goods. Titania NPs are largely used in everyday items, like paints, glues, and personal care products, especially sunscreens. Ceria NPs can be found in many applications, as in ultraviolet absorbers, automotive catalytic converters, and fuel additives. Thus, inhalation, skin contact, and ingestion are all possible routes for these NPs to enter the human body. In order to conduct systematic studies on the biological effects of oxidic NPs at the cellular level, we have synthesized and characterized reasonable quantities of fluorescently labeled NPs optimized for live-cell imaging.

The biological effects of NPs may be cell-specific, meaning that individual cell types respond differently to the entry of identical nanoparticles. Moreover, cells of the same type may react differently to NPs of distinct chemical composition, size, coating, etc. This thesis deals with many aspects of NP-cell interactions. These include studies covering cell type-dependent nanotoxicity and uptake kinetics of silica NPs, the cytotoxicity of coated sunscreen titania NPs of different physicochemical properties, as well as the particle size-dependent uptake of ceria NPs.

The scope of the most recent project is the interaction between endothelial cells and NPs emitted by catalytic converters. Although catalyst-derived NPs are recognized as growing burden added to environmental pollution, very little is known about their health impact. Our studies with platinum-decorated ceria NPs (as model compounds for the actual emitted NPs) focus on their fast uptake and accumulation in mitochondria, the cell's powerhouse.

Additionally, NPs have been designed for nanomedicine and biotechnological applications, such as biosensors, biomarkers, and drug delivery systems. Some NPs are functionalized to specifically target molecules overexpressed on the surface of cancer cells, which are significantly less abundant in normal cells. This therapeutic strategy allows drugs to be delivered into tumor cells with high efficiency and minimal side effects. Mesoporous silica nanoparticles (MSNs) have been extensively studied as drug delivery vehicles due to their excellent materials features, such as good biocompatibility, and large cargo capacity. This work describes newly designed MSNs coated with PAMAM dendrons (branched poly(amidoamine) molecules). We use live-cell imaging to show that dendronized MSNs provide a successful mechanism for cell targeting, endosomal escape, and drug release.

Finally, the last research project focuses on quantitative live-cell imaging applied to measure the influence of physiological flow conditions on the cellular uptake of NPs. The flow is generated by a novel microfluidic device based on acoustic streaming induced by surface acoustic waves. Currently, most *in vitro* experiments are performed under static flow conditions. Therefore, the novel results described here provide a significantly improved framework for future experiments simulating *in vivo* conditions.

Results of this work will contribute to future development of nanotoxicology and nanomedicine, thus promoting the safe use of nanomaterials.

This thesis is organized as follows:

After this introduction (Chapter 1), the next two chapters will provide a general overview about the research fields encompassing this work. Different aspects of the interaction of NPs with biological components and/or systems are described in Chapter 2, which is based on a book chapter written in collaboration with other SPP1313 members [4]. Chapter 3 presents principles of fluorescence microscopy, highlighting the benefits of combining live-cell microscopy with quantitative digital image analysis.

Following the introductory part, the results, discussions, and conclusions of specific project are presented in Chapters 4 to 10 in a partly cumulative way. Chapter 4 describes the Particle\_in\_Cell-3D method in detail, while further applications of this approach are presented in

Chapters 5, 7, 9, and 10. The method is published in *Nanomedicine* [5] and can be downloaded online [6]. Chapter 5 presents cell type-dependent uptake kinetics and cytotoxicity of silica NPs. The results of which are published in *Small* [7]. In Chapter 6, a study on the effects of the physicochemical properties on the cytotoxicity of sunscreen titania NPs is presented. This work is published in the *Journal of Nanoparticle Research* [8]. The particle size-dependent uptake of ceria NPs interacting with endothelial cells is described in Chapter 7. This study appeared in the *Beilstein Journal of Nanotechnology* [9]. Chapter 8 focuses on a recent study on cell membrane penetration and mitochondrial targeting by platinum-decorated ceria NPs (manuscript in preparation). The results on endosomal escape and cytosolic drug release of dendronized mesoporous silica NPs are presented in Chapter 9. This work is submitted for publication [10]. Finally, the novel surface acoustic wave-driven microfluidic system that allows NP uptake investigation under physiological flow conditions is described in Chapter 10. Obtained results are published in the *Beilstein Journal of Nanotechnology* [11]. The experimental methods are described in Chapter 11.

## 2 Biological responses to nanoparticles

*This chapter is based on the following publication:*

*R. Zellner, J. Blechinger, C. Bräuchle, I. Hilger, A. Janshoff, J. Lademann, V. Mailänder, M.C. Meinke, G.U. Nienhaus, A. Patzelt, F. Rancan, B. Rothen-Rutishauser, R.H. Stauber, A.A. Torrano, L. Treuel, and A. Vogt;*

*Chapter 6 "Biological Responses to Nanomaterials" In "Safety Aspects of Engineered Nanomaterials" Eds.: W. Luther and A. Zweck. Pan Stanford Publishing (2013), p. 157-218.*

### 2.1 Introduction

With the advent of nanotechnology the interaction of nanoparticles with biological systems (including living cells) has become one of the most stimulating areas of basic and applied research. Since nanoparticles (NPs) are of the same size scale as typical cellular components and proteins, they can surpass the natural defenses of the human organism and lead to permanent cell damages. Unintentional or purposeful human exposure to NPs is inevitable as they have been increasingly used. However, despite intensive investigations, our current understanding of the biological responses to NPs is still fragmentary [12-14]. Besides the wide use of nanomaterials in industrial products [1], the biomedical use of NPs has also enjoyed increasing interest over the past decade [15]. The ability to manipulate distinct particle features, such as their physical and chemical properties, opens up a variety of possibilities in designing NPs for gene and drug delivery, for diagnostic purposes, or as imaging agents [16-18]. As more data regarding the potential cytotoxic properties of NPs have become available in recent years, the interest in nanotoxicology and in the safety of nanomaterials for biomedical applications continues to increase [12-14, 19].

The biological effects of NPs are not restricted to the nanometer range (1-100 nm), but are also observed for particles of a few hundreds of nanometers. A strict size definition of nanoparticles is therefore questionable in this context and should be avoided [20]. Accordingly, all particles of up to a few hundreds of nanometers described throughout this work are termed nanoparticles (NPs).

This chapter is organized sequentially according to the different aspects of the interaction of NPs with biological components and/or systems: entry routes of NPs into the human body, interaction with blood proteins, interaction with endothelial cells, uptake and intracellular fate, and cytotoxic potential.

## 2.2 Entry of nanoparticles into the human body

The skin, the respiratory system as well as the gastrointestinal tract are considered the main routes by which NPs may access the body (Figure 2.1) [12]. These biological compartments act as natural barriers against external threats, such as pathogens and particulate matter [21]. Although efficient, those are not perfect biological defenses, and NPs have the possibility to overcome them and enter the human body.

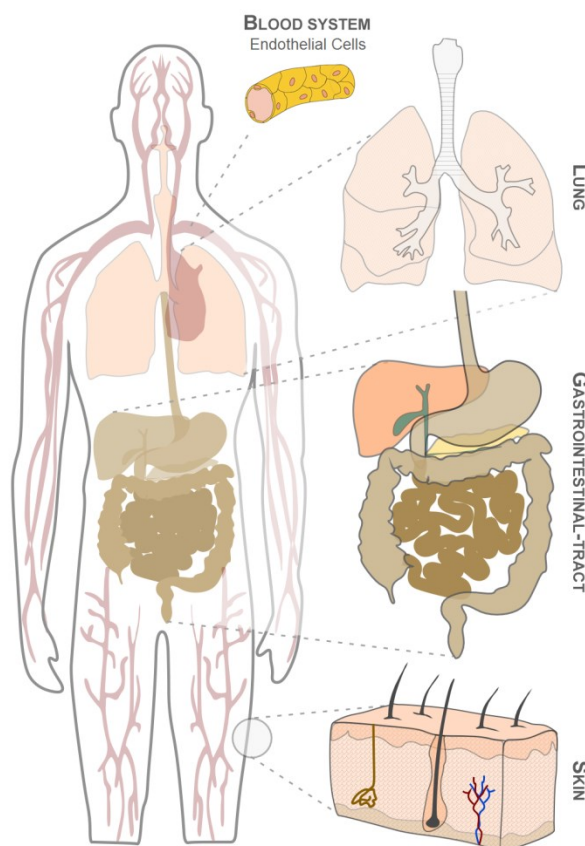


**Figure 2.1 Illustration of the main routes by which NPs may access the body.** Lungs, gastrointestinal tract, and skin are the major NP pathways into the human body. In all three cases, NPs can reach the blood circulation system and interact with endothelial cells. Image of endothelial cells taken from Carmeliet [22].

### 2.2.1 Uptake of nanoparticles by the lung

The lung is considered by far the most important portal of entry for NPs into the human body. The respiratory tract has a large internal surface area ( $>150 \text{ m}^2$ ) and a very thin alveolar-capillary barrier ( $<1 \mu\text{m}$ ). Both characteristics are essential for an optimal gas exchange between the air and blood by diffusion [23].

But not only air is inhaled with every breath we take; millions of particles enter the respiratory system as well. For that reason, our lungs have a series of structural and functional barriers that systematically protect the respiratory system against particulate material [24]. Under normal



conditions, ambient air is efficiently modified and cleansed of much of the larger particulate material by mucociliary activity before being conducted deep into the lungs. Into the deep lungs, the alveolar-capillary barrier comprises the surfactant film, the epithelial cellular layer, macrophages (professional phagocytes), and a network of dendritic cells inside and underneath the epithelium (Figure 2.2) [23, 25-27].

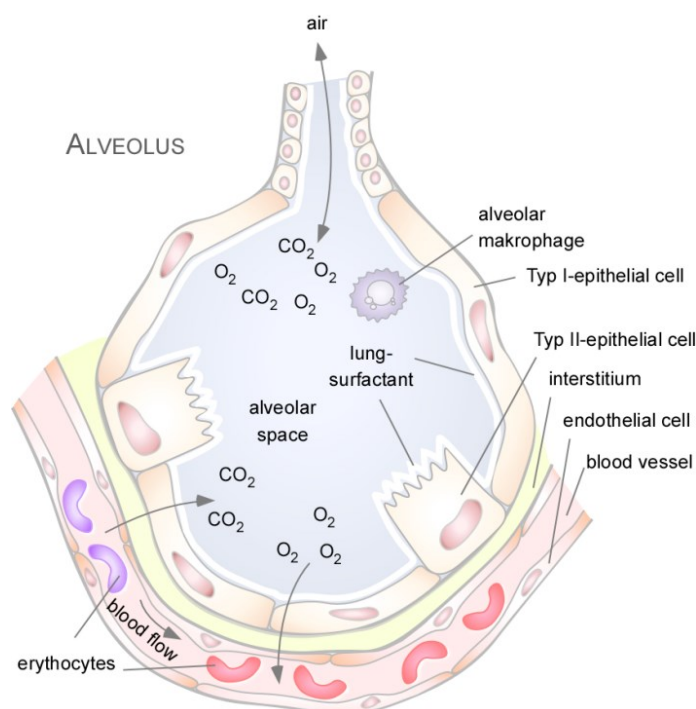


**Figure 2.2 Schematic illustration of an alveolus.** The main task of the alveolar region is gas exchange of oxygen and carbon dioxide with the blood. The alveolar-capillary (or air-blood) barrier can be considered as one of the key targets of inhaled NPs. Note the very thin cellular barrier from airspace to capillary blood flow presented by the epithelial cells, the interstitium (connective tissue), as well as the endothelial cells.

Once deposited into the alveoli, NPs can interact with pulmonary surfactant and pulmonary cells [27]. Depending on the particle properties and the rate of clearance, interaction with lung cells may cause a degree of inflammation or other potentially adverse cellular effects [28]. Particles are cleared by macrophages through phagocytosis (see Section 2.5.1), by mucociliary clearance within the conducting airways, or by translocation through the air-blood barrier [29, 30]. NPs that are able to cross the air-blood barrier of the lung can thus enter the bloodstream and interact with endothelial cells [31-35]. In addition, NPs transported by the blood circulation have been reported to reach secondary organs, including the liver and the heart [32, 36]. Yet most studies indicate a low degree of NP translocation.

### 2.2.2 Interaction of nanoparticles with the skin

With approximately 2 m<sup>2</sup> the skin is the largest organ of the human body. The complete skin, especially its upper layer (stratum corneum), represents the main barrier of the body toward the environment. The stratum corneum consists of cornified dead cells surrounded by lipids. As long as the skin is healthy, an efficient barrier is normally provided. As a consequence, only small fractions of drugs, NPs, and other substances applied topically to skin in dermatology and cosmetics succeed in penetrating through the stratum corneum [37].

At present, distinct skin penetration pathways have been proposed. Among them, the most relevant ones are the intercellular penetration within the lipid layers around the cornified cells and the hair follicular penetration. Hair follicles are invaginations of the epidermis that extend deep into the dermis. They represent interruptions in an otherwise highly tight skin barrier and may act as traps for topically applied particles [37].

In recent years, the follicular route has gained particular importance for the penetration of NPs [37, 38]. Investigations using coated titania NPs of ~100 nm (commonly used as UV filter in sunscreens) revealed an efficient follicular penetration after repeated applications [39]. In this study, most NPs were found in the upper part of the stratum corneum. However, NPs were also detected in the lower parts of the skin in the hair follicles. Interestingly, not all hair follicles are open to interact with NPs, but just those that are active and displaying either sebum excretion or hair growth [40]. In Figure 2.3, a histological section of a porcine hair follicle is presented. The corresponding biopsy was removed 30 min after treatment with a formulation containing fluorescence-labeled polymer NPs with a size of 320 nm. The distribution of the particles in the stratum corneum and in the hair follicle is marked in red.

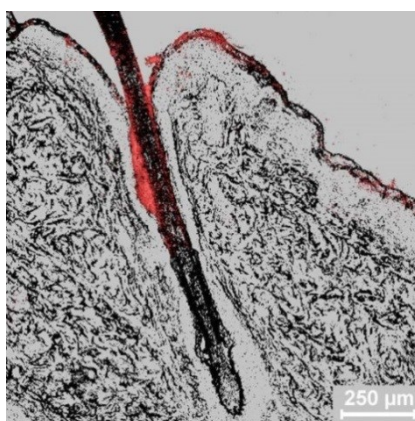


**Figure 2.3 Interaction of NPs with the skin around a hair follicle.** Histological section of a porcine hair follicle showing the distribution of 320 nm polymer NPs (in red) 30 min after topical application. Most NPs are either within the upper layer of the skin (stratum corneum) or in the hair follicle.

Although the intact skin is an efficient biological barrier, a higher degree of NP penetration with subsequent access to the circulatory system can occur in areas of disturbed skin barriers (wounds, lesions, and skin disease) [41-43]. *In vivo* studies in mice demonstrated that the hair follicles are the major sites of such translocation, and diffusion of topically applied NPs into the tissues surrounding hair follicle occurred over the time [44].

### 2.2.3 Uptake of nanoparticles by the gastrointestinal tract

The human gastrointestinal tract is a complex organ system responsible for the digestion of food, absorption of nutrients, and elimination of waste. It has a large absorptive mucosal surface area of about 32 m<sup>2</sup> [45], providing an attractive site for NP uptake [46]. External sources of NPs found in the gastrointestinal tract are food (e.g., table salt, dry foods and supplements), personal care products (e.g., toothpaste and lipstick), and pharmaceuticals [1, 41]. In addition, inhaled NPs that are cleared by the mucociliary activity in the lungs can also be partially ingested [41].

The gastrointestinal tract is the main route for macromolecules to enter the body, and ingested material will come in close contact with the epithelium of small and large intestines. The mucosal barrier that line the luminal surface of the small and large intestines is based on the columnar layer of epithelial cells (enterocytes) [41, 46]. The enterocytes are covered by the glycocalyx, a thick network of glycoproteins and polysaccharides, and by the mucus, a lubricant diffusion barrier that is constantly supplied by goblet cells. Consequently, NPs in the intestinal lumen first come in contact with these two layers. If the mucus and the glycocalyx are penetrated, the final NP translocation to the bloodstream is still strictly controlled by the epithelial cells connected to each other by tight junctions (Figure 2.4) [46].

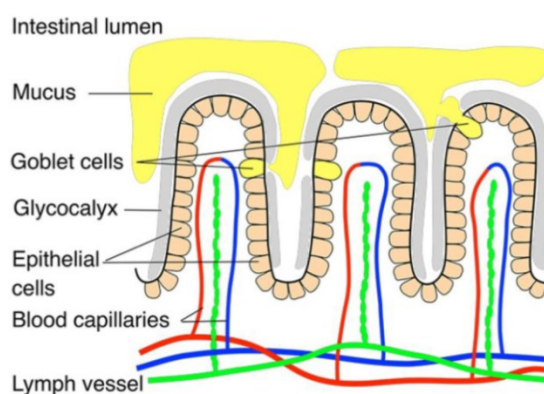


**Figure 2.4 Schematic overview of the columnar layers and main components lining the intestinal walls.** A tight layer of epithelial cells (enterocytes) lines the undulated construction of the gut walls. The enterocytes are covered by the glycocalyx and also by the mucus secreted by goblet cells. Ingested NPs in the intestinal lumen can be translocated to the blood capillaries (or to the lymph vessels) if they succeed in overcoming this highly regulated physiological barrier. Figure taken from Sinnecker *et al.* [46].

Most studies on ingested NPs indicate a rather low NP translocation rate. As much as 98 % of particles are normally excreted in the feces within the first 48 h, and most of the remainder is eliminated via urine [41]. In line with these results, the fate of ingested model polystyrene NPs (20–200 nm) in the gut was investigated by Sinnecker *et al.* [46]. Using an isolated rat intestine model, they showed that the small intestinal tract provides an effective barrier against NP uptake. Upon an intestinal exposure to large doses of NPs, most particles did not reach the epithelium layer, but were either trapped in the mucus or directly discarded from the gut. However, other studies have showed that NPs can overcome the mucosal barrier and enter the circulatory system [41, 47]. There are reports in the literature showing that ingested NPs can even translocate to other organs, such as liver, spleen, kidney, lungs, brain, and lymph nodes [42, 48]. In general, the degree of NP translocation via the gastrointestinal tract will be influenced by many factors, including particle size, surface chemistry, dose, exposure time, and constituents of intestinal fluid [41, 49].

### **2.3 Interaction of nanoparticles with proteins**

If NPs succeed in penetrating across one of the abovementioned barriers, they will reach the circulatory system and be exposed to components of the body fluids, including proteins. The interaction of NPs with proteins normally results in a corona of surface-absorbed proteins [50–52]. This so-called “protein corona” forming around the NP can define the biological identity of the NP, and the efficiency of this interaction may influence the translocation behavior in biological systems [42]. Understanding the formation and persistence of the protein corona is important for the elucidation, interpretation and assessment of the biological effects of NPs. The formation process is essentially a rapid competition of proteins and other biomolecules for binding to the NP surface.

In typical body fluids and intracellular environments, the protein concentrations can be up to  $0.35 \text{ g mL}^{-1}$  [50], comprising more than 3,000 different proteins at different individual concentrations [53]. While highly abundant proteins will likely dominate the protein corona for short time periods, proteins with lower abundance but higher affinities might prevail on longer timescales [13, 54]. A key aspect of the adsorption of proteins onto NP surfaces is that it can lead to structural changes within the protein and hence altered protein conformations. However, the exact driving forces and mechanistic details of protein unfolding at NP surfaces remain unidentified and are a focus of current research [13, 55].

## 2.4 Interaction of nanoparticles with endothelial cells

Additionally to the interaction with proteins, NPs that reach the bloodstream will be in contact with endothelial cells – the cells that line the inner surface of the blood vessel system (see inset in Figure 2.1) [31, 42]. Endothelial cells form the interface between blood and tissue and have strong anti-thrombotic and anti-inflammatory characteristics, playing a crucial role in the process of physiological blood flow. By contrast, an altered endothelial cell function can be found in almost all diseases of the respiratory, neurologic and cardiovascular system [22, 56]. Endothelial cells are therefore ideally suited as a model system to investigate the cellular uptake and toxicity of nanoparticles. In the present work, two endothelial cell lines were used; namely HUVEC (human umbilical vein endothelial cells) and HMEC-1 (human microvascular endothelial cell).

## 2.5 Cellular uptake mechanisms

The cell plasma membrane forms an effective selective barrier between the cytosol and the extracellular environment. The most abundant molecules forming the cell membrane are lipids, such as phospholipids and cholesterol. Lipids are responsible for the structural integrity of the membrane, which can be regarded as two parallel monolayers with their polar groups on the outside surface (inner and outer surfaces) and the non-polar tails pointing inward. Within the lipid bilayer, the cell membrane contains a variety of polysaccharides and proteins [57, 58].

Transfer of molecules or cargo of any kind across the membrane can be either passive, without consumption of chemical energy, or active, requiring the cell to expend energy. Small molecules such as saccharides and amino acids enter the cell through mediated transport involving specialized transporter proteins. Larger objects such as proteins and nanoparticles, however, require different entry routes [59].

Surface chemistry, particle size and shape are usual factors governing the uptake efficiency of NPs as well as the route to enter the cell [60-63]. The conventional entry routes belong to the process of endocytosis; though direct translocation through membrane holes (as described in Section 2.5.3) can occur for special types of macromolecules and NPs.

During endocytosis the plasma membrane basically wraps the cargo to be internalized. The membrane deformation pinches off on the inside of the cell by creating an endocytic vesicle (endosome) that contains membrane components, fluid, and the captured cargo. The vesicular cargo is shielded from the cytosol inside early and late endosomes. Late endosome deliver the cargo molecules to lysosomes, where they are degraded [64-66]. Endocytosis regulates the access into the cells and plays a crucial role in complex physiological process, such as immune

response, tissue and organ development, intercellular communication, and cellular and organismal homeostasis [64].

Different endocytic pathways have been described so far. They occur by several diverse mechanisms that can be divided into two categories: phagocytosis and pinocytosis [64, 65]. Phagocytosis comprises the uptake of large particles and is typically restricted to specialized mammalian cells. Pinocytosis, on the other hand, comprehends the uptake of small particles, fluid, and solutes; it occurs in all cell types by different basic mechanisms. The most relevant and better understood mechanisms of pinocytosis are macropinocytosis, clathrin-mediated endocytosis, and caveolin-mediated endocytosis [64]. The most important endocytic pathways are schematically depicted in Figure 2.5 and are further described in the following sections.

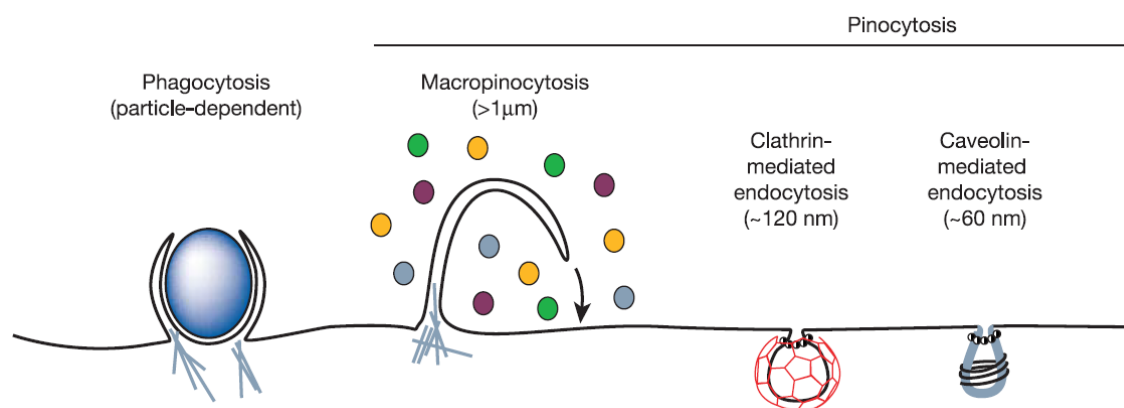


**Figure 2.5 Endocytic pathways into mammalian cells.** Distinct uptake pathways can be separated into two broad categories: phagocytosis (or cell eating) and pinocytosis (or cell drinking). Pinocytosis can be further categorized into other mechanisms. Distinct endocytic pathways differ with regard to the mechanism of vesicle formation, the size of the endosome, and the characteristics of the cargo. Figure adapted from Conner & Schmid [64].

### 2.5.1 Phagocytosis

Phagocytosis is characterized by the actin-driven assembly of plasma membrane protrusions that embrace and engulf large particles (Figure 2.5). It is performed mainly by specialized cells, including macrophages and monocytes. This endocytic mechanism runs to eliminate large pathogens, such as bacteria, and large remains, as those from dead cells. Phagocytosis is a highly regulated and active process that involves specific surface receptors and signaling cascades. Diverse modes of phagocytosis exist, and they are defined by the type of particle to be ingested and the given receptor that recognizes it [64].

## **2.5.2 Pinocytosis**

### **2.5.2.1 Macropinocytosis**

Macropinocytosis describes a form of internalization that frequently involves actin-driven protrusions from the plasma membrane. These membrane ruffles wrap the cargo and subsequently fuse, resulting in the uptake of large volumes of extracellular components (Figure 2.5). Macropinocytosis is induced in a variety of cell types upon stimulation by growth factors or other signals [59, 64].

### **2.5.2.2 Clathrin-mediated endocytosis**

Clathrin is a protein that forms a three-legged structure called triskelion. Clathrin triskelions can spontaneously self-assemble into closed polygonal shapes. Clathrin-mediated endocytosis is characterized by a sequential assembly of cytosolic coat components to form a clathrin-coated pit (Figure 2.5). The clathrin-coated pit eventually invaginates and pinches off into the cytosol to form an endocytic vesicle, and the coat constituents are recycled for reuse [64, 67]. A large number of membrane proteins and nanomaterials enter cells by clathrin-mediated endocytosis. It occurs in all mammalian cells and helps to provide the continuous uptake of essential nutrients. For example, iron-laden transferrin (that binds to transferrin receptors) and cholesterol-laden low-density lipoprotein (LDL) particles (that binds to the LDL receptors) are constantly internalized by this pathway [59, 64].

### **2.5.2.3 Caveolin-mediated endocytosis**

Caveolins are proteins that play a major role in the formation of small flask-shaped plasma membrane invaginations, or caveolae. They act as scaffolding proteins to generate caveolae microdomains, which constitute a special kind of membrane rafts. Caveolae are present on many cell types. They have an important role in the regulation of vasodilation, intracellular cholesterol trafficking, and transcellular transporting of serum proteins from the bloodstream into tissues [59, 64].

## **2.5.3 Direct translocation through the cell plasma membrane**

In contrast to conventional endocytic pathways, cationic NPs and cell-penetrating peptides (CPPs) can enter cells by a direct translocation move across the plasma membrane. This unconventional pathway is characterized by rapid cellular uptake, without perceptible cell membrane disruption and cytosolic location of NPs/CPPs [68, 69]. CPPs [70], 8 nm CdSe/ZnS core/shell quantum dots (coated with D-penicillamine) [71] and ultrasmall noble metal NPs (typically smaller than ~10 nm), such as gold [68, 69, 72-74] and platinum [75, 76], were

observed to perform a direct translocation across the plasma membrane. Notably, our recent results described in Chapter 8 show that  $\sim 50$  nm ceria NPs decorated with ultrasmall platinum NPs (2–5 nm) can also enter cells by a direct translocation mechanism.

The mechanisms of direct translocation, however, are not completely understood. Recently, Lin & Alexander-Katz [68] used molecular dynamics simulations to demonstrate that membrane holes are induced by 2.2 nm gold NPs (as well as distinct CPPs) due to the alteration of the local transmembrane potential. The induced holes were proposed to assist the spontaneous translocation of cationic NPs and CPP into the cytosol. After translocation, the gold NP can move freely in the cytoplasm region and the membrane rapidly resealed itself (Figure 2.6).

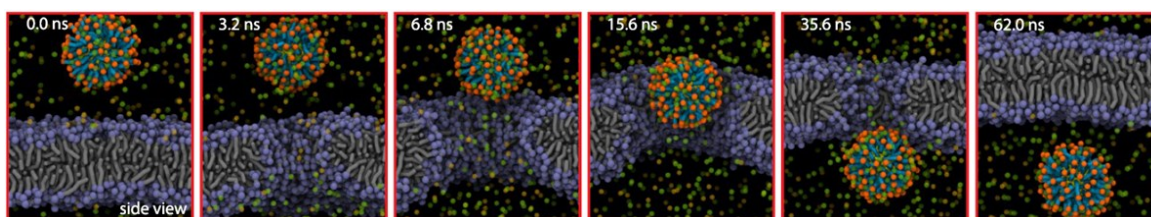


**Figure 2.6 Direct translocation through the cell membrane.** Molecular dynamics simulations were used to demonstrate the direct translocation of cationic NPs and cell-penetrating peptides across lipid bilayers. Membrane holes are induced under a transmembrane potential. The figure shows side view snapshots of a 2.2 nm gold NP and a model membrane at the beginning of the simulation (0.0 ns) and at further time points throughout the very fast translocation process. The gold NP penetrates through the transient hole and the membrane reseals itself. Adapted from Lin & Alexander-Katz [68].

## 2.6 Trafficking and intracellular distribution of nanoparticles

When studying the interactions of NPs with cells, it is of central interest to assess: the amount of NPs that are internalized; which mechanisms are operative to promote such internalizations; and how NPs distribute throughout the cell. Fluorescence techniques in live-cell imaging (see Chapter 3) are a powerful tool to answer such questions.

For example, fluorescence-labeled NPs can be followed during their pathway into the cell. The positions of the particles are determined for a series of consecutive frames in time, resulting in detailed trajectories of their movements. As a result, information about the location and velocity of single NPs on their way into and throughout the cell can be obtained with great precision [77]. This technique was used to elucidate the typical trajectory of a NP that is internalized by endocytosis. Interestingly, the trajectory can be divided into three different phases [78]. In phase I, the NP attaches to and moves with the cell membrane while an endocytic vesicle is formed. This phase is characterized by slow directed motion with an additional diffusion component. After the first phase, the loaded vesicle pinches off from the cell membrane and is



released into the cytoplasm. Phase II is characterized by a mixture of free, anomalous, and also confined diffusion. Free diffusion is often hindered by the local micro-environment, such as the cytoskeleton and large cell organelles. Phase III is distinguished by a long-range active transport of the particle, located inside the vesicle, throughout the cell. This transport is mediated by motor proteins that travel along the cellular microtubules with velocities up to  $4 \mu\text{m s}^{-1}$ . This three-phase behavior is characteristic for NP uptake and can be found for many particle types, while the relative duration and the order of appearance of phases II and III can vary [78, 79].

The trajectories of 310 nm silica NPs in a living cell are shown in Figure 2.7. Selected trajectories of single silica NPs trafficking into and throughout a human cervix carcinoma cell (HeLa) are numbered and displayed as overlays (Figure 2.7A). The detailed movement of particle number 3 is depicted in Figure 2.7B. Its tracking lasted 5 min and started when the particle was about to be internalized. During phase I (in cyan) the particle moved with slow diffusive drift and was finally internalized via endocytosis. Thereafter, phase II and phase III (traces in blue and red, respectively) occurred in alternate orders.

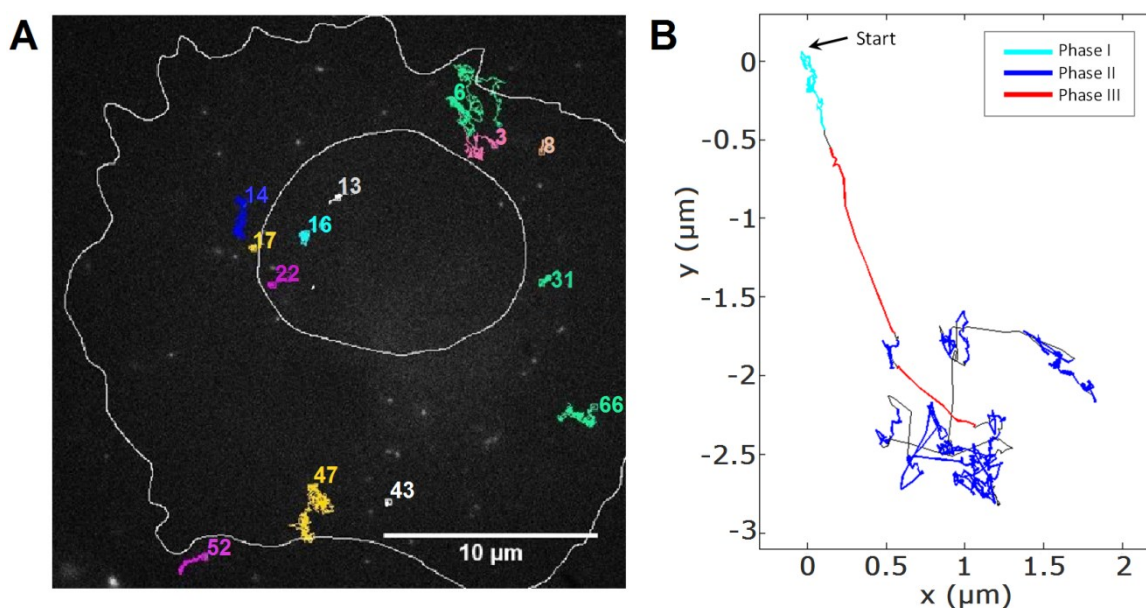


**Figure 2.7 Trajectory of 310 nm single silica NPs during uptake by a cell. (A)** Plasma membrane and nuclear outlines of a HeLa cell. Selected trajectories of silica NPs interacting with the cell were recorded during 5 min. Particles 13, 16 and 22 are not localized inside the nucleus, as could be suggested by the two-dimensional image, but rather are located above the nucleus. **(B)** Detailed tracked movement of particle 3. The initial point of the NP is indicated by the arrow. During phase I (in cyan), the particle attaches to the cell membrane and is slowly transported. Once the particle is inside the cell, phase II and phase III can occur in alternate orders. In the present case, just after entering the cell, the NP inside an endocytic vesicle undergoes a long-range active transport and is rapidly moved with motor proteins along microtubules, characterizing a phase III (in red). Stop and go movements for binding and unbinding of motor proteins to microtubules is also typical and can be seen between the red traces. Next, the NP enters in phase II (in blue) and moves mostly by anomalous and confined diffusion, as intracellular structures hinder free diffusional movement.

In addition to the detailed dynamics of internalization, the number of particles taken up by an individual cell is of substantial toxicological interest. A novel method to quantify the uptake and visualize the intracellular distribution of NPs, Particle\_in\_Cell-3D, is fully described in Chapter 4.

## **2.7 Cytotoxic potential of nanoparticles**

NPs that enter the human body (see Section 2.2) may cause several cytotoxic responses, including the enhanced expression of pro-inflammatory mediators [80], DNA strand breaks [81], and the generation of reactive oxygen species [82]. The combinations of these cellular responses following NP exposure are interesting. The association between oxidative stress and inflammatory responses are widely described in the literature as leading to decreased cellular function [83, 84], which is strongly connected to the onset of adverse health effects [85-87].

Substantial interferences of NPs with the subcellular metabolic pathways were shown to be associated with the generation of radicals that induce damage on the protein, lipid or nucleic acid level. The cellular response is the induction of apoptosis (programmed cell death) or necrosis (dead of a cell by injury or other pathologic factors) [13, 88].

The fundamental understanding of the biological responses to NPs therefore requires a thorough knowledge of NP-induced effects on cells. Yet, assessing and interpreting these effects represents a complex task [14, 19]. Nevertheless, several common features and biological effects of NPs have been recognized. Overall, the cytotoxic potential of NPs are related to the physicochemical properties of particles (size, shape, material, surface charge, coating, etc.) and are dependent on the assay and conditions used (e.g., biological medium, NP dose, exposure time) as well as the cell type(s) employed [13, 14, 62, 63].

## **2.8 Conclusions**

Taken together, the biological responses to NPs depend strongly on the NP particular physicochemical properties and are influenced by the biological environment and conditions. These factors combined determine the NP interactions with the biological barriers, the mechanisms and the extent of uptake, together with their intracellular fate. In view of the large variability of possible NP features that can be manufactured today, much work remains to be done to fully elucidate and understand potential adverse cellular effects, particularly if they are intended for the use in biomedical applications. Hence, the emerging science of nanotoxicology and nanomedicine requires a thorough understanding of the physicochemical properties of NPs combined with a profound knowledge of the molecular mechanisms of cells, which ultimately trigger the biological responses.

## **3 Quantitative live-cell imaging**

### **3.1 Introduction**

Fluorescence microscopy of live cells has become an essential method of modern cell and molecular biology [89]. The strength of live-cell fluorescence imaging lies in the specificity with which proteins, cellular structures and other objects of interest can be labeled, imaged and quantitatively analyzed [90, 91]. In this thesis, highly sensitive live-cell imaging techniques combined with quantitative image analysis provide powerful tools for studying interactions between fluorescently labeled nanoparticles and single cells in great detail. This chapter provides an introduction to key aspects of quantitative live-cell imaging. The following section summarizes fundamentals in fluorescence. Next, fluorescence live-cell imaging is presented, with emphasis to spinning disk confocal microscopy. Finally, the last section describes crucial aspects of quantitative image analysis of biological systems like cells.

### **3.2 Principles of fluorescence**

In fluorescence microscopy it is required that the objects of interest fluoresce. Fluorescence is the emission of light occurring within nanoseconds after light absorption [89]. Molecules featuring fluorescent properties (fluorophores) typically have some degree of conjugated double bonds. Fluorophores often have ring structures with pi bonds resulting in outer orbital electrons distributed over a relatively large area. In general, the energy needed to excite a molecule decreases with the number of conjugated bonds [89, 92].

When light is absorbed by a fluorophore, the complete energy of an absorbed photon is transferred to the molecule. The photon's energy is inversely proportional to its wavelength. When the absorbed photon has enough energy, it can excite an electron to a higher orbital (higher energy level), and the atom or molecule is then said to be in an excited state. Excited states tend to be relatively short-lived and eventually the molecule returns to its electronic states of lower energy by losing its excess energy. Fluorophores returning to low-energy levels may involve radiative transitions, such as fluorescence and phosphorescence, as well as radiationless transitions, for example, internal conversion, vibrational relaxation, and intersystem crossing (Figure 3.1) [89].

The absorbance and the emission spectra of a fluorophore are related to the magnitude of the energy gaps needed to bring a molecule from one energy level to another. Since the range of

fluorescence emission starts from the lowest energy level of  $S_1$ , this range is typically smaller than the range of energies that can excite the same molecule. This means that the energy of emitted photons is in average lower than the energy of the absorbed ones. The difference between the exciting and emitting energies (and wavelengths) is known as Stokes shift. Stokes shift plays a crucial role in fluorescence microscopy as it permits the spectral separation of excitation and emission light [89]. For example, by means of dichroic mirrors, fluorescence microscopes are designed to block specific excitation laser wavelengths, while the emission signal from the specimen can reach the camera to form an image. Therefore, knowledge about absorbance and emission spectra of fluorophores is an integral part of live-cell imaging, being constantly used to achieve optimal exposure and detection conditions.

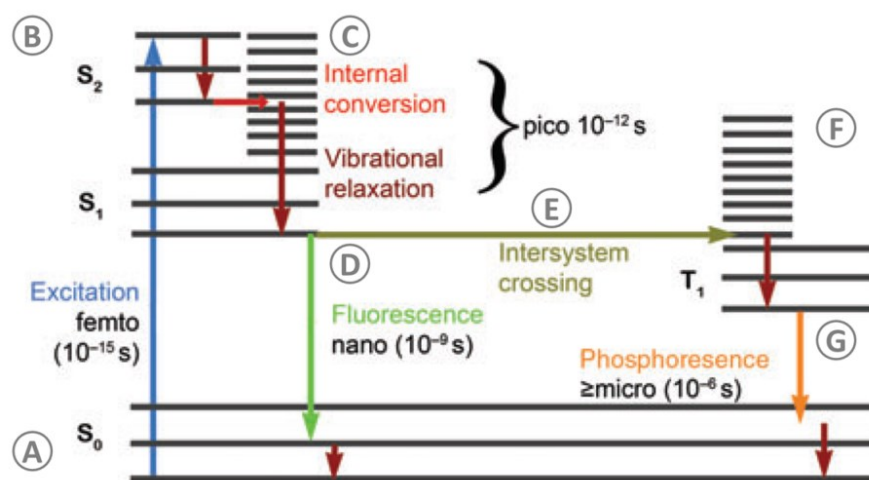


**Figure 3.1** Details of excitation and emission processes displayed in a Jablonski diagram.  $S_0$  is the electronic ground state. It represents the energy of a molecule not excited by light.  $S_1$  and  $S_2$  are excited singlet states of the molecule in which an outer electron is promoted into an orbital of higher energy. Note the typical duration of distinct energy states of a molecule during excitation and emission processes. (A) The blue arrow on the left exemplifies the energy of a photon that is absorbed by the molecule, causing a transition from  $S_0$  to  $S_2$  within femtoseconds. (B) Once excited, the molecule can lose the absorbed energy by a number of different pathways and return to  $S_0$ . (C) Internal conversion (transition between electron orbital states, such as  $S_2$  to  $S_1$ ; red arrow) and vibrational relaxation (transfer of fluorophore's vibrational energy to nearby molecules; brown arrows) typically bring the molecule back to the lowest vibrational energy level of  $S_1$ . (D) The most likely final path back to the ground state in good fluorophores is the spontaneous emission of a photon within nanoseconds (green arrow). The energy (and wavelength) of the emitted photon will be in the range covered by the lowest vibrational state of  $S_1$  and one of the vibrational or rotational states of  $S_0$ . The range of possible wavelengths this photon can have results in the emission spectrum of the fluorophore. (E) Another path of energy loss occurs through a forbidden transition from  $S_1$  to overlapping triplet state vibrational energy levels, such as  $T_1$ , present in many molecules (intersystem crossing; gray arrow). (F) Further internal conversion can bring the molecule to the lowest energy of  $T_1$ . (G)  $S_0$  may eventually be reached by triplet-state molecules without radiative emission; however, in many cases photon emission known as phosphorescence occurs (orange arrow). Since it depends on another unlikely forbidden transition, this process can take microseconds. Adapted from Lichtman & Conchello [89].

### 3.3 Live-cell imaging

Fluorescence microscope techniques provide powerful tools to investigate almost any cellular process under the microscope [90]. Multicolor imaging is extensively used for the simultaneous visualization of distinct cellular and subcellular components, as well as other materials of interest, such as nanoparticles. This approach is possible due to the wide range of available synthetic fluorophores, live cell imaging dyes, and fluorescent protein tags [89, 90, 93]. The main experimental challenges in (multicolor) live-cell imaging are maintaining a physiological environment for cells and minimizing photodamage, while extracting data with the most spatial and temporal resolution possible [90, 94]. Wide-field, confocal scanning, and spinning disk confocal microscopes are setups commonly applied in fluorescence microscopy of living cells [93].

Wide-field microscopes offer excellent temporal resolution and submicrometer spatial resolution for observation of dynamics in live cells. However, background fluorescence originating from out-of-focus planes is not discriminated, resulting in a blurry image of 3D objects, such as cells and tissues [95]. This problem was solved with the advent of confocal microscopy, in which out-of-focus signal is effectively blocked by a pinhole positioned before the detector. This main feature of confocal microscopes allows the construction of 3D images of thick specimens by means of successions of thin optical sections acquired along the Z-direction [92, 95]. Nevertheless, laser scanning microscopes suffer from very limited acquisition speeds, as the specimen is raster scanned point by point by a single-beam laser light. The most certain approach to reduce photodamage is to limit excitation light exposure as much as possible. One of the best solutions for multicolor 3D live-cell imaging in real time is spinning disk confocal microscopy (SDCM). SDCM is the most important high-resolution method for imaging intracellular dynamics [90]. It combines the advantages of scanning confocal microscopy with high-performance real time imaging and is especially appropriate to imaging for quantitative analysis [96].

In spinning disk confocal microscopy, two fast rotating disks with a large number of either pinholes or microlenses are used to parallelizing confocal imaging [94]. Thus, as the disks rotate, thousands of discrete points are simultaneously raster scanned over every location in the specimen. Microlenses are used to guide and focus light onto perfectly aligned pinholes [92, 97]. The unique pinhole spiral pattern (Nipkow disk) provides homogeneous illumination and increased light throughput. This results in a dramatic reduction of excitation light exposure when compared to laser scanning and wide-field microscopes. Taken together, spinning disk

microscopes are capable of multicolor 3D imaging of living cells with high resolution and minimal specimen photodamage [97].

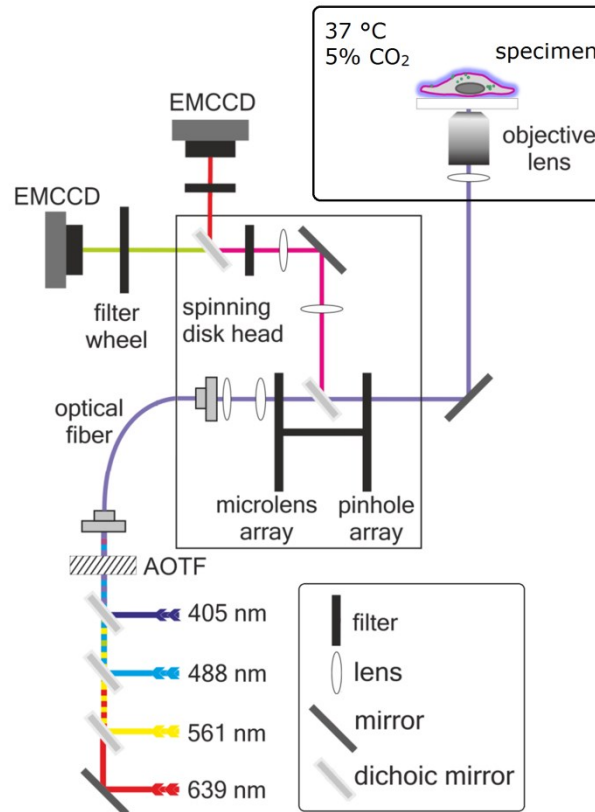


**Figure 3.2 Spinning disk confocal microscope setup.** The intensity of the laser light of different wavelengths (405, 488, 561, 639 nm) is controlled by an acousto-optic tunable filter (AOTF) device. Laser light (purple line) is then guided through the spinning disk head and focused on living cells by the microscope objective. Cells are kept under controlled physiological conditions. A fraction of the fluorescence emission is collected by the objective to be measured by two electron multiplying charge-coupled device (EMCCD) cameras. Before reaching the detectors, the emitted signal travels back the optical path until being reflected by a dichroic mirror positioned between the disks. Next, the emission beam is divided into two image channels (red and green lines) according to the wavelength set by another dichroic mirror. Fluorescence emission is split into two discrete wavelength bands that are transferred to the respective cameras. This allows simultaneous two-color imaging. Further colors can be imaged by using sequential illumination and the filter wheel. Additional filters help to eliminate cross-talk between channels. Lenses and mirrors are used to regulate the light beams throughout the setup. Adapted from a figure kindly provided Dr. Veronika Weiß.

Lateral resolution ( $r$ ) in SDCM is essentially the same as in wide-field or confocal fluorescence microscopy. It is given by  $r = 0.61 \cdot \lambda / NA$ , where  $\lambda$  is the wavelength of the excitation light and  $NA$  is the numerical aperture of the objective [97]. Calculations of axial resolution in SDCM are intricate and there is no simple equation to determine it. In addition to physical configurations of the microscope (e.g., pinhole size and objective numerical aperture), axial resolution is also influenced by a variety of specimen parameters, such as labeling patterns and sample thickness.

As a general rule, axial resolution in SDCM approximates that of scanning confocal microscopes and is typically three to four times larger than the lateral resolution [92, 96].

Recent developments in imaging have enhanced the resolution of light microscopes below the diffraction limit [93]. The Nobel Prize in Chemistry 2014 was awarded for the development of super-resolved fluorescence microscopy techniques. Stimulated emission depletion (STED) microscopy [98], PALM (photo-activated localization microscopy) [99], and STORM (stochastic optical reconstruction microscopy) [100] can currently achieve resolutions of about 20 nm. These approaches can be applied to live cells; however, there are still limitations to overcome. The most important ones are related to severe photodamage caused by high laser powers and long exposure times commonly used in these techniques [101].

### **3.4 Quantitative image analysis**

Quantitative image analysis is used to investigate many different questions about biological specimens, including living cells. There has been a huge increase in the use of image analysis to quantify fluorescence microscopy images [102, 103].

Image analysis is mostly performed on digital images. A digital image is formed when the optical image of the specimen is recorded by a detector (normally a charge-coupled device camera). The detector consists of a 2D grid of equally sized pixels. During image acquisition, photons detected at each pixel are converted into intensity values that correlate with the number of collected photons. This means that pixel intensity is related to the number of fluorophores in the corresponding imaged region of the sample [92, 103]. Notably, the intensity values of digital images do not only contain the signal of interest, but also background and noise. A common source of background signal is out-of-focus fluorescence, which is significantly blocked in confocal microscope setups, including SDCM. Poisson noise is intrinsic to photon detection and cannot be eliminated. Noise originating from the detector (thermal and readout noise) can be reduced to very low levels, as in modern electron multiplying charge-coupled device (EMCCD) cameras [97, 103]. Optimizing live-cell imaging is very important to ensure accurate and meaningful quantification measurements.

Important applications using live-cell imaging combined with quantitative approaches are colocalization [104], fluorescence resonance energy transfer (FRET) [105], fluorescence recovery after photobleaching (FRAP) [106], single-particle tracking [77], and quantitative measurements of intensity information in different cellular compartments [103].

Image analysis of biological microscopy data typically requires algorithms written as a series of simple programming commands (e.g., macro or script). The algorithm thus defines a specific sequence of operations that are consistently applied to a set of images [107]. ImageJ is the most popular multipurpose image-analysis tool [102, 107]. Many digital methods are available within this software aimed at accomplishing various image-analysis tasks in many different areas of biological research [102]. Analyses of biological image data normally share similar general goals that will include one or more of the following procedures: segmentation of objects of interest; reconstruction of image volumes from many overlapping parts; tracking objects across space and time; and quantifying the local concentration of objects of interest [103, 107]. The subject of the next chapter is Particle\_in\_Cell-3D, an ImageJ digital method that executes a series of image analysis commands for achieving: detection and segmentation of optical slices of single cells; reconstruction of cell volumes in 3D; measurements of intracellular nanoparticles; and finally, creation of a 3D color-coded image of nanoparticles and cells.



## 4 Image analysis method 'Particle\_in\_Cell-3D'

*This chapter is based on the following publications:*

*Adriano A. Torrano, Julia Blechinger, Christian Osseforth, Christian Argyo, Armin Reller, Thomas Bein, Jens Michaelis, and Christoph Bräuchle;*

*"A fast analysis method to quantify nanoparticle uptake on a single cell level."*

*Nanomedicine (Lond) 8, 1815-1828 (2013).*

*Adriano A. Torrano and Christoph Bräuchle;*

*"Precise quantification of silica and ceria nanoparticle uptake revealed by 3D fluorescence microscopy."*

*Beilstein Journal of Nanotechnology 5, 1616-1624 (2014).*

### 4.1 Introduction

Measuring the interaction between nanomaterials and cells is a mandatory step for the investigation of nanoparticles (NPs) designed for medical treatment, and also for a correct risk assessment of engineered NPs. In both cases, knowledge regarding the kinetics of particle internalization reveals the dose as a function of time and allows the investigation of a variety of parameters on which the uptake behavior might be dependent. Typical examples are NP characteristics such as size, morphology, chemical composition, surface charge and functionalization [13, 108, 109]. What all these investigations have in common, though, is the need for a fast and accurate method to quantify nanoparticle uptake by cells.

*In vitro* cell culture experiments are well-known models to study the uptake of NPs into human cells. Basically, a monolayer of cells is grown on the bottom of a chamber slide and NPs are added to this culture to interact with the cells.

Fluorescence microscopy is commonly the method of choice to visualize this interaction because it can be performed on live cells with high spatial and temporal resolutions. Finally, outcomes of the uptake process are normally assessed via qualitative and semiquantitative analyses of images.

The need for a method to rapidly quantify the absolute number of NPs internalized by cells led us to the development of a highly innovative method that integrates high resolution confocal microscopy with automatic image analysis. This method is called Particle\_in\_Cell-3D and is described in detail in this chapter. In addition, Section 4.3.2 illustrates how Particle\_in\_Cell-3D was successfully applied to measure the uptake of 80 nm mesoporous silica NPs into HeLa cells,

and Section 4.3.3 describes how it was used to precisely quantify the absolute number of 100 nm polystyrene NPs forming agglomerates of up to five particles. Since its development, Particle\_in\_Cell-3D has been extensively applied. Further applications of our method are presented in Chapters 5, 7, 9 and 10.

This method was developed together with Dr. Julia Blechinger (Group of Prof. Dr. C. Bräuchle; LMU Munich). It is the result of a successful cooperation project involving the synthesis of mesoporous silica NPs by Dr. Christian Argyo (Group of Prof. Dr. T. Bein; LMU Munich), the synthesis of amorphous silica NPs by Dr. Rudolf Herrmann (Group of Prof. Dr. A. Reller and Group of Prof. Dr. A. Wixforth; University of Augsburg), and stimulated emission depletion (STED) microscopy by Dr. Christian Osseforth (Prof. Dr. J. Michaelis; University of Ulm).

## 4.2 The Particle\_in\_Cell-3D ImageJ macro

Particle\_in\_Cell-3D is a custom-made macro for the widely used ImageJ software [107] and can be downloaded from the ImageJ Documentation Portal [6]. It is a semiautomatic image analysis routine designed to quantify the cellular uptake of NPs by processing image stacks obtained by two-color confocal fluorescence microscopy. One emission channel is reserved for the plasma membrane and the other one for the NPs. This means that cell membrane and particles must be fluorescently labeled with spectrally separable markers. The two image stacks acquired can then be processed by Particle\_in\_Cell-3D.

Once the images are loaded, it will execute a series of ImageJ commands to accomplish its goals. The initial part (files selection, input of analysis parameters and 3D reconstruction of the cell) are user-assisted. After these preliminary steps, automatic processing takes place (Figure 4.1). Particle\_in\_Cell-3D uses the image of the membrane to define two subcellular regions of interest: intracellular volume and membrane region. Each particle (or agglomerate of particles) is color-coded according to its location and quantified according to its fluorescence intensity.

A final analysis report delivers information about the position of each object, the number of NPs forming that object, and its location in x,y,z coordinates. All input parameters, processed images, and results are saved and can be accessed at any time. Furthermore, as a calibration experiment is needed for measuring the fluorescent intensity of individual NPs, Particle\_in\_Cell-3D has a routine to perform these measurements.

### 4.2.1 Main features

The main advantages of this method are its speed, reliability and accuracy. The complete analysis of one cell is performed in a few minutes. Moreover, the results are consistent, that is to say, Particle\_in\_Cell-3D substitutes the subjective character of human-assisted image analysis by its unbiased outcomes.

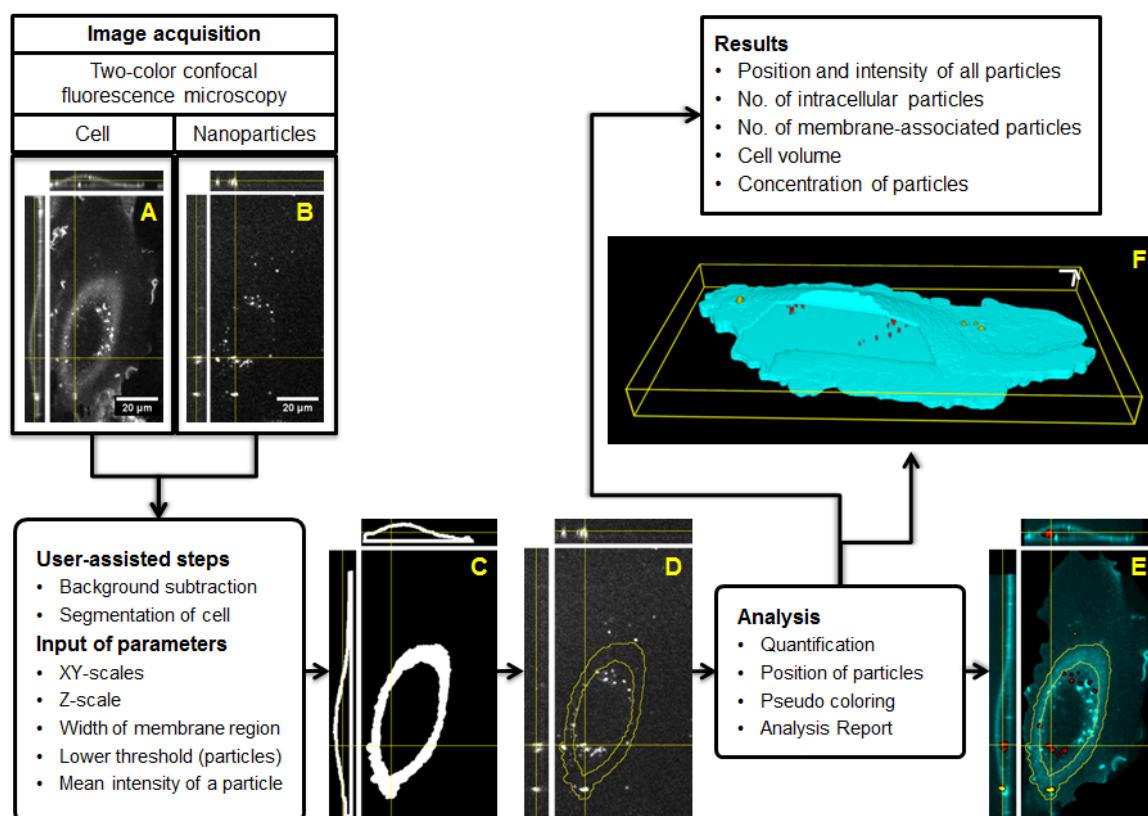


**Figure 4.1 Particle\_in\_Cell-3D processing overview.** The first step is the acquisition of two confocal image stacks representing (A) the cell membrane and (B) the respective image of nanoparticles. The 3D location of an intracellular particle can be seen in the orthogonal views and is marked by the crossing yellow lines. Next in processing are user-assisted steps and the input of analysis parameters. (C) The image of the cell is transformed into a white mask in 3D that defines the membrane region and the intracellular volume. (D) The cellular boundaries are then used to segment the image of the nanoparticles (yellow outline). Quantitative image analysis takes place. The intensity of each object (particle or agglomerate) is compared to the intensity of a single particle previously measured in a calibration procedure. (E) Nanoparticles are color-coded according to the cellular region they belong to. In this example the cell membrane is shown in cyan, the intracellular nanoparticles appear in red, and the membrane-associated nanoparticles in yellow. (F) 3D representation of nanoparticle uptake after image analysis with Particle\_in\_Cell-3D. Intracellular nanoparticles can be seen through the window intentionally open in the membrane region. 3D scale bars = 5  $\mu\text{m}$ .

The cell segmentation strategy employed by Particle\_in\_Cell-3D includes the formation of a three-dimensional membrane region. The width of this region is set by the user and defines an enlarged transition region between extra- and intracellular spaces. This region is much wider

than the real cell membrane. The accuracy of the cell segmentation strategy and the typical thickness of the enlarged membrane region were studied by comparing the results achieved with Particle\_in\_Cell-3D with quenching experiments (see Section 4.3.1). It was shown that the typical width of the membrane region is about 1.4  $\mu\text{m}$  and that our method is able to create a consistent 3D reconstruction of the cell.

As regards the accuracy, Particle\_in\_Cell-3D counting strategy is based on the fluorescence intensity of the NPs. The mean intensity of a single NP, obtained via a calibration experiment, is compared to the intensity of each object and determines the number of NPs forming it. This approach was proved to be accurate by independent stimulated emission depletion (STED) microscopy (see Section 4.3.3), a super-resolution technique [98, 101].

#### 4.2.2 Comparison to other methods

Customary techniques performed for achieving the dosage of NPs taken up by cells include flow cytometry, mass spectroscopy, electron and light microscopy [110-116]. Flow cytometry provides sound statistics due to the large number of cells evaluated in a short time. Nevertheless, it does not deliver spatial information about the position of NPs interacting with a cell, e.g., if they are membrane-associated or intracellular particles. Mass spectroscopy offers very high sensitivity but is a sample destructive technique, meaning that spatial information is not obtained. Moreover, results are normally expressed in arbitrary units, and not in absolute numbers. Electron microscopy allows achieving detailed information with very high spatial resolution, but the price to pay is to work on fixed cells, with an elaborated sample preparation and time-consuming measurements.

Light microscopy can be used on live cells to acquire loads of data relatively fast (see Chapter 3). On the other hand, standard light microscopes such as confocal and wide-field instruments are limited by diffraction. The resolution of light microscopes is not sufficient to resolve particles smaller than approximately 200 nm and a direct quantification of NPs is not possible. Complications to count NPs are further increased by their tendency to agglomerate in biological medium [117]. Our digital method was designed to circumvent the abovementioned restrictions of conventional light microscopy. It enables the absolute quantification of particles not by overcoming the diffraction barrier, but by inferring particle numbers from the fluorescence intensity of particles. Interestingly, because NPs are smaller than the resolving power for a confocal microscope, quantification of NPs in absolute numbers was previously considered "not achievable" by the scientific community (see, for example, Elsaesser *et al.* 2011 [114]). Particle\_in\_Cell-3D proved that in fact it is achievable.

### 4.2.3 Routine selection

Particle\_in\_Cell-3D is separated into five different routines. At the beginning of the digital evaluation, the user is guided through easy-to-follow dialog boxes and is required to select one routine to run and the image files to be analyzed. The first three routines are devoted to the visualization and quantification of NPs in cell uptake experiments. They permit quantification with increasing levels of accuracy: *qualitative*, to visualize the intracellular distribution of particles; *semiquantitative*, to measure and compare the amount of particles in different cells or regions based on particles' fluorescence intensity; and *quantitative*, to count the absolute number of particles internalized by a cell. The last two routines are aimed at the characterization of nanoparticles, microparticles and agglomerates: *calibration*, to measure the mean intensity of particles; and *only particles*, to count the absolute number of NPs in cell-free regions.

#### 4.2.3.1 Routine 1: qualitative – to visualize the intracellular distribution of particles

In this qualitative routine the cell boundaries are used to define two cellular regions of interest: the intracellular and the membrane region. Particles are classified and color-coded according to their location (center of brightness). The cell and all NPs interacting with it can be visualized in an intuitive 3D reconstructed image (Figure 4.2 & Figure 4.3).

#### Three-dimensional reconstruction of the cellular region of interest (ROI)

The spatial position of the cell volume is determined by processing the confocal stacks representing the cellular membrane (Figure 4.2A). Particle\_in\_Cell-3D is designed for single-cell and multiple-cell experiments. If more than one cell appears in the image, the user has the possibility to select the target cell before the segmentation process takes place. Likewise, if a single cell exists in the image, no preselection by the user has to be performed. The segmentation starts by smoothing the image with a Gaussian filter and is followed by an automatic threshold selection (for cases in which the automatic threshold is not satisfactory, the user can set the threshold). Pixels above the threshold are used to convert the image stack of the cell into a binary image – the mask of the cell membrane (Figure 4.2B). Next, the user is requested to verify the image stack and enter the first and the last slices constraining the cell along the Z-direction. Accordingly, the image stack of the cell is reduced to a substack. In the following, two independent segmentation strategies – segmentation strategy 1 (S1) and segmentation strategy 2 (S2) – are applied to allow evaluation of a variety of cell shapes. The segmentation S1 uses the cell membrane position on the top plane of the stack as a seed. This seed is used to track down the mask throughout the image stack. Slice after slice, the mask of the fluorescent membrane is transformed into the mask of the whole cell volume by filling closed

patterns with white pixels and clearing the outside of the patterns (Figure 4.2C). The segmentation S2 uses basically the same processes as S1; slice after slice, the mask of the fluorescent membrane becomes the mask of the whole cell volume. Furthermore, before filling closed patterns with white pixels, the image of every individual slice is copied and then pasted over the following slice. S2 is therefore more robust and was devised to be an option when the delicate and more accurate strategy S1 fails. The user has the possibility to choose the segmentation strategy that best represents the cellular boundaries in a particular experiment. The outlines of the chosen strategy form the outer cellular region of interest (outer ROI; Figure 4.2C).

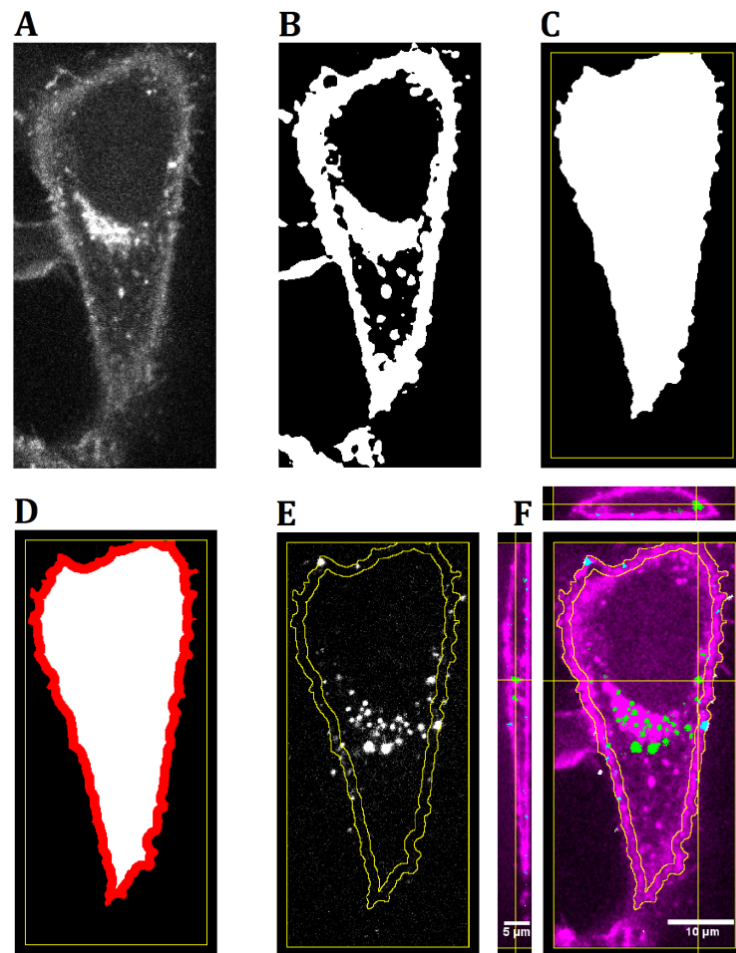


**Figure 4.2 Three-dimensional reconstruction of the cell and assignment of nanoparticles to different regions.** (A) Representative confocal cross-section image of a HeLa cell plasma membrane stained with CellMask. (B) The image of (A) is transformed into a white mask. (C) Further segmentation processes form the final mask of the cell. (D) Afterwards, its outer border is shrunk to define the enlarged membrane region (in red) and the region inside the cell (in white). The procedure occurs throughout the image stack, leading to a 3D reconstruction of the system. (E) Membrane region outlines (in yellow) are used to segment the image of the fluorescent particles. (F) Merged image with orthogonal views along the yellow lines displaying the entire stack. The cell plasma membrane appears in magenta, while the membrane region outlines are shown in yellow. Nanoparticles are assigned to two different regions: intracellular (in green) and the membrane region (in cyan).

In a subsequent step, the outer ROI is shrunk by a given distance set by the user (see Section 4.2.4 'Input of analysis parameters'), generating the inner ROI. The distance between the inner and the outer ROI defines the width ( $w$ ) of the membrane region. This space can be used as a threshold between extracellular and intracellular volumes. Hence, particles bound to the apical membrane should appear in this region if an adequate value for  $w$  is set. The position and shape of the membrane region depends directly on the appearance of the apical plasma membrane. It means that experimental conditions, such as the choice of the membrane marker, labeling protocol and cell type might influence the final geometry of the membrane region. An example on how to estimate the extension of the membrane region is presented in Section 4.3.1. The formation of a membrane region with an intracellular space by Particle\_in\_Cell-3D is shown in Figure 4.2A–D.

The volume of the cell and of the subcellular regions are calculated in volumetric pixels (voxels) and then converted to  $\mu\text{m}^3$  according to the preset XY- and Z-scales.

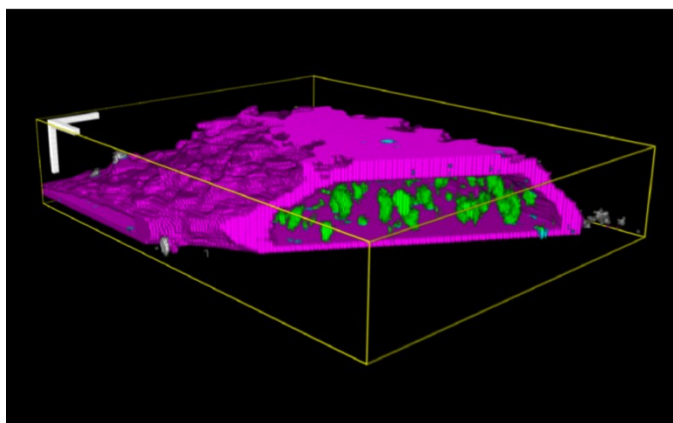


**Figure 4.3** Transversal cut of a 3D image after evaluation of nanoparticle uptake with Particle\_in\_Cell-3D. Cellular boundaries were reconstructed by the membrane region and are shown in magenta. The analyzed nanoparticles are color-coded in green if intracellular and in cyan if membrane associated; nanoparticles lying outside the cell volume are displayed in gray. The projection was created with the ImageJ plugin 3D Viewer [118]. 3D scale bars = 4  $\mu\text{m}$ .

#### **Assignment of nanoparticles to different cellular regions**

Particles are classified and color-coded according to their position with respect to the inner and the outer ROI (Figure 4.2E). In order to do so, the spatial coordinates describing the center of intensity of every single object are automatically measured and recorded by the ImageJ plugin 3D Object Counter [104]. Particle\_in\_Cell-3D uses this information as input data. If the center of intensity of an object is located inside the inner ROI, it is assigned as intracellular and color-coded in green (the user can also set a different color). In addition, if it is positioned between the inner and the outer ROI, it is classified as belonging to the membrane region and color-coded in

cyan (Figure 4.2F). It is important to note that only objects above the lower threshold for particles and within a preselected size range (in number of voxels) are analyzed (see Section 4.2.4).

Finally, a text file is created containing a report documenting the input parameters and the results. In addition, the main processed images and results tables are saved.

#### 4.2.3.2 Routine 2: semiquantitative – to measure the fluorescence intensity of particles

All aspects of routine 1 are present in routine 2. Additionally, it is able to quantify the fluorescence intensity of all intracellular and membrane-associated objects.

##### Fluorescence intensity-based approach for quantifying nanoparticles

The spatial coordinates of every single object (i.e., a single NP or a cluster of NPs) are specified by its center of intensity. The total fluorescence of an object is digitally assessed by the sum of all pixel intensities forming it. This parameter is named integrated density (IntDens; Equation 4.1). During the image acquisition the photons that are collected at each pixel (e.g., by a charge-coupled device) are converted into pixel intensities (PI). For example, each 16-bit pixel carries an intensity value that ranges from 0 to 65,535 correlating to the number of fluorophores present in the scanned volume [103]. Thus, we assume that the IntDens, which is the sum of all pixel intensities in a region, is proportional to the amount of particles in that region, and we also assume that the self-quenching of fluorescence in particle agglomerates is negligible. Particle\_in\_Cell-3D thereby does not count individual NPs by simple counting of bright spots, but accesses the number of NPs indirectly by integrating their fluorescence intensities. It is therefore able to correctly estimate the quantity of particles, even if they are agglomerated. The assumptions of negligible self-quenching and linear proportionality between the IntDens and the number of particles were validated for NPs of 100 nm and agglomerates of up to five particles. The accuracy of these results was proved by comparative experiments with super-resolution microscopy (see Section 4.3.3).

The IntDens of an object  $i$  formed by  $V$  pixels is calculated as follows:

$$IntDens_i = \sum_{k=1}^V (PI)_k \quad (\text{Equation 4.1})$$

where each pixel is indexed by the letter  $k$ .

As mentioned above, the ImageJ plugin 3D Object Counter [104] is employed by Particle\_in\_Cell-3D to localize fluorescent objects in the image stack of the particles. In addition, it delivers a results table containing all measured objects with their respective position. Our



macro automatically and systematically uses this information in order to calculate the IntDens of all objects.

#### **Lower threshold & volume of nanoparticles**

The lower threshold applied to particles is a key parameter for correct quantification. Objects are selected for analysis based on this value, that is, only pixels with intensity values above the threshold enter the calculation. In addition, the user is given the possibility to set the minimum and maximum volume (number of voxels) of pixels to be considered as an object (see Section 4.2.4).

#### **Total fluorescence intensity of particles in a region**

The total IntDens (TIntDens) of a region (R) – intracellular or membrane region – is defined as the sum of the IntDens over all objects belonging to that region (Equation 4.2):

$$TIntDens_R = \sum_{i=1}^n (IntDens_i)_R \quad (\text{Equation 4.2})$$

where i indexes all objects from 1 to n.

TIntDens is therefore proportional to the number of particles in the region where it is calculated and semiquantitative results can be achieved by comparing the TIntDens of different region or cells.

#### **4.2.3.3 Routine 3: quantitative – to count the absolute number of particles**

Routine 3 includes all features presented in routines 1 and 2. It additionally permits the absolute quantification of NP uptake at the single-cell level.

#### **Particle number distribution in agglomerates**

The calculation is straightforward and the number of particles forming an object i is given by:

$$No\_P_i = \frac{IntDens_i}{Mean\_IntDens} \quad (\text{Equation 4.3})$$

The mean IntDens of a single NP can be measured via routine 4 (see Section 4.2.3.4).

#### **Absolute number of nanoparticles taken up by cells**

The total number of intracellular particles is calculated by simple addition over all particles within the inner ROI. The same consideration holds for the total number of membrane-associated particles, but this time accounting for all particles located within the inner and the outer ROI. The general equation can be written as follows:

$$No\_P_R = \sum_{i=1}^n (No\_P_i)_R \quad (\text{Equation 4.4})$$

where  $i$  indexes all objects from 1 to  $n$  in the cellular region  $R$ .

#### **Concentration of nanoparticles**

The concentration of particles within each region is obtained by dividing the number of particles by the respective cellular volume (Equation 4.5):

$$C\_P_R = \frac{No\_P_R}{V_R} \quad (\text{Equation 4.5})$$

Concentration-based approaches can be useful for cases in which the volume ratio of the two regions differs over time or within cells. Since the volume, the concentration and the number of particles in each region are automatically saved in a report file, it is straightforward to calculate new parameters based on the particle concentration.

#### **4.2.3.4 Routine 4: calibration – to measure the mean intensity of single particles**

Routine 4 is used to obtain the distribution of IntDens of all objects. This parameter is essential for routines 3 and 5. From this data set one can derive the mean IntDens of a single NP. Objects of interest are automatically selected in the image of the particles and added to the ImageJ ROI Manager. One after the other, each selected object is measured. In the end, a report of results shows the IntDens of all evaluated objects. However, analyzed objects are not only comprised of single NPs but also of agglomerates. It is necessary to exclude agglomerates from the data set to yield just the mean IntDens of individual NPs. This can be verified by other means, for example, super-resolution microscopy. In this project we used STED microscopy to accomplish this task (see Section 4.3.3).

#### **4.2.3.5 Routine 5: only particles – to quantify particles in cell-free regions**

Routine 5 was designed to characterize the concentration and agglomeration of particles in control experiments without cells. This information is extremely relevant because the exposure of NPs to cells in a monolayer culture may vary with time owing to sedimentation and diffusion of particles in the cell medium [119]. The user is requested to define the 3D region of interest to be analyzed. Next, if the mean IntDens is known, the total number of NPs, their concentration and the particle number distribution are calculated within the selected region as defined by Equations 4.3–4.5.

#### 4.2.4 Input of analysis parameters

The possibility of adapting the analysis parameters according to experimental conditions increases the flexibility of Particle\_in\_Cell-3D. The following parameters have to be set by the user during analysis and are saved in a final report.

##### **XY-scale**

This parameter is the image size of each pixel in real space. It corresponds to the magnification calibration of the microscope system. The XY-scale has to be entered in nm per pixel. This value, together with the Z-scale, is used to calculate the volume of the cell and the concentration of particles.

##### **Z-scale or interslice distance**

The Z-scale is the depth of each volumetric pixel (voxel) in real space. It defines the distance between two adjacent images in an image stack. This parameter is directly given by the interslice distance that is set during acquisition in a confocal microscope. The units to be used are nm per pixel. To avoid under- and over-sampling, images should be acquired following the Nyquist criterion [92].

##### **Width of the cell membrane region ( $w$ )**

This parameter defines the distance  $w$  in pixels between the inner and the outer ROI. It is thereby equal to the width of the region between the intra- and the extra-cellular environments, which is the membrane region (Figure 4.2D). The membrane region represents a transition space every particle has to pass through to be internalized by a cell. One should keep in mind that the membrane region is typically much wider than the actual membrane. Another point to be considered is that the amount of membrane-associated NPs depends on how cells are exposed to the particles and on how cells are treated prior to imaging. For example, NPs that were loosely bound to the membrane may be removed during staining and washing steps.

##### **Background to be subtracted**

This parameter is used to correct for the background present in the image stack of the particles. The entered value is subtracted from the intensity value of each pixel. If no subtraction is needed (e.g., background was removed by another method), this parameter should be set to 0.

##### **Lower threshold for nanoparticles**

Only pixels with intensity values exceeding this threshold will be considered particles and thus analyzed. When a correct threshold is set, the bright spots associated with the fluorescent

objects form clusters of adjacent pixels and only these pixels are evaluated. This choice is fundamental for the whole analysis process as it has major influence on the results. If the threshold is set too low, artifacts such as background noise and cellular autofluorescence might be counted as particles. On the other hand, if it is set too high, dimmer particles will not be considered and agglomerates will be overestimated. In summary, the threshold must be set as low as possible, but high enough to allow object segmentation. When absolute quantification is intended, the lower threshold should be the same as the one used during calibration.

#### **Minimum & maximum number of voxels**

The volume of the objects under investigation (in number of voxels, after applying the lower threshold) can be used to eliminate background noise and to avoid analyzing dimmer or brighter objects. If absolute quantification is intended, these values should also be the same as the ones used during calibration.

#### **Threshold for segmenting the cell**

This is the lower threshold value applied to segment the cell and define its position.

#### **Mean IntDens of a single nanoparticle**

This value characterizes the mean fluorescence intensity of individual NPs. It can be obtained from the data set provided by running routine 4. The mean IntDens is not necessary in routines 1 and 2, but crucial to calculate the absolute number of NPs in routines 3 and 5.

## **4.3 Results & Discussion**

### **4.3.1 Cell segmentation strategy**

The 3D reconstruction of the cellular region of interest employed by Particle\_in\_Cell-3D includes the formation of a membrane region, typically much wider than the actual plasma membrane. The width of the cell membrane region ( $w$ ) is a very important parameter (see Section 4.2.4). It defines the thickness of the transition region between extracellular and intracellular space and is freely set by the user. With the aim of validating the cell segmentation strategies S1 and S2 (see Section 4.2.3.1) and identifying the magnitude of  $w$ , we analyzed the uptake of 80 nm mesoporous silica nanoparticles labeled with Cy3 (MSN-Cy3) into HeLa cells via the well-established quenching method [78, 79]. This procedure is commonly applied to characterize the kinetics of internalization of NPs functionalized with a quenchable dye (e.g., Cy3). Briefly, after the intended incubation time, a cell membrane-impermeable dye (e.g., trypan blue) is added to the cell culture while monitoring the NPs' fluorescence by live-cell imaging. The dye quenches

the fluorescence of the NPs that are in the extracellular space whereas intracellular NPs remain fluorescent. By comparing images before and after quenching, the fraction of NPs taken up by single cells can be calculated [78]. Here, the images before and after quenching of the MSN-Cy3 were processed by Particle\_in\_Cell-3D using different values for the width of the membrane region. By comparing the images before and after quenching, we determined  $w = 1.4 \mu\text{m}$  as the most suitable value for our experiments. This was the smallest possible  $w$  in which intracellular particles were never quenched and membrane-associated particles were either quenched or remained fluorescent. Therefore, the 3D reconstruction of the cell performed by our method succeeded to create an intracellular space and a transition region.

### 4.3.2 Fraction of nanoparticles internalized by single cells

In order to confirm the correctness of setting  $w$  equal to  $1.4 \mu\text{m}$  in the present set of experiments, the uptake of 80 nm MSN-Cy3 into HeLa cells was measured. The outcome was compared with data obtained from quenching experiments conducted in parallel.

HeLa cells were incubated with the mesoporous silica nanoparticles from 1 to 6 h. More than 70 cells were randomly selected, imaged with a confocal spinning disk microscope and then analyzed via Particle\_in\_Cell-3D. The fraction of NPs taken up by single cells was assessed similarly to quenching experiments; that is, the amount of internalized particles was divided by the sum of intracellular and membrane-associated particles (as described below). The fraction of internalized particles (FIP) was thus calculated by Equation 4.6:

$$FIP = \frac{TIntDens_{INTRACELLULAR}}{TIntDens_{INTRACELLULAR} + TIntDens_{MEMBRANE}} \quad (\text{Equation 4.6})$$

and then plotted against time (Figure 4.4A). The values at specific time points after incubation are shown as gray circles. We found that after 1:15 (h:min) approximately 25 % of the MSN-Cy3 were taken up by the cell, and 50 % was reached after 2:45. The internalization increased constantly, reaching 92 % after 5:45 (Figure 4.4B).

In the following we compare the abovementioned results obtained by Particle\_in\_Cell-3D with the outcome of independent quenching experiments (see Section 4.3.1). As described by Equation 4.6, the fraction of internalized particles is given by the number of intracellular particles (number of non-quenched particles detected after quenching) divided by the sum of intracellular and membrane-associated particles (number of particles in contact with the cell detected before quenching). We determined the uptake kinetics of the MSN-Cy3 by analyzing more than 50 individual HeLa cells within a period of 6 h. Figure 4.4A (black squares) shows the fraction of

internalized particles at different time points after incubation. Each data point represents an individual cell. For a clearer insight into the behavior, the corresponding median values are shown in Figure 4.4B as black squares. After approximately 3 h, 50 % of the NPs were taken up by the cells.

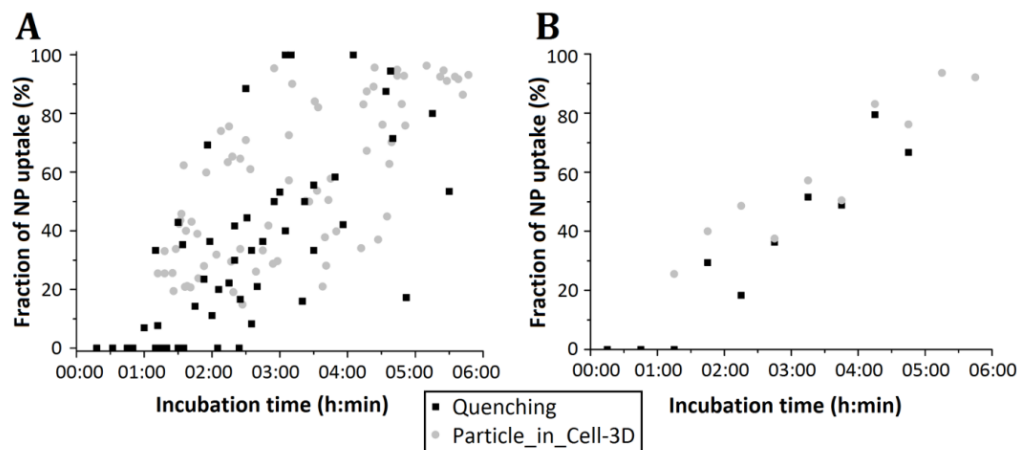


**Figure 4.4** Fraction of Cy3-labeled mesoporous silica nanoparticles (MSN-Cy3) internalized by HeLa cells as analyzed by Particle\_in\_Cell-3D and by quenching experiments. **(A)** The fraction of nanoparticle (NP) uptake of individual cells is plotted with respect to their incubation time. The heterogeneity is typical for single-cell experiments. **(B)** For a better overview, the median values are presented.

The wide spread within the data of both experiments is typical for single-cell measurements and represents the heterogeneity from cell to cell. Taking this heterogeneity into account, the data sets obtained by quenching experiments and by our new analysis method correspond very well and thereby proved that Particle\_in\_Cell-3D can be successfully applied to determine the fraction of particles internalized by cells.

### 4.3.3 Accuracy of absolute quantification

Fluorescent polystyrene beads with a diameter of 100 nm (Red Fluospheres®, Life Technologies) were dispersed on a cover slip (see Experimental Section 11.1.1). Image stacks in confocal mode were recorded as described in Section 11.1.5. Routine 4 was used to measure the IntDens (Equation 4.1) of the beads (Figure 4.5A & B). One stack with 321 objects was analyzed and the values for the IntDens were plotted in a histogram (Figure 4.5C). A Gaussian fit was used to calculate the intensity values of the first and second peaks. Interestingly, the IntDens corresponding to the second peak (22,562 PI) was approximately twice the value for the first peak (11,360 PI). This is an indication that the first peak corresponded to single NPs while the second peak consisted of dimers. To validate this assumption, the same image area was analyzed in super-resolution STED mode [120] (see Experimental Section 11.1.5).

The super-resolved STED image gives direct access to absolute quantification of previously blurred NP agglomerates. Additionally, the biggest advantage of employing this particular super-resolution technique is the possibility to readily analyze the same region in confocal and STED mode. As shown in Figure 4.6, this allows for comparison between the data calculated by Particle\_in\_Cell-3D and the actual numbers of NPs present in the imaged area without doing any modification to the sample in between imaging in the two modes.

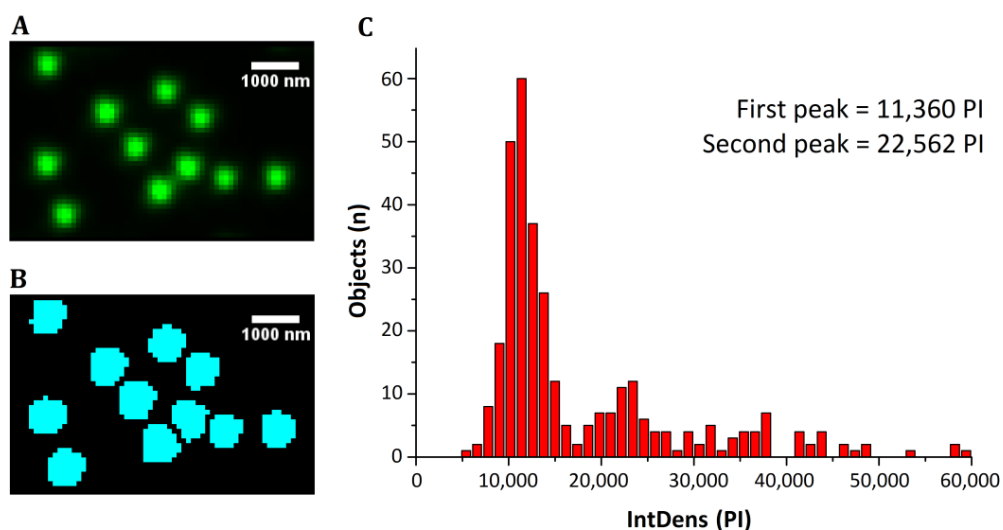


**Figure 4.5 Calibration experiment.** (A) Subregion of a confocal image stack of fluorescent 100 nm polystyrene nanoparticles. (B) Z-projection of (A) followed by threshold and automatic segmentation of objects. (C) IntDens measured for all segmented objects of one stack. The mean IntDens corresponds to the IntDens of the first peak, 11,360 PI (Gaussian fit not shown). The second peak has roughly twice the value of the first one; a good indication that the first peak value characterizes single nanoparticles, while the second peak characterizes dimers. This indication was confirmed by super-resolution stimulated emission depletion measurements. IntDens: Integrated density; PI: Pixel intensity.

The resolution of our setup [120] was sufficient to resolve individual NPs. Bead size in STED mode was measured to be  $98 \pm 5$  nm ( $n = 10$ ) in good agreement to the actual diameter of 100 nm [121]. Even two beads lying side-by-side in direct contact were resolved as individual beads (Figure 4.7). By comparing the super-resolved image to the results of Particle\_in\_Cell-3D, the first peak in the histogram of Figure 4.5 could be identified to be comprised of single NPs. The mean IntDens of a single NP was therefore 11,360 PI. With this value at hand we analyzed independent regions and compared the data of our macro with the number of NPs detected via STED microscopy. In total 615 objects were analyzed and the results were in good agreement up to agglomerates of five NPs (Figure 4.8). For higher numbers of NPs per object it was difficult to achieve good statistics because most NPs were monodispersed in our images. In summary, the intensity-based approach of Particle\_in\_Cell-3D is able to correctly quantify 100 nm NPs in absolute numbers, from single NPs up to, at least, agglomerates of five NPs.

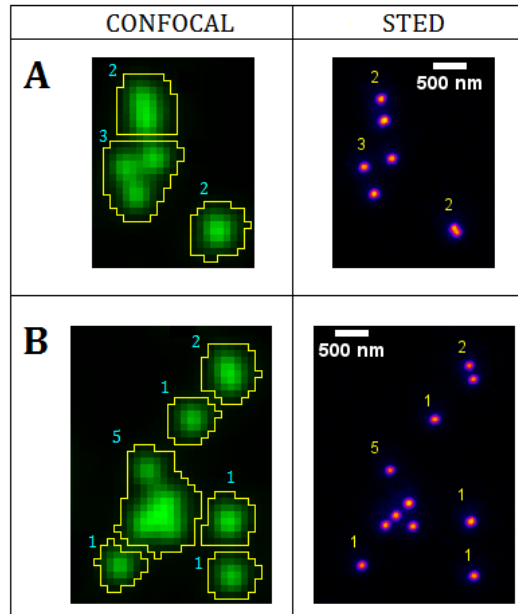


**Figure 4.6 Quantification of 100 nm fluorescent nanoparticles via the fluorescence intensity-based method Particle\_in\_Cell-3D in comparison with super-resolution stimulated emission depletion microscopy. (A)** Representative region in which three objects were analyzed by Particle\_in\_Cell-3D (numbers in blue, confocal micrograph). STED microscopy can clearly resolve the two objects formed by two nanoparticles (NPs) and one formed by three NPs (numbers in yellow, STED micrograph). **(B)** Another representative region in which four single NPs, a dimer and one cluster formed by five NPs were quantified by our fluorescence intensity-based method and STED. The results show that Particle\_in\_Cell-3D accurately counted the number of either single or agglomerated NPs.

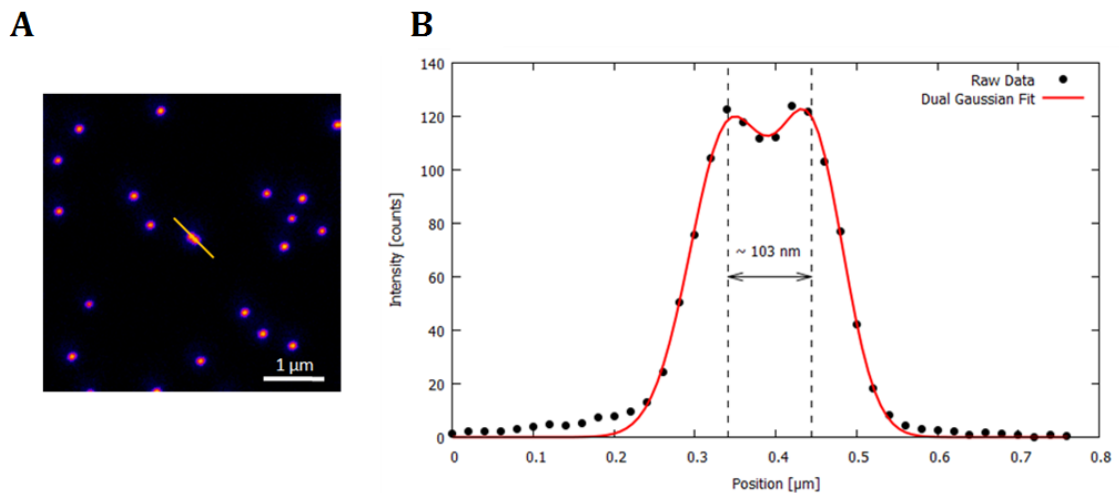


**Figure 4.7 Individual nanoparticles can be resolved with stimulated emission depletion microscopy. (A)** Stimulated emission depletion image of 100 nm fluorescent NPs. Using the stimulated emission depletion technique, individual NPs can be resolved even when they are in direct contact. An example is marked by the yellow line. **(B)** The cross-section marked in (A) shows that even neighboring NPs can be resolved. A dual Gaussian fit is applied to fit the intensity profile, yielding a separation of the two NP centers of 103 nm (red line).



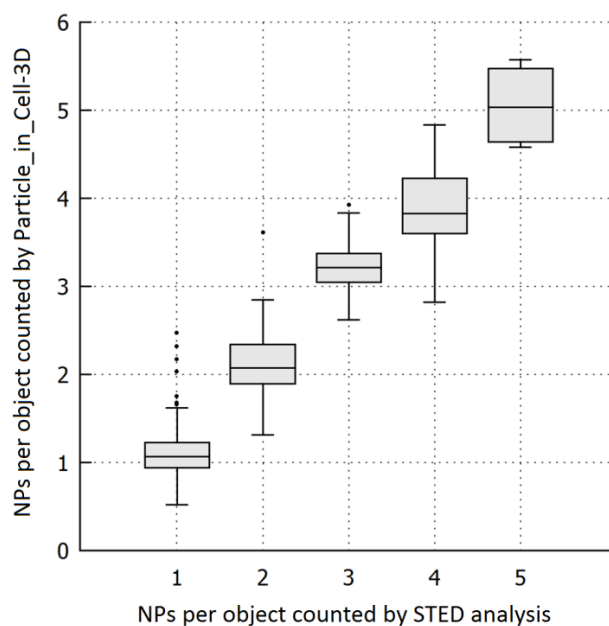


**Figure 4.8 Performance of the Particle\_in\_Cell-3D macro compared with stimulated emission depletion analysis.** The calculated number of 100 nm NPs in an object agrees well with the actual number as determined with STED analysis. Two  $30 \times 30\text{-}\mu\text{m}$  stacks were analyzed, resulting in 615 objects. A total of 443 objects were composed of one NP, 100 objects of two NPs, 43 objects of three NPs, 25 objects of four NPs and four objects were made up of five NPs, as determined by super-resolution imaging. Error bars extend up to 1.5-times the interquartile range; points represent outliers.

#### 4.4 Conclusions

Particle\_in\_Cell-3D is able to analyze the uptake of NPs by single cells from dual-color confocal images in a semiautomatic way. The cell is reconstructed in 3D and two distinct spaces are automatically defined: intracellular and the membrane region. Furthermore, nanoparticles can be visualized in great detail, as they are color-coded according to their position with respect to the cell. The processed images, input parameters and results are all saved and can be accessed at any time.

As shown by comparative investigation of the fraction of internalized 80 nm mesoporous silica NPs, results obtained by employing Particle\_in\_Cell-3D were in good agreement with those assessed by quenching experiments. Advantages over quenching experiments include the reduced need of material and the throughput of analysis. Furthermore, evaluation by the macro provides the possibility to measure several cells per experiment.

Particle\_in\_Cell-3D is fast and accurate. For NPs of approximately 100 nm, single or forming agglomerates of up to five NPs, it permits a rapid counting of large numbers of nanoparticles that are correctly quantified even when agglomerated. These results have been proved by comparison with STED microscopy, a super-resolution technique. The resolution of the STED

setup used was able to resolve individual 100 nm beads even when in direct contact with neighboring beads.

Particle\_in\_Cell-3D overcomes some drawbacks of commonly applied methods such as mass spectroscopy, flow cytometry, electron microscopy and single-cell quenching experiments, offering new possibilities to characterize nanoparticle-cell interactions.

## 5 Cell type-dependent uptake kinetics and cytotoxicity of silica nanoparticles

*This chapter is based on the following publication:*

*Julia Blechinger, Alexander T. Bauer, Adriano A. Torrano, Christian Gorzelanny, Christoph Bräuchle, and Stefan W. Schneider;*

*“Uptake kinetics and nanotoxicity of silica nanoparticles are cell type dependent.”*

*Small 9, 3970-3980 (2013).*

### 5.1 Introduction

Synthetic amorphous silicas are used in a variety of products such as cosmetics, pharmaceuticals and food due to their inert nature. In 2002, the annual estimated production of synthetic amorphous silicas and silicates in a size range between one and several  $\mu\text{m}$  was about  $5.0 \times 10^5$  tons. The toxicity of these particles has been evaluated in various studies and they are classified as harmless [122, 123]. However, throughout the last decade the spectrum of synthesized silica species has been enlarged to even smaller sized particles. Nanoscaled silica particles have found application in food and beverages (table salt, seasonings, dry foods and supplements), cleaning products, cosmetics, water repellent nano-coating for textiles, and sporting goods [1, 124]. They have also been applied in nanomedicine and biotechnological fields, such as biosensors, biomarkers and drug delivery systems (see Chapter 9) [125, 126]. Inhalation, skin contact or ingestion of silica NPs are possible entry routes into the human body (see Section 2.2). Silica NPs that succeed in penetrating across the natural barriers of the lungs, skin or gastrointestinal tract will reach the circulatory system, where they can interact with endothelial cells and disturb their normal activity (see Section 2.4). A considerable number of *in vitro* studies concerning the cytotoxicity of silica NPs have been published throughout the last years. Several studies show that an increased toxicity can be found for increasing doses, exposure times, or decreasing particle sizes [124, 127-129]. For example, a decreasing cytotoxic response with increasing silica nanoparticle sizes (14–335 nm) was found for EA.hy926 cells [128]. Another study reported a size-independent cytotoxic effect on human cells derived from bronchoalveolar carcinoma cells for 15 nm and 46 nm silica NPs [127]. In addition, 10 nm and 30 nm silica NPs inhibited stem cell differentiation of mouse embryonic cells whereas 80 nm and 400 nm particles had no such effect [130]. Nevertheless, most of the studies are not comparable as they have been carried out applying a variety of different NPs and cell types, and it is therefore not possible to draw general conclusions about the underlying mechanisms of nanotoxicity.

The aim of this study was to investigate the impact of silica NPs on human umbilical vein endothelial cells (HUVEC) in comparison to a standard cancer cell line derived from the cervix carcinoma (HeLa). We quantified and characterized the uptake of 310 nm silica NPs into HUVEC and HeLa cells. The localization of the NPs was imaged by atomic force microscopy (AFM) and by spinning disk confocal fluorescence microscopy. In order to assess the absolute number of NPs in contact with the cells, fluorescence images were evaluated with Particle\_in\_Cell-3D (see Chapter 4). Normally, in this type of *in vitro* experiments, a monolayer of cells grows adhered to the bottom of a culture well, and nanoparticles are added to the cell medium. NPs diffuse and sediment in the media in a very dynamic way. For this reason, the number of NPs in contact with the cells can significantly deviate from the amount of NPs added to the cell culture [119, 131]. So as to investigate if uptake results were influenced by strong agglomeration followed by deposition of particles, we measured the hydrodynamic diameter of the particles under the very same particle preparation conditions applied for live-cell imaging experiments. Additionally, we measured the metabolic activity (MTT assay) and the membrane integrity (LDH assay) of the cells to compare the cell type-dependent cytotoxicity of the silica NPs. Finally, flow cytometry was used to quantify nanoparticle-induced cell death.

Silica NPs were synthesized by Dr. Rudolf Herrmann (Group of Prof. Dr. A. Reller and Group of Prof. Dr. A. Wixforth; University of Augsburg). The atomic force microscopy measurements and the cytotoxicity assays of silica NPs were performed by Dr. Alexander T. Bauer and by Dr. Christian Gorzelanny (Group of Prof. Dr. S. W. Schneider; University of Heidelberg). The cellular uptake of silica NPs was investigated together with Dr. Julia Blechinger (Group of Prof. Dr. C. Bräuchle; LMU Munich).

## **5.2 Results & Discussion**

### **5.2.1 Characterization of silica nanoparticles**

For the purpose of this study, perylene-labeled (SiO<sub>2</sub>-310-P) and unlabeled (SiO<sub>2</sub>-304) silica NP species were synthesized [132, 133]. From preceding experiments investigating the labeling efficiency, we estimated that the perylene covers only about 0.16 % of the particles surface. Due to this very low surface coverage, the perylene should not influence the interactions between cells and particles. By comparing cytotoxicity measurements of labeled silica NPs to experiments with unlabeled particles, we were able to unravel the mechanism of NP uptake applying fluorescence-based techniques, while additionally ensuring that the label did not influence the NP-cell interactions.

Particle sizes were determined by transmission electron microscopy (TEM) showing NP diameters of  $310 \text{ nm} \pm 37 \text{ nm}$  ( $\text{SiO}_2\text{-310-P}$ ) and  $304 \text{ nm} \pm 16 \text{ nm}$  ( $\text{SiO}_2\text{-304}$ ), thus the particles are within the same size range (Table 5.1). The hydrodynamic diameter and the agglomeration behavior of the particles over time were assessed by measuring the sizes in water and in cell medium by dynamic light scattering (DLS) measurements. For measurements of small particles in cell medium, the same incubation times used for NP uptake analyses were selected. Table 5.1 shows that the mean size of the particles in water was 450 nm. The mean particle diameter increased up to values within 550 nm and 650 nm for all analyzed time points. The zeta potential of both NP types was determined in cell medium, showing values of  $-14.1 \text{ mV} \pm 1.5 \text{ mV}$  ( $\text{SiO}_2\text{-310-P}$ ) and  $-17.1 \text{ mV} \pm 1.3 \text{ mV}$  ( $\text{SiO}_2\text{-304}$ ).

**Table 5.1 Physical characterization of silica nanoparticles used in this study.**

Particle	Zeta potential [mV]	Primary particle size [nm] <sup>a)</sup>	Size in cell medium <sup>b)</sup> after specific time points [nm] <sup>c)</sup>						
			0 h <sup>d)</sup>	1 h	2 h	3 h	4 h	10 h	24 h
$\text{SiO}_2\text{-310-P}$	-14.1	310	450	551	558	633	650	605	614
$\text{SiO}_2\text{-304}$	-17.1	304				n.d. <sup>e)</sup>			

a) Particle diameter measured by transmission electron microscopy; b) Supplemented with 10 % fetal bovine serum; c) Hydrodynamic diameter determined by dynamic light scattering measurements; d) Size in  $\text{H}_2\text{O}$ ; e) Not determined.

For the quantitative evaluation carried out in this study, it was necessary to assess the mean fluorescence intensity of a single NP. The latter was determined by spinning disk microscopy in combination with the Particle\_in\_Cell-3D calibration routine (see Section 4.2.3.4). The intensities of  $\text{SiO}_2\text{-310-P}$  showed a Gaussian distribution with a mean value of 48,090 counts per NP for HeLa cells and 49,430 counts per NP for HUVEC (Figure 5.1). Minor differences in intensity probably arise from the different cell media used for HUVEC and HeLa cells.

## 5.2.2 Quantification of silica nanoparticle uptake by cells

First of all, the deposition of NPs on the cell membrane was analyzed by fluorescence microscopy combined with atomic force microscopy (AFM) at different time points upon stimulation with NPs [134]. AFM images, as shown in Figure 5.2, display the cellular destination of silica particles after exposure to the different cell types. The results show that labeled NPs adhered to the HUVEC cell membrane after 2 h (Figure 5.2A, red dots). In the following, small humps on the cell surface indicate that the silica particles entered the cells within 24 h of incubation (Figure 5.2B, red dots). After NP incubation of HeLa cells for 2 h, all analyzed particles were located on the cell

membrane (Figure 5.2C, red dots). In contrast to endothelial cells, NPs were still found in strong association to the cell membrane after an exposure of 24 h, indicative for a distinct cellular destination and transport compared to the primary endothelial cells (Figure 5.2D, red dots).

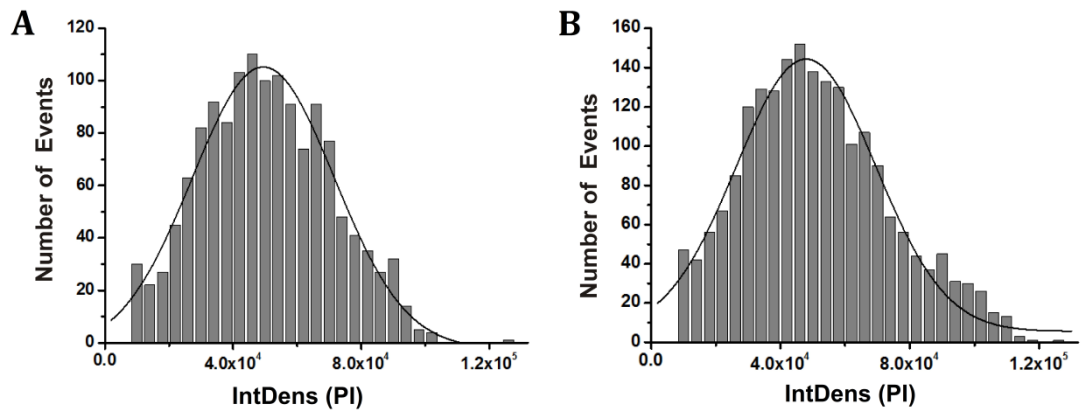


**Figure 5.1 Fluorescence intensity distribution of individual silica nanoparticles.** Gaussian distribution of the integrated density (IntDens) with mean values for **(A)** HUVEC: 49,430 PI and **(B)** HeLa: 48,090 PI per nanoparticle. PI: Pixel intensity.

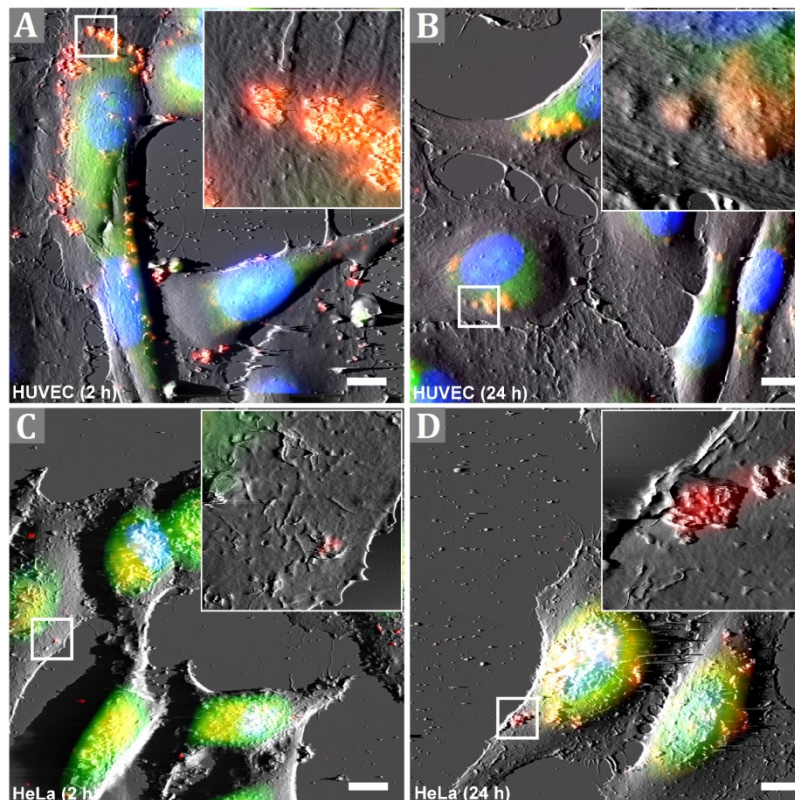


**Figure 5.2 Distinct cellular uptake of nanoparticles in HUVEC and HeLa cells.** Three-dimensional atomic force microscopy (AFM) was combined with fluorescence microscopy. **(A)** Nanoparticles (NPs) were visible on the cell membrane outside HUVEC cells after exposure of 2 h. **(B)** 24 h after incubation with NPs, the surface of the cells is characterized by homogeneous distribution of only small humps, indicating intracellular localization of NPs. By contrast, NPs were found on the cell membrane of HeLa cells after **(C)** 2 h and **(D)** 24 h of incubation, demonstrating a distinct cellular destination and transport compared to HUVEC. Scale bars = 5  $\mu\text{m}$ .

In order to elucidate if the observed effects are reflected by different uptake kinetics of SiO<sub>2</sub>-310-P, living cells were incubated with the NPs for varying time periods from 1 up to 24 h. The cell membrane was stained and stacks of confocal cross-sections of individual living cells were acquired by highly sensitive spinning disk confocal microscopy. Figure 5.3 shows representative images for both cell types with incubation times of 1, 4, 10, and 24 h. The images depict three-dimensional reconstructions of confocal images after evaluation with Particle\_in\_Cell-3D. With this method, we were able to localize and quantify NPs in contact with single cells. The image reveals that NPs (green) are localized within the cellular boundaries showing their uptake into the cell. Additional NPs (yellow) are present in the cell membrane region. The NPs were distributed more or less regularly throughout the cell for both cell types during the first 3 h. For longer incubation times, a distinct subcellular particle localization in the perinuclear region was observed, indicating that intracellular transport of these NPs takes place on longer time scales.

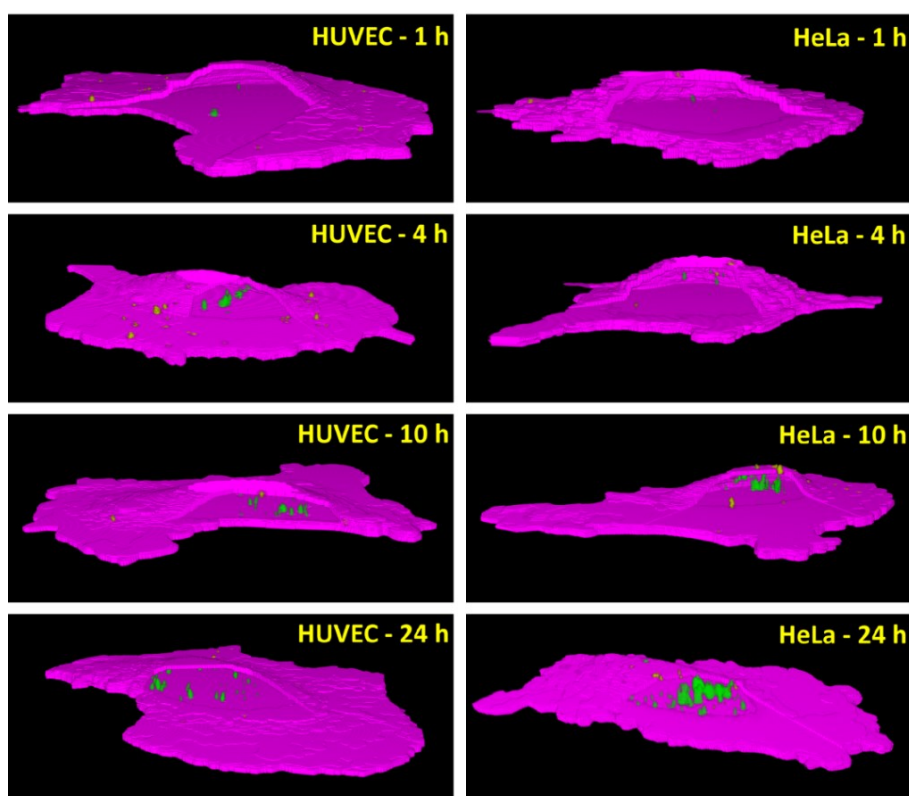


**Figure 5.3 Representative three-dimensional reconstruction of nanoparticle uptake by single cells.** Live-cell imaging was used to acquire dual-color fluorescent confocal images (one of the stained plasma membrane and the other of the labeled silica nanoparticles) with high temporal and spatial resolutions. Each pair of images was analyzed by Particle\_in\_Cell-3D (see Chapter 4). The magenta region corresponds to the cell membrane region, i.e., the space between the intra- and the extracellular environments. Intracellular nanoparticles are color-coded in green and particles associated to the plasma membrane appear in yellow. The increasing number of incorporated nanoparticles with increasing time is clearly visible for both cell types, being more pronounced for HeLa cells, as described by the quantitative results of more than 360 single cells illustrated in Figure 5.4.

The amount of NPs present in the cytoplasm varies considerably from cell to cell. Around 30 cells of each cell type were analyzed per time point for incubation times of 1, 2, 3, 4, 10, and 24 h applying the same controlled conditions. This means that more than 180 cells were investigated per cell type, in total. The mean numbers of NPs inside individual HUVEC and HeLa cells for each time point are shown as a histogram in Figure 5.4. Both cell types show a time-dependent increase for the number of intracellular NPs. It is remarkable that HUVEC cells internalized much more of the provided NPs than HeLa cells within the first 4 h. After 4 h, only 20 NPs on average were taken up into the cellular boundaries of HeLa cells, whereas HUVEC incorporated an average number of 113 NPs in the same period. It is even more interesting how the situation was completely changed after an incubation time of 10 h, when the mean number of intracellular particles for HeLa cells significantly exceeded the amount of NPs inside HUVEC cells. These differences are most likely caused by cellular characteristics, as each cell type has an individual surface property and cellular morphology [58, 135]. Furthermore, each cell type shows a distinct metabolic activity [136]. These parameters strongly influence NP-cell interactions and, therefore, the NPs uptake behavior. Interestingly, the cell cycle can also influence the cellular uptake behavior, as was shown recently [137]. Since during our experiments cells were not synchronized and randomly selected to be measured, we presented a mean value of particle uptake representing cells in all mitotic states.

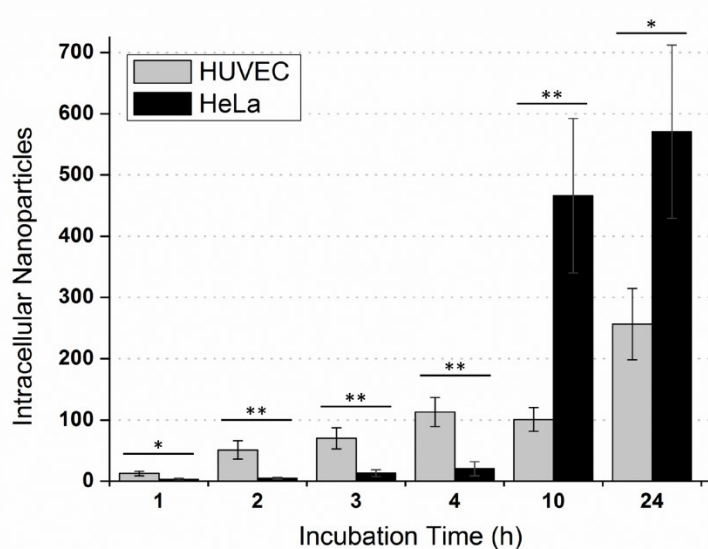


**Figure 5.4 Uptake kinetics of SiO<sub>2</sub>-310-P nanoparticles in HUVEC and HeLa cells.** Within the first 4 h the mean number of internalized nanoparticles increases almost linearly for both cell types, reaching an average number of 113 nanoparticles for HUVEC (gray columns) and only 20 particles for HeLa cells (black columns). Interestingly, after 10 h, the situation is reversed and a larger number of nanoparticles are internalized by HeLa than by HUVEC cells. Finally, after 24 h, the mean value of intracellular particles for HeLa cells is 570, whereas for HUVEC cells it is 256. Results are statistically different (\*  $p < 0.05$ ) for time points 1 and 24 h and highly statistically different (\*\*  $p < 0.01$ ) for all other incubation times. The histograms depict the mean  $\pm$  standard error of at least three independent experiments ( $n = 28\text{--}32$ ).



### 5.2.3 Cytotoxicity of silica nanoparticles

We analyzed the cytotoxic response of both HUVEC and HeLa cells to silica NPs by investigating the mitochondrial activity (MTT assay), the membrane leakage (LDH assay) and cell death. To ensure that the perylene molecules labeling SiO<sub>2</sub>-310-P do not influence the results, we additionally investigated the cytotoxic response to similar unlabeled particles (SiO<sub>2</sub>-304).

#### Dose-dependent cytotoxicity of silica nanoparticles

HUVEC and HeLa cells were exposed for 24 h to the following SiO<sub>2</sub>-310-P and SiO<sub>2</sub>-304 particle concentrations:  $1.0 \times 10^3$ ;  $1.5 \times 10^4$ ;  $3.0 \times 10^4$ ; and  $6.0 \times 10^4$  NPs per cell.

As shown in Figure 5.5, mitochondrial activity decreased significantly as a function of dosage levels in HUVEC (Figure 5.5A). When compared to control (dashed line), the metabolic activity was not significantly changed after exposure to  $1.0 \times 10^3$  NPs per cell for 24 h. In contrast, mitochondrial activity was reduced by more than 35 % upon incubation with nanoparticles at concentrations of  $1.5 \times 10^4$  NPs per cell and further decreased gradually at doses of  $3.0 \times 10^4$  NPs per cell and  $6.0 \times 10^4$  NPs per cell after exposure for 24 h. Interestingly, this effect strongly correlated with an elevated LDH release due to membrane leakage, and is therefore indicative for a reduced cell viability (Figure 5.5B).

Based on the dose-effect studies, a concentration of  $1.0 \times 10^3$  NPs per cell showed a slight reduction of 10 % for the MTT value in HeLa cells (Figure 5.5C). A dosage of  $1.5 \times 10^4$  NPs per cell resulted in a reduced mitochondrial activity by more than 30 %, comparable to the results in HUVEC, whereas a higher concentration of silica particles induced no enhanced effects on metabolic activity. Moreover, the cells showed no signs of membrane damage in all particle concentrations if compared to the control group (Figure 5.5D). Therefore, MTT and LDH assays revealed a different extent of NP-induced cytotoxicity in HUVEC versus HeLa cells.

The differences in cytotoxicity caused by the nanoparticles may arise from deviations in metabolism and cell proliferation in both cell types [136]. In this context, it has been shown that ultrafine silica particles influence cell viability of human endothelial cells [128]. Others reported that fibroblasts are more susceptible for cytotoxic effects due to silica NPs compared to tumor cells [136]. It is interesting to see that initially (up to at least 4 h) HUVEC cells take up the SiO<sub>2</sub>-310-P particles more efficiently than HeLa cells (Figure 5.3 & Figure 5.4) and that this situation is completely reversed after an exposure of 10 h. A correlation between silica NP uptake behavior and cytotoxic effects has been observed comparing macrophages and cancer epithelial cells. Here macrophages showed 10–15 times more particles interacting with the cells, and this was reflected in the level of cell membrane damage [138].

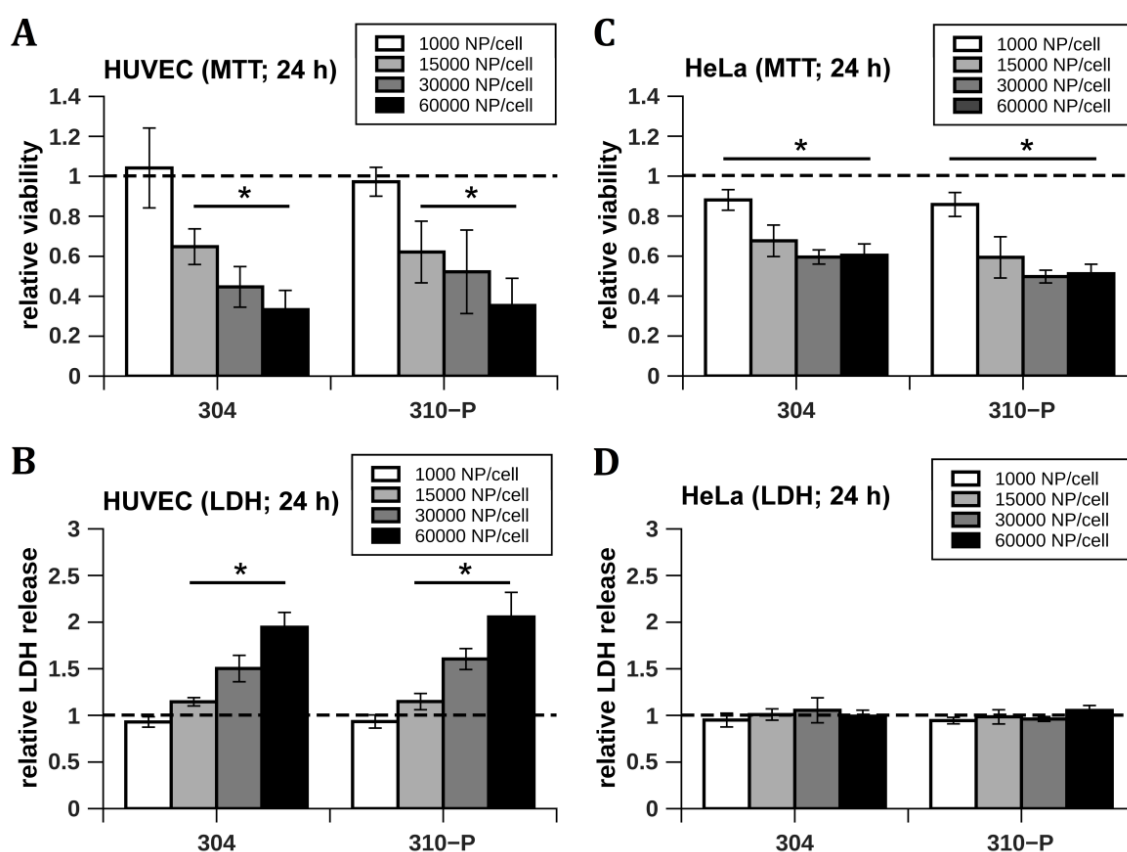


**Figure 5.5 Nanoparticle-induced cytotoxicity in HUVEC and HeLa cells.** Cytotoxic effects of unlabeled silica nanoparticles (SiO<sub>2</sub>-304) and perylene-labeled silica nanoparticles (SiO<sub>2</sub>-310-P) on HUVEC and HeLa cells were analyzed by MTT and LDH measurements. Quantitative analysis revealed a strong correlation between **(A)** reduced metabolic activity and **(B)** membrane damage followed by LDH release in HUVEC. **(C)** Mitochondrial activity in HeLa cells decreased within the first 24 h of exposure **(D)** without showing altered membrane leakage compared to the control (dashed line). Particles with modified surface (SiO<sub>2</sub>-310-P) showed no different toxicity compared to the unlabeled controls (SiO<sub>2</sub>-304). Data represent mean  $\pm$  standard deviation from three independent experiments (n = 6–9) or with pooled triplicates (\* p < 0.05).

### Influence of the perylene-surface functionalization on the toxicity of silica nanoparticles

To analyze cellular uptake and subcellular localization in different cell types, perylene-labeled silica NPs were used. As the toxicity of nanomaterials may depend on factors such as chemical composition and surface (see Section 2.7), we compared cytotoxic effects of unlabeled (SiO<sub>2</sub>-304) and fluorescence-labeled (SiO<sub>2</sub>-310-P) nanoparticles. In our case, the MTT (Figure 5.5A & C) and LDH data (Figure 5.5B & D) were not significantly different. Therefore, we concluded that the surface functionalized with perylene does not affect cytotoxicity of the used NPs neither in HUVEC nor in HeLa cells. These results are in line with a previous publication showing no difference of NPs labeled with perylene compared with blank NPs in regard to cytotoxicity [134].

**Silica nanoparticle-induced cell death**

To gain further insights into cytotoxicity caused by silica NPs, cell death was quantified by flow cytometric analysis after DNA staining with propidium iodide (Figure 5.6). Quantification of fluorescence allows distinguishing between living and dead cells, as cell death correlates with the exclusion of parts of the labeled DNA. As the labeling of the silica NPs with perylene may interfere with the propidium iodide used in this assay, nanoparticle-induced cell death was quantified after exposure to the unlabeled SiO<sub>2</sub>-304. In line with our MTT and LDH results, the rate of viable cells in HUVEC after exposure to  $3.0 \times 10^4$  NPs per cell for 24 h was significantly reduced to 25.9 % compared to the untreated control group. The amount of living endothelial cells treated with  $6.0 \times 10^4$  NPs per cell further decreased to 18.3 % (Figure 5.6A & B). In contrast to HUVEC, SiO<sub>2</sub>-304 showed no effect on the viability of HeLa cells neither after incubation with a concentration of  $3.0 \times 10^4$  NPs per cell nor with  $6.0 \times 10^4$  NPs per cell (Figure 5.6C & D). Quantitative analysis revealed a relative viability of 1.01 for exposure to  $3.0 \times 10^4$  NPs per cell and 0.95 after incubation with  $6.0 \times 10^4$  NPs per cell (Figure 5.6D). These findings are in accordance with LDH assays showing no differences in membrane leakage compared to control (Figure 5.5D). Thus, treatment with silica NPs with a diameter of 304 nm is associated with cell death of HUVEC, whereas an effect on the viability of HeLa cells can be excluded. These results are in agreement with those obtained from an earlier report, where a reduction of viability was observed in different cell types after incubation with amorphous silica [136]. By contrast, nanoparticles caused less cytotoxicity in different tumor cell lines in the same study. Silica nanoparticles-induced cell death has been also reported for different cell types [139]. In this context, it has been shown that the cytotoxicity of silica NPs induces necrotic processes in HUVEC and not apoptosis [134].

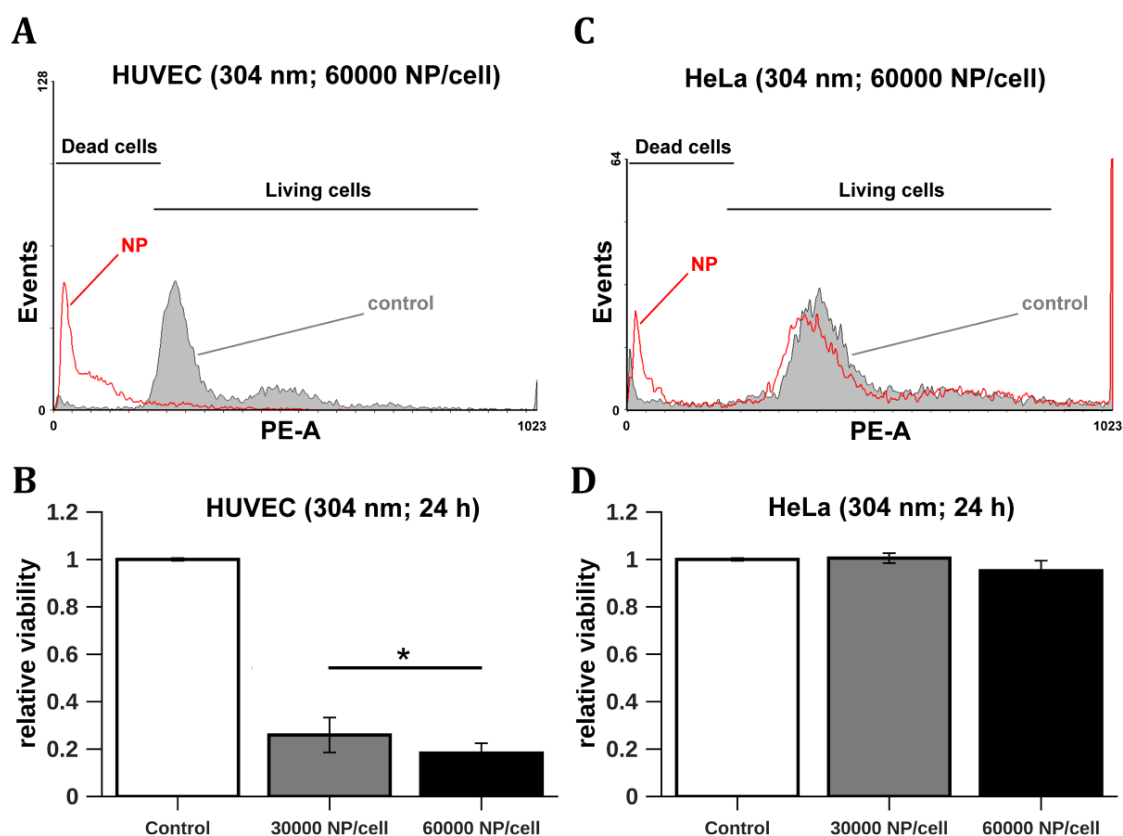


**Figure 5.6 Silica nanoparticles-induced cell death in HUVEC and HeLa cells.** HUVEC and HeLa cells were exposed to silica nanoparticles (NPs) with a diameter of 304 nm at concentrations of  $3.0 \times 10^4$  NPs per cell and  $6.0 \times 10^4$  NPs per cell for 24 h. Cell viability was assessed by propidium iodide staining. **(A)** Fluorescence-activated cell sorting (FACS) analysis and **(B)** quantitative analysis showed a significantly reduced cell viability of HUVEC after exposure to nanoparticles. **(C–D)** In contrast, HeLa cells showed no signs of cell death neither after exposure to  $3.0 \times 10^4$  NPs per cell or after  $6.0 \times 10^4$  NPs per cell. Results represent the means of two independent experiments ( $n = 2–5$ ) and error bars represent the standard deviation (\*  $p < 0.05$ ). PE-A: fluorescence intensity in the PE (phycoerythrin) channel.

### 5.3 Conclusions

In summary, the current study clearly indicates that the cytotoxic impact as well as the uptake kinetics of 310 nm silica NPs are cell type dependent. We showed that, within 4 h of interaction NP-cell, the intracellular accumulation of silica NPs was up to 10 times higher for HUVEC than for HeLa cells. At this point, the uptake behavior followed another trend: between 4 and 10 h, the mean number of intracellular particles increased more than 20 times for HeLa cells, whereas the same parameter was kept almost constant for HUVEC cells. Interestingly, the differences in numbers of NPs taken up by the cells are not directly reflected in the cytotoxic response of HUVEC and HeLa cells to the NPs. While mitochondrial activity and membrane leakage were affected for the endothelial cells, silica particles induced no alterations in the membrane permeability of the tumor cells. As the number of intracellular particles after 24 h is twice as

large for HeLa cells, it can be concluded that the absolute doses of intracellular particles is not responsible for the different level of nanotoxicity observed between HUVEC and HeLa cells. With these experiments, we were also able to show that the surface functionalization of the silica NPs with perylene did not introduce an artificial effect altering the NP-cell interactions. Flow cytometric analyses demonstrated nanoparticle-induced cell death in HUVEC, whereas the viability of HeLa cells was unaffected. Our results clearly show that cytotoxic effects of NPs cannot be generalized and transferred from one cell type to another. This was also shown for a variety of other nanoparticle and cell types. In the current state of knowledge about nanotoxicity, it is inevitable to assess the data for each cell type of interest experimentally. Therefore, in order to predict the potential toxicity effects of NPs on humans, it is important to analyze cells with physiological relevance, such as endothelial cells, and to compare the interactions of defined NPs with different human cell types.

## 6 Effects of the physicochemical properties on the cytotoxicity of sunscreen titania nanoparticles

*This chapter is based on the following publication:*

*Claudia Strobel, Adriano A. Torrano, Rudolf Herrmann, Marcelina Malissek, Christoph Bräuchle, Armin Reller, Lennart Treuel, and Ingrid Hilger;*

*“Effects of the physicochemical properties of titanium dioxide nanoparticles, commonly used as sun protection agents, on microvascular endothelial cells.”*

*Journal of Nanoparticle Research 16, 2130 (2014).*

### 6.1 Introduction

Titania (TiO<sub>2</sub>) nanoparticles are widely used in everyday items, like paints, glues, cosmetics, and personal care products [1]. A major application is found in sunscreens, where the enhanced properties of nanoscaled titania particles are used to protect the skin against the harmful effects of UV solar light. With regard to the application of personal care products, the human skin works as an effective biological barrier against external threat, and sunscreen nanoparticles (NPs) cannot penetrate deeper than a few microns, or layers of skin cells [140]. It follows that NPs deposited on the skin are normally washed away or removed by friction forces (air, water, clothes, etc.). Nevertheless, there are two possible ways by which sunscreen titania NPs might harm our health: photodamage to skin cells, and NP access to the blood system.

In the first case, so as to mitigate the photodamage to skin cells, an alumina, silica, or organic coating is applied to titania NPs. The coating is able to suppress the photocatalytic activity of titania NPs that otherwise would generate undesired free radicals in skin [140]. Titania absorbs about 70 % of incident UV light, and the single electrons produced in this process are translocated to the particle surface [141]. If there is no coating, single electrons can react with oxygen, hydroxyl ions, or water to generate superoxide and hydroxyl radicals and thus initiate oxidative stress in skin cells. However, the photocatalytic activity of coated titania NPs is reduced to safe levels because the coating captures this radical formation. For that reason, basically only coated titania NPs are applied as raw materials for sunscreens [141, 142].

In the second case, penetration of NPs through the skin with subsequent access to the blood vessel system could occur in areas of injured skin (wounds, lesions, and skin disease), especially via hair follicles penetration (see Section 2.2.2). Once in the circulatory system, NPs can interact with endothelial cells and disturb their normal activity (see Section 2.4).

Nowadays, a large number of different titania NPs are commercially available. They may differ in size, shape, crystalline structure (anatase or rutile), but also in their surface properties (e.g., coating), agglomeration, and sedimentation behavior [143, 144]. With respect to the crystalline structures, anatase and rutile polymorphic forms of titania differ in the lattice constants, mobility of charge carriers, width of the optical band gap, and photoactivity [145, 146]. To date, there have been hardly any studies that systematically evaluated the impact of titania NPs on cells in dependence on particles' physicochemical properties. Moreover, the majority of studies addressing the effects of titania NPs on cells deal with uncoated NPs (irrelevant for use in sunscreens), or with NPs that were insufficiently characterized (e.g., no coating mentioned or no indication of titania crystalline form) [147-151]. On the whole, the potential effects of coated titania NPs on endothelial cells are not well understood [152].

Accordingly, in this project we investigate the potential cytotoxicity of coated titania NPs on human microvascular endothelial cells (HMEC-1). First, we selected titania NPs that are commonly present in sunscreens. Three samples are commercialized as additives for personal care products, and another three samples were extracted from different sunscreens available in the market. Next, we systematically characterized all six titania NP samples. The following physicochemical properties were studied: size, shape, crystalline structure, surface coating, zeta potential, surface area, agglomeration, and sedimentation. Finally, the impact on the cellular metabolic activity and the pro-inflammatory response of titania NPs were studied. To assess the impact on the metabolism of cells, the cellular dehydrogenase activity and the adenosine triphosphate (ATP) content were determined. The release of monocyte chemoattractant protein-1 (MCP-1) was used as marker for evaluating the pro-inflammatory response.

Dr. Rudolf Herrmann (Group of Prof. Dr. A. Reller and Group of Prof. Dr. A. Wixforth; University of Augsburg) was responsible for the extraction of titania NPs from sunscreens, for Fourier transform infrared (FT-IR) measurements, transmission electron microscopy (TEM), and for measuring the specific surface area (SSA) of NPs. The cytotoxic effects of titania NPs were evaluated by Claudia Strobel (Group of Prof. Dr. I. Hilger; University of Jena). In our laboratories (Group of Prof. Dr. C. Bräuchle; LMU Munich) we performed particle size distribution determinations via dynamic light scattering (DLS), zeta potential measurements, and studies on the agglomeration and sedimentation behavior of titania NPs.

## 6.2 Results & Discussion

### 6.2.1 Characterization of titania nanoparticles

#### 6.2.1.1 Sunscreen nanoparticles used in this study

Three types of titania NPs applied as raw materials for sunscreens were obtained from Merck KGaA (Germany) EU SOLEX<sup>®</sup> portfolio [153]: samples Eusolex T (anatase, simethicone-coated), Eusolex T-2000 (rutile, alumina- and simethicone-coated) and Eusolex T-Eco (rutile, alumina- and simethicone-coated). Eusolex T-Eco is a modified version of Eusolex T-2000 (undisclosed physical treatment) with a positive impact on dusting and processing [154]. In addition, three titania NP samples were directly isolated from sunscreens with a protection factor of 50+: the sample Babysmile was obtained by extracting titania NPs from BABYSMILE<sup>®</sup> SONNENMILCH (Win Cosmetic, Germany); Ladival NPs were isolated from LADIVAL<sup>®</sup> SONNENSCHUTZMILCH (Stada, Germany); and the sample Babylove is composed of titania NPs extracted from BABYLOVE<sup>®</sup> SONNENCREME (dm-drogerie markt, Germany). Remarkably, we found that the sample Babysmile is in fact composed of Eusolex T titania NPs included in the formulation of BABYSMILE<sup>®</sup> SONNENMILCH. This information was confirmed by the manufacturer. Further details about the extraction of titania NPs from sunscreens are given in Experimental Section 11.3.1.

#### 6.2.1.2 Primary size, shape, and crystalline structure

Transmission electron microscopy (TEM) was performed to determine the primary size, shape, and crystalline structure of the titania NPs. The shape of the anatase NPs Eusolex T and Babysmile (Figure 6.1A & B, respectively) can be approximated as prolate ellipsoid (egg-shaped), having a mean aspect ratio of 1.12 (core diameters: 19 x 17 nm). In contrast, rutile NPs Ladival, Eusolex T-2000, Eusolex T-Eco, and Babylove (Figure 6.1C–F, respectively) are rod-like structures with an aspect ratio ranging from 2.91 (Ladival, core diameters: 64 x 22 nm), passing by 4.36 (Babylove, core diameters: 48 x 11 nm) and going up to 6.69 (Eusolex T-2000 and Eusolex-Eco, core diameters: 87 x 13 nm). The physicochemical properties of the titania NPs used in this study are summarized in Table 6.1.

#### 6.2.1.3 Hydrodynamic particle size distribution

Dynamic light scattering (DLS) measurements were employed to determine the hydrodynamic diameter of the particles. Measurements were performed on colloidal NP suspensions (100  $\mu\text{g mL}^{-1}$ ) in either ultrapure water or cell culture medium supplemented with 10 % fetal bovine serum (FBS). By comparison of the particle sizes obtained by TEM and DLS measurements, diverse larger sizes were observed via DLS (see Table 6.1).



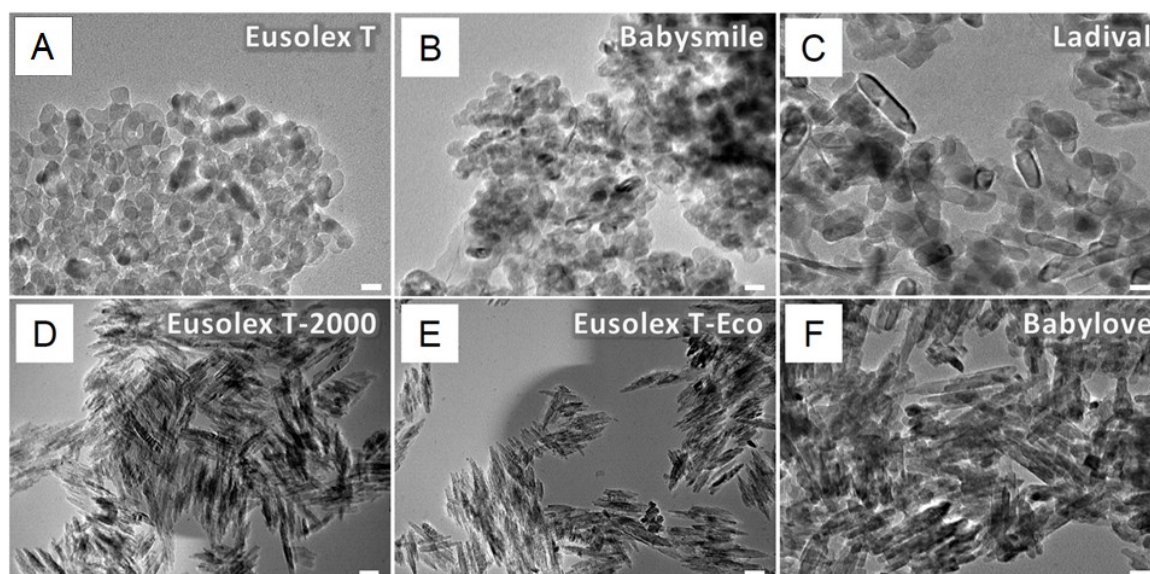








**Figure 6.1** TEM images of titania NPs used in this study. Scale bars = 20 nm.

The adsorption of proteins from the cell culture medium can have distinct effects on the agglomeration behavior of the NPs. It may result in a reduced agglomeration behavior by steric stabilization, or it may lead to a cross-linking of the NPs [155]. The particle size distributions in ultrapure water ranged from 68 nm (Babysmile) to 3628 nm (Babylove), and from 56 nm (Eusorex T-Eco) to 2623 nm (Ladival) in 10 % FBS cell medium. In fact, only Eusorex T-Eco showed comparable size distribution between TEM and DLS measurements in cell medium, and consequently little clustering. With regard to the distinct agglomeration behavior of titania NPs in water or in cell medium, Babysmile, Ladival, and Eusorex T-2000 presented larger hydrodynamic diameters in cell medium. On the other hand, Eusorex T, Eusorex T-Eco, and Babylove showed an increased hydrodynamic diameter in water. These results therefore show that titania NP samples have a tendency to agglomerate in water and in cell media containing serum proteins.

#### 6.2.1.4 Coating and secondary shell compositions

The composition analysis of the NPs by Fourier transform infrared (FT-IR) spectroscopy confirmed the presence of dimethicone/simethicone coating in the three titania NP samples commercialized as raw materials: Eusorex T, Eusorex T-2000, and Eusorex T-Eco ( $1,256\text{ cm}^{-1}$ , symmetric bending of Si-CH<sub>3</sub> groups, and slightly overlapping peaks at  $1,016$  and  $1,096\text{ cm}^{-1}$  due to Si-O stretch and Si-O-Si bending) [156]. Simethicone was also present in the analyses of samples Babysmile and Ladival. The rutile samples Eusorex T-2000 and Eusorex T-Eco are commercialized with an additional alumina coating.

Table 6.1 Physicochemical characteristics of titania NPs

TiO <sub>2</sub> nanoparticles	Eusolex T	Babysmile	Ladival	Eusolex T-2000	Eusolex T-Eco	Babylove
<b>Crystalline polymorphic form of TiO<sub>2</sub> (modification)</b>	anatase	anatase	rutile	rutile	rutile	rutile
<b>Size by TEM [nm] (length x width)</b>	19 ± 5 x 17 ± 4	19 ± 5 x 17 ± 4	64 ± 25 x 22 ± 5	87 ± 31 x 13 ± 3	87 ± 31 x 13 ± 3	48 ± 25 x 11 ± 5
<b>Aspect Ratio</b>	1.12	1.12	2.91	6.69	6.69	4.36
<b>Size in H<sub>2</sub>O by DLS [nm]</b>	1179 ± 309	68 ± 24	166 ± 49	113 ± 31	369 ± 65	3628 ± 746
<b>Size in 10% FBS medium by DLS [nm]</b>	97 ± 18	123 ± 71	2623 ± 1129	190 ± 47	56 ± 21	194 ± 50
<b>SSA accessible to N<sub>2</sub> molecules (m<sup>2</sup>/g)</b>	50.0	2.8	22.0	83.2	83.8	42.0
<b>Zeta potential [mV] in 10% FBS medium</b>	-15.0	-16.6	-14.9	-14.2	-13.7	-15.7
<b>Schematic representation with coating/secondary shell</b>						
	— TiO <sub>2</sub> anatase modification — TiO <sub>2</sub> rutile modification	— simethicone — alumina & simethicone	— alumina — esters	— hydrophilic compounds like polyols (e.g. glycols)		

Our results revealed that titania NPs extracted from sunscreens usually have a secondary shell composed of residual materials from the sunscreen formulations. Secondary shells were detected in all three samples. In Babysmile and Ladival NPs, it consisted of esters of aromatic acids. Ladival NPs additionally contained the surfactant stearylalkonium hectorite (strong band at 1,060 cm<sup>-1</sup> due to Si–O–Si units present in this surfactant). Polyols were detected in the sample Babylove. Since the functional groups contained in such polymers (mainly esters) are the same as in many other ingredients of the formulations, FT-IR spectroscopy does not allow determining their presence at the particle surface with certainty.

The presence of a secondary shells around titania NPs extracted from sunscreens can be detected as small regions of low contrast around the particles in the TEM images of samples Babysmile, Ladival, and Babylove (Figure 6.1B–C & F, respectively). A schematic representation of NPs and respective coatings and secondary shells is given in Table 6.1.

#### 6.2.1.5 Zeta potential

Investigations on the electrophoretic mobility of the titania NPs were carried out to determine the zeta potential. Measurements were performed on colloidal NP suspensions ( $100 \mu\text{g mL}^{-1}$ ) in 10 % FBS cell culture medium. Similar zeta potential values, in the range between  $-13.7$  and  $-16.6$  mV, were determined for all titania NPs (see Table 6.1). Thus, the different NP morphologies or surface coatings did not result in distinct surface charge profiles of these particles in cell medium.

#### 6.2.1.6 Specific surface area

The specific surface area (SSA) accessible to  $\text{N}_2$  molecules was obtained by Brunauer–Emmett–Teller (BET) measurements [157]. The SSA for the investigated titania NPs ranged between  $2.8$  and  $83.8 \text{ m}^2 \text{ g}^{-1}$  (see Table 6.1). The reason for the relatively low surface area of Ladival ( $22.0 \text{ m}^2 \text{ g}^{-1}$ ) might be due to the presence of the sticky organic/inorganic surfactant stearalkonium hectorite in the formulation of this sunscreen. The sample Babysmile showed a very low SSA ( $2.8 \text{ m}^2 \text{ g}^{-1}$ ), especially when compared with the starting material (Eusolex T,  $50.0 \text{ m}^2 \text{ g}^{-1}$ ). This is very probably due to polymeric ingredients with low solubility present only in BABYSMILE® sunscreen (e.g., VP/eicosene copolymer, acrylate/C10–30 alkyl acrylate crosspolymer, and xanthan gum).

#### 6.2.1.7 Agglomeration and sedimentation behavior

The agglomeration and the sedimentation behavior of titania NPs in cell medium were investigated via light microscopy especially prepared to mimic the exposure of cells to NPs. The time points selected for this assessment correspond to those applied in our cytotoxicity assays (3, 24, 48, and 72 h), and therefore revealed the agglomeration and local concentration of NPs as they approached the cells (Figure 6.2).

This important information for *in vitro* experiments has been poorly considered in nanotoxicology studies up to now. Samples with distinct particle sedimentation rates will result in different amounts of NPs in contact with cells, despite the fact that the cells were treated with the same NP concentration. Therefore, the obtained cytotoxicity results could be influenced by differences in agglomeration and sedimentation behavior of the NPs, rather than by the biological effects.

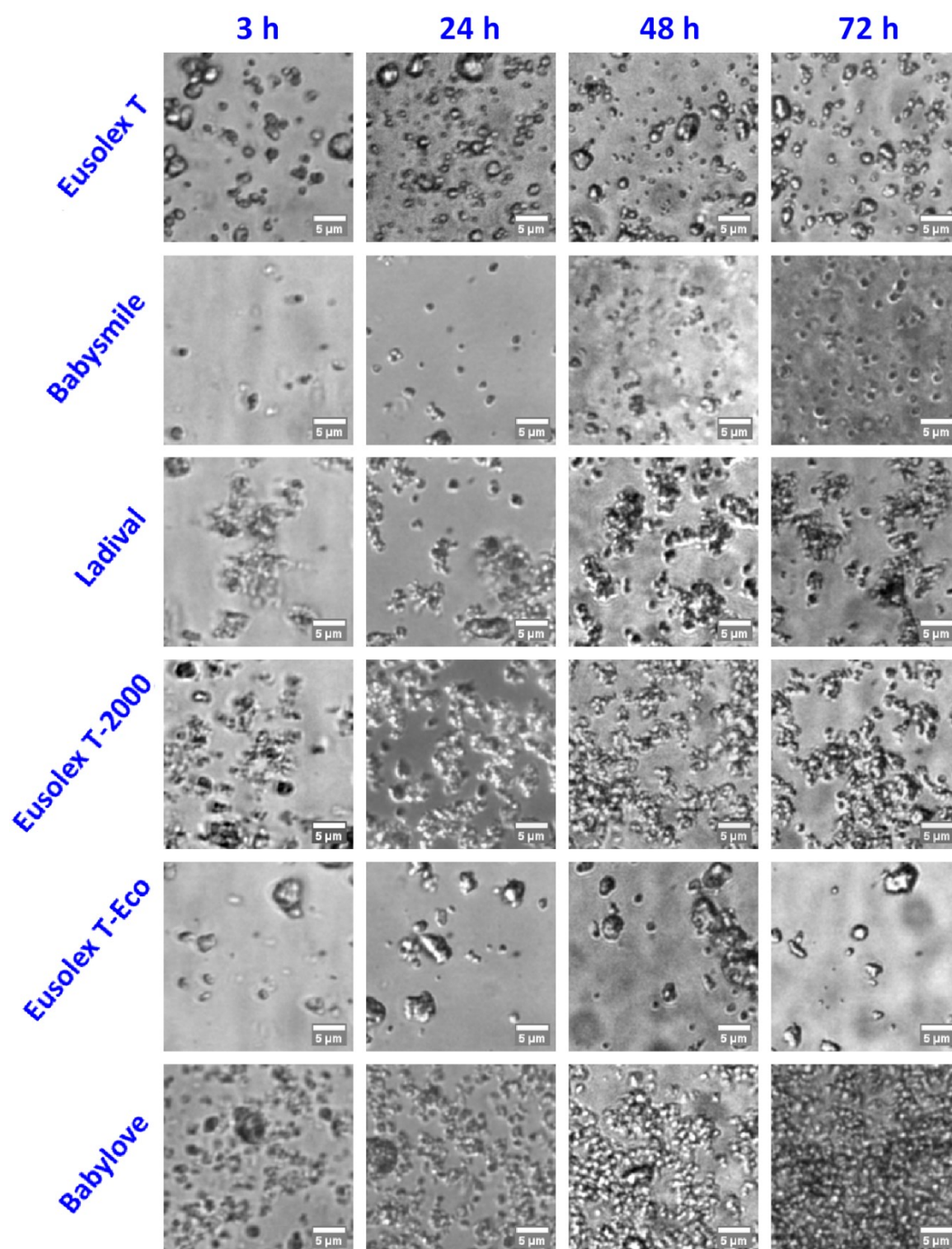


**Figure 6.2 Agglomeration and sedimentation behavior.** Titania NPs differ enormously in their agglomeration state and sedimentation behavior. Colloidal suspensions were added to cell culture chambers deprived of cells in order to mimic the exposure of NPs to cells. Along the same time points, there were distinct differences in the agglomeration and amount of deposited titania NPs for different samples.

Bright field images were acquired with a spinning disk confocal microscope. In brief, titania NPs ( $100 \mu\text{g mL}^{-1}$ ) were added to cell culture chambers (deprived of cells) and imaged at the abovementioned specific time points. Figure 6.2 presents representative images of the bottom of cell culture chambers to reveal the agglomeration state and sedimentation behavior of the investigated titania NPs. Interestingly, whereas the amount and size distribution of deposited Eusolex T, Eusolex T-2000, and Eusolex T-Eco NPs did not change considerable between 3 and 72 h of incubation, the alterations for the three NP formulations isolated from sunscreens (Babysmile, Ladival, and Babylove) were evident, with a time-dependent increase in the local amount of deposited NPs. When comparing the hydrodynamic particle size distributions with the image of sedimented particles, it is important to remember that the first gives instant information about the whole sample, while the second shows the accumulation of sedimented particles close to the bottom of a cell culture chamber. Notably, neither the morphology nor the zeta potential were found to be associated with the agglomeration and sedimentation behavior of titania NPs.

## 6.2.2 Cytotoxicity of titania nanoparticles

### 6.2.2.1 Assessment of the metabolic activity and pro-inflammatory response of endothelial cells exposed to titania nanoparticles

To investigate the impact of titania NPs on the metabolism of HMEC-1 cells, the cellular dehydrogenase activity and the adenosine triphosphate (ATP) content were determined. First of all, we established the lowest concentration that caused an adverse effect on cells (i.e., the lowest-observable-adverse-effect level). For that, we measured the cellular dehydrogenase activity of cells treated with titania NPs at different concentrations (ranging from  $10 \text{ fg mL}^{-1}$  to  $100 \mu\text{g mL}^{-1}$ ), and at defined incubation times (3, 24, 48, and 72 h). Measurement data were evaluated and presented as relative cellular dehydrogenase (rcDH) activity normalized to untreated controls. Transient effects on the rcDH activity were especially detected at a concentration of  $100 \mu\text{g mL}^{-1}$ . At this concentration, rcDH values lower than the cytotoxicity threshold (according to DIN EN ISO 10993-5:2009-10) were observed. Representative results for anatase titania NPs are presented in Figure 6.3A–D, and for rutile NPs in Figure 6.4A. On the basis of these results, we determined  $100 \mu\text{g mL}^{-1}$  as the lowest-observable-adverse-effect level. This concentration was then applied for all further cytotoxicity assays, namely the relative cellular adenosine triphosphate (rATP) content and the release of monocyte chemoattractant protein-1 (MCP-1).

To assess the ATP content, cells were treated with cell medium containing  $100 \mu\text{g mL}^{-1}$  of titania NPs during 3, 24, 48 and 72 h. The ATP content of the cells was measured and expressed as relative values (rATP) compared to untreated control cells. To interpret the impact of the NPs on endothelial cells, we also considered here the threshold for cytotoxicity according to DIN EN ISO 10993-5:2009-10.

In order to determine the pro-inflammatory impact of the NPs, HMEC-1 cells were incubated with cell medium containing  $100 \mu\text{g mL}^{-1}$  of NPs. The cell culture supernatants were collected after 24, 48, and 72 h of incubation, and the content of monocyte chemoattractant protein-1 (MCP-1) was determined. MCP-1 is known to be an important chemoattractant for the recruitment and activation of monocytes in areas of inflammation, and it plays an important role, among others, in the development of chronic inflammation [158]. To control the ability of HMEC-1 cells to produce MCP-1 after a corresponding stimulus, the cells were incubated with  $2,000 \text{ pg mL}^{-1}$  of interleukin-1b (IL-1 $\beta$ ) as positive control.

#### **6.2.2.2 Cytotoxicity of anatase titania nanoparticles**

The metabolic activity of HMEC-1 cells exposed to anatase titania NPs (Eusolex T and Babysmile) was assessed by measuring the relative cellular dehydrogenase (rcDH) activity (Figure 6.3A–D), and the relative adenosine triphosphate (rATP) content of cells (Figure 6.3E). Our results revealed a slight impact on the rcDH activity and also a decrease in the rATP content. Babysmile NPs (simethicone coating with an ester-based secondary shell) were significantly more cytotoxic than Eusolex NPs (simethicone coating) in most of the evaluated time points. An exception is found after 48 h of incubation at a concentration of  $100 \mu\text{g mL}^{-1}$ . Here, the cytotoxic threshold (75 %) is only surpassed by Eusolex T NPs. Moreover, Babysmile NPs caused a reduction in the rATP content to values below the cytotoxic threshold within 24 and 72 h, while Eusolex T NPs such an effect was observed only for 24 h. The pro-inflammatory response of cells within 48 and 72 h to both anatase titania NPs was significantly larger than the untreated control (Figure 6.3F). In addition, consistent with the findings regarding the metabolic impact, Babysmile NPs induced more pro-inflammatory response on endothelial cells than Eusolex T.

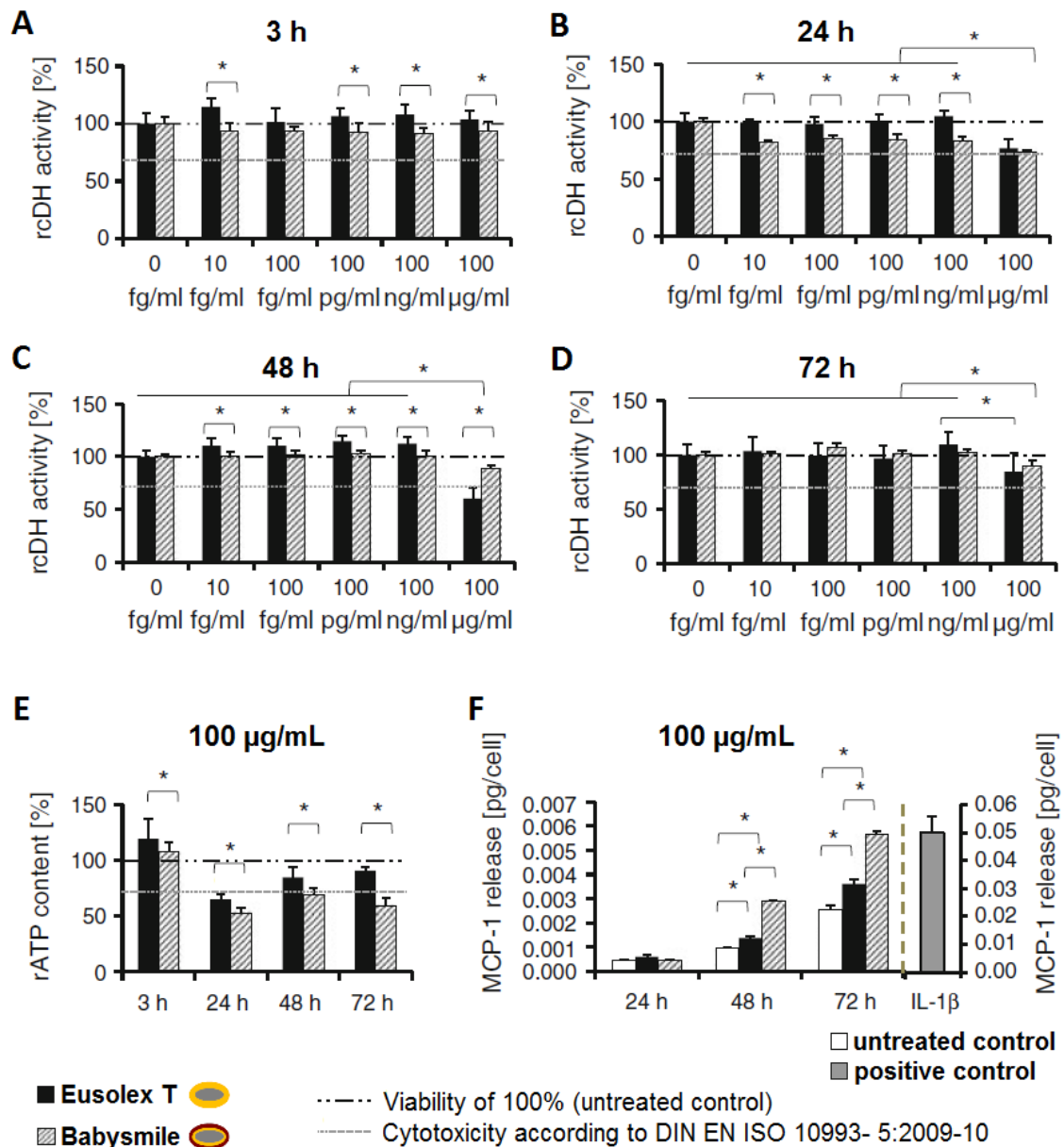


**Figure 6.3 Metabolic activity and pro-inflammatory response of anatase titania NPs on endothelial cells.** Cytotoxicity of HMEC-1 cells treated with Eusolex T (black bars) and Babysmile (striped bars) at different concentrations ranging from 10 fg mL<sup>-1</sup> to 100 µg mL<sup>-1</sup>. Cells were incubated with the NPs for 3, 24, 48, and 72 h. **(A–D)** Relative cellular dehydrogenase (rcDH) activity of cells after exposure to distinct NP concentrations. In most of the cases, Babysmile was significantly more cytotoxic than Eusolex T. Significant differences between the rcDH activity at the highest investigate concentration and all other concentrations were verified for both anatase titania NPs within 24 and 72 h. **(E)** Relative ATP (rATP) content after incubation with 100 µg mL<sup>-1</sup> of NPs for 3–72 h. Babysmile NPs were significantly more cytotoxic that Eusolex NPs in all time points. **(F)** Release of the monocyte chemoattractant protein-1 (MCP-1) after incubation with 100 µg mL<sup>-1</sup> of NPs for 24–72 h. Cells treated with interleukin-1b (IL-1β) served as positive control (gray bar, MCP-1 release scale on the right side). The pro-inflammatory response of cells within 48 and 72 h to both anatase titania NPs was significantly larger than the untreated control (white bars). Consistent with the findings regarding the metabolic impact (panels A–E), ester-coated Babysmile NPs induced significantly more MCP-1 release than the counterpart particles Eusolex T. Histograms represent mean ± standard deviation of six (A–E, n = 6) or three (F, n = 3) independent experiments (\* p < 0.05).

### 6.2.2.3 Cytotoxicity of rutile titania nanoparticles

In line with the results for anatase titania NPs, secondary shell-related cytotoxic effects were also detected for rutile titania NPs. Figure 6.4 presents the cytotoxic impact of rutile titania NPs on HMEC-1 cells. Assessment of the metabolic activity (Figure 6.4A) revealed that titania NPs isolated from sunscreens (Ladival: simethicone coating with an ester-based secondary shell; and Babylove: pure alumina ( $\text{Al}_2\text{O}_3$ ) coating with a polyol-based secondary shell) induced a rapid decrease in the rcDH activity, with values below the cytotoxic threshold within 24 and 72 h of incubation. The highest impact on the rcDH activity of endothelial cells was detected for Babylove NPs. In contrast, commercially available NPs (Eusolex T-2000 and Eusolex T-Eco: alumina-simethicone coating) caused a gradual decrease in the relative dehydrogenase activity of cells over time, with values below the cytotoxic threshold only after 72 h of incubation. All rutile titania samples affected the relative ATP content of endothelial cells (Figure 6.4B). Interestingly, the lowest value for all samples was observed after 24 h of incubation. Overall, while Ladival and Babylove consistently induced cytotoxic responses below the threshold (75 %) within 24 and 72 h, a similar effect was less often caused by Eusolex T-2000 and Eusolex T-Eco (Figure 6.4A & B). In terms of the pro-inflammatory impact (Figure 6.4C), all rutile titania NP samples presented significantly larger MCP-1 release values than the untreated control after 72 h. Remarkably, Babylove NPs triggered the strongest increase of MCP-1 release in comparison to all other investigated titania NPs.

### 6.2.2.4 Comparison between the cytotoxicity of anatase and rutile titania NPs

With the purpose of comparing the cytotoxicity of anatase and rutile titania NPs, we selected two NP samples of comparable coating and secondary shell compositions: Babysmile (anatase) and Ladival (rutile) NPs. Both particle types are coated by simethicone and have an ester-based secondary shell. We observed a higher impact of rutile NPs on the rcDH activity over time (Figure 6.5A). ATP levels were significantly different between rutile and anatase NPs (Figure 6.5B). Within 3 and 48 h, rutile Ladival NPs caused a larger reduction of the rATP than anatase Babysmile NPs. However, after 72 h the situation was reversed, with anatase NPs significantly more cytotoxic than rutile ones. On the whole, rutile Ladival NPs had a significantly larger impact on the metabolic activity than anatase Babysmile NPs. While Ladival NPs consistently surpassed the cytotoxicity threshold of 75 % within 24 and 72 h, a similar effect was less often observed for Babysmile NPs (Figure 6.5A & B). In agreement with these findings, rutile titania NPs induced a higher pro-inflammatory response when compared to their anatase counterparts (Figure 6.5C).



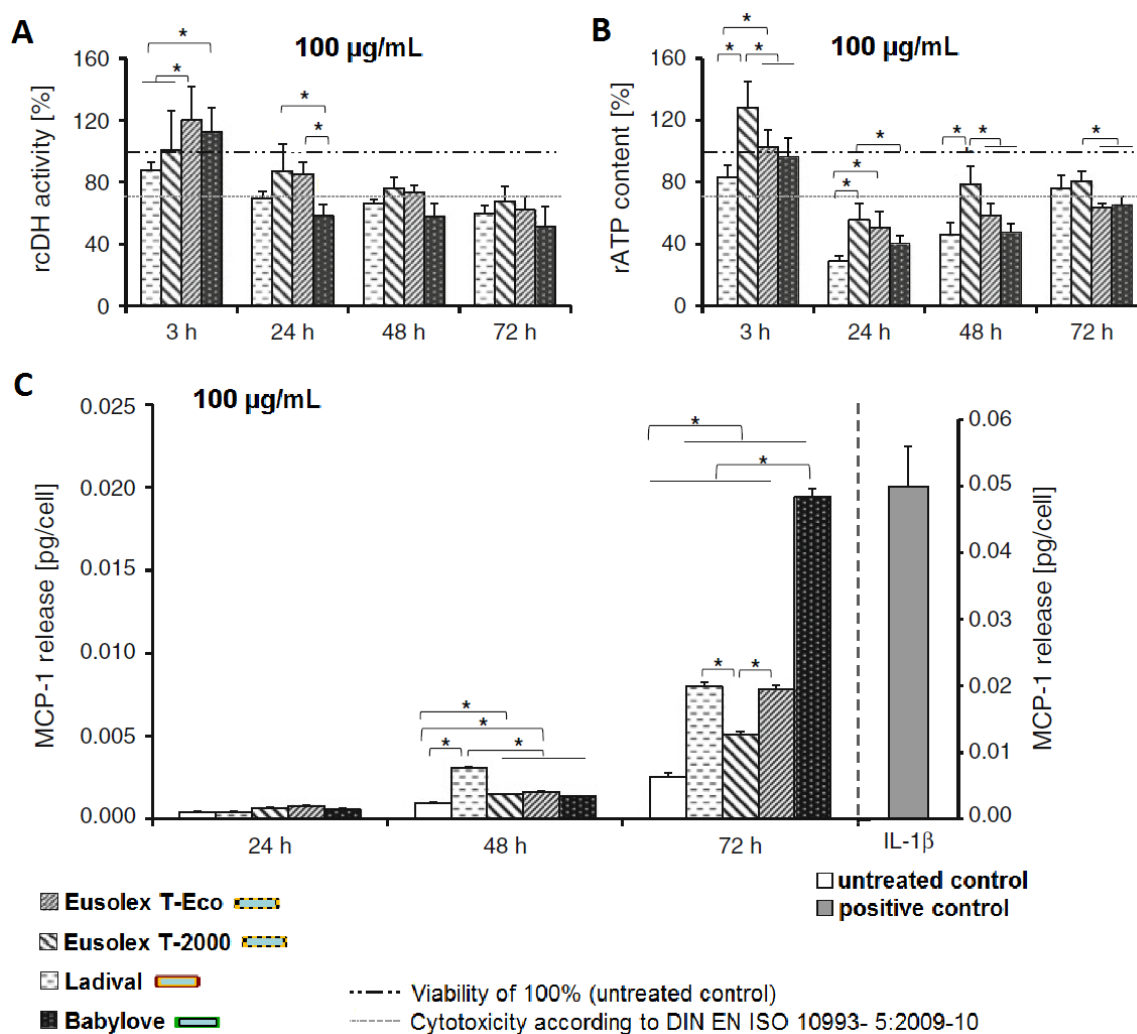


**Figure 6.4 Metabolic activity and pro-inflammatory response of rutile titania NPs on endothelial cells.** Cytotoxicity of HMEC-1 cells treated with  $100 \mu\text{g mL}^{-1}$  of Ladival (white punctuate bars), Eusolex T-2000 (thick striped bars), Eusolex T-Eco (thin striped bars), and Babylove (black punctuate bars) for 3, 24, 48, and 72 h. **(A)** Relative cellular dehydrogenase (rcDH) activity of cells. A time-dependent decrease of the rcDH activity was observed after exposure to rutile titania NPs. Particularly, Babylove NPs (alumina coating with a polyol-based secondary shell) led to the strongest decrease in the rcDH activity within 24 and 72 h. **(B)** Relative ATP (rATP) content. In general, rutile titania NPs extracted from sunscreens (Ladival and Babylove) had a significantly larger impact on the metabolic activity than commercialized NPs (Eusolex T-2000 and Eusolex T-Eco). **(C)** Release of the monocyte chemoattractant protein-1 (MCP-1) after incubation with rutile titania NPs for 24–72 h. Cells treated with interleukin-1b (IL-1 $\beta$ ) served as positive control (gray bar, MCP-1 release scale on the right side). The pro-inflammatory response of cells after 72 h was significantly larger than the untreated control (white bars) for all rutile titania NP samples, and the highest MCP-1 release was observed for cells treated with Babylove NPs. Interestingly, the largest pro-inflammatory response of cells after 48 h was measured for Ladival NPs. Histograms represent mean  $\pm$  standard deviation of six (A–B,  $n = 6$ ) or three (C,  $n = 3$ ) independent experiments (\*  $p < 0.05$ ).

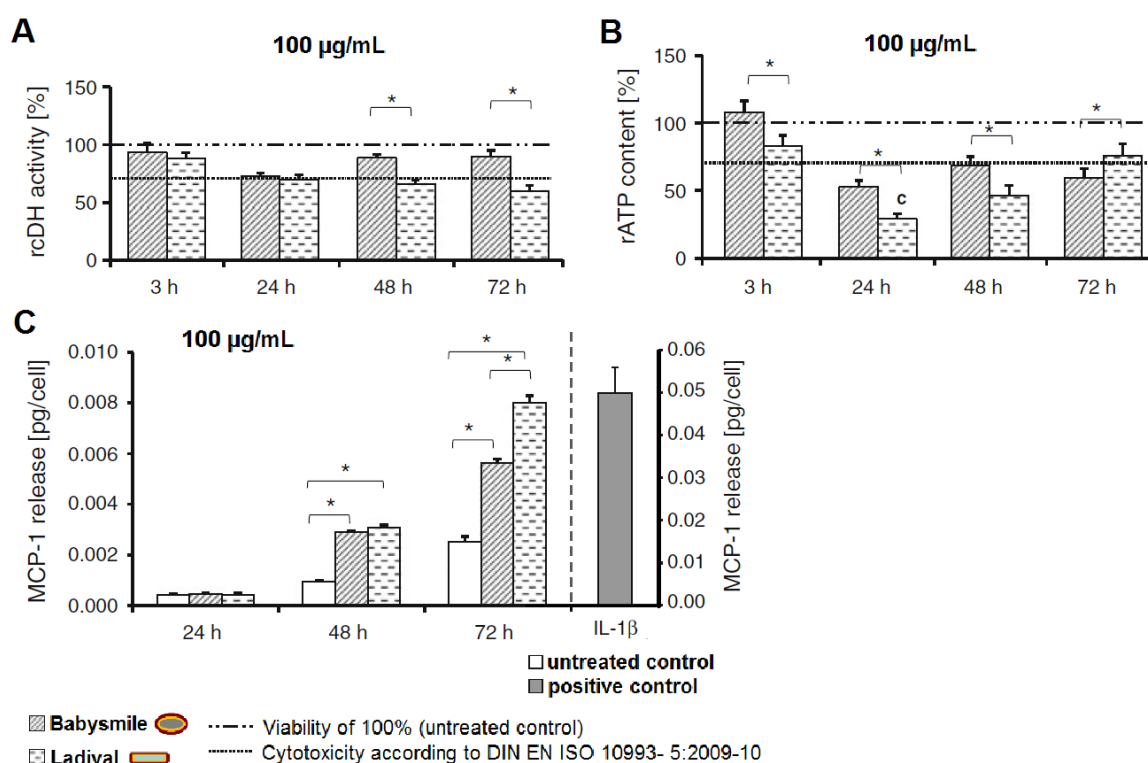


**Figure 6.5 Comparison between the cytotoxic impact of anatase and rutile titania NPs on endothelial cells.** Cytotoxicity of HMEC-1 cells treated with  $100 \mu\text{g mL}^{-1}$  of either anatase titania Babysmile NPs (striped bars) or with rutile titania Ladival NPs (punctuate bars) for 3, 24, 48, and 72 h. **(A)** Relative cellular dehydrogenase (rcdH) activity of cells. After 48 and 72 h of NP exposure, rutile titania NPs (Ladival) revealed a significantly larger decrease of rcdH than their anatase counterparts (Babysmile). **(B)** Relative ATP (rATP) content. The lowest relative ATP content was measured after 24 h of exposure to both samples. Overall, rutile Ladival NPs had a significantly larger impact on the metabolic activity than anatase Babysmile NPs. **(C)** Release of the monocyte chemoattractant protein-1 (MCP-1) after incubation with anatase and rutile titania NPs for 24–72 h. Cells treated with interleukin-1b (IL-1 $\beta$ ) served as positive control (gray bar, MCP-1 release scale axis on the right). After 48 and 72 h of NP exposure, a significant increase of MCP-1 release with respect to untreated control (white bars) was observed for both Babysmile and Ladival NPs. After 72 h of incubation, the rutile NPs led to a stronger release of MCP-1. Histograms represent mean  $\pm$  standard deviation of six (A–B,  $n = 6$ ) or three (C,  $n = 3$ ) independent experiments (\*  $p < 0.05$ ).

### 6.3 Conclusions

Taken together, our results shed light on the mostly neglected potential cytotoxicity related to titania particles' crystalline structure and coating composition. Altogether, titania NPs with a rutile core had a stronger effect on cell metabolism than anatase titania NPs. Remarkably, the presence of an organic secondary shell on titania NPs extracted from sunscreens (regardless the crystalline structure) correlated with an enhanced impact of NPs on the metabolic activity and pro-inflammatory response of endothelial cells. Further distinct correlations between

cytotoxicity of titania NPs and other physicochemical properties (particle size, zeta potential, surface area, agglomeration, and sedimentation behavior) were not observed.

The present work indicates that the lowest-observable-adverse-effect level of titania NPs to endothelial cells *in vitro* is fairly high ( $100 \mu\text{g mL}^{-1}$ ). In real-life situations, however, endothelial cells would come in contact with considerably lower titania NP doses. Such high concentrations typically applied in *in vitro* studies may overestimate the effects that can be found *in vivo*. Nevertheless, *in vitro* investigations are very important as they collaborate to elucidate the cellular mechanisms of nanotoxicity.

## 7 Particle size-dependent uptake of ceria nanoparticles

*This chapter is based on the following publication:*

*Adriano A. Torrano and Christoph Bräuchle;*

*“Precise quantification of silica and ceria nanoparticle uptake revealed by 3D fluorescence microscopy.”*

*Beilstein Journal of Nanotechnology 5, 1616-1624 (2014).*

### 7.1 Introduction

Ceria NPs can be found in many applications, as in ultraviolet absorbers, automotive catalytic converters, fuel additives, and oxygen sensing [159-162]. Nanoparticles, such as ceria and platinum-decorated ceria NPs (see Chapter 8) released from catalytic converters, may be taken up via the respiratory tract and then be transferred into the bloodstream. Next, the NPs will be in contact with endothelial cells lining the inner surface of our blood vessel system. As described in Section 2.4, endothelial cells play a crucial role in many physiological processes and an altered endothelial cell function can be found in innumerable diseases of the cardiovascular, pulmonary, and neurologic systems [22, 56]. Due to the extensive range of applications and to the potential risks of nanomaterials, a growing number of studies regarding the cytotoxicity of NPs can be found in the literature. In the case of ceria NPs, very contradictory findings have been reported. On the one hand, the anti-inflammatory, antioxidant and radio-protective properties have been described as beneficial for applications in nanomedicine [163-166]. On the other hand, oxidative stress and impaired cell viability were shown to be a function of the particle dose and the exposure time [108, 167]. However, most of the studies concerning the interaction of ceria NPs with cells cannot be directly compared as they were performed by applying different cell types and a variety of different particles.

This chapter is dedicated to present quantitative results on the particle size-dependent uptake kinetics of ceria ( $\text{CeO}_2$ ) NPs of 8 nm and 30 nm. Nanoparticles at a concentration of  $10 \mu\text{g mL}^{-1}$  were incubated with human microvascular endothelial cells (HMEC-1) for 3, 24, 48 and 72 h and imaged through live-cell confocal microscopy. In order to measure the absolute number of intracellular particles, fluorescence images were evaluated with Particle\_in\_Cell-3D (see Chapter 4).

Cytotoxicity assays performed on similar NPs have shown that, in general, the impact of ceria NPs on endothelial cells (HUVEC and HMEC-1) is not significant, and that adverse effects can only be observed at concentrations as high as  $100 \mu\text{g mL}^{-1}$  [168]. Such doses exceed the maximum possible *in vivo* concentrations.

Ceria NPs were synthesized by Dr. Rudolf Herrmann (Group of Prof. Dr. A. Reller and Group of Prof. Dr. A. Wixforth; University of Augsburg). Dr. Herrmann was also responsible for transmission electron micrographs.

## 7.2 Results & Discussion

### 7.2.1 Characterization of ceria nanoparticles

In order to be investigated with fluorescence microscopy, the particles were marked with Atto 647N. The synthesis of the ceria NPs investigated in this study is described in the literature [133]. The labeling of these particles with Atto 647N did not alter the biological response of the cells, as assessed by cytotoxicity assays. HMEC-1 cells were incubated over 48 h with  $100 \mu\text{g mL}^{-1}$  of either non-labeled or Atto 647N-labeled ceria NPs. After this period, the relative adenosine triphosphate (rATP) content was analyzed to determine the metabolic impact of NPs on cells. One hundred percent rATP content would mean that the cellular viability of the cells treated with NPs matches the viability of untreated cells. As shown by Strobel *et al.* [168], incubation with non-labeled 8 nm and 30 nm ceria NPs resulted in rATP values (mean  $\pm$  standard deviation) of  $82.0 \pm 5.6 \%$  and  $76.3 \pm 10.8 \%$ , respectively. The rATP contents measured after the exposure to Atto 647N-labeled NPs of 8 nm and 30 nm were  $80.1 \pm 6.2 \%$  and  $79.5 \pm 14.9 \%$ , respectively. Therefore, the fluorescent labeling of the ceria NPs presented in this work did not significantly alter the cytotoxicity of these particles on HMEC-1 cells. The primary size of the two NPs was determined through transmission electron microscopy (TEM). One particle type has a diameter of 8 nm and is spherical ( $\text{CeO}_2$ -8 nm), while the other particle type has a diameter of roughly 30 nm ( $\text{CeO}_2$ -30 nm) (ellipsoid of  $27 \text{ nm} \times 30 \text{ nm}$ ). It has been shown that the smaller the NPs, the stronger the agglomeration [117]. This has been confirmed by determination of the hydrodynamic diameter of these particles. DLS measurements were carried out and the size of  $\text{CeO}_2$ -8 nm increased up to 417 nm in cell medium. In the case of the  $\text{CeO}_2$ -30 nm particles, the diameter in cell medium was determined to be 316 nm. The aggregation of ceria NPs is also evident in the representative TEM images depicted in Figure 7.1. The zeta potential was determined with NPs dispersed in cell medium. The following values were measured: -11.3 mV for sample  $\text{CeO}_2$ -8 nm and -12.3 mV for sample  $\text{CeO}_2$ -30 nm.

The Particle\_in\_Cell-3D calibration routine procedure described in Section 4.2.3.4 was used to measure the mean fluorescence of single ceria particles. The results were intensities of 131,201 pixels ( $\text{CeO}_2$ -8 nm) and 742,814 pixels ( $\text{CeO}_2$ -30 nm), respectively. There is an important particularity to be mentioned here. The mean intensity of the single particles is in fact the mean intensity of single agglomerates, as it was not possible to obtain single NPs of primary sizes for the calibration experiments. Those agglomerates, however, are in fact the particles that interact with the cells.

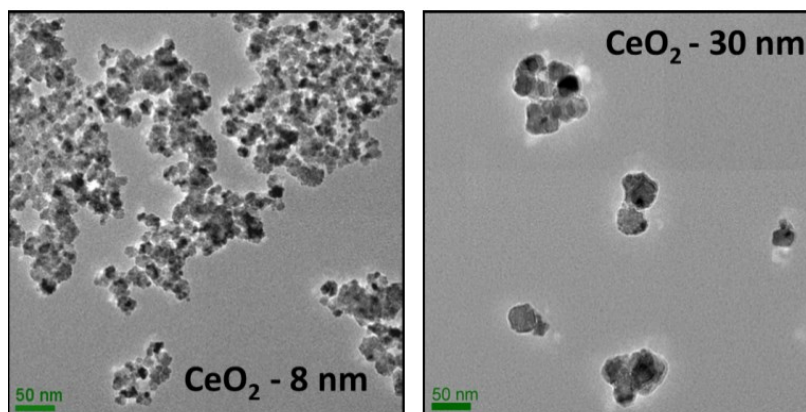


**Figure 7.1** TEM images of ceria NPs samples with a primary size of 8 nm ( $\text{CeO}_2$ -8 nm) and 30 nm ( $\text{CeO}_2$ -30 nm). Large aggregates of synthesized NPs are visible in both samples. A massive agglomeration was also observed when NPs were dispersed in cell medium. DLS measurements revealed that  $\text{CeO}_2$ -8 nm and  $\text{CeO}_2$ -30 nm NPs clustered into 417 nm and 316 nm agglomerates, respectively.

## 7.2.2 Quantification of ceria nanoparticle uptake by cells

With the purpose of investigating the size-dependent uptake kinetics of ceria NPs for a longer time than traditionally, HMEC-1 cells were incubated with 8 nm (417 nm) and 30 nm (316 nm) NPs for 3, 24, 48 and 72 h. Figure 7.2 presents illustrative images of the interaction of ceria NPs with endothelial cells. Approximately 15 single cells were measured per time point and per particle type, resulting in a total of 115 cells analyzed in great detail by Particle\_in\_Cell-3D. These quantitative results are presented in Figure 7.3 and show that the number of incorporated particles increases steeply between 3 and 24 h, with no significant difference between the two particle sizes. The number of internalized agglomerates of  $\text{CeO}_2$ -8 nm NPs increased from  $337 \pm 66$  to  $2,069 \pm 248$ , whereas it increased from  $363 \pm 37$  to  $2,567 \pm 297$  for  $\text{CeO}_2$ -30 nm agglomerates. After this point in time, however, the number of intracellular particles decreases until reaching approximately the initial levels,  $185 \pm 61$  agglomerates for  $\text{CeO}_2$ -8 nm and  $836 \pm 155$  for  $\text{CeO}_2$ -30 nm particles. The dilution of intracellular NPs is probably caused by cell division, as reported in a recent publication [137]. As cells undergo mitosis, intracellular particles of the mother cells are shared with the daughter ones. Cell division may therefore have direct

influence by decreasing the number of taken up particles with time. Since the doubling time of HMEC-1 cells is 28.6 h [169], and the dilution of intracellular ceria NPs occurs after 24 h, cell division probably plays an important role in our findings.

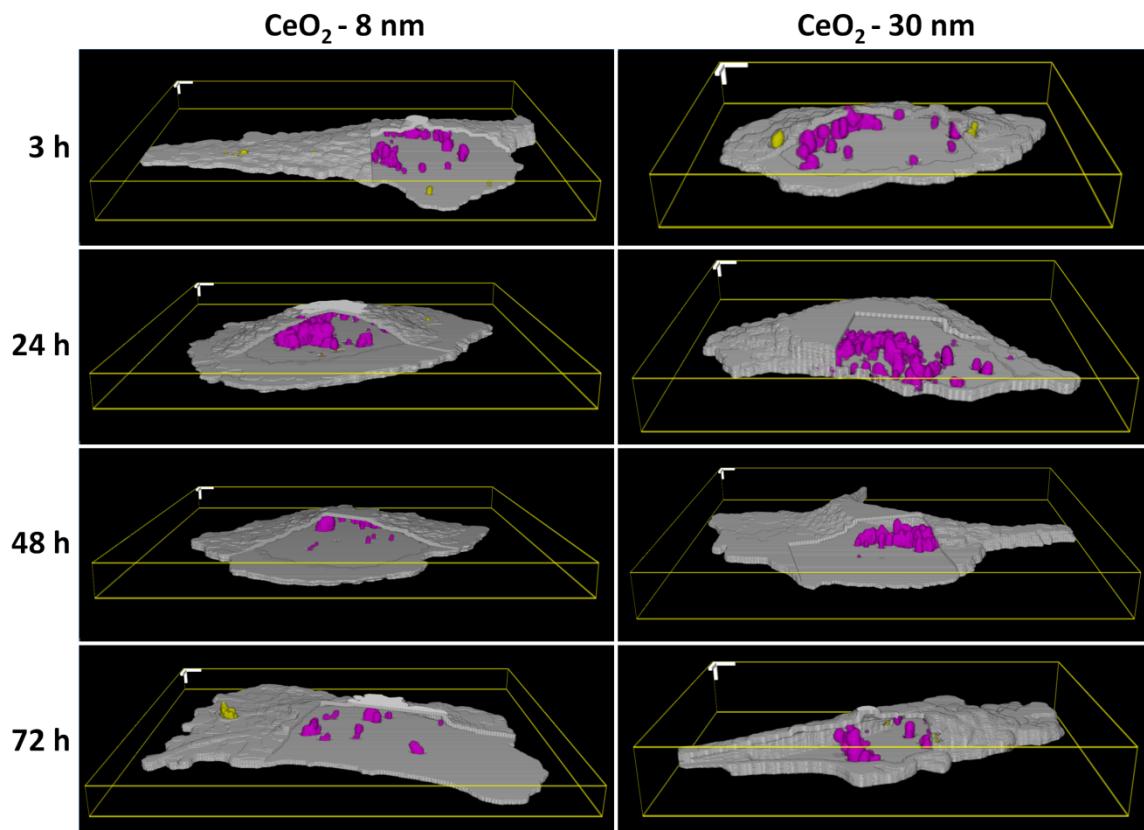


**Figure 7.2 Particle size-dependent uptake kinetics of ceria NPs by HMEC-1 cells.** Representative three-dimensional images of 8 nm and 30 nm ceria NPs interacting with endothelial cells for 3, 24, 48 and 72 h are shown. Due to the strong agglomeration of particles, the individual particles quantified by Particle\_in\_Cell-3D are actually individual agglomerates of 417 nm ( $\text{CeO}_2$ -8 nm) and 316 nm ( $\text{CeO}_2$ -30 nm). The membrane region outlining the cells appears in gray. The intracellular NPs are visualized in magenta and particles interacting with the membrane appear in yellow. The agglomerates are taken up by cells inside endosomes and accumulate in the perinuclear region. The amount of internalized particles is increasing over 24 h, but after this incubation time, however, the number of particles inside the cells starts to decrease. This effect is more remarkable for the 8 nm NPs than for the 30 nm NPs. 3D scale bars = 5  $\mu\text{m}$ .

Cell division is probably among the dominant causes for the observed dilution of NPs. Yet, other time-dependent parameters may also influence the uptake dynamics. For example, exocytosis, as recently reported by Strobel *et al.* [170], or degradation of intracellular particles, cell uptake behavior (e.g., cell-cycle phase dependency, and load capacity), and the number of NPs available for uptake.

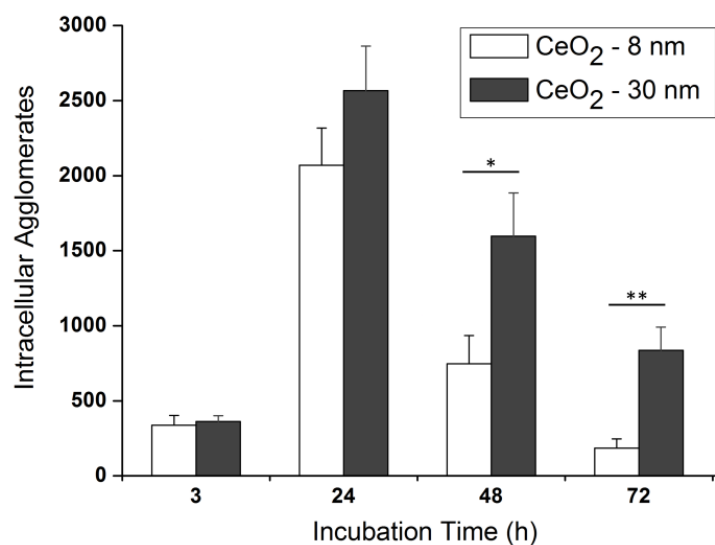


**Figure 7.3 Uptake kinetics of 8 nm (white) and 30 nm (dark gray) ceria NPs in HMEC-1 cells.** The number of internalized NPs after 3 h is practically the same for both particle sizes. These numbers then escalate to reach a maximum at around 24 h. After 48 and 72 h, however, the number of particles incorporated by the cells is reduced back to amounts similar to that measured after 3 h. The histograms show the mean  $\pm$  standard error of at least two independent experiments ( $n = 12-16$ ). Results were statistically different ( $* p < 0.05$ ) for an incubation time of 48 h and highly statistically different ( $** p < 0.01$ ) for 72 h.

### 7.3 Conclusions

The possibility to quantify NPs at the single-cell level is an important step to better understand the mechanisms of NPs-cell interactions. In this work it was demonstrated that results achieved with Particle\_in\_Cell-3D were decisive to show that there is a significant difference in the uptake kinetics of 8 nm (agglomerate size 417 nm) and 30 nm (agglomerate size 316 nm) NPs. After 48 h, the particles that form smaller agglomerates, i.e., 30 nm NPs, are internalized more efficiently by endothelial cells. In addition, our findings offered a new insight into the remarkable dilution of intracellular NPs, possibly influenced by cell division.



## 8 Cell membrane penetration and mitochondrial targeting by platinum-decorated ceria nanoparticles

*This chapter is based on the manuscript:*

*Adriano A. Torrano, Rudolf Herrmann, Claudia Strobel, Armin Reller, Ingrid Hilger, Achim Wixforth, and Christoph Bräuchle;*

*“Cell membrane penetration and mitochondrial targeting by platinum-decorated ceria nanoparticles.”  
In preparation.*

### 8.1 Introduction

Air pollution is a complex mixture of natural and man-made substances. The six most common air pollutants are particle pollution, ground-level ozone, carbon monoxide, sulfur dioxide, nitrogen oxides, and lead [171]. Particle pollution, specifically, is made up of extremely small liquid droplets and solid particles from a variety of components, including acids, organic compounds, soot (carbon particles generated during the incomplete combustion of hydrocarbons), dust and metals. With regard to the size distribution in the ambient atmospheric environment, particles <300 nm represent more than 99 % of the total number concentration [172]. Exposure to particle pollution has been associated with a number of respiratory, cardiovascular and neurologic diseases [41, 86, 173, 174]. Notably, particle pollution has recently been classified as carcinogenic to humans [175], and outdoor air pollution has been pointed as a leading cause of cancer deaths [176]. Alarming concentrations of these particles are found in the air of urban areas, where they are therefore inhaled on a regular basis. On a recent release, the World Health Association reported that in 2012 around 7 million people died as result of exposure to air pollution [177]. Globally, the main source of nano-sized particles in urban air is motor traffic [41, 178].

In order to mitigate the emission of particles and other dangerous substances from the engine, modern vehicles are equipped with catalytic converters. Automobile catalytic converters are able to transform more than 90 % of total unburned hydrocarbons, carbon monoxide, and nitrogen oxides into rather harmless compounds, such as carbon dioxide, nitrogen and water [179, 180]. On the whole, they consist of a porous carrier material (e.g., CeO<sub>2</sub>, or ceria) that is decorated with active noble metals (normally platinum, but also palladium and rhodium). Although playing a fundamental role in reducing the emission of pollutants from vehicles, catalytic converters decompose with time and generate new particle emissions in the nano- and micrometer ranges.

Catalyst-derived particles consisting of carrier material and decorated with noble metals are thus formed and released into the environment [179-186]. As a result of the escalating traffic worldwide, the concentration of noble metals (free or bound to the carrier material) has been increasing in urban areas. Wichmann *et al.* [180] reported that the concentration of catalyst-derived platinum in the air of Braunschweig City (Germany) jumped from 6.0  $\text{pg m}^{-3}$  in 1999 to 159  $\text{pg m}^{-3}$  in 2005. Nanoparticles (NPs) generated by catalytic converters are therefore a growing burden added to particle pollution.

Since very little is known about the health impact of catalyst-derived NPs, our goal in this project is to investigate the biological effect of these NPs at the cellular level. To study the interaction of catalyst-derived NPs with biological systems directly is hardly possible due to the low concentrations in samples like road dust. For this purpose, reasonable quantities of model compounds that resemble the actual catalyst-derived NPs were synthesized. Our mimetic compounds consist of a ceria NP core (defined sizes between 8 and 285 nm) decorated with ultrasmall platinum NPs (2–5 nm). The interaction between platinum-decorated ceria nanoparticles (Pt-ceria NPs) and human microvascular endothelial cells (HMEC-1) was studied in detail by live-cell imaging. Surprisingly, Pt-ceria NPs of specific characteristics were rapidly found inside living cells and selectively accumulated in mitochondria. These exciting findings focused our investigations on the biological effects related to the unusual fast NP uptake mechanism as well as the mitochondrial-targeting properties of the model compounds.

Mitochondria are the cell's powerhouse, producing energy (ATP) through oxidative phosphorylation [187]. Hence, they are indispensable for the survival of eukaryotic cells. Additionally, mitochondria play a central role as regulators of apoptosis [188]. In the case of cancer cells, the activation of the cell death machinery by the delivery of specific mitochondria-targeted compounds represents a promising therapeutic approach [189]. The safe drug delivery to mitochondria, however, is a challenging task. In most cases, clinical trials show that the toxicity associated with high doses of the therapeutics aimed to treat mitochondrial disorders is a limiting factor [190]. Delivery of payloads by NPs that are able to rapidly enter cells and accumulate in mitochondria has a great potential to advance the treatment of such disorders.

The interaction of Pt-ceria NPs with cells is therefore highly interesting for the two complementary fields of nanotoxicology and nanomedicine, and was investigated by us accordingly. Pt-ceria NPs were synthesized by Dr. Rudolf Herrmann (Group of Prof. Dr. A. Reller and Group of Prof. Dr. A. Wixforth; University of Augsburg). Dr. Herrmann was also responsible for characterizing the particles as regards transmission electron microscopy (TEM) and energy-

dispersive X-ray (EDX) spectroscopy. The metabolic impact of Pt-ceria NPs on cells was evaluated by Claudia Strobel (Group of Prof. Dr. I. Hilger; University of Jena).

## 8.2 Results & Discussion

### 8.2.1 Characterization of platinum-decorated ceria nanoparticles

A reproducible method for the synthesis of Pt-decorated ceria NPs that resemble those emitted from catalytic converters was developed and published in the literature by Herrmann *et al.* [133]. Basically, the model compounds are made up of a ceria NP core of defined size (between 8 and 285 nm) decorated with ultrasmall platinum NPs (2–5 nm). Particles are labeled with covalently-bound fluorophores (Atto 647N or perylenediimide) to allow the detection by fluorescence microscopy techniques. Labeling was performed with modified dyes containing triethoxysilyl groups. These groups react and form covalent bonds with the hydroxyl groups commonly present at the surface of ceria and other oxidic nanoparticles [133].

The size and shape of the model compounds synthesized for our investigations were characterized by transmission electron microscopy (TEM) measurements. Figure 8.1 shows TEM images of 8 nm ceria NPs decorated with platinum and labeled with Atto 647N (Pt-Ceria-8-atto). The primary particle size was determined by image analysis of TEM micrographs. In addition, energy-dispersive X-ray (EDX) spectroscopy (Figure 8.1C) was used to prove the elemental composition of the model particles, with platinum (in blue) deposited on ceria NP cores (cerium in red).

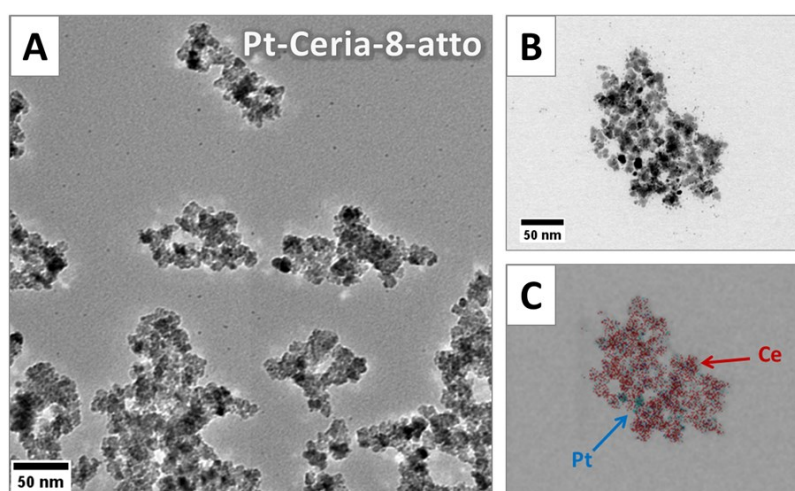


**Figure 8.1** TEM and EDX images of 8 nm ceria NPs decorated with platinum (Pt-Ceria-8-atto). **(A)** Electron micrograph of Pt-Ceria-8-atto NPs. Strong aggregation of model compounds resemble the actual catalyst-derived NPs found in the environment. **(B)** Representative aggregate of Pt-Ceria-8-atto NPs. **(C)** EDX mapping of the same region in **B**. This technique was used to confirm the deposition of platinum (blue) on ceria NP cores (red).

Airborne NPs, like those released by automobile catalytic converters, tend to form aggregates in the nano- and micrometer ranges. A comparable tendency towards aggregation was observed during the synthesis of our model compounds. Large and irregular aggregates of Pt-Ceria-8-atto NPs of different sizes and shapes can be easily identified in Figure 8.1.

The aggregation of particles was further characterized by dynamic light scattering (DLS) measurements. In DLS measurements, the particle size distribution of a sample can be described by the mean hydrodynamic size followed by the polydispersity index (PDI), a width parameter. PDI values <0.1 are an indication of spherical, reasonably narrow monodisperse particles; PDI values between 0.1 and 0.5 are normally found in samples with relatively broad size distributions; and PDI values >0.5 are typically measured in polydisperse particles with broad size distributions. In the case of PDI >0.5, the mean hydrodynamic size is inaccurate and should not be used. Instead, it is recommended using a distribution analysis to determine the peak position. Thus, any improvement towards the narrowing of the particle size distribution can be followed by comparing the PDI of different samples.

The DLS measurements of Pt-Ceria-8-atto NPs revealed a mean hydrodynamic diameter of 129 nm with a relatively broad size distribution (PDI = 0.121). Analogous model compounds of 8 nm Pt-ceria NPs were prepared and labeled with a perylenediimide-derived dye with a triethoxysilyl anchor group [133] (sample Pt-Ceria-8-pery). The mean hydrodynamic size of Pt-Ceria-8-pery NPs was determined to be 154 nm (PDI = 0.116). These results are summarized in Table 8.1 and discussed in Figure 8.2.

**Table 8.1 Characterization of ceria and Pt-ceria NPs used in this study.**

Particle	Fluorescent dye	Primary particle size [nm] <sup>a)</sup>	Aggregate size [nm] <sup>a)</sup>	Hydrodynamic size [nm] <sup>b) c)</sup>	PDI <sup>c) d)</sup>	Zeta Potential [mV] <sup>c)</sup>
Pt-Ceria-8-atto	Atto 647N	8	n.d. <sup>e)</sup>	129	0.121	35.1
Pt-Ceria-8-pery	Perylenediimide	8	n.d. <sup>e)</sup>	154	0.116	27.1
Ceria-47-atto	Atto 647N	8	47	110	0.096	36.4
Pt-Ceria-46-atto	Atto 647N	8	46	103	0.157	45.9
Pt-Ceria-143-atto	Atto 647N	8	143	167	0.020	35.3
Pt-Ceria-285-atto	Atto 647N	8	285	292	0.060	49.2

a) Particle diameter measured by transmission electron microscopy (TEM); b) Mean hydrodynamic diameter determined by dynamic light scattering (DLS) measurements; c) NP solution in ethanol; d) Polydispersity index (PDI) is a width parameter describing the hydrodynamic particle size distribution. Shortly, PDI <0.1 indicates monodisperse samples with narrow size distributions, PDI between 0.1 and 0.5 characterizes a relatively broad size distribution, and PDI >0.5 point to polydisperse samples with broad size distributions; e) Not determined.

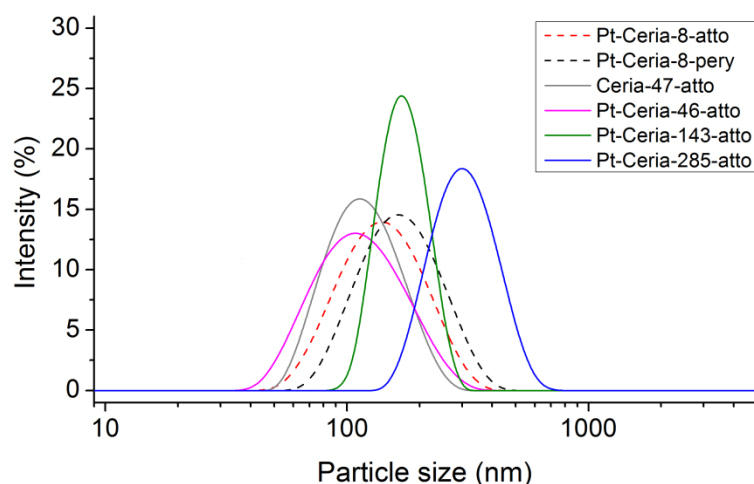


**Figure 8.2 Hydrodynamic particle size distributions of ceria and Pt-ceria NPs measured by dynamic light scattering (DLS).** Three distinct comparisons among the six samples presented in this plot are important. First, the similarity between two equivalent 8 nm Pt-ceria NPs labeled with either Atto 647N (Pt-Ceria-8-atto, red dashed line) or perylenediimide (Pt-Ceria-8-pery, black dashed line). As presented in Table 8.1, both samples are characterized by the same relative broad size distribution. There was no aggregation control during the synthesis of these particles, and the ~25 nm shift towards larger sizes observed for Pt-Ceria-8-pery NPs with respect to Pt-Ceria-8-atto NPs is attributed to differences between batches. Second, the comparison between 47 nm ceria NPs (Ceria-47-atto, gray line) and the counterpart NPs decorated with platinum (Pt-Ceria-46-atto, magenta line). Aggregation control of ceria NPs during the synthesis resulted in a reasonable narrow size distribution of NPs (Figure 8.3). However, the spherical Ceria-47-atto NPs produced by this method clustered to form super-aggregates. Decoration of similar ceria NP cores with platinum to obtain sample Pt-Ceria-46-atto caused further super-aggregation of NPs. Importantly, in both samples the super-aggregates are formed by ~50 nm NPs, and the mean size of these samples are smaller than those measured for NPs without aggregation control (Pt-Ceria-8-atto, Pt-Ceria-8-pery; dashed lines). Third, the size distribution of three distinct samples of Pt-ceria NPs obtained by aggregation control is to be noticed. Particles of 46 nm (Pt-Ceria-46-atto, magenta line), 143 nm (Pt-Ceria-143-atto, green line), and 285 nm (Pt-Ceria-285-atto, blue line) were prepared. In contrast to the super-aggregation observed for 46 nm Pt-ceria NPs, a very narrow size distribution was found for the two other samples composed of 143 and 285 nm particles.

On the one hand, it is desirable to investigate the interaction of model compounds that closely resemble not only the composition but also the aggregation behavior of actual catalyst-derived NPs. On the other hand, it is of paramount interest to find out whether model compounds of different sizes would have distinct biological effects. Ideal samples to investigate particle-size dependent cellular responses should thus have very narrow size distributions. To accomplish this task we developed a strategy to synthesize Pt-ceria NPs samples with reasonable monodisperse size distributions (i.e., PDI <0.1). The method is based on using polyvinylpyrrolidone (PVP), a surface-active reagent, to obtain the aggregation control of 8 nm ceria NPs during the synthesis [133]. This means that NP aggregation is not avoided, but rather controlled. Figure 8.3 shows representative TEM images of stable, uniform and almost spherical aggregates achieved by using this strategy. Ceria NPs of 8 nm are the building blocks to form new NPs of 47 nm (Ceria-47-atto,

Figure 8.3A). Nearly spherical ceria NP aggregates are the ideal starting material for mimetic catalyst-derived NPs of defined core sizes and decorated with platinum. By using this procedure, Pt-decorated ceria NPs of three different core sizes were produced: 46 nm (Pt-Ceria-46-atto), 143 nm (Pt-Ceria-143-atto), and 285 nm (Pt-Ceria-285-atto). TEM images of these particles are shown in Figure 8.3 B–D, respectively.

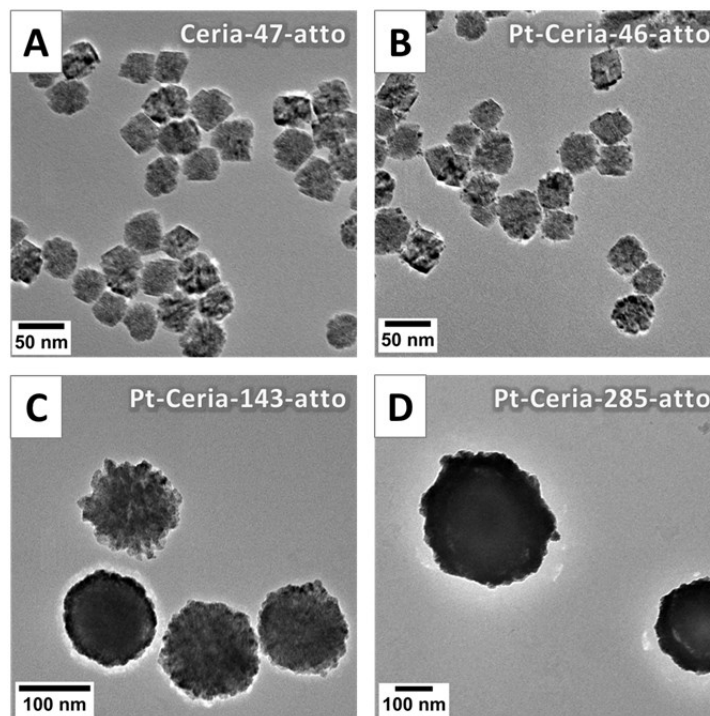


**Figure 8.3 TEM images of ceria and Pt-ceria NPs of different sizes.** Electron micrographs of (A) non-decorated ceria NPs with a mean size of 47 nm, (B) Pt-decorated ceria NPs of 46 nm, (C) 143 nm, and (D) 285 nm.

DLS measurements revealed the hydrodynamic diameter and the PDI values of the new samples. The results presented in Table 8.1 and Figure 8.2 show that reasonable narrow size distributions were achieved. Ceria-47-atto and Pt-Ceria-46-atto, the smaller model compounds, still presented a tendency to increase their sizes by clustering with neighboring aggregates in a process that can be termed as super-aggregation (Figure 8.3A & B). This is directly reflected by the mean hydrodynamic sizes/PDI of these samples: 110 nm/0.096 for Ceria-47-atto NPs and 103 nm/0.157 for Pt-Ceria-46-atto NPs. Even more satisfactory results were obtained with the larger model compounds Pt-Ceria-143-atto and Pt-Ceria-285-atto. Very small PDI values were achieved and the mean hydrodynamic sizes were just slightly larger than those measured by TEM (as expected, due to hydration and solvation effects). The mean hydrodynamic sizes/PDI were determined to be 167 nm/0.020 for Pt-Ceria-143-atto NPs and 292 nm/0.060 for Pt-Ceria-285-atto NPs.

The surface charge, or zeta potential, of all samples was determined based on electrophoretic mobility measurements (Table 8.1 and Figure 8.4). Positive surface charges with comparable magnitudes were measured in all samples, with values ranging from +27.1 mV for Pt-Ceria-8-pery NPs to +49.2 mV for Pt-Ceria-285-atto NPs.

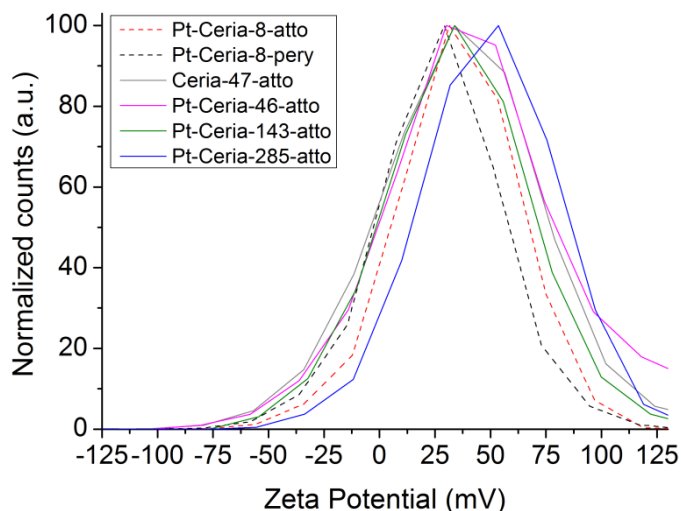


**Figure 8.4 Zeta potential of ceria and Pt-ceria NPs determined by electrophoretic mobility measurements.** The surface charge profiles of all samples were found to be similar. They are characterized by very broad distributions with mean positive values ranging from +27.1 mV (Pt-Ceria-8-pery) to +49.2 mV (Pt-Ceria-285-atto). These results indicate that the zeta potential values were not considerably altered by labeling, platinum decoration, or differences in the particle size. Therefore, all samples used in this study have a comparable surface charge. Determination of the zeta potential was performed with NPs dispersed in ethanol, the solvent in which the NPs are synthesized.

Characterization of NPs, such as zeta potential and hydrodynamic size measurements, intended to probe how the cells “see” the NPs should preferably be performed under the same experimental conditions applied in cell-based assays, that is, with NPs dispersed in a biologically relevant fluid (e.g., cell culture medium). Performing the characterization of NPs in cell medium, however, is usually complicated and occasionally not possible. Both zeta potential and hydrodynamic size measurements may be influenced by common cell medium components, like electrolytes and proteins [191]. In the case of size measurements, small cell medium components of typically ~10 nm can influence the result if the concentration of NPs is low. Conversely, if the concentration of NPs is increased, aggregation may occur and hence the introduction of new inconsistencies. In the present study, the best possible procedure found to characterize the size and the surface charge of Pt-ceria NPs in solution was to measure them in the environment that they are stored and stable, i.e., in ethanol.

Characterization of NPs in cell medium was reasonably circumvented for DLS measurements, but could certainly not be avoided for live-cell imaging experiments, because it would imply the

addition of NPs in ethanol solution for cells. The transfer of ceria and Pt-ceria NPs from ethanol into cell medium, while keeping the NPs with the same size distribution, was a considerable challenge. The traditional method to redisperse NPs (centrifugation followed by washing steps and a final redispersion in water) failed completely. Using this procedure, aggregates in the micrometer range were formed and could not be broken down again to the original particle sizes. After innumerable trials with different conditions and methods, an efficient and yet simple procedure was designed. Shortly, a small aliquot of well-dispersed NPs in ethanol is added to a microreaction tube; ethanol is left to evaporate; dried NPs are then redispersed directly in cell medium. The final NP solution in cell medium, prepared as just described, maintained most of the particles closer to the original sizes. Importantly, NPs smaller than ~100 nm were still present after redispersion, as evidenced by the remarkable and consistent particle-size dependent uptake behavior of Pt-ceria NPs described in Section 8.2.2.4.

As mentioned above, studying the dynamics of aggregation of NPs in cell medium is a demanding task. To precisely describe the size of NPs interacting with cells would need sophisticated approaches such as live-cell super-resolved fluorescence microscopy [101]. Employing these elaborated techniques is out of the scope here and left as a potential future work. In this project, the diameter of the particles determined by TEM is used when referring to different samples. Nevertheless, it should be kept in mind that the mean sizes of the particles, aggregates or super-aggregates interacting with cells are most likely those described by the particle hydrodynamic size distributions presented in Table 8.1 and Figure 8.2.

## **8.2.2 Cellular uptake behavior of platinum-decorated ceria nanoparticles**

### **8.2.2.1 Uptake kinetics and intracellular fate**

The cellular uptake of catalyst-derived model NPs was investigated by live-cell imaging. Basically, endothelial cells (HMEC-1) were incubated with cell culture medium containing 20–100  $\mu\text{g mL}^{-1}$  of ceria or Pt-ceria NPs under controlled conditions and imaged live afterwards.

The very first uptake experiments in which HMEC-1 cells were incubated with Pt-Ceria-8-atto NPs revealed remarkable results: NPs were rapidly internalized by cells and were found selectively accumulated in mitochondria. As depicted in Figure 8.5A, a substantial amount of Pt-Ceria-8-atto NPs is found associated with the mitochondria after just 10 min of incubation time. Determination of Manders' overlap coefficient [104] revealed that as much as 91 % of NPs are overlapping the mitochondria. Time-lapse confocal live-cell studies confirmed the association of NPs with mitochondria. In Figure 8.5B, the typical dynamics of mitochondria inside the cells can



be appreciated. The translational motion and the bending of mitochondria are exactly followed by the associated NPs, resulting in a perfect colocalization in space and time.

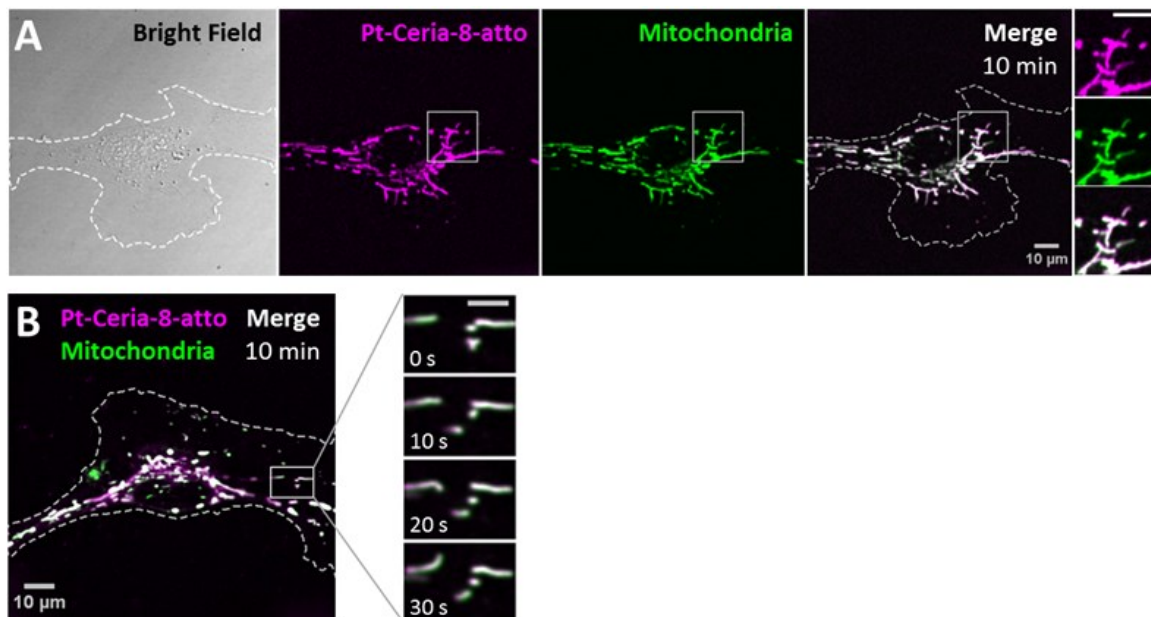


**Figure 8.5 Live-cell imaging studies on the cellular uptake behavior of Pt-Ceria-8-atto NPs during a short interaction time.** (A) Bright-field (left panel) and confocal images of a representative HMEC-1 cell (dashed line) incubated with Pt-Ceria-8-atto NPs ( $100 \mu\text{g mL}^{-1}$ ) for 10 min. After this short period, a considerable number of NPs (middle left panel, magenta) were internalized and accumulated in mitochondria (middle right panel, green: MitoTracker). Note the high degree of colocalization in the merge image (right panel, white). **Inset:** boxed regions of confocal images in detail. Remarkably, the mitochondrial network and the distribution of Pt-Ceria-8-atto NPs are characterized by overlapping filament-like structures. Scale bar =  $10 \mu\text{m}$ . (B) Confocal image of another representative HMEC-1 cell with Pt-Ceria-8-atto NPs (magenta) accumulated in mitochondria (green; colocalizing pixels in white). **Inset:** time-lapse images of the boxed region. Note that the typical mitochondrial dynamics (e.g., translational motion, bending, stretching) is perfectly followed by associated NPs. Scale bar =  $5 \mu\text{m}$ . Altogether, these results point to a very fast cellular uptake mechanism of Pt-Ceria-8-atto NPs, followed by a selective NP accumulation in mitochondria.

Interestingly, traditional endocytosis does not seem to be the uptake pathway taken by Pt-Ceria-8-atto NPs after short incubation times. In the live-cell imaging study illustrated in Figure 8.6A, the cell plasma membrane was stained just before the addition of NPs, and thus every new endosomes formed from the cell surface (and possibly enclosing a NP) was fluorescently marked. Our results consistently showed no endosomal localization of Pt-Ceria-8-atto NPs (here, only 1 % of the NPs signal is overlapping the endosomes). The particles were instead distributed along with the filament-like structures of the mitochondrial network, as elucidated in Figure 8.5. After relatively long incubation times, however, the results were different. The peculiar uptake behavior of Pt-Ceria-8-atto NPs after 18 h of incubation time with HMEC-1 cells is depicted in Figure 8.6B. Pt-ceria NPs do not only accumulate in mitochondria but also in lysosomes, the

terminal vesicles that receive the cargo from endosomes [66]. On the whole, a mixed uptake pathway was observed. Our findings points to the presence of two populations of particles in the sample: one population that escapes the endocytic pathway, is rapidly internalized, and accumulates in mitochondria; and another population that follows traditional endocytosis, is less efficiently internalized, and is delivered to the lysosomes. Further research has demonstrated that particle size is a crucial factor determining the uptake mechanism of Pt-ceria NPs (see Section 8.2.2.4).

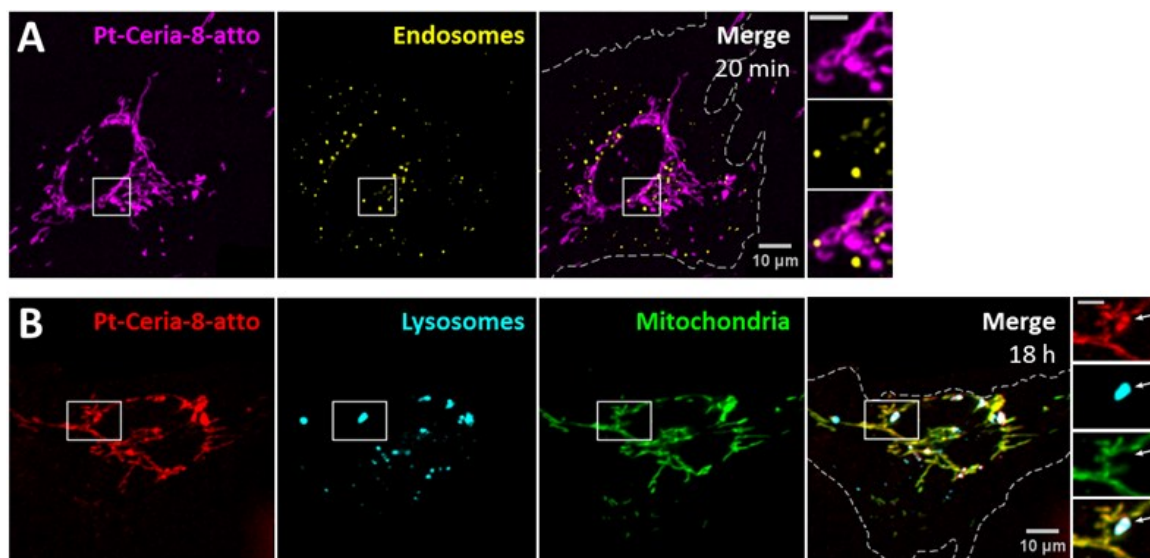


**Figure 8.6 Intracellular fate of Pt-Ceria-8-atto NPs after short and long interaction times. (A)** Live-cell confocal images of a HMEC-1 cell (dashed line) incubated with Pt-Ceria-8-atto NPs (left panel, magenta) for 20 min. Endosomes formed from the cell surface during the interaction with NPs were fluorescently labeled (middle panel, yellow: WGA 488). Large amounts of Pt-ceria NPs were promptly internalized, and colocalization between NPs and endosomes would mean an endocytic entry route. However, this does not seem to be the case for short incubation times, as illustrated in the merge image (right panel). **Inset:** boxed regions in detail. Endosomes form a punctuate pattern, while Pt-Ceria-8-atto NPs are distributed in the characteristic filament-like structures of the mitochondrial network. Note the lack of endosomal localization of NPs. Scale bar = 5  $\mu\text{m}$ . **(B)** Parallel experiments in which HMEC-1 cells (dashed line) were incubated with Pt-Ceria-8-atto NPs (left panel, red) for 18 h. Cellular lysosomes (middle left panel, cyan: LysoTracker) and mitochondria (middle right panel, green: MitoTracker) were stained before imaging. Interestingly, some Pt-Ceria-8-atto NPs were accumulated in lysosomes (right panel, colocalizing pixels in white), while others in mitochondria (right panel, colocalizing pixels in yellow). **Inset:** boxed regions in detail. The filament-like structures of NPs associated with mitochondria can be distinguished from the punctuate pattern of those NPs with lysosomal localization (arrow). Scale bar = 5  $\mu\text{m}$ .

### 8.2.2.2 Mitochondrial targeting

As emphasized in the previous section, not only the fast NP uptake was remarkable, but also the efficient and selective mitochondrial targeting by Pt-Ceria-8-atto NPs. Targeting mitochondria with lipophilic cations, such as triphenylphosphonium, has been shown to be a successful strategy [189, 192]. Due to the large mitochondrial membrane potential, lipophilic cationic

moieties are attracted by and accumulate within mitochondria. Interestingly, Atto 647N is also a lipophilic cationic dye with affinity to mitochondria [193].

In order to investigate if the mitochondrial-targeting property observed for Pt-Ceria-8-atto NPs is an intrinsic ability of Pt-ceria NPs, regardless the attached fluorophores, we prepared 8 nm Pt-ceria NPs labeled with perylenediimide (Pt-Ceria-8-pery), a neutral and chemically quite inert fluorescent dye [133]. Missing the mitochondrial-targeting moieties, perylenediimide-labeled NPs would still be able to perform a rapid cell-membrane penetration, but would not accumulate selectively in mitochondria. Our hypothesis was confirmed by live-cell confocal studies. HMEC-1 cells were incubated with cell culture medium containing  $50 \mu\text{g mL}^{-1}$  of either Pt-Ceria-8-atto or Pt-Ceria-8-pery NPs for 2 h. Cell exposed to  $50 \mu\text{g mL}^{-1}$  of Pt-Ceria-8-pery NPs presented a blurry cytosolic distribution of NPs. In order to enhance the effect and optimize the visualization, the concentration of Pt-Ceria-8-pery NPs was increased to  $500 \mu\text{g mL}^{-1}$ . As depicted in Figure 8.7, both Pt-Ceria-8-atto and Pt-Ceria-8-pery NPs were internalized by cells, but while Atto 647N particles are mostly accumulated in mitochondria, perylenediimide-labeled particles are clearly distributed throughout the cytosol. The fraction of Pt-Ceria-8-atto NPs overlapping mitochondria for the upper cell in Figure 8.7A is 86 %. In contrast, the fraction of Pt-Ceria-8-pery NPs overlapping mitochondria for the cell on the left in Figure 8.7B is 46 %. Nevertheless, since perylenediimide-labeled NPs are covering the entire cytosolic region, 46 % may be an overestimation caused by the diffraction-limited signal of NPs that are not physically associated with mitochondria, but rather diffusely surrounding them. Atto 647N dye has therefore two functions in our model NPs: labeling and mitochondrial targeting.

This comparison study indicates that only under the assistance of a mitochondrial-targeting moiety (here, Atto 647N) the selective mitochondrial localization of cytosolic NPs is promoted. Further experiments with cryo-TEM imaging, a technique that allows for an even better spatial resolution, are under evaluation. These results are expected to elucidate the degree of accumulation and the precise location of NPs within the mitochondrial structure.

Since fluorescence microscopy relies on the use of fluorophores to label the objects of interest, eventual dye leakage or dye transfer to other objects may lead to misleading interpretations. It is therefore worth emphasizing why the findings presented in this work cannot be attributed to dye leakage from NPs. First of all, perylenediimide and Atto 647N are covalently bonded to the particle surface [133]. Second, we simulated the leakage of Atto 647N dye from NPs in the cell medium under comparable live-cell imaging conditions. The outcomes were that free Atto 647N molecules are not able to efficiently cross the plasma membrane of cells, and no accumulation of Atto 647N dye in mitochondria was observed (data not shown). Finally, equivalent NPs lacking

the decoration with platinum or larger than  $\sim 150$  nm do not display any mitochondrial localization, although labeled with Atto 647N (see Sections 8.2.2.3 & 8.2.2.4).

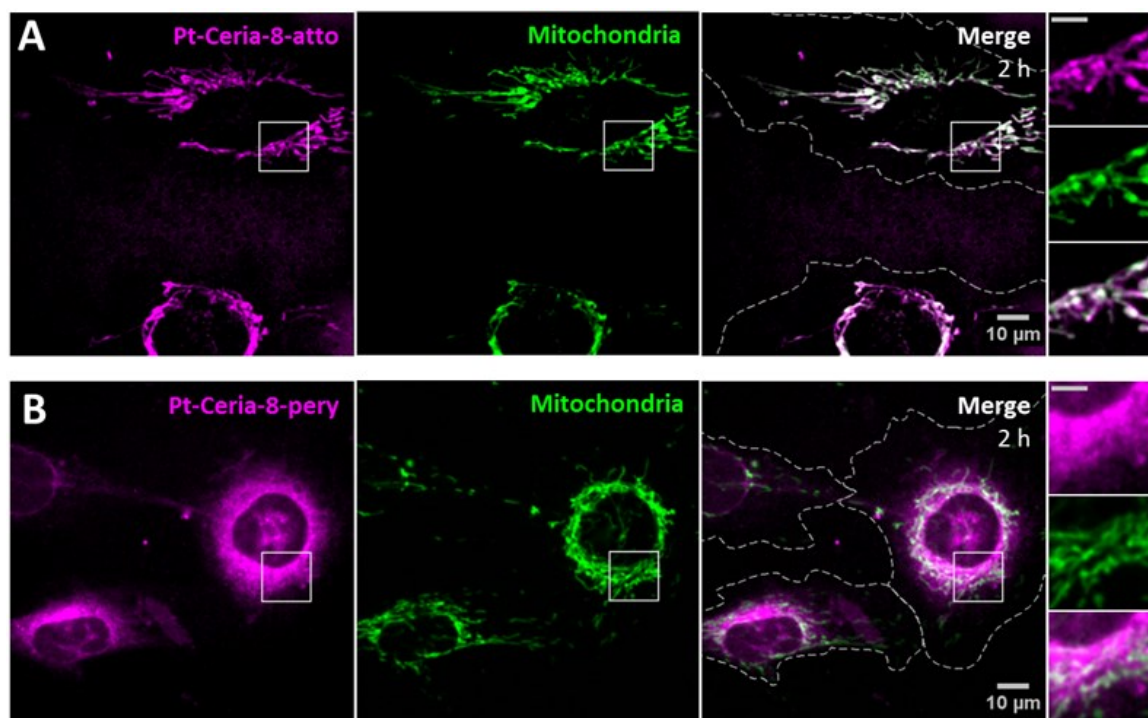


**Figure 8.7 Intracellular fate of 8 nm Pt-ceria NPs labeled with either Atto 647N or perylene diimide dyes.** **(A)** HMEC-1 cells (dashed lines) were incubated with Atto 647N-labeled NPs (Pt-Ceria-8-atto) for 2 h. The expected selective accumulation of NPs (left panel, magenta) in mitochondria (middle panel, green: MitoTracker) is evidenced in the merge image (right panel, white). **Inset:** boxed regions in detail. Note the typical filament-like structures of colocalizing mitochondria and NPs. Scale bar = 5  $\mu\text{m}$ . **(B)** Parallel experiments in which HMEC-1 cells (dashed line) were incubated with perylene diimide-labeled NPs (Pt-Ceria-8-pery). A considerable amount of Pt-Ceria-8-pery NPs (left panel, magenta) can be seen inside the cells. However, in contrast to the selective mitochondrial localization of Atto 647N-labeled NPs, perylene diimide-labeled NPs are mostly diffusely distributed in the cytoplasm region. **Inset:** boxed regions in detail. Note the massive presence of NPs in the cytosol and the absence of a selective accumulation in mitochondria. Scale bar = 5  $\mu\text{m}$ .

### 8.2.2.3 Influence of platinum decoration

Previously, we studied the cellular uptake behavior and cytotoxicity of 8 and 30 nm ceria NPs without platinum decoration (see Chapter 7). Among other interesting results, we described the massive aggregation of ceria NPs. In the present work we found a similar uncontrolled aggregation of 8 nm Pt-ceria NPs. Obviously, an effective investigation on the influence of only platinum decoration requires NPs of similar properties, except for the presence of platinum. For this reason, the samples Ceria-47-atto and Pt-Ceria-46-atto, synthesized under aggregation control conditions and holding similar properties (Table 8.1), were used in this study.

HMEC-1 cells were incubated with cell media containing  $20 \mu\text{g mL}^{-1}$  of either Ceria-47-atto or Pt-Ceria-46-atto NPs, washed and imaged afterwards. The results presented in Figure 8.8 show the

effect of ultrasmall platinum NPs (2–5 nm) on the surface of ceria NPs. While Pt-Ceria-46-atto NPs are mostly found distributed as filament-like structures that coincide with the mitochondrial network (Figure 8.8A), internalized Ceria-47-atto NPs appear as punctate fluorescence patterns that characterizes the endocytosis uptake route (Figure 8.8B). The same peculiar uptake behavior of Pt-Ceria-8-atto NPs after long incubation times (Figure 8.6B) was observed for Pt-Ceria-46-atto NPs. Importantly, after very short incubation periods such as 20 min, Pt-Ceria-46-atto NPs were already detected in mitochondria, but Ceria-47-atto NPs were not even detected inside the cell (data not shown). It was necessary to perform longer incubation time experiments, such as 8 h, to detect a reasonable amount of intracellular Ceria-47-atto NPs. In the present case, 83 % of mitochondria are overlapped by Pt-Ceria-46-atto NPs Figure 8.8A. In contrast, only 4 % of mitochondria are overlapped by Ceria-47-atto NPs (Figure 8.8B). In fact, a similar result (3 %) was measured for the signal of lysosomes overlapping mitochondria in Figure 8.6B. Such small values for the degree of colocalization (Manders' overlapping coefficient) can therefore be attributed to the proximity between vesicles and mitochondria in the cytoplasm.

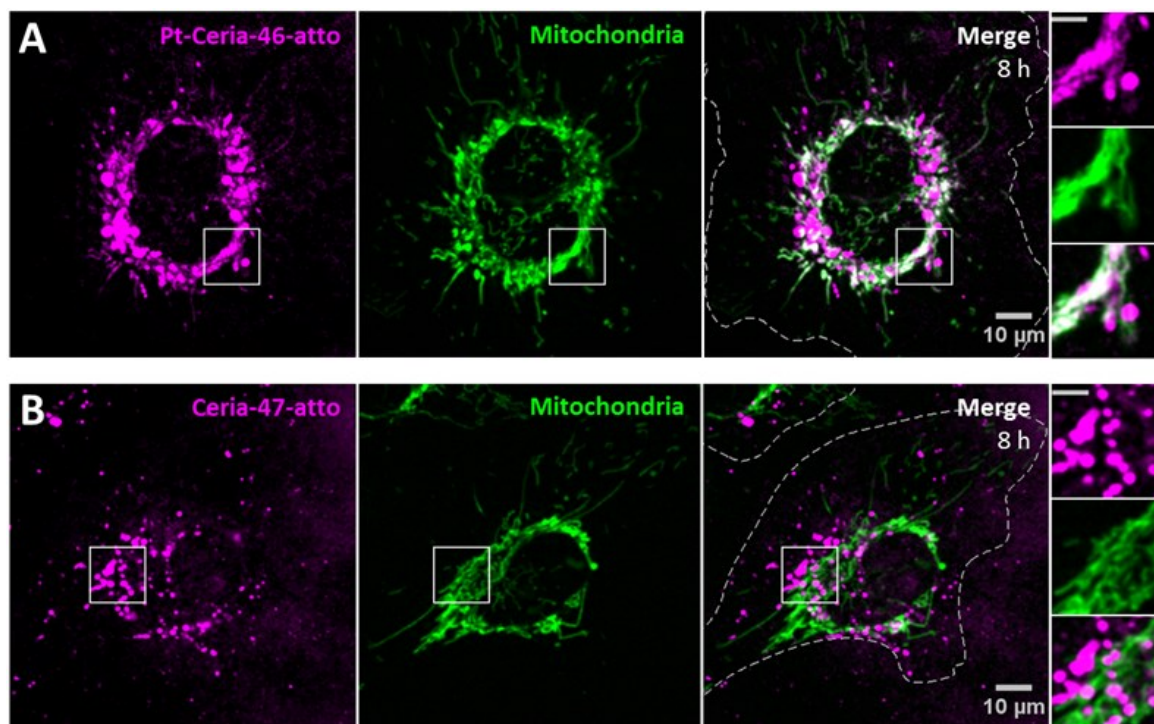


**Figure 8.8 Influence of platinum decoration on the cellular uptake behavior of ceria NPs. (A)** Live-cell confocal images of a representative HMEC-1 cell (dashed line) incubated with Pt-Ceria-46-atto NPs (left panel, magenta) for 8 h. Cellular mitochondria (middle panel, green: MitoTracker) was stained prior to imaging. Note that NPs displaying a filament-like structure colocalize with mitochondria (right panel, white pixels), while punctate NPs do not. **(B)** Parallel experiments in which HMEC-1 cells (dashed lines) were incubated with Ceria-47-atto NPs (left panel, magenta). Remarkably, only the punctate pattern of NPs, characteristic of endocytic pathway and vesicle localization, can be observed. Moreover, no evidence of colocalization between mitochondria (middle panel, green: MitoTracker) and NPs was detected in the merge image (right panel). **Inset:** boxed regions in detail. Scale bars = 5 μm.

Hence, platinum decoration has an enormous influence on the cellular uptake behavior of our model compounds for catalyst-derived NPs. The presence of ultrasmall platinum NPs on the surface of ceria NPs is a necessary condition for the unusual uptake mechanism under investigation.

#### 8.2.2.4 Influence of particle size

The influence of the particle core size on the uptake behavior of catalyst-derived model NPs was investigated by comparison studies with samples synthesized under aggregation control conditions (see Section 8.2.1). Pt-ceria NPs of three distinct sizes were prepared: 46 nm (Pt-Ceria-46-atto), 143 nm (Pt-Ceria-143-atto), and 285 nm (Pt-Ceria-285-atto). Except for the determined differences in the particle sizes, no other remarkable difference in the physicochemical properties of the samples has been noticed (Table 8.1).

Cellular uptake experiments parallel to those presented in Section 8.2.2.3 were prepared. The peculiar uptake behavior of the 46 nm Pt-ceria NPs was depicted in Figure 8.8A. Crucially, the same trend in the uptake mechanism was not observed for larger Pt-ceria NPs. The results in Figure 8.9 show that, although decorated with platinum and labeled with Atto 647N, both Pt-Ceria-143-atto and Pt-Ceria-285-atto NPs fail to accumulate in mitochondria. Moreover, after short incubation times, such as 20 min, no evidence of NP internalization was found (data not shown). Intracellular NPs were only detected after longer incubation times. After 8 h, a punctuate pattern of internalized Pt-Ceria-143-atto NPs and Pt-Ceria-285-atto NPs can be visualized (Figure 8.9A & B). As described previously, such a NP pattern distribution is characteristic of particle endocytosis. The fraction of mitochondria overlapped by Pt-Ceria-143-atto and Pt-Ceria-285-atto NPs was negligible (2 % and 6 %, respectively), and it can be attributed to the signal overlapping of NPs inside endocytic vesicles and neighboring mitochondria.

Altogether, the unusual uptake behavior observed for 46 nm Pt-ceria NPs (hydrodynamic size 103 nm) after short or long incubation times was not observed for 143 and 285 nm Pt-ceria NPs (hydrodynamic sizes 167 and 292 nm, respectively). These results point to a remarkable particle size effect: Pt-ceria NPs smaller than ~50–100 nm escape the usual endocytic pathway and are transported directly to the cytosol by a fast uptake process; Pt-ceria NPs larger than ~150 nm, in contrast, are taken up via the conventional endocytosis route.

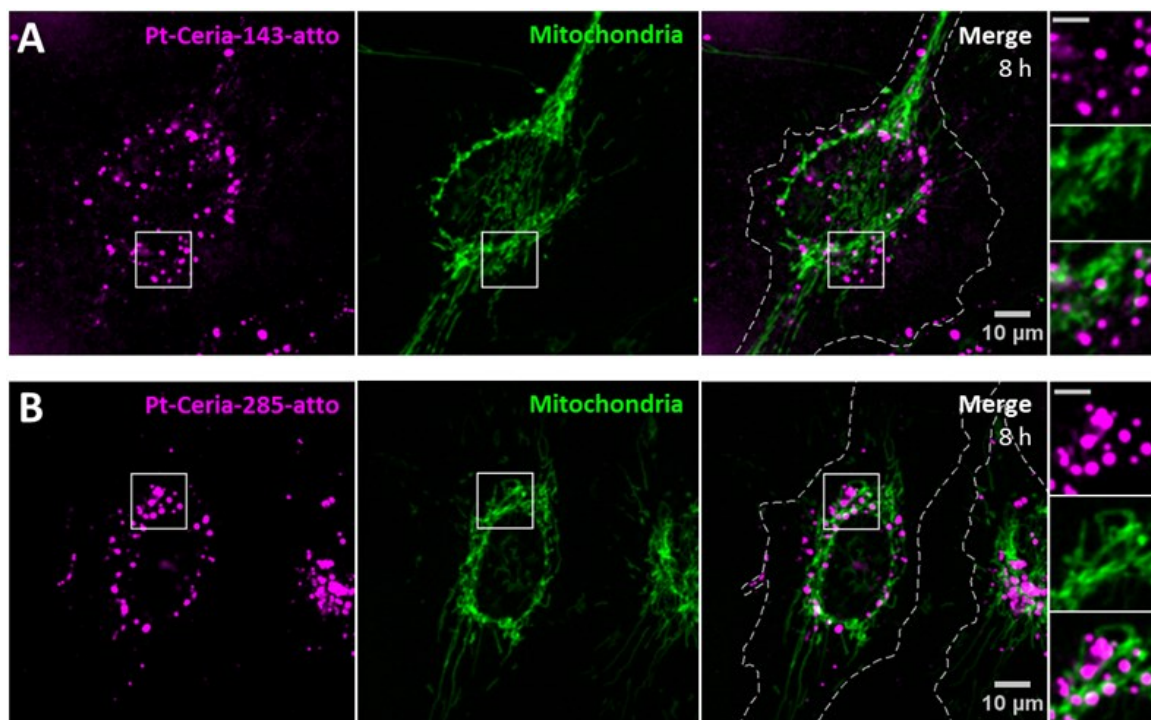


**Figure 8.9 Influence of particle size on the cellular uptake behavior of Pt-ceria NPs.** Live-cell confocal images of a HMEC-1 cells (dashed lines) incubated with either **(A)** Pt-Ceria-143-atto NPs or **(B)** Pt-Ceria-285-atto NPs for 8 h. Similar results were achieved with both samples, and a punctuate pattern typical of particle endocytosis can be observed (left panels, magenta). In addition, the absence of NP accumulation in mitochondria (middle panels, green: MitoTracker) can be noticed in the merge images (right panels). **Insets:** boxed regions in detail. Note the punctuate pattern of NPs distributed in the vicinity, but not at the mitochondria. Scale bars = 5  $\mu\text{m}$ .

### 8.2.2.5 Inhibitor studies

After examining the influence of platinum decoration and particle size in the uptake behavior of Pt-ceria NPs, we investigated whether clathrin-mediated endocytosis was involved in the fast uptake mechanism observed. (The influence of the caveolin-mediated uptake process is also planned to be tested.) Several pathways have been discussed for the cellular uptake via endocytosis (see Section 2.5). Generally, the functionality of distinct pathways is verified by live-cell imaging studies using specific dye-labeled substrates along with endocytic inhibitors [7, 194, 195]. Transferrin glycoproteins, for example, are specifically and rapidly internalized by the clathrin-mediated pathway. Such a fast uptake, followed by a sudden endosomal escape, would be a possible mechanism to deliver NPs directly in the cytosol.

To visualize the uptake, the cellular membrane was stained prior to confocal imaging. As can be seen in Figure 8.10A, transferrin is clearly detectable within the outlines of HMEC-1 cells. Transferrin is present in the cell culture medium as well, leading to a staining of the extracellular space. Figure 8.10B shows a parallel experiment in which the clathrin-mediated pathway of cells was completely inhibited with 15  $\mu\text{g mL}^{-1}$  chlorpromazine (CP) during 30 min and, after that, co-

incubated transferrin was no longer internalized. Finally, HMEC-1 cells with the clathrin-mediated pathway completely blocked by CP were co-incubated with Pt-Ceria-46-atto NPs ( $100 \mu\text{g mL}^{-1}$ ). The panels of Figure 8.10C demonstrate that a considerably amount of NPs was already detected inside the cell after a short incubation time of 20 min. Once inside the cells, Pt-ceria NPs accumulated in mitochondria. The colocalization between NPs and mitochondria is evident. These results indicate that the clathrin-mediated endocytosis is not involved in this uptake process.

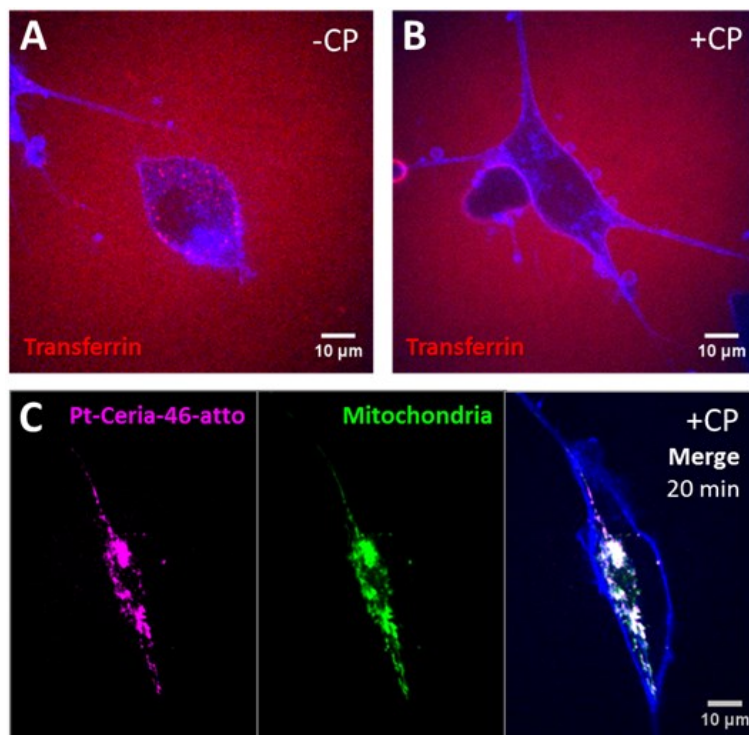


**Figure 8.10** Live-cell confocal study on the role of clathrin-mediated endocytosis during the uptake of small Pt-Ceria NPs by HMEC-1 cells. **(A)** Transferrin (red) is taken up into the cellular outlines (blue: CellMask) in the absence of chlorpromazine (CP-). **(B)** The clathrin-mediated pathway is inhibited by chlorpromazine (CP+), and transferrin (red) is no longer internalized by cells. **(C)** Inhibition with (CP+) under the same experimental conditions of **B**, however, does not hinder the entry of Pt-Ceria-46-atto NPs (left panel, magenta) into cells. After 20 min, a large number of NPs is already accumulated in mitochondria (middle panel, green: MitoTracker). Note the clear colocalization between NPs and mitochondria in the merge image (right panel, colocalization pixels in white; blue: CellMask).

#### 8.2.2.6 Protein corona

As described in Section 2.3, NPs are normally covered by a protein corona as they interact with proteins present in biological media. The protein corona can largely define the biological identity of a given NP, and can therefore influence the effect of this NP on a cellular level. The results described so far were all obtained with cell media supplemented with 10 % fetal bovine serum (FBS). With the purpose of verifying if the presence of serum proteins in cell culture medium plays a decisive role in the interaction between Pt-ceria NPs and cells, we incubated HMEC-1 cells



with Pt-ceria-46-atto NPs ( $100 \mu\text{g mL}^{-1}$ ) in a cell medium formulation deprived of FBS. Interestingly, the outcomes were not distinct from those measured in the presence of serum protein, and NPs were found inside the cells and accumulated in mitochondria (Figure 8.11). Thus, the presence of serum proteins (in solution or forming a protein corona adsorbed to the NP surface) does not influence the unusual uptake behavior observed for small Pt-Ceria NPs. These results indicate an uptake mechanism driven by the physicochemical properties of the bare surface of NPs, and they point to a partial or a complete lack of the protein corona [51]. In addition, these results are in line with the cell membrane-penetration by ultrasmall gold NPs in both serum-free and serum-containing cell medium [69].

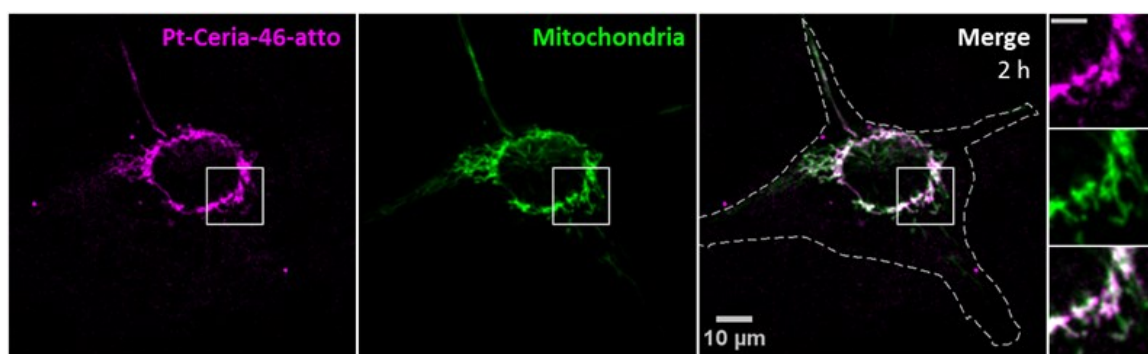


**Figure 8.11 Influence of the protein corona on the cellular uptake behavior of small Pt-Ceria NPs.** The protein corona is believed to have a strong influence in the interactions between NPs and cells. In all uptake experiments of this work, except this one, cells were incubated in serum-containing cell medium. Here, however, HMEC-1 cells were incubated with Pt-Ceria-46-atto NPs for 2 h in serum-free medium. Under this special experimental condition, NPs are not covered by adsorbed proteins. Interestingly, the absence of serum proteins did not alter the uptake route. Pt-Ceria-46-atto NPs (left panel, magenta) were rapidly internalized by HMEC-1 cells (dashed line) and accumulated in mitochondria (middle panel, green: MitoTracker). Colocalization between NPs and mitochondria can be clearly visualized in the merge image (right panel, white). **Inset:** boxed regions in detail. The typical filament-like structures of mitochondria and associated Pt-Ceria-46-atto NPs are evident. Scale bar =  $5 \mu\text{m}$ .

### 8.2.2.7 Cell membrane integrity

So far, all results point toward a cell membrane penetration by small Pt-ceria NPs. Cell membrane penetration by NPs can cause the disruption of the plasma membrane and induce cytotoxic effects [196]. In addition, the leakage of ions or molecules into or out of the cell through permanent holes on the membrane can lead to cell death [69]. To verify whether Pt-ceria NPs cause permanent holes or any other damage to the plasma membrane integrity, we performed calcein leakage in and out assays.

First, we tested if the direct translocation of Pt-ceria NPs through the membrane was accompanied by the leakage in (or penetration) of co-incubated calcein. The fluorescent dye calcein cannot penetrate an intact cell membrane directly, but is normally internalized by

endocytosis and remains enclosed by intracellular vesicles. However, if the membrane is disrupted, calcein can penetrate the cell and a diffuse pattern is observed throughout the cytosol. Scoring the percentage of cells without cytosolic calcein distribution is a convenient and conventional way to access the viability of cells after exposure to external agents. Cell membrane damage by external agents is typically characterized by the majority of cells exhibiting cytosolic calcein. For example, cationic gold nanoparticles (coated with 11-mercaptoundecane-tetramethylammonium chloride) which are able to disrupt cell membranes, led to cytosolic calcein distribution in ~50 % of the dendritic cells, while in the control samples not treat with gold NPs, 95 % of the cells were found without calcein cytosolic distribution [69].

HMEC-1 cells were co-incubated with cell medium containing  $0.1 \text{ mg mL}^{-1}$  calcein and  $100 \text{ } \mu\text{g mL}^{-1}$  Pt-Ceria-46-atto NPs for 3 h. After this time, cells were washed and imaged live. Representative cells of untreated controls and co-incubation experiments with Pt-Ceria-46-atto NPs are given in Figure 8.12A & B, respectively. The percentage of cells without calcein distribution was above 97 % in both cases, as shown in Figure 8.12C. Besides, no significant difference in the viability of untreated and NP treated cells was found.

Next, we performed complementary studies on the particle-induced leakage out (or release) of previously internalized cytosolic calcein. The cell-permeant and nonfluorescent calcein-AM dye can access the cytosolic compartment of living cells and, once there, it is converted to the fluorescent calcein by intracellular esterases and stays trapped in the cytosol. In our experiments, HMEC-1 cells were preincubated with  $5 \text{ } \mu\text{M}$  calcein-AM for 45 min. Calcein-loaded cells were washed with cell medium and incubated with  $100 \text{ } \mu\text{g mL}^{-1}$  Pt-Ceria-46-atto NPs for 0.5 and 3 h. After the respective incubation periods, cells were washed again and imaged live. The mean fluorescence intensity of cytosolic calcein was measured in untreated cells and in cells treated with Pt-ceria NPs (Figure 8.13A & B, respectively). The data presented in Figure 8.13C show that no leakage out of pre-loaded cytosolic calcein was induced by the uptake of NPs. Moreover, no significant difference between untreated and NP treated cells was detected. These results are in line with the previous findings on the leakage in of calcein (Figure 8.12). Altogether, calcein leakage in and out assays offer supporting evidence that small Pt-ceria NPs can access the cytosol without causing noticeable membrane disruption.

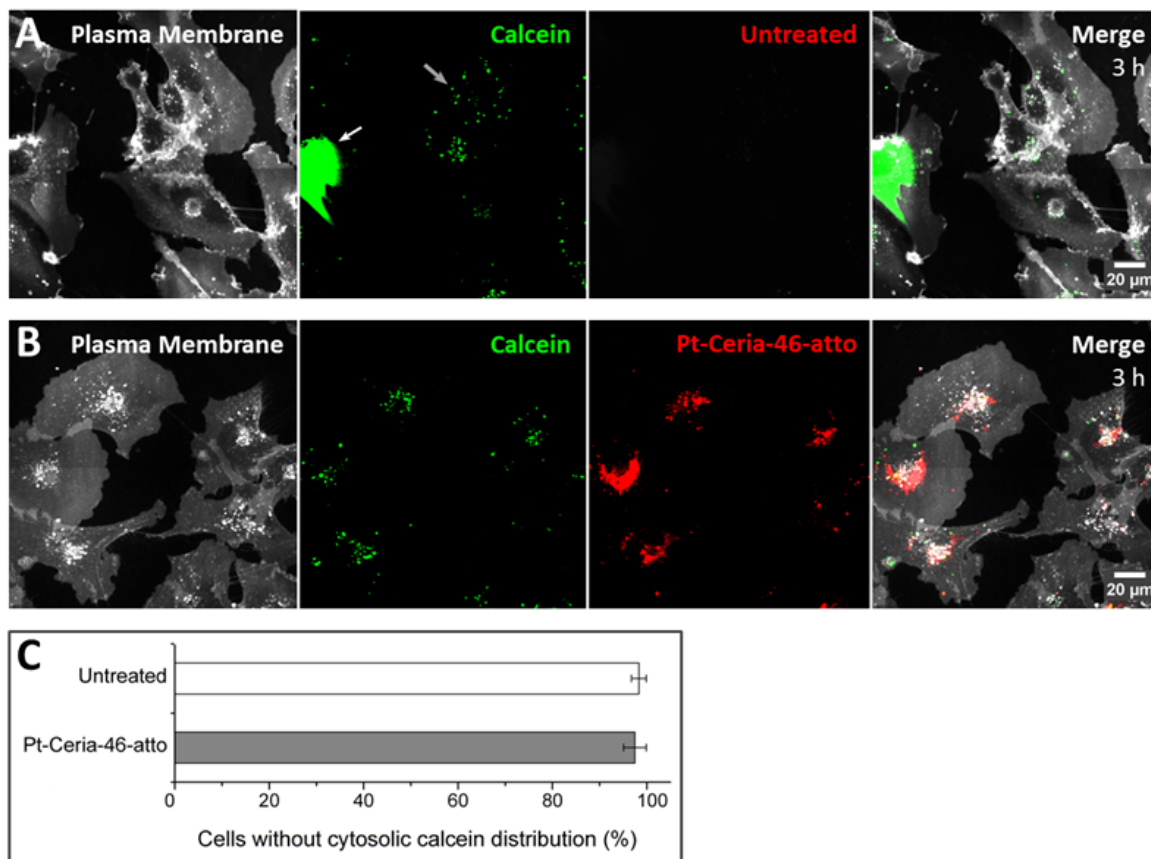


**Figure 8.12 Impact of small Pt-Ceria NPs on the membrane integrity: calcein leakage in assay.** Z-projection of live-cell confocal images depicting HMEC-1 cells (left panels, CellMask) co-incubated with calcein (middle left panels, green) and **(A)** untreated or **(B)** treated with  $100 \mu\text{g mL}^{-1}$  Pt-Ceria-46-atto NPs for 3 h (middle right panels, red). Calcein is a cell-impermeant fluorescent dye that is internalized via endocytosis by healthy cells and displays a punctuate pattern (gray arrow in **A**). However, when the cell membrane integrity is compromised, calcein dye molecules leak into the cell and a diffuse pattern of cytosolic calcein distribution is observed (white arrow in **A**). NP and calcein internalization by cells can be appreciated in the merge images (right panels). Scoring the percentage of cells without cytosolic calcein distribution is a conventional method to assess the impact of NPs on the membrane integrity and the cellular viability. **(C)** Percentage of cells without cytosolic calcein distribution for untreated and NP treated experiments (gray and white bars, respectively). In total, the plasma membrane integrity of more than 340 cells was evaluated. For both untreated and NP treated cells, the percentage of viable cells was above 97 %. Hence, these results point to a cellular uptake process of small Pt-Ceria NPs that does not impair the plasma membrane integrity. Data represent mean  $\pm$  standard error of two independent experiments.

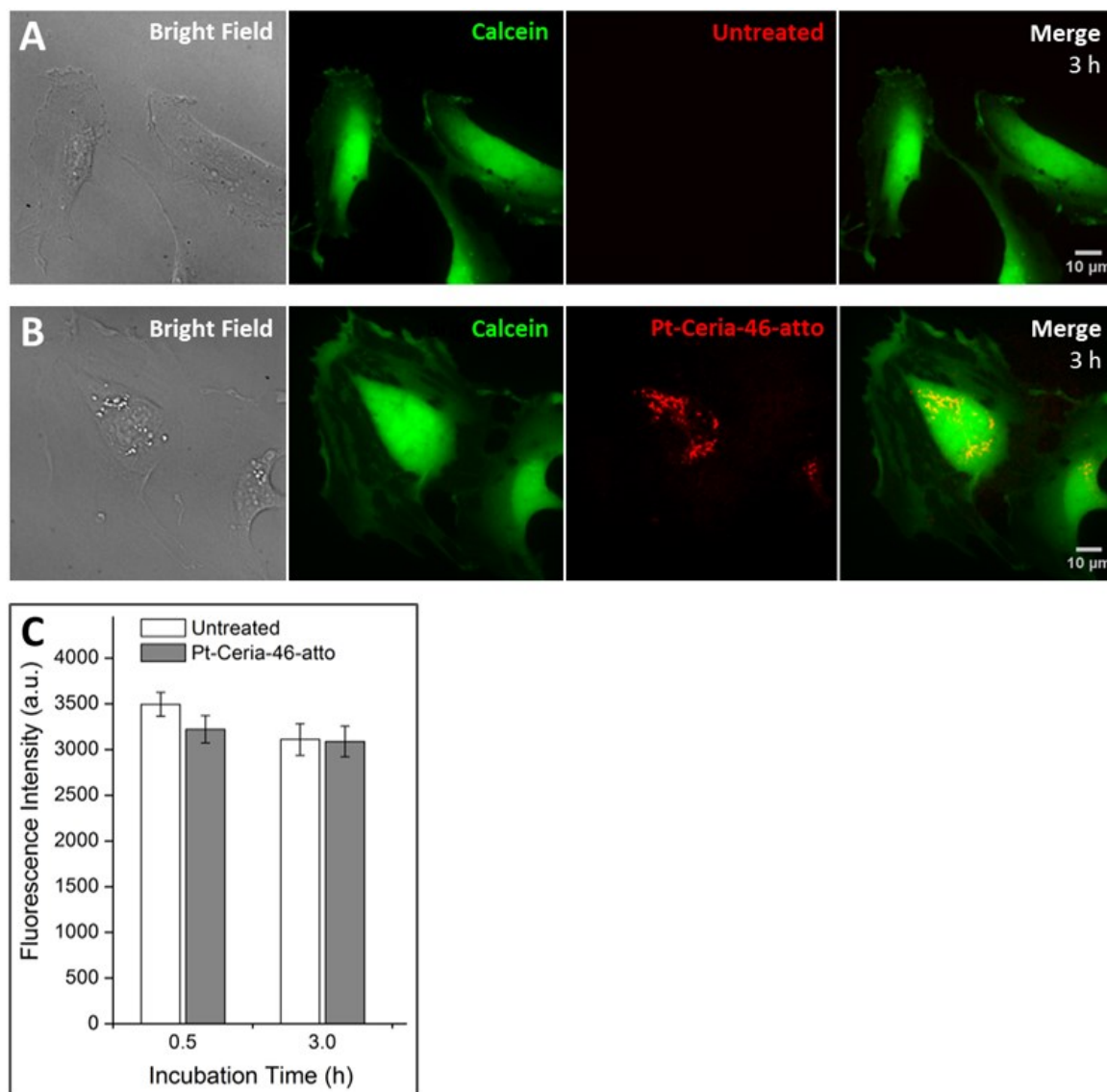


**Figure 8.13 Impact of small Pt-Ceria NPs on the membrane integrity: calcein leakage out assay.** Bright field (left panels) and Z-projection of live-cell confocal images. HMEC-1 cells were pre-loaded with cytosolic calcein (middle left panels, green) and subsequently **(A)** untreated or **(B)** treated with  $100 \mu\text{g mL}^{-1}$  Pt-Ceria-46-atto NPs for 0.5 and 3 h (middle right panels, red). In this assay, if the plasma membrane is disrupted, pre-loaded calcein dye molecules can leak out the cell, and an overall reduction in the cytosolic fluorescence intensity occurs. Thus, a reduction in the mean fluorescence intensity can be correlated with particle-induced cell membrane damage. Intracellular NPs and cytosolic calcein can be clearly visualized in the merge images (right panels). **(C)** Mean fluorescence intensity of calcein measured in the cytosolic region of individual HMEC-1 cells. In total, more than 70 single cells were analyzed per time point. Remarkably, no significant difference ( $p < 0.01$ ) between untreated and Pt-Ceria-46-atto NPs treated cells was detected (white and gray bars, respectively). Data represent mean  $\pm$  standard error of two independent experiments ( $n = 35\text{--}40$ ).

### 8.2.2.8 Impact of ceria and Pt-ceria NPs on the cellular ATP level

In order to further investigate if small Pt-ceria NPs can have an impact on the cellular viability, we measured and compared the particle-induced cytotoxicity of Ceria-47-atto, Pt-Ceria-46-atto, and Pt-Ceria-143-atto NPs. HMEC-1 cells were incubated at two distinct concentrations:

$10 \mu\text{g mL}^{-1}$  and  $100 \mu\text{g mL}^{-1}$ . After specific incubation periods of 3, 24, 48 and 72 h, the relative adenosine triphosphate (rATP) content was analyzed to assess the metabolic impact of NPs on cells. One hundred percent rATP content represents the cellular viability of untreated cells. As presented in Figure 8.14, the rATP contents of cells treated with Pt-ceria-46-atto NPs do not significantly differ from the rATP content values of cells incubated with either ceria-47-atto or Pt-ceria-143-atto NPs. This means that platinum decoration and the unconventional uptake mechanism of Pt-Ceria-46-atto NPs do not induce a different nanotoxicity under the investigated conditions. Moreover, rATP values were found to be above the cytotoxic threshold of 75 % (dashed line) in all investigated conditions. This is a clear indication that ceria and Pt-ceria NPs are well tolerated by HMEC-1 cells in short-term exposure experiments (3–72 h).

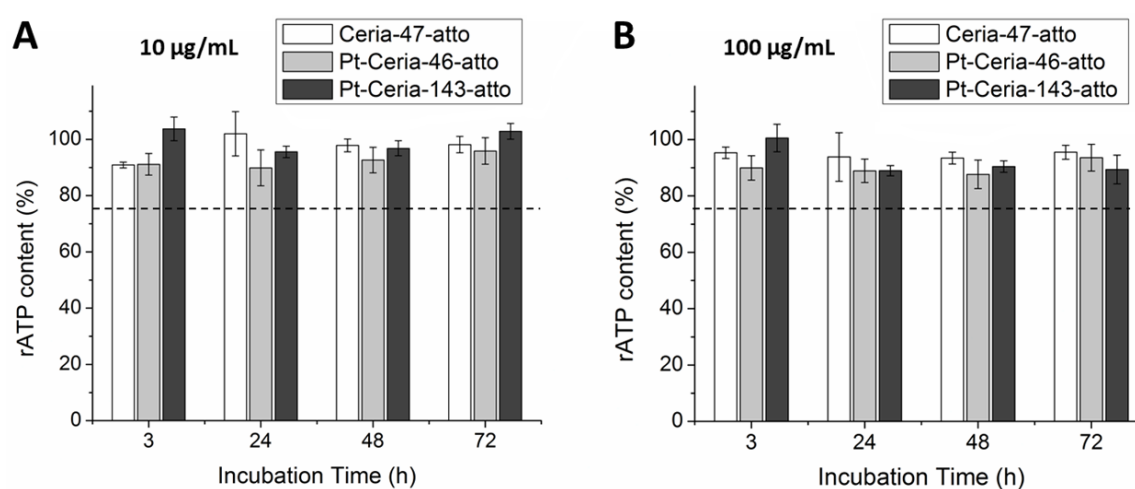


**Figure 8.14 Cellular viability of cells treated with ceria and Pt-ceria NPs.** HMEC-1 cells were exposed to either (A)  $10 \mu\text{g mL}^{-1}$  or (B)  $100 \mu\text{g mL}^{-1}$  of three distinct NP samples: Ceria-47-atto NPs (white bars), Pt-Ceria-46-atto NPs (light gray bars), and Pt-Ceria-143-atto NPs (dark gray NPs). The incubation time extended from 3 to 72 h. Within this time, no significant difference ( $p < 0.01$ ) was detected in the relative adenosine triphosphate (rATP) content of cells exposed to any NP type (in comparison to the other two NP types). In addition, the rATP content measured was always above the cytotoxicity threshold of 75 % (dashed line, cytotoxicity according to DIN EN ISO 10993-5:2009-10). This means that the metabolic impact induced by all three NP types on HMEC-1 cells was quite low. Histograms represent mean  $\pm$  standard error from three independent experiments.

### 8.2.2.9 Cell membrane penetration

Cell-penetrating peptides [70], 8 nm CdSe/ZnS core/shell quantum dots (coated with D-penicillamine) [71] and ultrasmall noble metal NPs (typically smaller than  $\sim 10$  nm), such as gold [68, 69, 72-74] and platinum [75, 76], can escape the traditional endocytosis pathway and perform a fast direct translocation across the cell membrane into the cytosol. This unconventional uptake mechanism is characterized by fast and efficient cellular uptake, without perceptible cell membrane disruption and no cytotoxic effects at low concentrations. This

definition almost perfectly matches our findings on the unusual fast uptake mechanism and cytosolic delivery of small Pt-ceria NPs. The exception is the presence of a relatively large ceria NP core.

Nevertheless, the mechanism of cell membrane penetration is not fully understood. Using coarse-grained molecular dynamics simulations, Lin & Alexander-Katz [68] proposed that cell membranes generate nanoscale transient holes to assist the fast and spontaneous translocation of cell-penetrating peptides as well as ultrasmall cationic NPs into the cytoplasm. According to this model, when ultrasmall 2.2 nm cationic gold NPs approach the membrane, they are attracted to negatively charged membrane proteins. Once a certain number of NPs is located in the membrane region, nanoscale holes are formed due to the alteration of the local electric field across the plasma membrane. NPs that are already in the region will then use these holes to direct translocate into the cytosol. After translocation, the transmembrane potential is strongly reduced and the membrane rapidly reseals itself.

On the basis of our findings and the literature, we propose the following uptake mechanism for small Pt-ceria NPs: as one NP diffuses and approaches a cell, the ultrasmall platinum NPs on its surface generate multiple transient nanoscale holes. These holes combine and allow the membrane penetration of the NP up to a core size of ~50–100 nm. After the passage of the particle, the membrane rapidly reseals itself. Once inside the cells, the diffusing NP will come into contact with cell organelles and, in the case of Pt-ceria NPs labeled with Atto 647N, will accumulate in mitochondria owing to the lipophilic cationic moieties of this dye. Figure 8.15 illustrates graphically the cell membrane penetration and mitochondrial targeting by a 50 nm Pt-ceria NP.

So as to test the generality of our results, we prepared 8 nm ceria NPs decorated with other noble metals; namely, rhodium and palladium. In addition, we synthesized platinum-decorated 50–80 nm mesoporous silica NPs. Preliminary results indicate that in all cases the same trend, with cell-membrane penetration and mitochondrial targeting by Atto 647N NPs was achieved. Moreover, we investigated if the uptake trend observed for small Pt-ceria NPs is cell-type dependent. Human cervical cancer cells (HeLa) cells were incubated with Pt-ceria-8-atto NPs, and the same unusual uptake behavior observed before was observed for HeLa cells (data not shown). Finally, the intracellular targeting with other moieties is under investigation.

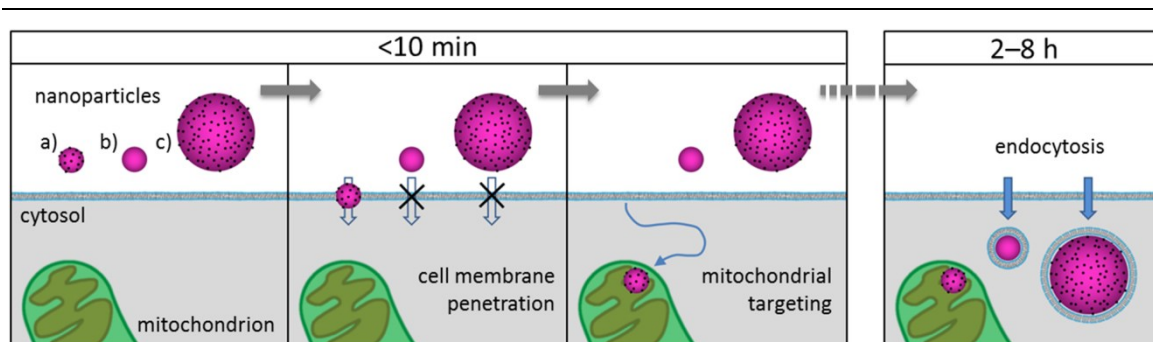


**Figure 8.15 Cell membrane penetration and mitochondrial targeting by Pt-ceria NPs.** Within a few minutes of incubation time, three mitochondria-targeted NPs approach a cell: a) 50 nm Pt-ceria NP, b) 50 nm ceria NP, c) 150 nm Pt-ceria NP. In the case of particle a), ultrasmall platinum NPs decorating its surface induce nanoscale holes on the cell membrane, and the NP directly translocates from the extracellular environment into the cytosol. Particle b) is not able to translocate the membrane because it is deprived of ultrasmall platinum NPs on its surface. Particle c) is too large to pass through the eventually induced holes. After translocation, particle a) diffuses freely in the cytosol and the membrane reseals. Next, the diffusing NP reaches a mitochondrion. After a few hours, the particles b) and c) are internalized by the conventional endocytic pathway and stay trapped in vesicles.

### 8.3 Conclusions

In summary, platinum-decorated ceria NPs that resemble catalyst-derived NPs can escape the traditional endocytosis uptake pathway and perform a rapid and direct translocation through the cell membrane. If properly targeted, these NPs are able to selectively accumulate in cellular organelles like the mitochondria. Interestingly, similar ceria NPs deprived of platinum do not translocate through the membrane, but are internalized by endocytosis. In addition, the particle size is a crucial parameter – only Pt-ceria NPs smaller than  $\sim 50\text{--}100$  nm are able to perform cell-membrane penetration. Mitochondrial targeting was achieved with Atto 647N, a fluorescence dye with high affinity to this cell organelle. Remarkably, although the uptake mechanism proposed involves the direct translocation of Pt-ceria NPs into the cytosol through transient membrane holes, we consistently observed no plasma membrane disruption or any other significant adverse effects on cells.

As regards the biological impact of the model NPs emitted from automobile catalytic converters, our findings suggest that the short-term nanotoxicology of high doses of Pt-ceria NPs (within 72 h,  $100\ \mu\text{g mL}^{-1}$ ) is rather low. However, the long-term effects of continuous exposure to much lower doses, as in human exposure to air pollution, remain to be investigated.

Pt-ceria NPs (and conceivably other noble-metal decorated NPs) are fascinating materials that perform a fast direct translocation into the cytosol along with a good short-term biocompatibility. These properties combined grant them a high potential to become important platforms for intracellular-targeted drug and gene delivery.

## 9 Endosomal escape and successful cytosolic drug release of dendronized mesoporous silica nanoparticles

*This chapter is based on the following publication:*

*Veronika Weiss, Christian Argyo, Adriano A. Torrano, Claudia Strobel, Stephan A. Mackowiak, Tim Gatzemaier, Ingrid Hilger, Christoph Bräuchle, and Thomas Bein;*

*“Dendronized mesoporous silica nanoparticles provide an internal endosomal escape mechanism for a successful cytosolic drug release.”*

*Submitted.*

### 9.1 Introduction

In recent years, mesoporous silica nanoparticles (MSNs) have been intensively studied as drug delivery vehicles due to their excellent materials features, such as good biocompatibility, large cargo capacity and versatile organic surface functionalization [16].

In general, an ideal drug delivery platform has to meet several requirements to achieve specific drug delivery, including biocompatibility, specific targeting, and stimuli-responsive drug release behavior [197-199]. Nanoscaled drug delivery systems, such as multifunctional MSNs, encounter many challenges on their way towards reaching their desired target and efficiently releasing their cargo. In particular, endosomal entrapment is faced by nanoparticles that are internalized by cells via endocytosis (see Section 2.5), and it represents a major obstacle for drug delivery [200]. Especially for membrane impermeable or immobilized cargo molecules, the nanocarriers need to access the cytosol in order to achieve efficient delivery to the targeted cell compartments. Several strategies have already been described to address or bypass the demanding task of endosomal escape, including pore formation, membrane fusion, photoactivated membrane rupture, and the proton sponge effect [125, 201-203].

Particularly, the proton sponge effect is a promising automatic strategy for endosomal release of the nanocarriers. The mechanism of the proton sponge effect follows an intrinsic osmotic swelling during endosomal acidification caused by the buffering capacity of modified nanocarriers, such as cationic polymers [204, 205]. Furthermore, a destabilization of the membrane caused by such positively charged vehicles might occur. Ultimately, this results in rupture of the endosomal membrane [206].

Poly(amidoamine) (PAMAM) dendrons or dendrimers provide high buffering capacity and have been found to be suitable for gene delivery, exhibiting extraordinary stability in forming



complexes with DNA [207, 208]. The resulting transfection efficiency was explicitly attributed to an activated proton sponge mechanism. Compared with simple amines, PAMAM dendrons (depicted in Figure 9.2A) have an increased tendency towards protonation which is caused by a fixed arrangement of two amino groups in close vicinity such that they can easily be connected by a hydrogen bond [209].

Here we have established a newly designed multifunctional core-shell MSNs coated with PAMAM dendron structures on the outer surface. These systems combined provide a successful mechanism for endosomal escape and subsequent cytosolic drug release from the silica nanocarriers. Dendronized MSNs feature a high buffering capacity acting as a potential trigger for a pH-responsive endosomal escape mechanism conceivably via the proton sponge effect, as illustrated in Figure 9.1.

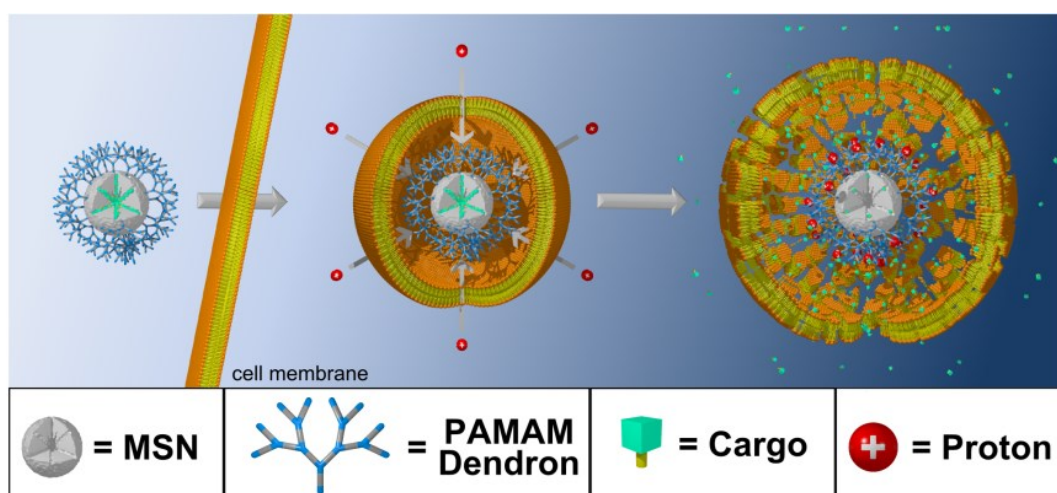


**Figure 9.1 Schematic illustration of the proposed intrinsic endosomal escape mechanism.** PAMAM dendron-coated MSNs are internalized into a cell via endocytosis. Endosomal acidification leads to intrinsic osmotic swelling caused by the high buffering capacity of the dendron-coated MSNs. Subsequently, endosomal membrane rupture occurs which provides access to the cytosol. In this reductive environment the immobilized (disulfide bridges) cargo molecules can be released.

This is a collaborative project with the Group of Prof. Dr. T. Bein, at the University of Munich (LMU), and the Group of Prof. Dr. I. Hilger, at the University of Jena. Synthesis and characterization of MSNs were performed by Dr. Christian Argyo and Tim Gatzemeier (Prof. Dr. T. Bein; LMU Munich). The cytotoxicity experiments were carried out by Claudia Strobel (Prof. Dr. I. Hilger; University of Jena). In our laboratories (Group of Prof. Dr. C. Bräuchle; LMU Munich) we carried out a series of cell-based microscopy assays, including cell targeting, endosomal escape, and drug release experiments (performed by Dr. Veronika Weiss and Dr. Stephan A. Mackowiak), as well as cellular uptake kinetics. In particular, quantitative live-cell imaging based on Particle\_in\_Cell-3D, as described in Chapter 4, was employed to determine the absolute number

of PAMAM dendron-coated MSNs internalized by single cells. These outcomes were recorded under the same experimental conditions applied for the cytotoxicity experiments and contributed to establish the low cytotoxicity of these nanocarriers.

## 9.2 Results and Discussion

### 9.2.1 Synthesis and characterization of dendronized MSNs

MSNs coated with different generations of PAMAM dendrons (D1, D2 and D3) were synthesized via a delayed co-condensation approach to create core-shell functionalized MSNs [210, 211]. Specifically, bifunctional MSNs consist of a thiol-functionalized particle core and additionally an external PAMAM dendron shell. The amino-terminated PAMAM dendrons (Figure 9.2A) are covalently bound to the particle surface via silane linkers attached to the propargyl groups [211]. The PAMAM moieties are exclusively located at the external particle surface resulting in an organic polymer coating of MSNs featuring high buffering capacity. MSNs coated with third generation PAMAM dendrons (MSN-D3) showed optimal properties and are expected to have great potential for generating the proton sponge effect. Hence, we focused our attention on the investigation of the MSN-D3 particles for cargo release, cell uptake, cytotoxicity and cell targeting experiments.

Transmission electron microscopy (TEM) revealed spherically shaped MSN-D3 with sizes of about 70 nm in diameter and a worm-like porous structure consisting of radially grown mesoporous channels (Figure 9.2B).

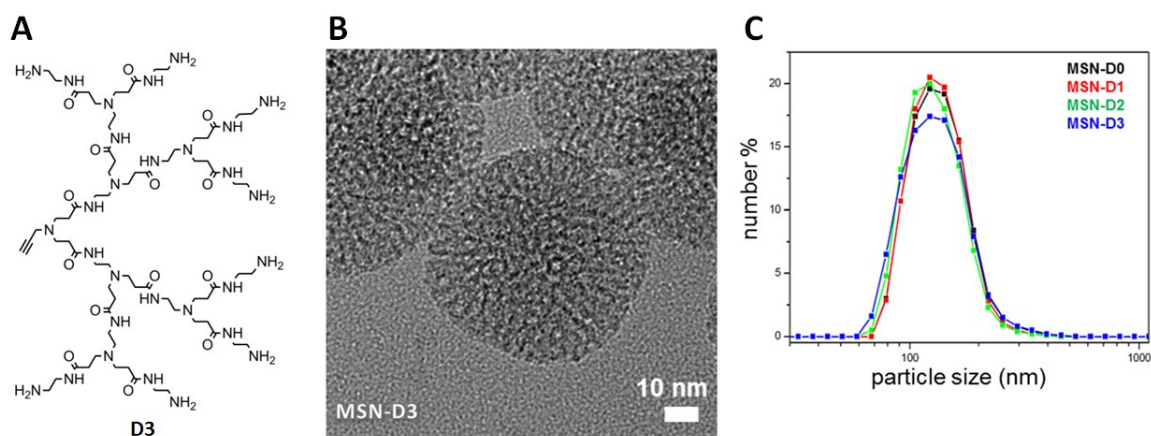


**Figure 9.2 Dendronized mesoporous silica nanoparticles.** (A) Amino-terminated propargyl-PAMAM dendron D3. (B) Representative TEM image of MSN-D3. (C) Dynamic light scattering (DLS) measurements were performed to determine the hydrodynamic size distribution of MSN-D0 (black), MSN-D1 (red), MSN-D2 (green), and MSN-D3 (blue). All samples featured narrow size distributions with an average particle size of about 122 nm.

Hydrodynamic size and structural parameters of MSNs were measured by dynamic light scattering (DLS) and nitrogen sorption measurements, respectively, and are summarized in Table 9.1. DLS measurements confirmed that both the reference sample MSN-D0 (MSNs without PAMAM dendron functionality) and MSN-D3 featured narrow size distributions with an average particle size of about 122 nm (Table 9.1 and Figure 9.2C). The size difference between TEM (~70 nm) and DLS (~122 nm) data is attributed to a tendency for weak agglomeration in solution. For the reference sample MSN-D0, relatively high BET surface area and pore volume were observed. In the case of MSN-D3, these porosity parameters were decreased. This effect was partially due to the increasing sample mass by addition of the non-porous organic polymer. Furthermore, large PAMAM dendron generations might have caused clogging of some pore entrances towards to access of nitrogen molecules at the low measurement temperatures (-196 °C). A slight average pore constriction could also be observed in the presence of the attached PAMAM structures. This decrease could be due to the reduction of the pore mouth diameters partially covered by frozen organic PAMAM moieties. Nevertheless, PAMAM dendron-coated MSNs still exhibited a large accessible mesoporous structure offering enough space for the incorporation of cargo molecules.

**Table 9.1 Structural parameters of functionalized MSNs.**

Sample	Particle size <sup>[a]</sup> [nm]	BET surface area [m <sup>2</sup> /g]	Pore volume <sup>[b]</sup> [cm <sup>3</sup> /g]	DFT pore size <sup>[c]</sup> [nm]
MSN-D0	122	1190	0.74	2.9 – 4.4
MSN-D3	122	497	0.24	2.2 – 3.8

a) Particle size is given by the hydrodynamic diameter and refers to the peak value of the size distribution derived from DLS measurements; b) Pore volume is calculated up to a pore size of 8 nm to remove the contribution of the interparticle porosity; c) DFT pore size refers to the full width at half maximum of the corresponding pore size distribution using the density functional theory (DFT) approach.

Zeta potential measurements showed drastic changes in the surface charge of MSN-D3 compared to MSNs without PAMAM dendron functionality (MSN-D0). As presented in Figure 9.3A, highly positive surface charges were observed at acidic pH values for MSN-D3 (+60 mV at pH 2). In contrast, the reference sample MSN-D0 exhibited an isoelectric point close to pH 2, which results in a negatively charged particle surface over the full pH range. Additional titration measurements of MSN-D3 against an aqueous solution of NaOH (0.01 M) gave evidence for a high proton acceptance of the polymer shell resulting in a high buffering capacity. As depicted in Figure 9.3B, MSN-D3 featured a significant increase in required volume of NaOH solution to be neutralized (+ 1.4 mL). MSN-D3 provided great potential to act like a proton

sponge showing optimal buffering behavior in the pH range 5.5 to 6.5, which perfectly fits the endosomal acidification range [212].

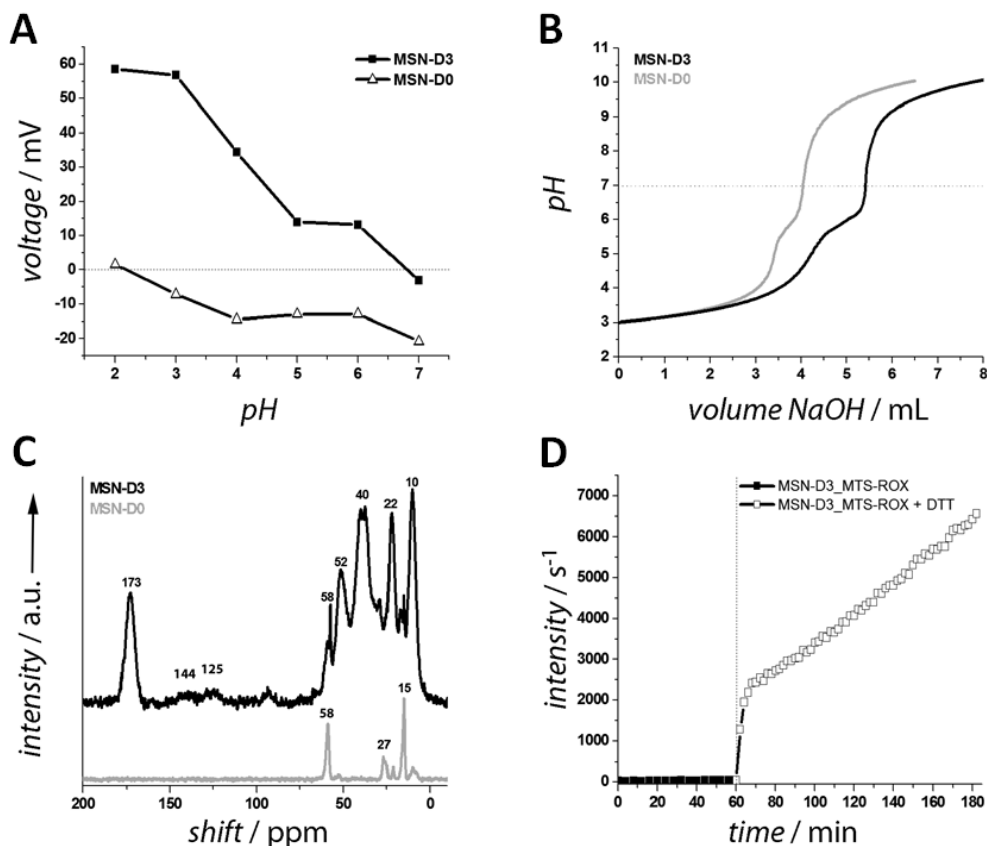


**Figure 9.3 Characterization of PAMAM dendron-coated MSNs.** (A) Zeta potential measurements, (B) titration data and (C) solid-state NMR measurements (for clarity the graphs have been shifted along the y-axis) of MSN-D3 and MSN-D0. (D) Redox-responsive release kinetics of MTS-ROX before (filled squares) and after (empty squares) addition of dithiothreitol (DTT) to simulate the reductive milieu of the cytosol. Before medium change, MSN-D3 shows no premature release of the fluorescent cargo molecules which are attached to the mesopores via disulfide bridges. Only in reductive milieu a significant increase in fluorescent intensity can be observed, demonstrating a redox-responsive release behavior of the MTS-ROX due to cleavage of the disulfide bridges.

Further characterization of the attached functional groups was performed by <sup>13</sup>C solid state NMR analysis (Figure 9.3C). MSN-D3 featured characteristic peaks for the amide groups of the PAMAM dendrons at 173 ppm (C=O). Furthermore, weak signals at 144 and 125 ppm derived from the triazole click connection. Various strong signals in the range between 60 to 10 ppm correspond to different types of methylene groups which belong to the PAMAM moieties (52 and 40 ppm (N-CH<sub>2</sub>-R), 21 and 10 ppm (R-CH<sub>2</sub>-R)).

To prove a stimuli-responsive cargo release behavior of MSN-D3, time-based release experiments of a fluorescent and thiol-reactive model drug (MTS-ROX; methanethiosulfonate 5(6)-carboxy-X-rhodamine) were performed. MSN-D3 with immobilized MTS-ROX in the

mesopores showed no cargo release in aqueous solution under non-reductive conditions within the first hour (Figure 9.3D). The cargo molecules were covalently attached via disulfide bridges preventing premature leakage of the dye. Only upon addition of a reducing agent (simulation of the cytosol) an increase in fluorescence intensity was shown. This indicated a redox-responsive cleavage of the disulfide bridges and subsequently a specific stimuli-responsive release of the fluorescent model drug occurred.

From all these results we conclude a successful synthesis of core-shell functionalized MSNs with third generation PAMAM dendrons via the delayed co-condensation approach. The PAMAM moieties are exclusively located at the external particle surface, resulting in an organic polymer coating of MSNs featuring a high buffering capacity. In addition, the redox-responsive behavior provide great potential for a specific cargo release once the mesoporous silica nanocarriers have escaped from the endosomes and entered the cytosol of the targeted cell.

### 9.2.2 Cellular uptake kinetics and cytotoxicity studies

In order to study the cytotoxicity of PAMAM dendron-coated MSNs, the uptake kinetics and the relative cellular dehydrogenase activity of endothelial cells (HMEC-1) were analyzed. First, the NP uptake kinetics was investigated to gain detailed information about the dose of MSNs effectively internalized by cells at defined incubation times (Figure 9.4A–D). HMEC-1 cells were exposed to a concentration of  $100 \mu\text{g mL}^{-1}$  MSN-D3 from 3 to 48 h and subsequently imaged by live-cell fluorescence microscopy. Confocal stack images of single cells interacting with fluorescence-labeled MSNs were acquired and evaluated with Particle\_in\_Cell-3D (see Chapter 4). Quantitative image analysis revealed that  $2,752 \pm 887$  MSNs were taken up by each cell after just 3 h. The number of intracellular particles reached  $13,480 \pm 1,824$  NPs per cell after 24 h, and it then decreased until reaching approximately  $10,047 \pm 1,192$  MSNs after 48 h. Interestingly, the amount of intracellular particles can diminish with time by cell division process and by exocytosis, as recently reported in the literature [137, 170]. The cell division possibility would be in accordance with the reported doubling time of HMEC-1 cells, namely 29 h [169]. The relative cellular dehydrogenase activity (rcDH) of HMEC-1 cells after exposure to MSN-D3 is presented in Figure 9.4E. Although the cells were shown to become packed with thousands of particles, MSN-D3 revealed no adverse effects over all investigated concentrations ( $10 \text{ fg mL}^{-1}$  to  $100 \mu\text{g mL}^{-1}$ ) and exposure times (3 to 72 h). All rcDH values assessed were well above 75 %, the cytotoxicity threshold according to according to DIN EN ISO 10993-5:2009-10. PAMAM dendron-coated MSNs therefore have a tendency to have low cytotoxicity, comparable to other PAMAM-coated materials, as previously described [213].

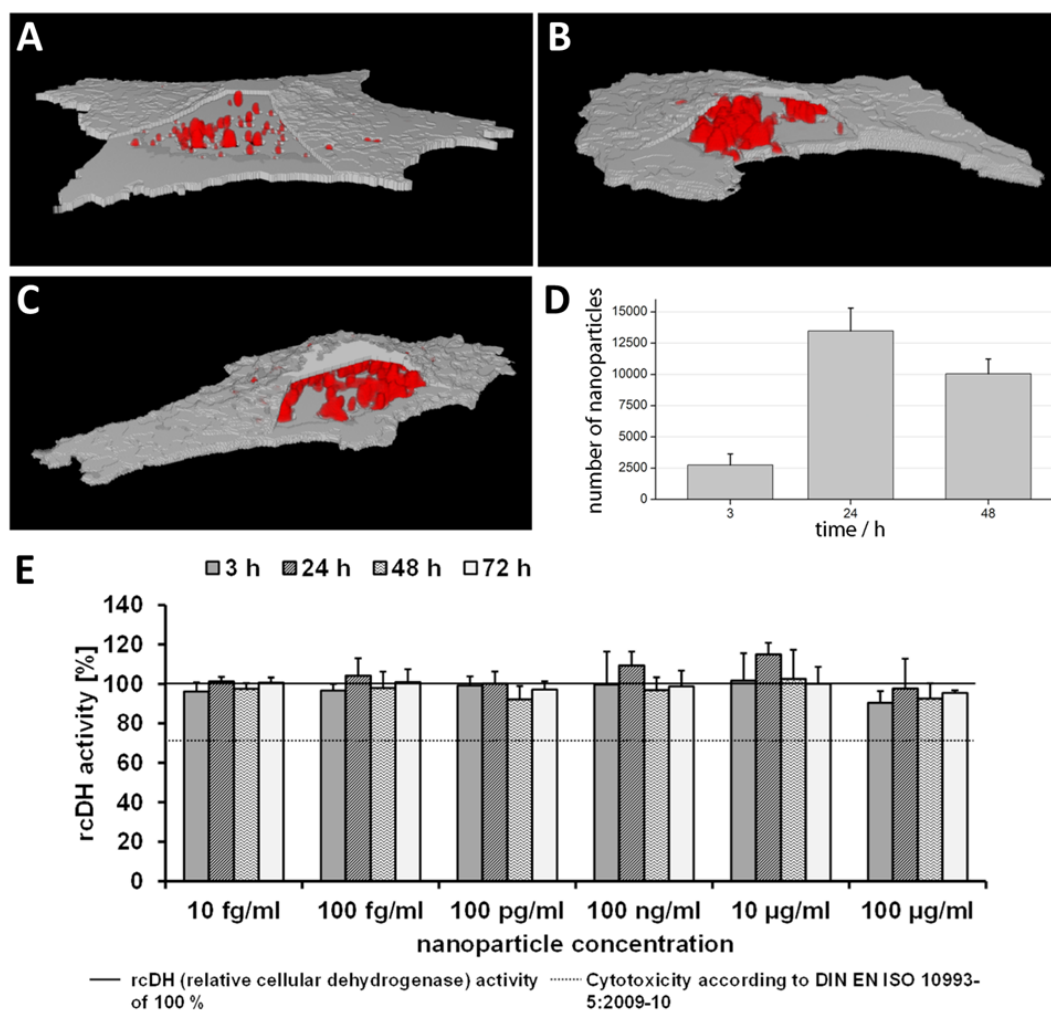


**Figure 9.4 Cellular uptake kinetics and cytotoxicity studies of dendronized MSNs.** (A–C) Representative 3D images of single cells (gray) and intracellular MSN-D3 (red) after 3 h, 24 h and 48 h, respectively. (D) The absolute number of NPs internalized by single cells increases steeply within the first 24 h. Remarkably, the number slightly decreases after 48 h. The histogram depicts the mean  $\pm$  standard error of two independent experiments ( $n = 15$ ). (E) Relative cellular dehydrogenase activity (rcDH) of human microvascular endothelial cells (HMEC-1) after exposure to particles. MSN-D3 revealed no cytotoxic impact ( $n = 3$  independent experiments).

### 9.2.3 Specific receptor-mediated cell uptake

Another key feature for a capable drug delivery vehicle is specific targeting of the desired tissue, mainly cancer cells, which can be achieved by exploiting a receptor-mediated cellular uptake of the nanocarriers. Targeting ligands, such as folic acid (FA), can be attached to the periphery of the MSN-D3 via a bifunctional PEG linker [211]. Application of the PEG-linkers is considered to reduce unspecific cellular uptake of the particles [214]. Atto 633-labeled MSN-D3 functionalized with PEG-FA (MSN-D3-PEG-FA) were incubated for 5 h with KB cells (cervix carcinoma cells derived from HeLa) to investigate a possible receptor-mediated endocytosis. Two cellular uptake experiments were performed simultaneously (Figure 9.5). On the one hand, KB cells were

pretreated with free FA to gain full saturation and blockage of the cell receptors before incubation with particles. Here, only unspecific cell uptake was observed to a minor degree (Figure 9.5A). On the other hand, a much higher efficiency of particle internalization by cells occurred for KB cells without pretreatment with FA. This efficient cellular uptake can be attributed to the receptor-mediated endocytosis of MSN-D3-PEG-FA (Figure 9.5B).

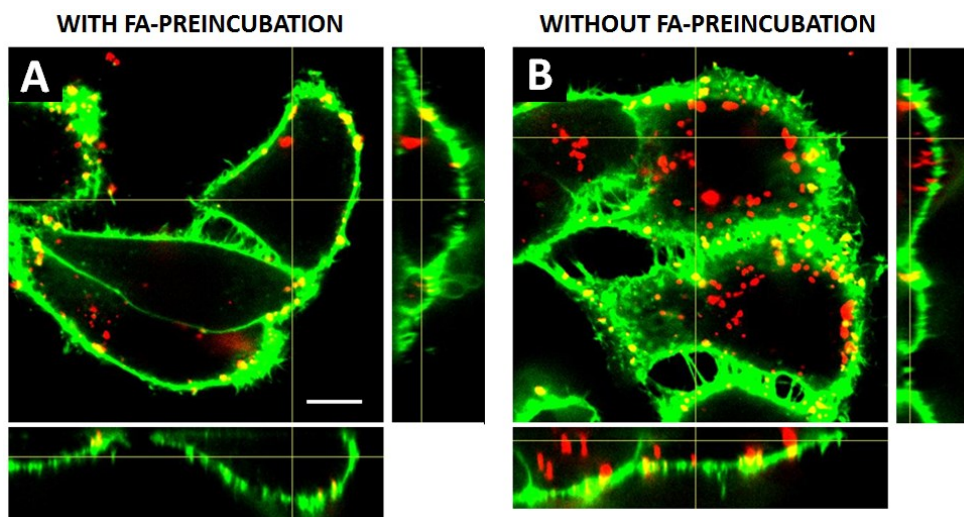


**Figure 9.5 Specific receptor-mediated cell uptake of MSN-D3-PEG-FA. (A)** Unspecific and **(B)** receptor-mediated endocytosis of MSN-D3 with targeting ligand folate (MSN-D3-PEG-FA, red) by KB cells (membrane staining WGA 488, green). Indication of the particle location (inside or outside the cell) can be noticed by in the cross-section and orthogonal views. In panel **B**, a specific receptor-mediated cell uptake can be observed for MSN-D3-PEG-FA with KB cells after 5 h incubation at 37 °C. In contrast, as shown in panel **A**, the incubation of MSN-D3-PEG-FA with FA-preincubated KB cells for 5 h at 37 °C showed only minor unspecific cellular uptake. Scale bar = 10  $\mu$ m.

#### 9.2.4 Endosomal escape and drug release

The potential of MSN-D3 to achieve an intrinsic endosomal escape was investigated by *in vitro* release experiments of the nuclei staining DAPI on HeLa cancer cells [215, 216]. A thiol-reactive derivative of DAPI (MTS-DAPI) was covalently attached to the mercapto-functionalized walls of the mesopores. The established covalent disulfide bridges should be cleaved only when endosomal escape was achieved and the nanocarriers have reached the reductive milieu of the cytosol [217, 218]. HeLa cells were incubated with MSN-D3 loaded with MTS-DAPI for 5, 10 and 22 h. Figure 9.6 shows an efficient cellular uptake behavior of the NPs labeled with Atto 633 (red) already after 5 h. Moreover, only weak staining of the nuclei (DAPI, blue) was observed at this time point. In contrast, free DAPI molecules were able to efficiently stain nuclei already within a few minutes (5 min), as described by standard nucleus staining protocols [219]. Over the entire time range, a successive increase in fluorescence intensity of the DAPI-stained nuclei was observed (Figure 9.6D). Sample MSN-D3 showed a prominent increase in fluorescence intensity

monitored for a total time period of 61 h. The results indicate that endosomal escape for the cytosolic delivery of the cargo molecules was achieved. The gradual release behavior of DAPI is attributed to the relatively slow proton sponge effect caused by the PAMAM dendron content of these nanocarriers. The increasing level of nuclei fluorescence staining proved an effective DAPI delivery to the cells. Reference samples (MSN-D0 and supernatant of MSN-D3 after particle separation by centrifugation ‘Supernatant MSN-D3\_MTS-DAPI’) displayed no temporal increase of fluorescence intensity, proving that only marginal amounts of free dye were present in the solution. Most important, this demonstrates that the PAMAM dendron content of these drug delivery vehicles is essential to achieve successful cargo delivery to cancer cells. Of note, the MSNs remained stationary after the endosomal escape as already observed in previous reports [125, 220].

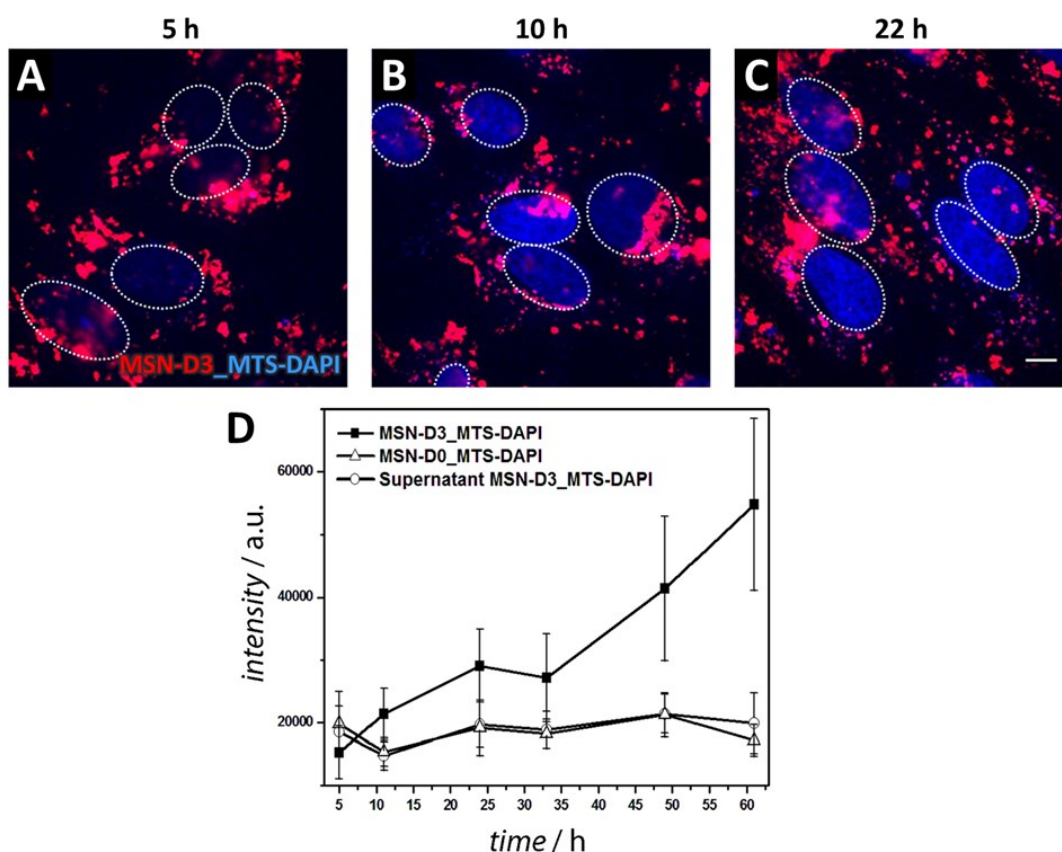


**Figure 9.6 Endosomal escape and DAPI release.** Fluorescence microscopy studies of HeLa cells incubated with MSN-D3 loaded with immobilized DAPI (MTS-DAPI, blue) inside the mesopores, and labeled with Atto 633 (red) after (A) 5 h, (B) 10 h and (C) 22 h. The nuclei are indicated with dashed ellipses. (D) Nuclei staining kinetics of DAPI delivery to HeLa cells from MSN-D3\_MTS-DAPI (squares), MSN-D0\_MTS-DAPI (triangles) and the supernatant (circles) of MSN-D3\_MTS-DAPI solution (after particle separation). The fluorescence intensity of distinct regions of interest (stained nuclei) was evaluated after different time points of sample incubation. Data represent average fluorescence intensity  $\pm$  standard deviation. A time-dependent increase of fluorescence intensity is observed only for MSN-D3\_MTS-DAPI, suggesting a gradual DAPI release from the nanocarriers. In contrast, the fluorescence intensity remains constant at a marginal level for the reference samples. Scale bar = 10  $\mu$ m.



The anticancer drug colchicine (Col) is known to cause inhibition of the microtubuli polymerization due to irreversible binding to tubulins, ultimately leading to cell death [221, 222]. A thiol-reactive derivative of Col (MTS-Col) was immobilized at the inner mesoporous surface of MSN-D3 and, subsequently, these loaded-drug-delivery vehicles were incubated with tubulin-GFP-transfected KB cells. In Figure 9.7A/E, the fluorescence-labeled microtubule network (green) of untreated KB cells is depicted for comparison. After 2 h of particle incubation (Atto 633-labeled MSN-D3, red), endocytosis occurred to a high degree, but the microtubule network was still intact, suggesting that no release of Col had occurred at this time point (Figure 9.7B/F). A partial destruction of the microtubule network could only be observed after 7 h (Figure 9.7C/G). After 22 h, cell death finally occurred, as indicated by vanishing of the tubulin structure (blurred green fluorescence signal) and by the spherical shape of the cells (Figure 9.7D/H). The present cell experiments therefore suggest a time-dependent intracellular release of immobilized MTS-Col from the mesoporous drug delivery vehicles. The acidification of the endosomal compartment during trafficking possibly triggered the endosomal escape. By means of the high buffering capacity of MSN-D3, a high internal osmotic pressure led to the rupture of the endosomal membrane with subsequent access of MSNs to the cytosol. Reducing agents present in the cytosol were able to cleave the disulfide bridges and Col was efficiently released.

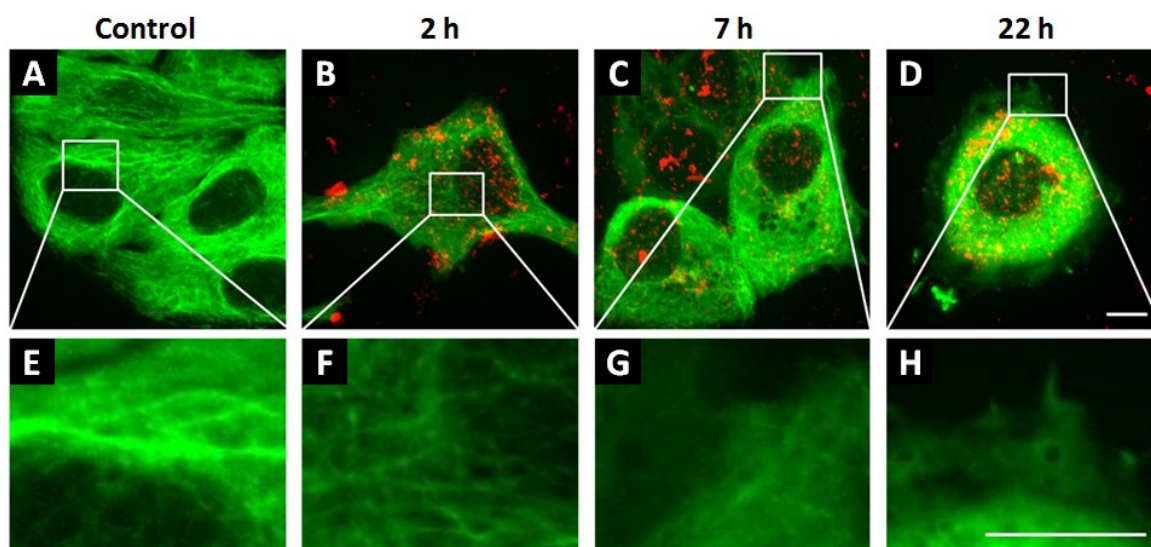


**Figure 9.7 Endosomal escape and drug release.** Fluorescence microscopy studies of (A/E) control (untreated) KB cells with GFP-tagged tubulin (green). The cells were incubated with MSN-D3 loaded with immobilized colchicine (MTS-Col) inside the mesopores and labelled with Atto 633 (red) for (B/F) 2 h, (C/G) 7 h, and (D/H) 22 h. Panels E–H show zoom-in representative microtubule structures (without MSN-D3). A time-dependent destruction of the tubulin network by colchicine was observed, finally causing cell death. Scale bars = 10  $\mu\text{m}$ .

### 9.3 Conclusions

In conclusion, these *in vitro* release experiments with different cell lines and different cargo molecules incorporated into the mesoporous system of PAMAM dendron-coated MSNs suggest an intrinsic endosomal escape pathway followed by an intracellular redox-driven release of immobilized cargo molecules. Furthermore, they feature optional attachment of various cargos inside the mesopores via disulfide bridges and binding of different targeting ligands to the outer periphery of the particles, which can be precisely tuned to target specific cancer cell lines. MSNs uptake kinetics and cytotoxicity studies suggest a good bio-tolerability, since no adverse effects of the PAMAM dendron-coated MSNs on the metabolism of endothelial cells were observed. The combination of all these essential features into one multifunctional nanocarrier is anticipated to result in a powerful drug delivery system.

## 10 A surface acoustic wave-driven microfluidic system for nanoparticle uptake investigation under physiological flow conditions

This chapter is based on the following publication:

Florian G. Strobl, Dominik Breyer, Phillip Link, Adriano A. Torrano, Christoph Bräuchle, Matthias F. Schneider, and Achim Wixforth;

“A surface acoustic wave-driven micropump for particle uptake investigation under physiological flow conditions in very small volumes.”

*Beilstein Journal of Nanotechnology* 6, 414-419 (2015).

### 10.1 Introduction

Most *in vitro* experiments performed to investigate nanoparticle-cell interactions are done under static flow conditions, with adherent cells residing at the bottom of a culture slide. This can be an important flaw when it comes to the quantitative interpretation of experimental data [119]. Providing that the cellular uptake mechanisms are fast enough, the nanoparticle (NP) uptake rate at a given NP concentration in the medium,  $C_m$ , will be limited by the NP motion and the re-supply in the medium. For small particles, diffusion will dominate the delivery rate  $dN/dt$ . For the sake of simplicity, it is assumed that the observed cell is a half-sphere with radius  $R$  as depicted in Figure 10.1.

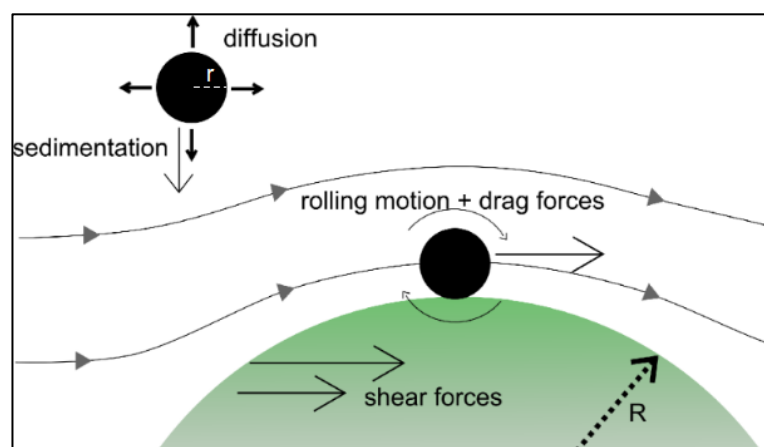


**Figure 10.1 Nanoparticle uptake under flow.** The uptake of NPs by a cell is influenced by different factors: diffusion and sedimentation will limit the maximum NP delivery for static conditions. Under flow, these factors become less important, but shear forces acting on the cell and the NPs will influence the uptake mechanisms.

If the influence of gravity can be neglected, the NP delivery rate at equilibrium can then be derived from Fick's law [223]:

$$\frac{dN}{dt} = 2\pi D_{eff} RC_m \quad (\text{Equation 10.1})$$

Here  $D_{eff}$  denotes an effective diffusion constant.

In an *in vitro* experiment without fluid motion, however, also sedimentation will contribute to the delivery rate. For very large NPs or, probably more relevant, for NP agglomerates, the delivery rate will be determined by the rate of descent, which can be calculated by the Stokes equation:

$$\frac{dN}{dt} = \pi R^2 C_m v_{sed} = \pi R^2 C_m \frac{g(\rho_p - \rho_m)}{9\eta} 2r^2 \quad (\text{Equation 10.2})$$

where  $v_{sed}$  is the sedimentation velocity,  $r$  the radius of the particle, and  $\rho_p$  and  $\rho_m$  are the densities of particle and medium, respectively.

Under realistic conditions, there will be, after some time, an equilibrium between sedimentation and back-diffusion and, hence, the cell will be exposed to an elevated local NP concentration  $C_{loc} > C_m$ . Ignoring these effects can in fact lead to misinterpretation of experimental data, especially to an overestimation of the impact of large NPs or agglomerates [119].

Furthermore, particles on a cell surface under shear are subject to drag and torsion forces [224]. For spherical particles in the nano-regime it can be easily derived from the Stokes equation that these drag forces are typically of the order of a few piconewtons or below, i.e, one or more orders of magnitude weaker than typical receptor-ligand binding strengths [225]. Nevertheless, in the case of weak unspecific NP adhesion, these forces can be strong enough to induce a rolling motion over the cell, which in turn significantly reduces the mean contact time between NP and cell and, hence, the uptake probability. Assuming a rolling particle with radius  $r = 50$  nm and following its center streamline at a shear rate of  $2000 \text{ s}^{-1}$ , its rolling velocity will be of the order of  $100 \text{ } \mu\text{m s}^{-1}$ . Relevant disruption forces for specific bindings can be achieved for large NP agglomerates, since the drag force scales with  $r^2$ . An agglomerate with a hydrodynamic radius of  $r = 500$  nm at a shear rate of  $2000 \text{ s}^{-1}$ , for instance, experiences a force of approximately 77 pN [226].

Finally, endothelial cells are of special interest due to their outstanding role regarding the distribution of NPs by the vascular system. Hence, another important issue is that a static medium is certainly not a physiological environment for these cells, which are exposed *in vivo* to

shear rates of up to  $3000 \text{ s}^{-1}$  [227]. It was recently shown that the glycocalyx of endothelial cells is substantially reorganized under shear [228], and several effects of shear stress on cellular uptake mechanisms have been reported [229-231].

One solution to the aforementioned problems is to perform experiments under realistic flow conditions. In the following, a novel device for inducing high shear rates at the bottom of an arbitrary cell culture chamber is introduced. The device is based on SAW-driven acoustic streaming. Many different applications of this effect in the area of microfluidics and life science have been developed so far [232, 233]. In the past, the Research Group of Prof. Dr. A. Wixforth, at University of Augsburg already introduced SAW devices for quantifying cell association of targeted NPs [234] and cell adhesion on implant materials [235]. One of the advantages of SAW-driven systems is their applicability to very small samples without having to deal with any dead volume. Thus, the demand for sample material is extremely low and the small surfaces in general reduce the risk of sample contamination. Moreover, the devices are typically very robust and inexpensive to produce. However, the shear rates that were reported so far for “conventional” SAW-driven microfluidic devices are usually one or two orders of magnitude below the typical shear rates of the capillary system and therefore not suitable for mimicking capillary blood flow. High input power to the SAW generator is no solution to that problem since dissipation would heat the sample. However, as shown below, the application of focusing interdigital transducers (FIDTs) in an L-shape configuration allows for shear rates of up to  $4000 \text{ s}^{-1}$  without significant sample heating.

Here, a versatile microfluidic device based on acoustic streaming induced by surface acoustic waves (SAWs) is presented. The device offers a convenient method for introducing fluid motion in standard cell culture chambers and for mimicking capillary blood flow. It is demonstrated that shear rates over the whole physiological range in sample volumes as small as  $200 \mu\text{L}$  can be achieved. A precise characterization method for the induced flow profile is presented and the influence of flow on the uptake of platinum-decorated ceria NPs by endothelial cells (HMEC-1) is demonstrated. The microfluidic system was designed, fabricated and characterized by Florian G. Strobl, Dominik Breyer, and Phillip Link (Group of Prof. Dr. A. Wixforth; University of Augsburg, Germany, in collaboration with Dr. M. F. Schneider; Boston University, USA). The nanoparticle uptake experiments (cell culture, live-cell imaging and quantitative image analysis) were performed in our laboratories (Group of Prof. Dr. C. Bräuchle; LMU Munich, Germany).

## 10.2 Results & Discussion

### 10.2.1 Microfluidic setup

The device is illustrated in Figure 10.2. In short, applying a high-frequency voltage to an interdigital transducer (IDT) on a piezoelectric substrate induces Rayleigh-mode SAWs. The latter couple into the fluid medium and excite longitudinal pressure waves. As such high-frequency pressure waves are attenuated on short distances, acoustic radiation pressure is generated which eventually induces fluid motion [236].

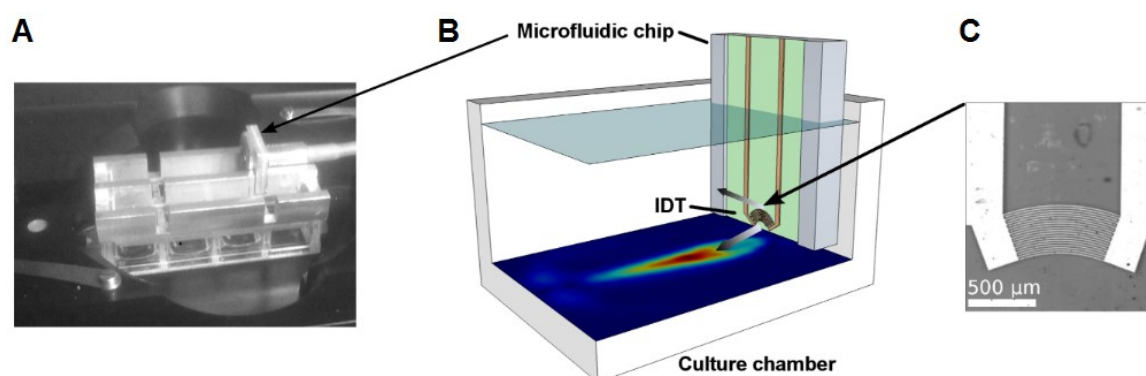


**Figure 10.2 Microfluidic setup.** (A) Photograph of the sample system on a live-cell microscope stage. The chip is mounted onto a culture chamber by a metal frame. (B) Sketch of the chip. A focusing interdigital transducer induces acoustic streaming with the main flow component pointing downwards, incident at the bottom in an angle of approximately  $23^\circ$  and inducing shear stress on the surface. (C) Micrograph of the FIDT.

The device can in principle be attached to an arbitrary culture chamber. Its design offers a possibility to perform experiments under flow without changing the culture procedures or environments as compared to the static case. In the sample setup shown in Figure 10.2B the SAW-micropump is mounted on top of a Lab-Tek™ II 8-well chamber slide through an aluminum frame. Instead of a standard, straight IDT, a circular arc focusing IDT (FIDT) is employed. (For technical details see Experimental Section 11.7.1.) The steady body force and hence the streaming velocity scales quadratically with the amplitude of the sound waves [237]. As a consequence, focusing the acoustic energy results in a non-linear increase of the energy stored in the fluid motion. Singh *et al.* [238] analyze the effect of focusing on the streaming efficiency numerically and report significant advantages of focusing over standard, linear IDTs. Several groups used the advantages of focusing transducer devices for microfluidic applications before [239-242]. Unpublished data from experiments in the Group of Prof. Dr. A. Wixforth indicate that the integrated kinetic energy of the streaming profile can be several orders of magnitude larger

for optimized FIDTs than for standard IDTs at similar experimental conditions. This aspect is subject to ongoing work.

SAW-driven microfluidic pumps are usually designed as (horizontal) planar structures that require either a sample observation through the piezoelectric substrate or a coupling of the acoustic power into the sample chamber. This means a loss of either optical quality or energetic efficiency. The L-shape structure of this setup allows for the application of standard cell imaging slides while directly coupling the sound waves into the fluid medium. Additionally, the angle of incidence of the generated fluid jet in this design is equal to the Rayleigh angle of about 23° and thus favors the desired generation of shear force in the x-y plane without the need for a confinement of the flow profile. Moreover, the piezoelectric substrate has no direct connection to the bottom of the cell chamber and can transfer heat to the outer metal frame. This reduces the heat input into the sample chamber. Measuring the bulk temperature during experiments with living cells (systems at 37 °C) over 1 h showed no significant heating due to dissipation at the applied input power of  $P_{SAW} \approx 19$  dBm.

### 10.2.2 Characterization of the flow pattern

The characterization of the SAW-induced velocity field was done by particle image velocimetry (PIV). For improving the resolution while being able to capture the whole chamber the method is performed using a scanning approach (SPIV) that is described in the Experimental Section 11.7.2. This characterization procedure is necessary for each combination of IDT-parameters and chamber geometry, since both will change the flow profile. For the present purposes, the near bottom shear rate

$$S = \frac{d|\vec{v}|}{dz} \approx \frac{|\vec{v}|}{10\mu m} \quad (\text{Equation 10.3})$$

is the most interesting value. Figure 10.3 illustrates the bottom flow conditions at an effective input power of  $P_{SAW} \approx 19$  dBm.

Within the jet region, the whole range of physiological relevant shear rates, i.e., from 100 s<sup>-1</sup> up to 3000 s<sup>-1</sup> is covered. By observing cells within different areas of interest, several shear rates can be monitored in the same experiment. The peripheral regions exhibit only very little motion and can serve as reference for near-zero shear, although they still experience some medium exchange. It should be mentioned that even though the main streamline of the FIDT points towards the chamber bottom, some streaming in upper direction is generated, too. This represents an advantageous side effect, since both streams meet in the central region of the

chamber and generate streamline folding (see also Figure 10.2B), leading to an efficient mixing of the medium, as reported earlier [243].

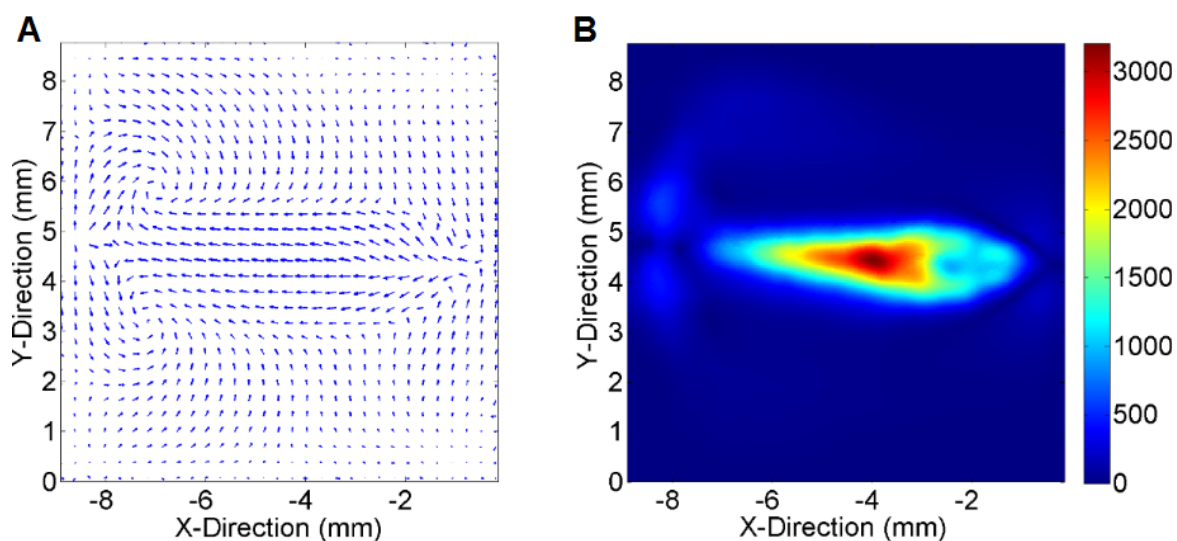


**Figure 10.3 Characterization of the flow pattern.** (A) The velocity profile at a distance of  $z = 10 \mu\text{m}$  from the chamber bottom. The vector length scales with the normalized logarithmic velocity. (B) The color code indicates the respective bottom shear rate in  $\text{s}^{-1}$ .

### 10.2.3 Nanoparticle uptake under flow

In order to show the relevance of physiological shear conditions for the uptake of NPs in cells and to prove the applicability of this system, the uptake of platinum-decorated ceria NPs (Pt-Ceria-46-atto; Chapter 8) by HMEC-1 cells was studied. The cells were incubated with cell medium containing the NPs ( $100 \mu\text{g mL}^{-1}$ ) and imaged live under flow conditions characterized as described above. The amount of NPs taken up by the cells was then analyzed by Particle\_in\_Cell-3D (see Chapter 4) at different incubation times. Figure 10.4 compares the results for two different regions of interest (ROIs) with shear rates of  $100 \text{ s}^{-1}$  and  $2000 \text{ s}^{-1}$ .

For both ROIs the uptake develops approximately linearly in time, but a clear difference in the uptake efficiency at different shear rates can be seen. At a moderate shear rate ( $100 \text{ s}^{-1}$ ), after 75 min the uptake is about seven times higher than at a high (physiological) shear rate of  $2000 \text{ s}^{-1}$ . Sedimentation and long range diffusion should not be relevant here, since under both shear conditions the flow provides continuous medium exchange. Hence, the observed effects are mainly related to the uptake process itself and its dependence on flow strength and NP-cell contact time.



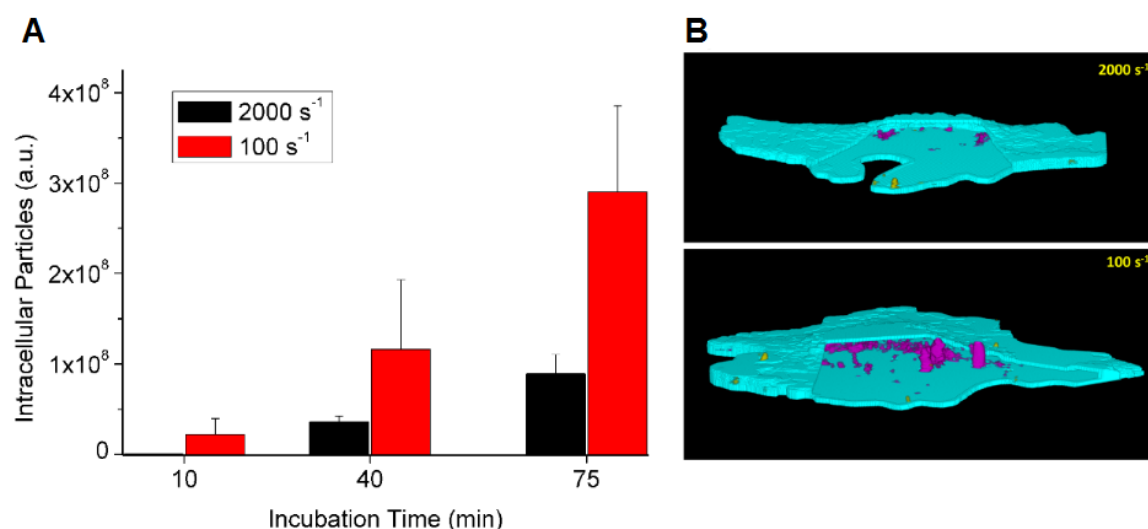


**Figure 10.4 Nanoparticle uptake under flow.** (A) Total fluorescence of internalized NPs ( $d = 50$  nm) at different shear rates. (B) Two representative cells, analyzed with Particle\_in\_Cell-3D. Internalized NPs appear in magenta, membrane-associated NPs in yellow. The histograms show the mean  $\pm$  standard error of five individual cells per time point and shear rate condition ( $n = 5$ ).

### 10.3 Conclusions

In summary, it was shown that fluidic conditions can be of vital importance for cellular uptake processes. This aspect is especially important when examining endothelial cells and/or the uptake of NPs where sedimentation could be an issue. In addition, a setup for SAW-induced pumping that can be used for mimicking physiological flow conditions in cell experiments was introduced. This microfluidic system has several advantages over state-of-the-art solutions, for instance, shear rates over the whole physiological range and applicability with arbitrary standard culture slides. Scanning particle imaging velocimetry was shown to be suitable for generating near bottom shear rate maps that can easily be correlated to biological results.

The experimental data on the uptake behavior of HMEC-1 cells reveal the NP uptake under physiological high shear conditions is much lower than at low shear rates. This underlines the high importance of fluidic conditions for cellular NP uptake and demonstrates that disregarding these aspects can lead to misinterpretation of experimental data.

## 11 Experimental methods

### 11.1 Methods used in Chapter 4

#### 'Image analysis method 'Particle\_in\_Cell-3D''

##### 11.1.1 Synthesis and preparation of nanoparticles

*Synthesis of fluorescent mesoporous silica nanoparticles (MSNs):* PEGylated MSNs of 50–80 nm in size were synthesized as described elsewhere [244]. MSNs were functionalized at their periphery with aminopropyl- and PEG-groups through co-condensation, followed by grafting the cyanine dye Cy3 N-hydroxysuccinimide (NHS) ester. The dye labeling was carried out with an ethanolic suspension of the particles having a concentration of  $1 \text{ mg mL}^{-1}$  by adding  $14.2 \text{ }\mu\text{L}$  of dye Cy3 NHS ester solution ( $2 \text{ mg mL}^{-1}$  in dimethylformamide). The reaction solution was stirred for 1 h at room temperature in the dark, then the Cy3-labeled MSNs (MSN-Cy3) were collected by centrifugation ( $14,000 \times g$  for 5 min), washed three-times with ethanol and finally redispersed in water to a final concentration of  $0.5 \text{ mg mL}^{-1}$ .

*Preparation of fluorescent polystyrene nanoparticles for STED & confocal microscopy:* Precision cover slips (LH24.1; Carl Roth GmbH, Germany) were cleaned with ethanol.  $50 \text{ }\mu\text{L}$  of poly-L-lysine 0.1 % solution (Sigma-Aldrich, Germany) was applied onto each cover slip. After 5 min the solution was removed with a pipette and the cover slip left to dry in air. Commercially available fluorescent polystyrene beads with a diameter of 100 nm (Red Fluospheres® 100 nm; Life Technologies, Germany) were diluted 1:1,000 in ethanol and sonicated for 10 min.  $5 \text{ }\mu\text{L}$  of this solution was then applied to the lysine-treated cover slips. After evaporation samples were mounted with  $7 \text{ }\mu\text{L}$  of 2,2'-thiodiethanol (Sigma-Aldrich, Germany) diluted to 97 % in phosphate buffered saline (PBS), put on an objective slide and sealed with clear nail varnish. Samples were imaged as described in Section 11.1.5.

##### 11.1.2 Cell culture

HeLa cells were grown in Gibco® Dulbecco's modified Eagle's medium (DMEM; Life Technologies, Germany) supplemented with 10 % fetal bovine serum (FBS; Life Technologies, Germany) at  $37 \text{ }^\circ\text{C}$  in a humidified atmosphere containing 5 %  $\text{CO}_2$ .

### 11.1.3 Incubation of cells with nanoparticles

For live-cell imaging experiments, cells were seeded 24 or 48 h before imaging on collagen A (Biochrom GmbH, Germany) in Lab-Tek™ II 8-well chamber slides (Thermo Fisher Scientific Inc., Germany) in a density of  $2.0 \times 10^4$  or  $1.0 \times 10^4$  cells  $\text{cm}^{-2}$ , respectively. HeLa cells were incubated with the MSN-Cy3 at a final concentration of 120–180  $\mu\text{g mL}^{-1}$ . The particle solution was prepared in  $\text{CO}_2$ -independent medium (Life Technologies, Germany) supplemented with 10 % FBS. Before addition to cells, the solution was vortexed for 10 s, treated in an ultrasonic bath for 10 min, and vortexed again for 10 s. Prior to live-cell imaging the membrane of the cells was stained with CellMask™ Deep Red (Life Technologies, Germany) by replacing the particle-containing cell medium by the staining solution. The latter was prepared by adding 0.2  $\mu\text{L}$  of CellMask™ into 400  $\mu\text{L}$  of cell medium. After 1–2 min of incubation, the staining solution was replaced by fresh and warm  $\text{CO}_2$ -independent medium with 10 % FBS.

### 11.1.4 Live-cell imaging

*Quenching experiments:* The quenching experiments were carried out on a custom-built wide-field microscope based on the Nikon Eclipse Ti microscope, as described before [79]. Samples were maintained at 37°C during imaging and were illuminated through a Nikon Plan APO TIRF 60 $\times$ /1.45 oil immersion objective with 532 nm laser light with an exposure time of 300 ms, exciting Cy3. The fluorescence was separated from the excitation light and image sequences were captured with an electron multiplier charge-coupled device camera (iXon+; Andor Technology, UK). Cy3 fluorescence was quenched by adding 10  $\mu\text{L}$  of a 0.4 % trypan blue solution into 400  $\mu\text{L}$  medium in the observed chamber during image acquisition and gently mixed. As trypan blue is a cell membrane-impermeable dye, it is not able to quench particles that have been taken up by the cells. By comparing images prior to and after quenching, the percentage of internalized particles is accessible. Quenching experiments were performed to validate Particle\_in\_Cell-3D performance in segmenting the cell and in measuring the fraction of internalized particles (see Sections 4.3.1 and 4.3.2, respectively).

*Spinning disk imaging for uptake experiments:* Uptake experiments with MSN-Cy3 were performed on a spinning disk confocal fluorescence microscope based on Nikon Eclipse TE 2000-E equipped with a Nikon Apo TIRF 100 $\times$ /1.49 oil immersion objective. Samples were maintained at 37°C during imaging and were illuminated with laser light alternating between 488 and 633 nm, exciting Cy3 and CellMask™ Deep Red, respectively. Image sequences were captured with an electron multiplier charge-coupled device camera (iXon DV887ECCS-BV; Andor Technology, UK). Before being captured by the camera, the emission signal was split by a dichroic

mirror at 592 nm. The bandpass detection filters used were 525/50 nm (Cy3 channel) and 730/140 nm (CellMask™ Deep Red channel). Exposure times were set to 300 ms. Z-stacks of single cells were imaged with an interslice distance of 166 nm, following the Nyquist criterion [92].

### **11.1.5 Super-resolution imaging of 100 nm nanoparticles**

To evaluate the absolute quantification algorithm of Particle\_in\_Cell-3D, samples were imaged with a custom-built STED microscope (as published by Osseforth *et al.* [120]) in confocal and super-resolution mode. The microscope can be operated in two modes, namely standard confocal and STED mode. In the confocal mode, only the excitation beam is active, while the depletion beam is inactivated by means of a mechanical shutter. Imaging in this mode yields diffraction-limited optical resolution. In STED mode, the excitation and STED beams are both focused onto the sample, rendering a resolution well below its confocal counterpart (~40 nm in imaging plane XY as opposed to 250 nm in confocal mode). In confocal mode, stacks were recorded with an area of 30 × 30 μm, a pixel-size of 100 nm and an interslice distance of 220 nm using an excitation intensity <1 μW. After recording the confocal stack, the focus was set to the position of the confocal image yielding the maximum signal. Next, the STED beam was turned on (STED beam intensity ~1 mW) and another image of the exact same area was recorded with a pixel size of 20 nm. Pixel dwell time was typically 280 μs in both modes. The time to switch from confocal to STED imaging mode was a couple of seconds (limited mainly by refocusing to the plane of interest).

## **11.2 Methods used in Chapter 5**

### **‘Cell type-dependent uptake kinetics and cytotoxicity of silica nanoparticles’**

#### **11.2.1 Synthesis and characterization of silica nanoparticles**

*Synthesis:* Silica (SiO<sub>2</sub>) nanoparticles were synthesized as described in the literature by Blechinger *et al.* [132] and by Herrmann *et al.* [133].

*Transmission electron microscopy (TEM):* TEM micrographs were obtained with a JEM 2100 F (JEOL, Japan) instrument. Silica NP dispersions were diluted with ethanol or methanol and applied onto carbon-coated copper grids (Plano, Formvar coal-film on a 200 mesh net). Particle

sizes were determined from TEM images by digital image analysis using the ImageJ software [107].

*Particle size distribution and zeta potential determinations:* Dynamic light scattering (DLS) measurements were employed to determine the hydrodynamic diameter of the nanoparticles. Investigations on the electrophoretic mobility of the silica NPs were carried out to determine the zeta potential. Both studies were conducted with a Zetasizer Nano equipment (Malvern Instruments, UK). Zeta potential measurements were performed on colloidal NP suspensions in CO<sub>2</sub>-independent medium supplemented with 10 % FBS (see Section 11.2.2). For DLS measurements, NPs were dispersed in either cell medium or ultrapure water. In order to break down agglomerates, the resulting solutions were vortexed for 10 s, treated with ultrasound for 10 min, and vortexed again for 10 s. To study the agglomeration dynamics of the particles under the same experimental condition applied for uptake experiments, NP dispersions in cell medium were incubated for specific time points at 37 °C in a 5 % CO<sub>2</sub> humidified atmosphere in culture slides without cells.

*Quantitative image analysis:* The fluorescence intensity distribution of single NPs was determined by confocal imaging with subsequent image analysis. For this purpose, we measured stacks of confocal images of NPs mounted on a cover slip and analyzed them applying the subroutine 'Calibration' of Particle\_in\_Cell-3D, described in Section 4.2.3.4. To mount the silica NPs on a cover slip we used SecureSeal Imaging Spacers (Grace Bio-Labs, USA). Thin chambers of 120 µm were assembled and poly-L-lysine 0.1 % solution (50 µL) (Sigma-Aldrich, Germany) was applied to each of them. After 5 min, the solution was removed with a pipette and the cover slip was left to dry. A silica NP solution in ethanol (80 µg mL<sup>-1</sup>) was prepared and sonicated for 10 min. This solution (5 µL) was applied onto the chambered and treated cover slips. After solvent evaporation, samples were mounted with cell culture medium and sealed on a microscope slide by using the adhesive surface of the spacers.

### **11.2.2 Cell culture**

HeLa cells were grown as described in Section 11.1.2. HUVEC cells were isolated using collagenase and were grown in Endothelial Cell Growth Medium (PromoCell, Germany) supplemented with 10 % fetal bovine serum (FBS), 5 U mL<sup>-1</sup> heparin (Biochrom, Germany), 1 % penicillin and streptomycin, and 1 % growth supplement derived from bovine retina. Cells were maintained with 5 % CO<sub>2</sub> at 37 °C and cultivated maximally up to the third passage.

### 11.2.3 Incubation of cells with silica nanoparticles

*Uptake kinetics:* For the live-cell imaging experiments,  $1.0 \times 10^4$  or  $2.0 \times 10^4$  (HeLa) and  $0.5 \times 10^4$  or  $1.0 \times 10^4$  (HUVEC) cells were seeded 48 h or 24 h before imaging on ibiTreat 8-well  $\mu$ -Slide chamber systems (Ibidi, Germany), reaching 70–85 % confluency at the time of experiment. Before imaging, HeLa cells were transferred to CO<sub>2</sub>-independent medium (Life Technologies, Germany) supplemented with 10 % FBS. The cells were incubated with the NPs at 37 °C at a concentration corresponding to the second highest concentration used for the assessment of cytotoxicity, namely  $3.0 \times 10^4$  NPs per cell. Before addition to cells, the solution was vortexed for 10 s, treated in an ultrasonic bath for 10 min, and vortexed again for 10 s. After the incubation, and just before measurements, the cell membrane was stained with CellMask™ Deep Red (Life Technologies, Germany). The staining solution was prepared by adding 0.2  $\mu$ L of CellMask™ into 400  $\mu$ L of the respective cell medium for HeLa or HUVEC cells. After 1–2 min of incubation, the staining solution was replaced by fresh and warm medium. Restaining was performed during the experiment when necessary.

*Cytotoxicity studies:* For assessment of their viability, HUVEC and HeLa cells were grown in gelatin-coated 96-well plates (Becton Dickinson, France) for 24 h. For nanoparticle treatment,  $1.5 \times 10^4$  cells were seeded into every well of the 96-well plates in triplicate. Cells were stimulated with the described particle suspensions in a dose of  $1.0 \times 10^3$ ,  $1.5 \times 10^4$ ,  $3.0 \times 10^4$ , and  $6.0 \times 10^4$  NPs per cell in 100  $\mu$ L of the corresponding medium without additives for 24 h. Cells incubated with ultrapure water and untreated cells served as controls.

### 11.2.4 Atomic force microscopy

For atomic force microscopy (AFM), cells were fixed with 2 % formaldehyde in phosphate buffered saline (PBS) after incubation with NPs. Experiments were performed without any preparation or manipulation of the sample, as described before [134]. AFM (The NanoWizard, JPK Instruments, Germany) analysis was performed by contact mode in PBS. The applied force in contact mode was 0.5 nN with a scan rate of 1 Hz. The spring constant of the cantilever (MLCT-AUHW cantilevers; Veeco Metrology Group, USA) was  $0.01 \text{ N m}^{-1}$ .

### 11.2.5 Live-cell imaging

Spinning disk confocal microscopy was performed on a setup based on the Zeiss Cell Observer SD equipped with a Zeiss Plan Achromat 63 $\times$ /1.40 Oil/DIC objective. Samples were maintained in a 5 % CO<sub>2</sub> atmosphere at 37°C during imaging and were illuminated with laser light alternating

between 488 nm and 639 nm, exciting perylenediimide and CellMask™ Deep Red, respectively. The emission signal was split by a dichroic mirror at 560 nm. The bandpass detection filters used were 525/50 nm (perylenediimide channel) and 690/50 nm (CellMask™ Deep Red channel). Exposure times were set to 100 ms. Z-stacks of single cells were imaged with an interslice distance of 190 nm, following the Nyquist criterion [92]. Separate images for each fluorescence channel were acquired using two separate electron multiplier charge-coupled device cameras (Evolve 512; Photometrics, USA). To reduce the bright autofluorescence in HUVEC and HeLa cells, each cell was treated with intense 488 nm laser light prior to imaging. However, it was insured that the bleaching did not affect cellular viability for the time of the experiment.

### 11.2.6 Cytotoxicity studies

*Determination of mitochondrial activity (MTT assay):* After exposure to the silica NPs, 100 µL of the medium was removed and mitochondrial activity of the cells was measured by the 3-(4,5-dimethylthiazol-2-yl)-2,5-diphenyltetrazolium bromide (MTT) reduction assay [245]. Cytotoxicity was calculated from the absorbances at 570 nm and expressed as relative values compared with untreated negative controls. For measurements of the intracellular ATP concentrations, cells were examined according to the manufacturer's instructions (Promega, Germany).

*Determination of cell membrane damage (LDH assay):* Membrane damage was quantified by the cellular level of lactate dehydrogenase (LDH) in the removed supernatant using LDH assay kit (Roche, Germany) [246]. The absorbance of the supernatants was measured at 490 nm by using Synergy 2 multi-mode microplate Reader (BioTek, USA) and results are presented as relative values compared to control.

*Flow cytometric analysis of cell damage:* Flow cytometric analysis of DNA content was performed using propidium iodide staining. After exposure to  $3.0 \times 10^4$  and  $6.0 \times 10^4$  NPs per cell for 24 h, HUVEC and HeLa cells were harvested with accutase (PAA, Austria), washed with PBS and permeabilized with 70 % ethanol for 1 h at 4 °C. The cells were then centrifuged, washed with PBS and resuspended in propidium iodide ( $50 \mu\text{g mL}^{-1}$ ) for 5 min. Cells were analyzed using FACS SLR11 and Diva Software. The percentage of dead cells was quantified with WinMDI software.

### 11.2.7 Statistical analysis

For statistical analysis, the unpaired Student's t-test was used. Values were expressed as the mean  $\pm$  standard error or standard deviation. Results were considered as statistically different at  $p < 0.05$  and highly statistically different at  $p < 0.01$ .

## 11.3 Methods used in Chapter 6

### 'Effects of the physicochemical properties on the cytotoxicity of sunscreen titania nanoparticles'

#### 11.3.1 Extraction of titania nanoparticles from sunscreens

To extract the titania (TiO<sub>2</sub>) nanoparticles, the corresponding sun protection agent (10.0 g) was stirred vigorously with isopropanol (100 mL; Merck KGaA, Germany) during 2 h, sonicated for 10 min, and stirred again for 6 h. After filtering (G4 glass filter), the solid was dispersed again in isopropanol (100 mL), stirred, sonicated, and filtered. The treatment was repeated once again using 50 mL of isopropanol. In order to remove water-soluble ingredients and zinc oxide, 5 mL of 6 % HCl (v/v; Merck KGaA, Germany) was added to the residue (200 mg), the mixture was dispersed by sonication and left standing for 16 h. After centrifugation (4,300 × g, 10 min), the pellet was washed with water (5 mL) and dried at 110 °C for 3 h. The total yield of nanoparticles was 210 mg (LADIVAL®), 590 mg (BABYSMILE®), and 1,550 mg (BABYLOVE®).

#### 11.3.2 Characterization of titania nanoparticles

*Fourier transform infrared (FT-IR) measurements:* To elucidate the coating composition and the presence and composition of the secondary shell on the titania NPs, FT-IR measurements were done with a Bruker Equinox 55 spectrometer in the range 400–4,000 cm<sup>-1</sup>, using the attenuated total reflectance technique which does not require sample preparation (32 scans).

*Transmission electron microscopy (TEM):* TEM micrographs were obtained with a JEM 2100 F (JEOL, Japan) instrument. To determine the nanoparticle size and shape, dispersions of the titania NPs in ethanol were applied onto carbon-coated copper grids (Plano, Formvar coal-film on a 200 mesh net).

*Particle size distribution and zeta potential determinations:* Dynamic light scattering (DLS) measurements were employed to determine the hydrodynamic diameter of the titania NPs. Investigations on the electrophoretic mobility of the nanoparticles were carried out to determine the zeta potential. Both studies were conducted with a Zetasizer Nano equipment (Malvern Instruments, UK). Measurements were performed on colloidal NP suspensions in either Millipore water or cell culture medium (see Section 11.3.3). The concentration of titania NPs in all samples was 100 µg mL<sup>-1</sup>.



*Determination of the specific surface area (SSA):* The SSA accessible to N<sub>2</sub> molecules was obtained by Brunauer–Emmett–Teller (BET) measurements according to Brunauer *et al.* [157]. The measurements were conducted with a Quantachrome Nova 2000 system (Quantachrome GmbH & Co., Germany).

*Agglomeration and sedimentation studies:* The agglomeration state and sedimentation behavior of the titania NPs were investigated by light microscopy especially prepared to mimic the exposure of cells to nanoparticles. The selected time points (3, 24, 48, and 72 h) for these studies correspond to those applied for metabolic activity determination, and therefore they show the local concentration and agglomeration state of NPs which approached the cells. Imaging was performed on a spinning disk confocal microscope based on Nikon Eclipse TE2000-E equipped with a Nikon Apo TIRF 100×/1.49 oil immersion objective. The differential interference contrast (DIC) mode was employed. In brief, 400 µL of titania colloidal suspensions (100 µg mL<sup>-1</sup>) were added to Lab-tek™ II 8-well chamber slides (Thermo Fisher Scientific Inc., Germany), and the bottom of the well was imaged at 3, 24, 48, and 72 h thereafter.

### **11.3.3 Cell culture**

HMEC-1 cells (Centers for Disease Control and Prevention, USA) were grown in Gibco® MCDB 131 medium supplemented with 10 % fetal bovine serum (FBS), 1 % GlutaMAX™-I (100X), 10 ng mL<sup>-1</sup> human epidermal growth factor (all purchased from Life Technologies, Germany), and 1 µg mL<sup>-1</sup> hydrocortisone (Sigma-Aldrich, Germany). Cells were maintained at 37 °C in a humidified atmosphere containing 5 % CO<sub>2</sub>. For experimentation, cells were seeded at a density of 1.2 × 10<sup>4</sup> cells cm<sup>-2</sup>, allowed to attach for 24 h, and incubated with the titania NPs as described below.

### **11.3.4 Cytotoxicity studies**

*Determination of relative cellular dehydrogenase activity:* To determine the relative cellular dehydrogenase activity, HMEC-1 cells were treated with titania NPs at different concentrations (10 fg mL<sup>-1</sup>, 100 fg mL<sup>-1</sup>, 100 pg mL<sup>-1</sup>, 100 ng mL<sup>-1</sup>, and 100 µg mL<sup>-1</sup>). After defined incubation times (3, 24, 48, and 72 h), the cells were washed with Hank's balanced salt solution (Hank's BSS), and incubated with 20 µL per well of CellTiter 96® Aqueous One Solution Reagent (Promega GmbH, Germany) in culture medium. Then, the absorbance of the supernatants containing the bio-reduced formazan was measured at 492 nm using a microplate reader (Sunrise™; Tecan Group Ltd., Switzerland). Data were presented as relative values normalized to untreated control cell populations. On the basis of these results, we determined the lowest-observable-adverse-

effect level ( $100 \mu\text{g mL}^{-1}$ ) and used this concentration for the further *in vitro* experiments. For data interpretation the cytotoxic threshold given by DIN EN ISO 10993-5:2009-10 was used.

*Determination of relative cellular ATP level:* To assess the relative cellular ATP content, HMEC-1 cells were exposed to culture medium containing  $100 \mu\text{g mL}^{-1}$  of titania NPs. After an incubation time of 3, 24, 48, or 72 h, the cells were washed with Hank's BSS and the CellTiter-Glo® Luminescent Cell Viability Assay (Promega GmbH, Germany) was performed according to manufacturer's instructions. The relative ATP content of the cells was calculated from the measured luminescence (LUMIStar Galaxy; BMG LABTECH GmbH, Germany) and expressed as relative values compared to untreated control cells. To interpret the impact of the nanoparticles on endothelial cells, the threshold for cytotoxicity according to DIN EN ISO 10993-5:2009-10 was considered.

*Assessment of MCP-1 release as marker for pro-inflammatory response:* To determine the pro-inflammatory impact of the nanoparticles, HMEC-1 cells were exposed to cell medium containing the titania NPs ( $100 \mu\text{g mL}^{-1}$ ). To control the ability of HMEC-1 to produce MCP-1 after a known stimulus, the cells were incubated with interleukin-1b (IL-1b,  $2,000 \text{ pg mL}^{-1}$ ; Sigma-Aldrich, Germany) as positive control. The nanoparticles and the IL-1b were diluted in Gibco® MCDB 131 medium supplemented with 0.2 % FBS. After 24, 48, and 72 h of incubation, the cell culture supernatants were collected. The MCP-1 content in the supernatant was determined using a commercial Human MCP-1 ELISA Kit (RayBiotech, USA) according to manufacturer's instructions. In brief, 2.5 h after adding various MCP-1 standard dilutions and samples into appropriate wells of an anti-human MCP-1 coated microplate, the wells were washed and biotinylated antibody was added. After 1 h of incubation and washing steps, incubation of 45 min with horseradish peroxidase-conjugated streptavidin followed. After another washing step and an incubation of 30 min with 3,3',5,5'-tetramethylbenzidine (TMB), sulfuric acid was added as stop solution and the absorbance was measured at 450 nm using a microplate reader (Sunrise™; Tecan Group Ltd., Switzerland).

### 11.3.5 Statistical analysis

The statistical analysis was carried out using IBM SPSS Statistics, version 19.0 (©2010 SPSS Statistics 19 Inc, an IBM Company, USA). Results are given as means  $\pm$  standard deviation and considered as statistically different at  $p \leq 0.05$ . Data were analyzed using ANOVA. The post hoc Bonferroni test was employed to determine differences between different treatment groups.

## 11.4 Methods used in Chapter 7

### 'Particle size-dependent uptake of ceria nanoparticles'

#### 11.4.1 Synthesis and characterization of ceria nanoparticles

*Synthesis:* Ceria (CeO<sub>2</sub>) nanoparticles were synthesized as described by Herrmann *et al.* [133].

*Transmission electron microscopy (TEM):* TEM micrographs were obtained with a JEM 2100 F (JEOL, Japan) instrument. Ceria NP dispersions were diluted with ethanol or methanol and applied onto carbon-coated copper grids (Plano, Formvar coal-film on a 200 mesh net). Particle sizes were determined from TEM images by digital image analysis using the ImageJ software [107].

*Particle size distribution and zeta potential determinations:* Dynamic light scattering (DLS) measurements were employed to determine the hydrodynamic diameter of the ceria NPs. Investigations on the electrophoretic mobility of the NPs were carried out to determine the zeta potential. Both studies were conducted with a Zetasizer Nano equipment (Malvern Instruments, UK). Zeta potential profiles and hydrodynamic diameter were measured in ultrapure water and in cell medium (see Section 11.4.2). In order to break down agglomerates, the resulting solution was vortexed for 10 s, treated in an ultrasonic bath for 10 min, and vortexed again for 10 s before measurements.

#### 11.4.2 Cell culture

HMEC-1 cells (Centers for Disease Control and Prevention, USA) were grown in Gibco® MCDB 131 medium supplemented with 10 % fetal bovine serum (FBS), 1 % GlutaMAX™-I (100X), 10 ng mL<sup>-1</sup> human epidermal growth factor (all purchased from Life Technologies, Germany), and 1 µg mL<sup>-1</sup> hydrocortisone (Sigma-Aldrich, Germany). Cells were maintained at 37 °C in a humidified atmosphere containing 5 % CO<sub>2</sub>.

#### 11.4.3 Incubation of cells with ceria nanoparticles

For live-cell imaging experiments, cells were seeded 24 h before imaging in Lab-Tek™ II 8-well chamber slides (Thermo Fisher Scientific Inc., Germany) in a density of  $1.1 \times 10^4$  cells cm<sup>-2</sup>. HMEC-1 cells were incubated with ceria NPs at 37 °C in a humidified atmosphere containing 5 % CO<sub>2</sub>. The 10 µg mL<sup>-1</sup> solution of ceria NPs was prepared in the same cell medium used for cell growth. Before addition to cells, the solution was vortexed for 10 s, treated in an ultrasonic bath

for 10 min, and vortexed again for 10 s. After the incubation time, and just before measurements, the cell membrane was stained with a solution of  $10 \mu\text{g mL}^{-1}$  wheat germ agglutinin Alexa Fluor® 488 conjugate (WGA 488; Life Technologies, Germany) in cell medium. After 1 min of incubation, the staining solution was removed and cells were washed twice with warm cell medium. Fresh and warm cell medium was then replaced.

#### **11.4.4 Live-cell imaging**

Spinning disk confocal microscopy was performed on a setup based on the Zeiss Cell Observer SD equipped with a Zeiss Plan Aplanachromat 63×/1.40 Oil/DIC objective. Samples were maintained in a 5 % CO<sub>2</sub> atmosphere at 37°C during imaging and were illuminated with laser light alternating between 488 nm and 639 nm, exciting WGA 488 and Atto 647N (labeling the ceria NPs), respectively. The emission signal was split by a dichroic mirror at 560 nm. The bandpass detection filters used were 525/50 nm (WGA 488 channel) and 690/50 nm (Atto 647N channel). Exposure times were set to 100 ms. Z-stacks of single cells were imaged with an interslice distance of 250 nm, following the Nyquist criterion [92]. Separate images for each fluorescence channel were acquired using two separate electron multiplier charge-coupled device cameras (Evolve 512; Photometrics, USA).

#### **11.4.5 Statistical analysis**

For statistical analysis, the unpaired Student's t-test was used. Values were expressed as the mean  $\pm$  standard error. Results were considered as statistically different at  $p < 0.05$  and highly statistically different at  $p < 0.01$ .

### **11.5 Methods used in Chapter 8**

#### **'Cell membrane penetration and mitochondrial targeting by platinum-decorated ceria nanoparticles'**

##### **11.5.1 Synthesis and characterization of platinum-decorated ceria nanoparticles**

*Synthesis:* Platinum-decorated ceria nanoparticles (Pt-ceria NPs) were synthesized as described by Herrmann *et al.* [133].

*Transmission electron microscopy (TEM) and energy-dispersive X-ray (EDX) spectroscopy:* TEM and EDX images were obtained with a JEM 2100 F (JEOL, Japan) instrument. Pt-ceria particle

dispersions were diluted with ethanol and applied onto carbon-coated copper grids (Plano, Formvar coal-film on a 200 mesh net). Particle sizes were determined from TEM images by digital image analysis using the ImageJ software [107].

*Particle size distribution and zeta potential determinations:* Dynamic light scattering (DLS) measurements were employed to determine the hydrodynamic diameter of the ceria and Pt-ceria NPs. Investigations on the electrophoretic mobility of the nanoparticles were carried out to determine the zeta potential. Both studies were conducted with a Zetasizer Nano equipment (Malvern Instruments, UK) on colloidal NP suspensions in ethanol.

### **11.5.2 Cell culture**

HMEC-1 cells were grown as described in Section 11.4.2.

### **11.5.3 Incubation of cells with platinum-decorated ceria nanoparticles**

*Uptake experiments:* For live-cell imaging experiments, cells were seeded 24 h before imaging in Lab-Tek™ II 8-well chamber slides (Thermo Fisher Scientific Inc., Germany) in a density of  $1.1 \times 10^4$  cells  $\text{cm}^{-2}$ . HMEC-1 cells were incubated with NPs at 37 °C in a humidified atmosphere containing 5 %  $\text{CO}_2$ .

*Redispersion of nanoparticles in cell medium:* Solutions of ceria NPs and Pt-ceria NPs were prepared in the same cell medium used for cell growth according to the following procedure: first, the stock solution of NPs (in ethanol) was vortexed for 10 s, treated in an ultrasonic bath for 10 min, and vortexed again for 10 s; next, a small aliquot (up to a few  $\mu\text{L}$ ) of the ethanolic suspension of NPs was added to a microcentrifuge tube (1.5–2 mL; Eppendorf, Germany); ethanol was then left to evaporate completely under a laminar flow or under a gentle stream of  $\text{N}_2$ ; after complete evaporation of ethanol, the tube with the dried NPs was closed and reserved for up to 6 hours; shortly before addition to cells, a given volume of cell medium (so as to reach the desired NP concentration) was added to the dried NPs in the tube; finally, particles were immediately dispersed in the medium by sonication, warmed up to 37 °C, and added to cells.

*Uptake kinetics, intracellular fate, and mitochondrial targeting:* The cell membrane was stained with wheat germ agglutinin Alexa Fluor® 488 conjugate (WGA 488, 10  $\mu\text{g mL}^{-1}$  in cell medium for 1 min) or with CellMask™ Orange (0.05 % (v/v) in cell medium for 1–2 min). The mitochondria were stained with MitoTracker Green® FM (100 nM in cell medium for 15–30 min) or with Mitotracker Red® CMXRos (60 nM in cell medium for 10 min). Cellular lysosomes were stained with LysoTracker® Red (150 nM in cell medium for 30 min; all organelle-specific stains were

purchased from Life Technologies, Germany). In all cases, after the indicated incubation times, the respective staining solution was removed and cells were washed twice with warm cell medium. Cell medium containing the NPs was then added to cells. Cells were imaged live as described in Section 11.5.4.

*Inhibitor studies:* To investigate if clathrin-mediated endocytosis was involved in the fast uptake behavior of Pt-ceria NPs, inhibition studies with chlorpromazine (Sigma-Aldrich, Germany) were conducted. To ensure a complete inhibition of the clathrin-dependent uptake pathway, HMEC-1 cells were incubated with  $15 \mu\text{g mL}^{-1}$  chlorpromazine for 30 min prior to addition of further substrates. To probe the clathrin-mediated endocytosis, inhibited cells were co-incubated with transferrin ( $20 \mu\text{g mL}^{-1}$ ) or Pt-ceria NPs ( $100 \mu\text{g mL}^{-1}$ ) for 20 min. To visualize the uptake, the cell membrane was stained with CellMask™ Orange (as described above, but in cell medium containing  $15 \mu\text{g mL}^{-1}$  chlorpromazine). Live-cell imaging was performed in the presence of the inhibitor, except for the uptake of transferrin in the absence of chlorpromazine, as shown in Figure 8.10A.

*Cell membrane integrity:* For calcein leakage in (or penetration) assay, HMEC-1 cells were co-incubated with cell medium containing  $0.1 \text{ mg mL}^{-1}$  calcein (Life Technologies, Germany) and  $100 \mu\text{g mL}^{-1}$  of Pt-ceria NPs for 3 h. After the incubation time, the cell membrane was stained with CellMask™ Orange (see above) and cells were washed and imaged as described in Section 11.5.4. For calcein leakage out (or release) assay, HMEC-1 cells were preincubated with  $5 \mu\text{M}$  calcein-AM (Life Technologies, Germany) for 45 min. Calcein-loaded cells were then washed with cell medium and incubated with  $100 \mu\text{g mL}^{-1}$  of Pt-ceria NPs for 0.5 and 3 h. After the respective incubation periods, cells were washed again and imaged live.

*Colocalization studies:* Manders' overlap coefficient were determined by using the ImageJ plugin JACoP developed by Bolte & Cordelieres [104].

*Cytotoxicity studies:* For cytotoxicity evaluation (Section 11.5.5),  $1.2 \times 10^4$  HMEC-1 cells  $\text{cm}^{-2}$  were seeded in 96-well cell culture plates. 24 h after seeding, cells were exposed to either ceria NPs or Pt-ceria NPs dispersed in cell medium (as described above) at  $37^\circ\text{C}$  in a humidified atmosphere containing 5 %  $\text{CO}_2$ .

#### **11.5.4 Live-cell imaging**

Spinning disk confocal microscopy was performed on a setup based on the Zeiss Cell Observer SD equipped with a Zeiss Plan Apochromat 63 $\times$ /1.40 Oil/DIC objective. Samples were maintained at  $37^\circ\text{C}$  in a 5 %  $\text{CO}_2$  atmosphere during imaging and were illuminated with laser light alternating

between 488 nm (exciting WGA 488, MitoTracker Green<sup>®</sup>, perylenediimide, or calcein), 561 nm (exciting CellMask<sup>™</sup> Orange, MitoTracker Red<sup>®</sup>, or LysoTracker<sup>®</sup> Red), and 639 nm (exciting Atto 647N). The emission signal was split by a dichroic mirror at 560 nm (for dual-color detection upon excitation with 488 or 639 nm light) or at 660 nm (for three-color detection upon excitation with 488, 561 or 639 nm light). Separate images for each fluorescence channel were acquired using two separate electron multiplier charge-coupled device cameras (Evolve 512; Photometrics, USA). The bandpass detection filters of the first camera, installed in an automatic revolving filter wheel, were 525/50 nm (WGA 488/ MitoTracker Green<sup>®</sup>/ perylenediimide/ calcein channel) and 629/62 (CellMask<sup>™</sup> Orange/ MitoTracker Red<sup>®</sup>/ LysoTracker<sup>®</sup> Red channel). The bandpass filter used for the second camera was 690/50 nm (Atto 647N channel). Exposure times were set to 100–500 ms. Z-stacks of single cells were imaged with an interslice distance of 250 nm, following the Nyquist criterion [92].

#### **11.5.5 Cytotoxicity studies**

To assess the relative cellular ATP content, cells were seeded (see Section 11.3.3) and the culture medium was replaced with a fresh one containing either 10  $\mu\text{g mL}^{-1}$  or 100  $\mu\text{g mL}^{-1}$  of NPs. After defined incubation times (3, 24, 48, and 72 h), the cells were washed with Hank's balanced salt solution (Hank's BSS), and incubated with 20  $\mu\text{L}$  per well of CellTiter 96<sup>®</sup> Aqueous One Solution Reagent (Promega GmbH, Germany) in culture medium. The relative ATP content of the cells was calculated from the measured luminescence (LUMIStar Galaxy; BMG LABTECH GmbH, Germany) and expressed as relative values compared to untreated control cells. To interpret the impact of the ceria NPs as well as Pt-ceria NPs on endothelial cells, the threshold for cytotoxicity according to DIN EN ISO 10993-5:2009-10 was considered.

#### **11.5.6 Statistical analysis**

For statistical analysis, the unpaired Student's t-test was used. Values were expressed as the mean  $\pm$  standard error. Results were considered as statistically different at  $p < 0.05$  and highly statistically different at  $p < 0.01$ .

## 11.6 Methods used in Chapter 9

### 'Endosomal escape and successful cytosolic drug release of dendronized mesoporous silica nanoparticles'

#### 11.6.1 Synthesis and characterization of dendronized MSNs

*Synthesis:* Dendronized mesoporous silica nanoparticles (MSN-Dn, n = 0–3) were prepared as described before by Cauda *et al.* [210] and by Argyo [211].

*Transmission electron microscopy (TEM):* TEM micrographs were obtained with a Titan 80–300 kV microscope. Samples were prepared by dispersing MSNs (1 mg) in 4 mL absolute ethanol and drying a drop of the resulting diluted suspension on a carbon-coated copper grid.

*Particle size distribution and zeta potential determinations:* Dynamic light scattering (DLS) measurements were employed to determine the hydrodynamic diameter of the MSNs. Investigations on the electrophoretic mobility of the nanoparticles were carried out to determine the zeta potential. Both studies were conducted with a Zetasizer Nano equipment (Malvern Instruments, UK). DLS measurements were directly recorded on aqueous colloidal suspension at a concentration of 1 mg mL<sup>-1</sup> for all sample solutions. For determination of the zeta potential profiles, one to three drop of the ethanolic suspension (~3 %) was mixed with 1 mL of commercial Hydrion Buffer solution of the appropriate pH prior to measurement.

*Nitrogen sorption:* The SSA accessible to N<sub>2</sub> molecules was obtained by Brunauer–Emmett–Teller (BET) measurements according to Brunauer *et al.* [157]. The measurements were conducted with a Quantachrome Nova 4000e system (Quantachrome GmbH & Co., Germany) at -196 °C. Pore size and pore volume were calculated using a non-local density functional theory (NLDFT) equilibrium model of N<sub>2</sub> on silica, based on the desorption branch of the isotherm.

*Titration:* Acid-base titrations were performed on a Metrohm 905 Titrand potentiometric titrator combined with the software tiamo. The samples were prepared as follows: a volume containing 13.7 mg particles from the suspensions was added to 30.0 mL H<sub>2</sub>O. The starting pH was set to 3.000 using HCl (0.1 M) and NaOH (0.01 M) from the dosing unit. The samples were titrated against NaOH (0.01 M).

*Solid state NMR:* Nuclear magnetic resonance (NMR) spectra were recorded on a Jeol Eclipse 270 (<sup>1</sup>H: 270 MHz, <sup>13</sup>C: 67.9 MHz), a Jeol Eclipse 400 (<sup>1</sup>H: 400 MHz, <sup>13</sup>C: 101 MHz) NMR, or a Jeol Eclipse 500 spectrometer (<sup>1</sup>H: 500.16 MHz, <sup>13</sup>C: 125.77 MHz; JEOL, Japan). <sup>13</sup>C solid-state NMR



measurements were performed on a Bruker DSX Avance500 FT spectrometer (Bruker, USA) in a 4 mm ZrO<sub>2</sub> rotor.

*Redox-driven cargo release:* Fluorescence spectra were recorded on a PTI spectrofluorometer (PTI, USA) equipped with a xenon short arc lamp (UXL-75XE USHIO) and a photomultiplier detection system (model 810/814). The measurements were performed in aqueous solution at 37 °C to simulate human body temperature. For time-based release experiments of MTS-ROX, a custom made container consisting of a Teflon tube, a dialysis membrane (Visking type 8/32 with a molecular weight cut-off of 14,000 g mol<sup>-1</sup>; Carl Roth GmbH, Germany) and a fluorescence cuvette were used. The excitation wavelength was set to  $\lambda = 575$  nm for MTS-ROX-loaded MSNs. Emission scans (585–650 nm) were performed every 2 min. All slits were adjusted to 1.0 mm (bandwidth 8 nm).

*Quantitative image analysis:* In order to reach an absolute quantification of nanoparticle uptake, calibration experiments were carried out with MSN-D3 deposited on a cover slip and covered with cell medium. Particles were imaged immediately by spinning disk confocal microscopy (63× objective; as described in Section 11.6.4) with an interslice distance of 250 nm, following the Nyquist criterion [92]. The acquired images were evaluated with the subroutine 'Calibration' of Particle\_in\_Cell-3D (see Section 4.2.3.4), and the mean intensity value showed a Gaussian distribution with the mean at 64,632 pixel intensities per MSN-D3.

## 11.6.2 Cell culture

HeLa and HMEC-1 cells were grown as described in Sections 11.1.2 and 11.4.2, respectively. KB cells were cultured in folic acid deficient Gibco® RPMI 1640 medium (Life Technologies, Germany) supplemented with 10 % fetal bovine serum (FBS; Life Technologies, Germany) at 37 °C in a humidified atmosphere containing 5 % CO<sub>2</sub>.

## 11.6.3 Incubation of cells with MSNs

### Uptake kinetics and cytotoxicity studies

*Uptake kinetics:* For evaluation of nanoparticle uptake kinetics,  $1.2 \times 10^4$  HMEC-1 cells cm<sup>-2</sup> were seeded in Lab-Tek™ II 8-well chamber slide (Thermo Fisher Scientific Inc., Germany). 24 h after seeding, cells were exposed to cell medium containing 100 µg mL<sup>-1</sup> of MSN-D3 for 3, 24 and 48 h. Subsequently, cells were washed twice with PBS and the cell membrane was stained with a solution of 10 µg mL<sup>-1</sup> wheat germ agglutinin Alexa Fluor® 488 conjugate (WGA 488; Life Technologies, Germany) in cell medium. After 1 min of incubation, the staining solution was

removed and cells were washed twice with warm cell medium. Fresh and warm cell medium was then replaced, and cells were imaged immediately by spinning disk confocal microscopy (63× objective; as described in Section 11.6.4) with an interslice distance of 250 nm, following the Nyquist criterion [92].

*Cytotoxicity studies:* For cytotoxicity evaluation (Section 11.6.5),  $1.2 \times 10^4$  HMEC-1 cells  $\text{cm}^{-2}$  were seeded in 96-well cell culture plates. 24 h after seeding, cells were exposed to cell medium containing MSN-D3 in different concentrations ( $10 \text{ fg mL}^{-1}$  to  $100 \text{ } \mu\text{g mL}^{-1}$ ) for 3 to 72 h.

#### **Cargo release, nuclei staining kinetics with DAPI, and cell targeting experiments**

For live-cell imaging experiments on cargo release, nuclei staining kinetics with DAPI, and cell targeting experiments, KB and HeLa cells were seeded 24 or 48 h before imaging in a density of  $2.0 \times 10^4$  or  $1.0 \times 10^4$  cells  $\text{cm}^{-2}$ , respectively. HeLa cells were seeded on collagen A (Biochrom GmbH, Germany) in Lab-Tek™ II 8-well chamber slides (Thermo Fisher Scientific Inc., Germany), while KB cells were seeded on ibiTreat 8-well  $\mu$ -Slide chamber systems (Ibidi, Germany).

*Cargo release:* For the *in vitro* cargo release experiments, cells were incubated with MSNs for 5–48 h prior to the measurements at 37 °C in a humidified atmosphere containing 5 %  $\text{CO}_2$ . Shortly before imaging, the medium was replaced by  $\text{CO}_2$ -independent medium (Life Technologies, Germany). During the measurements all cells were kept on a heated microscope stage at 37 °C. The subsequent imaging was performed as described in Section 11.6.4.

*Nuclei staining kinetics with DAPI:* HeLa cells were measured 5, 11, 24, 33, 49, and 61 h after incubation with the samples MSN-D3\_MTS-DAPI, MSN-DO\_MTS-DAPI and the supernatant of MSN-D3\_MTS-DAPI (after particle separation). Each time point was measured with an independently incubated monolayer of cells. In order to evaluate the fluorescence of nuclei staining with DAPI, the Z-stack position was set in the region of the cell nuclei. The mean pixel intensity of distinct regions of interest (ROI) corresponding to the nuclei was determined (44–104 nuclei for each data point). The averaged mean intensity per nuclei area  $\pm$  standard deviation was then plotted with respect to the incubation time.

*Cell targeting:* To evaluate the functionality of the folic acid (FA) ligand, KB cells were incubated with MSNs for 5 h at 37 °C in a humidified atmosphere containing 5 %  $\text{CO}_2$ . The cell membrane was stained shortly before the measurement with a solution of  $10 \text{ } \mu\text{g mL}^{-1}$  wheat germ agglutinin Alexa Fluor® 488 conjugate (WGA 488; Life Technologies, Germany) in cell medium. After 1 min, the cell medium was removed and cells were washed twice with warm cell medium. Fresh and warm cell medium was added and cells were imaged immediately by spinning disk confocal microscopy (as described in Section 11.6.4). In control experiments, before particles addition, the

FA receptors on the KB cells surface were blocked by preincubation with 3 mM folic acid (Sigma-Aldrich, Germany) for 2 h at 37 °C in a humidified atmosphere containing 5 % CO<sub>2</sub>.

#### **11.6.4 Live-cell imaging**

Spinning disk confocal microscopy was performed on a setup based on the Zeiss Cell Observer SD equipped with a Zeiss Plan Apochromat objective (63×/1.40 Oil/DIC or 100×/1.40 Oil/DIC). For all experiments the exposure time was 100 ms and Z-stacks were recorded. Samples were maintained at 37°C during imaging and were illuminated with laser light alternating either between 405 nm and 639 nm (exciting DAPI and Atto 633, respectively) or between 488 nm and 639 nm (exciting WGA 488 and Atto 633, respectively). In both cases the emission signal was split by a dichroic mirror at 560 nm, and the bandpass detection filters used were 525/50 nm (DAPI/WGA 488 channel) and 690/50 nm (Atto 633 channel). Separate images for each fluorescence channel were acquired using two separate electron multiplier charge-coupled device cameras (Evolve 512; Photometrics, USA).

#### **11.6.5 Cytotoxicity studies**

The cytotoxic impact of the MSN-D3 was determined by measuring the relative cellular dehydrogenase activity of HMEC-1 cells upon particle exposure. After the defined incubation times, the cells were washed with Hank's BSS and incubated with 20 µL per well of CellTiter 96<sup>®</sup> Aqueous One Solution Reagent (Promega GmbH, Germany) in culture medium. The absorbance of the supernatants was measured at 492 nm via a microplate reader (Sunrise™; Tecan Group Ltd., Switzerland) and the relative cellular dehydrogenase activity of endothelial cells was calculated by normalizing the values to untreated control cells. For data interpretation the cytotoxic threshold given by DIN EN ISO 10993-5:2009-10 was used.

### **11.7 Methods used in Chapter 10**

#### **'A surface acoustic wave-driven microfluidic system for nanoparticle uptake investigation under physiological flow conditions'**

##### **11.7.1 Microfluidic chip**

The general design of the setup is described in Section 10.2.1. The FIDT structure is circular focused with a focus distance of 750 µm from the electrode and an opening angle of 40°. The chip consists of 20 fingers with an interdigital distance of 15 µm. The structure is fabricated by

thermal evaporation of 50 nm gold on a LiNbO<sub>3</sub> substrate (128°-Y-cut). For the sake of chemical and electrical isolation, the whole chip was covered with a 200 nm thick silicon oxide layer by thermal evaporation of SiO. The micropump was driven by an input power of  $P_{SAW} \approx 19$  dBm at its resonance frequency of 126 MHz.

### 11.7.2 Flow characterization

The SAW-induced flow pattern was characterized by scanning particle imaging velocimetry (SPIV). The flow was made visible by 3  $\mu\text{m}$  polystyrene beads and the chamber was scanned in several x-y layers with position distances according to the field of view of the optical setup. With this approach, the whole chamber volume could be imaged with sufficiently high magnification (and respective numerical aperture) to achieve a z-resolution that was adequate for a reliable analysis of the near bottom shear rates. The layer-to-layer distance for recording the shear rate map presented in Figure 10.3 is  $\Delta z = 25$   $\mu\text{m}$ , with the first layer at a height  $z = 10$   $\mu\text{m}$  above the bottom. At each position, 50 frames at a rate of 3,000 fps were captured. A MATLAB script based on the open source PIVlab toolkit [247-249] was applied to extract the three-dimensional velocity profile in following steps: single videos were analyzed in a batch process by using PIVlab to determine the local velocity profiles; next, the results at single positions were stitched and missing data points were recovered by linear interpolation, ending up with layered x-y velocity profiles for the whole region of interest. If desired, z-velocities  $v_z$  can be extracted from the divergence  $\nabla(v_x, v_y)$  of the local field with appropriate boundary conditions.

### 11.7.3 Uptake experiments

HMEC-1 cells were cultured and seeded as described in Sections 11.4.2 and 11.5.3, respectively. Before starting the measurement, the cell membrane was stained with WGA 488 (see Section 11.5.3) and the culture medium was exchanged by medium containing Pt-Ceria-46-atto (see Chapter 8) with a concentration of 100  $\mu\text{g mL}^{-1}$ . Cells and NPs were then imaged with a spinning disk fluorescence microscope (see Section 11.5.4). Five randomly chosen cells were analyzed at every region of interest (ROI). Finally, the amount of internalized Pt-ceria NPs was determined for different incubation times employing the Particle\_in\_Cell-3D method, as detailed in Chapter 4.

## Bibliography

1. *Project on Emerging Nanotechnologies. Consumer Products Inventory*. Retrieved: June 11, 2015 from <http://www.nanotechproject.org/cpi>.
2. *German Federal Institute for Risk Assessment (BfR). Press Release 06/2015: How can the safety of nanomaterials be ensured?* Retrieved: June 11, 2015 from [http://www.bfr.bund.de/en/press information/2015/06/how can the safety of nanomaterials be ensured -193478.html](http://www.bfr.bund.de/en/press_information/2015/06/how_can_the_safety_of_nanomaterials_be_ensured_-193478.html).
3. Zellner, R., Biological responses to nanoscale particles. *Beilstein Journal of Nanotechnology*, 2015. **6**: p.380-382.
4. Zellner, R., Blechinger, J., Bräuchle, C., Hilger, I., Janshoff, A., Lademann, J., Mailänder, V., Meinke, M.C., Nienhaus, G.U., Patzelt, A., Rancan, F., Rothen-Rutishauser, B., Stauber, R.H., Torrano, A.A., Treuel, L., and Vogt, A., *Biological Responses to Nanoparticles*, in *Safety Aspects of Engineered Nanomaterials*, W. Luther and A. Zweck, Editors. 2013, Pan Stanford Publishing. p.157-218.
5. Torrano, A.A., Blechinger, J., Osseforth, C., Argyo, C., Reller, A., Bein, T., Michaelis, J., and Bräuchle, C., A fast analysis method to quantify nanoparticle uptake on a single cell level. *Nanomedicine (Lond)*, 2013. **8**(11): p.1815-28.
6. *ImageJ Documentation Wiki: Particle\_in\_Cell-3D*. Retrieved: June 11, 2015 from [http://imagejdocu.tudor.lu/doku.php?id=macro:particle\\_in\\_cell-3d](http://imagejdocu.tudor.lu/doku.php?id=macro:particle_in_cell-3d).
7. Blechinger, J., Bauer, A.T., Torrano, A.A., Gorzelanny, C., Bräuchle, C., and Schneider, S.W., Uptake kinetics and nanotoxicity of silica nanoparticles are cell type dependent. *Small*, 2013. **9**(23): p.3970-80, 3906.
8. Strobel, C., Torrano, A.A., Herrmann, R., Malissek, M., Bräuchle, C., Reller, A., Treuel, L., and Hilger, I., Effects of the physicochemical properties of titanium dioxide nanoparticles, commonly used as sun protection agents, on microvascular endothelial cells. *Journal of Nanoparticle Research*, 2014. **16**: p.2130.
9. Torrano, A.A. and Bräuchle, C., Precise quantification of silica and ceria nanoparticle uptake revealed by 3D fluorescence microscopy. *Beilstein Journal of Nanotechnology*, 2014. **5**: p.1616-24.
10. Weiss, V., Argyo, C., Torrano, A.A., Strobel, C., Mackowiak, S.A., Gatzemaier, T., Hilger, I., Bräuchle, C., and Bein, T., Dendronized mesoporous silica nanoparticles provide an internal endosomal escape mechanism for a successful cytosolic drug release. *Submitted*.
11. Strobl, F.G., Breyer, D., Link, P., Torrano, A.A., Bräuchle, C., Schneider, M.F., and Wixforth, A., A surface acoustic wave-driven micropump for particle uptake investigation under physiological flow conditions in very small volumes. *Beilstein Journal of Nanotechnology*, 2015. **6**: p.414-9.
12. Nel, A., Xia, T., Mädler, L., and Li, N., Toxic Potential of Materials at the Nanolevel. *Science*, 2006. **311**(5761): p.622-627.
13. Nel, A.E., Mädler, L., Velegol, D., Xia, T., Hoek, E.M.V., Somasundaran, P., Klaessig, F., Castranova, V., and Thompson, M., Understanding biophysicochemical interactions at the nano-bio interface. *Nature Materials*, 2009. **8**(7): p.543-557.
14. Oberdörster, G., Safety assessment for nanotechnology and nanomedicine: concepts of nanotoxicology. *Journal of Internal Medicine*, 2010. **267**(1): p.89-105.
15. Riehemann, K., Schneider, S.W., Luger, T.A., Godin, B., Ferrari, M., and Fuchs, H., Nanomedicine--challenge and perspectives. *Angewandte Chemie International Edition*, 2009. **48**(5): p.872-97.

16. Argyo, C., Weiss, V., Bräuchle, C., and Bein, T., Multifunctional Mesoporous Silica Nanoparticles as a Universal Platform for Drug Delivery. *Chemistry of Materials*, 2014. **26**(1): p.435-451.
17. Ferrari, M., Nanogeometry: beyond drug delivery. *Nature Nanotechnology*, 2008. **3**(3): p.131-2.
18. McNeil, S.E., Nanoparticle therapeutics: a personal perspective. *Wiley Interdisciplinary Reviews: Nanomedicine and Nanobiotechnology*, 2009. **1**(3): p.264-71.
19. Wiedemann, P., Schutz, H., Spangenberg, A., and Krug, H.F., Evidence maps: communicating risk assessments in societal controversies: the case of engineered nanoparticles. *Risk Analysis*, 2011. **31**(11): p.1770-83.
20. Krug, H.F. and Wick, P., Nanotoxicology: an interdisciplinary challenge. *Angewandte Chemie International Edition*, 2011. **50**(6): p.1260-78.
21. Stern, S.T. and McNeil, S.E., Nanotechnology safety concerns revisited. *Toxicological Sciences*, 2008. **101**(1): p.4-21.
22. Carmeliet, P., Angiogenesis in health and disease. *Nature Medicine*, 2003. **9**(6): p.653-60.
23. Gehr, P., Bachofen, M., and Weibel, E.R., The normal human lung: ultrastructure and morphometric estimation of diffusion capacity. *Respiration Physiology*, 1978. **32**(2): p.121-40.
24. Nicod, L.P., Lung defences: an overview. *European Respiratory Review*, 2005. **14**(95): p.45-50.
25. Brain, J.D., Lung macrophages: how many kinds are there? What do they do? *American Review of Respiratory Disease*, 1988. **137**(3): p.507-9.
26. McWilliam, A.S., Nelson, D.J., and Holt, P.G., The biology of airway dendritic cells. *Immunology and Cell Biology*, 1995. **73**(5): p.405-13.
27. Schürch, S., Gehr, P., Im Hof, V., Geiser, M., and Green, F., Surfactant displaces particles toward the epithelium in airways and alveoli. *Respiration Physiology*, 1990. **80**(1): p.17-32.
28. de Haar, C., Hassing, I., Bol, M., Bleumink, R., and Pieters, R., Ultrafine but not fine particulate matter causes airway inflammation and allergic airway sensitization to co-administered antigen in mice. *Clinical and Experimental Allergy*, 2006. **36**(11): p.1469-79.
29. Mühlfeld, C., Geiser, M., Kapp, N., Gehr, P., and Rothen-Rutishauser, B., Re-evaluation of pulmonary titanium dioxide nanoparticle distribution using the "relative deposition index": Evidence for clearance through microvasculature. *Particle and Fibre Toxicology*, 2007. **4**: p.7.
30. Semmler-Behnke, M., Takenaka, S., Fertsch, S., Wenk, A., Seitz, J., Mayer, P., Oberdörster, G., and Kreyling, W.G., Efficient elimination of inhaled nanoparticles from the alveolar region: evidence for interstitial uptake and subsequent reentrainment onto airways epithelium. *Environmental Health Perspectives*, 2007. **115**(5): p.728-33.
31. Nemmar, A., Hoet, P.H., Vanquickenborne, B., Dinsdale, D., Thomeer, M., Hoylaerts, M.F., Vanbilloen, H., Mortelmans, L., and Nemery, B., Passage of inhaled particles into the blood circulation in humans. *Circulation*, 2002. **105**(4): p.411-4.
32. Kreyling, W.G., Hirn, S., and Schleh, C., Nanoparticles in the lung. *Nature Biotechnology*, 2010. **28**(12): p.1275-6.
33. Choi, H.S., Ashitate, Y., Lee, J.H., Kim, S.H., Matsui, A., Insin, N., Bawendi, M.G., Semmler-Behnke, M., Frangioni, J.V., and Tsuda, A., Rapid translocation of nanoparticles from the lung airspaces to the body. *Nature Biotechnology*, 2010. **28**(12): p.1300-3.
34. Geiser, M. and Kreyling, W.G., Deposition and biokinetics of inhaled nanoparticles. *Particle and Fibre Toxicology*, 2010. **7**: p.2.
35. Semmler-Behnke, M., Kreyling, W.G., Lipka, J., Fertsch, S., Wenk, A., Takenaka, S., Schmid, G., and Brandau, W., Biodistribution of 1.4- and 18-nm gold particles in rats. *Small*, 2008. **4**(12): p.2108-11.
36. Brown, J.S., Zeman, K.L., and Bennett, W.D., Ultrafine particle deposition and clearance in the healthy and obstructed lung. *American Journal of Respiratory and Critical Care Medicine*, 2002. **166**(9): p.1240-7.

37. Patzelt, A., Richter, H., Knorr, F., Schäfer, U., Lehr, C.M., Dahne, L., Sterry, W., and Lademann, J., Selective follicular targeting by modification of the particle sizes. *Journal of Controlled Release*, 2011. **150**(1): p.45-8.
38. Lademann, J., Richter, H., Teichmann, A., Otberg, N., Blume-Peytavi, U., Luengo, J., Weiss, B., Schaefer, U.F., Lehr, C.M., Wepf, R., and Sterry, W., Nanoparticles--an efficient carrier for drug delivery into the hair follicles. *European Journal of Pharmaceutics and Biopharmaceutics*, 2007. **66**(2): p.159-64.
39. Lademann, J., Knorr, F., Richter, H., Blume-Peytavi, U., Vogt, A., Antoniou, C., Sterry, W., and Patzelt, A., Hair follicles--an efficient storage and penetration pathway for topically applied substances. Summary of recent results obtained at the Center of Experimental and Applied Cutaneous Physiology, Charite -Universitätsmedizin Berlin, Germany. *Skin Pharmacology and Physiology*, 2008. **21**(3): p.150-5.
40. Lademann, J., Otberg, N., Richter, H., Weigmann, H.J., Lindemann, U., Schaefer, H., and Sterry, W., Investigation of follicular penetration of topically applied substances. *Skin Pharmacology and Applied Skin Physiology*, 2001. **14 Suppl 1**: p.17-22.
41. Buzea, C., Pacheco, I., and Robbie, K., Nanomaterials and nanoparticles: Sources and toxicity. *Biointerphases*, 2007. **2**(4): p.MR17-MR71.
42. Oberdörster, G., Oberdörster, E., and Oberdörster, J., Nanotoxicology: an emerging discipline evolving from studies of ultrafine particles. *Environmental Health Perspectives*, 2005. **113**(7): p.823-39.
43. Vogt, A., Combadiere, B., Hadam, S., Stieler, K.M., Lademann, J., Schaefer, H., Autran, B., Sterry, W., and Blume-Peytavi, U., 40 nm, but not 750 or 1,500 nm, nanoparticles enter epidermal CD1a+ cells after transcutaneous application on human skin. *Journal of Investigative Dermatology*, 2006. **126**(6): p.1316-22.
44. Mahe, B., Vogt, A., Liard, C., Duffy, D., Abadie, V., Bonduelle, O., Boissonnas, A., Sterry, W., Verrier, B., Blume-Peytavi, U., and Combadiere, B., Nanoparticle-based targeting of vaccine compounds to skin antigen-presenting cells by hair follicles and their transport in mice. *Journal of Investigative Dermatology*, 2009. **129**(5): p.1156-64.
45. Helander, H.F. and Fandriks, L., Surface area of the digestive tract - revisited. *Scandinavian Journal of Gastroenterology*, 2014. **49**(6): p.681-9.
46. Sinnecker, H., Krause, T., Koelling, S., Lautenschläger, I., and Frey, A., The gut wall provides an effective barrier against nanoparticle uptake. *Beilstein Journal of Nanotechnology*, 2014. **5**: p.2092-2101.
47. Hoet, P.H., Bruske-Hohlfeld, I., and Salata, O.V., Nanoparticles - known and unknown health risks. *Journal of Nanobiotechnology*, 2004. **2**(1): p.12.
48. Jani, P., Halbert, G.W., Langridge, J., and Florence, A.T., Nanoparticle uptake by the rat gastrointestinal mucosa: quantitation and particle size dependency. *Journal of Pharmacy and Pharmacology*, 1990. **42**(12): p.821-6.
49. Sinnecker, H., Ramaker, K., and Frey, A., Coating with luminal gut-constituents alters adherence of nanoparticles to intestinal epithelial cells. *Beilstein Journal of Nanotechnology*, 2014. **5**: p.2308-2315.
50. Klein, J., Probing the interactions of proteins and nanoparticles. *Proceedings of the National Academy of Sciences*, 2007. **104**(7): p.2029-30.
51. Monopoli, M.P., Aberg, C., Salvati, A., and Dawson, K.A., Biomolecular coronas provide the biological identity of nanosized materials. *Nature Nanotechnology*, 2012. **7**(12): p.779-786.
52. Röcker, C., Pötzl, M., Zhang, F., Parak, W.J., and Nienhaus, G.U., A quantitative fluorescence study of protein monolayer formation on colloidal nanoparticles. *Nature Nanotechnology*, 2009. **4**(9): p.577-80.
53. Jeong, S.K., Kwon, M.S., Lee, E.Y., Lee, H.J., Cho, S.Y., Kim, H., Yoo, J.S., Omenn, G.S., Aebersold, R., Hanash, S., and Paik, Y.K., BiomarkerDigger: a versatile disease proteome

- database and analysis platform for the identification of plasma cancer biomarkers. *Proteomics*, 2009. **9**(14): p.3729-40.
54. Tenzer, S., Docter, D., Kuharev, J., Musyanovych, A., Fetz, V., Hecht, R., Schlenk, F., Fischer, D., Kiouptsi, K., Reinhardt, C., Landfester, K., Schild, H., Maskos, M., Knauer, S.K., and Stauber, R.H., Rapid formation of plasma protein corona critically affects nanoparticle pathophysiology. *Nature Nanotechnology*, 2013. **8**(10): p.772-81.
55. des Rieux, A., Fievez, V., Garinot, M., Schneider, Y.J., and Preat, V., Nanoparticles as potential oral delivery systems of proteins and vaccines: a mechanistic approach. *Journal of Controlled Release*, 2006. **116**(1): p.1-27.
56. Spiel, A.O., Gilbert, J.C., and Jilma, B., von Willebrand factor in cardiovascular disease: focus on acute coronary syndromes. *Circulation*, 2008. **117**(11): p.1449-59.
57. Oliveira, O.N., Jr., Langmuir-Blodgett Films - Properties and Possible Applications. *Brazilian Journal of Physics*, 1992. **22**(2): p.60-69.
58. van Meer, G., Voelker, D.R., and Feigenson, G.W., Membrane lipids: where they are and how they behave. *Nature Reviews: Molecular Cell Biology*, 2008. **9**(2): p.112-24.
59. Doherty, G.J. and McMahon, H.T., Mechanisms of endocytosis. *Annual Review of Biochemistry*, 2009. **78**: p.857-902.
60. Jiang, W., Kim, B.Y., Rutka, J.T., and Chan, W.C., Nanoparticle-mediated cellular response is size-dependent. *Nature Nanotechnology*, 2008. **3**(3): p.145-50.
61. Tarantola, M., Schneider, D., Sunnick, E., Adam, H., Pierrat, S., Rosman, C., Breus, V., Sonnichsen, C., Basche, T., Wegener, J., and Janshoff, A., Cytotoxicity of metal and semiconductor nanoparticles indicated by cellular micromotility. *ACS Nano*, 2009. **3**(1): p.213-22.
62. Verma, A. and Stellacci, F., Effect of Surface Properties on Nanoparticle–Cell Interactions. *Small*, 2010. **6**(1): p.12-21.
63. Zhang, S., Li, J., Lykotrafitis, G., Bao, G., and Suresh, S., Size-Dependent Endocytosis of Nanoparticles. *Advanced Materials*, 2009. **21**: p.419-424.
64. Conner, S.D. and Schmid, S.L., Regulated portals of entry into the cell. *Nature*, 2003. **422**(6927): p.37-44.
65. Hillaireau, H. and Couvreur, P., Nanocarriers' entry into the cell: relevance to drug delivery. *Cellular and Molecular Life Sciences*, 2009. **66**(17): p.2873-2896.
66. Luzio, J.P., Pryor, P.R., and Bright, N.A., Lysosomes: fusion and function. *Nature Reviews: Molecular Cell Biology*, 2007. **8**(8): p.622-632.
67. Marsh, M. and McMahon, H.T., The structural era of endocytosis. *Science*, 1999. **285**(5425): p.215-20.
68. Lin, J. and Alexander-Katz, A., Cell Membranes Open "Doors" for Cationic Nanoparticles/Biomolecules: Insights into Uptake Kinetics. *ACS Nano*, 2013. **7**(12): p.10799-10808.
69. Verma, A., Uzun, O., Hu, Y., Hu, Y., Han, H.-S., Watson, N., Chen, S., Irvine, D.J., and Stellacci, F., Surface-structure-regulated cell-membrane penetration by monolayer-protected nanoparticles. *Nature Materials*, 2008. **7**(7): p.588-595.
70. Foged, C. and Nielsen, H.M., Cell-penetrating peptides for drug delivery across membrane barriers. *Expert Opinion on Drug Delivery*, 2008. **5**(1): p.105-117.
71. Wang, T., Bai, J., Jiang, X., and Nienhaus, G.U., Cellular Uptake of Nanoparticles by Membrane Penetration: A Study Combining Confocal Microscopy with FTIR Spectroelectrochemistry. *ACS Nano*, 2012. **6**(2): p.1251-1259.
72. Arvizo, R.R., Miranda, O.R., Thompson, M.A., Pabelick, C.M., Bhattacharya, R., Robertson, J.D., Rotello, V.M., Prakash, Y.S., and Mukherjee, P., Effect of Nanoparticle Surface Charge at the Plasma Membrane and Beyond. *Nano Letters*, 2010. **10**(7): p.2543-2548.



73. Taylor, U., Klein, S., Petersen, S., Kues, W., Barcikowski, S., and Rath, D., Nonendosomal cellular uptake of ligand-free, positively charged gold nanoparticles. *Cytometry Part A*, 2010. **77A**(5): p.439-446.
74. Huang, K., Ma, H., Liu, J., Huo, S., Kumar, A., Wei, T., Zhang, X., Jin, S., Gan, Y., Wang, P.C., He, S., Zhang, X., and Liang, X.-J., Size-Dependent Localization and Penetration of Ultrasmall Gold Nanoparticles in Cancer Cells, Multicellular Spheroids, and Tumors in Vivo. *ACS Nano*, 2012. **6**(5): p.4483-4493.
75. Asharani, P.V., Xinyi, N., Hande, M.P., and Valiyaveetil, S., DNA damage and p53-mediated growth arrest in human cells treated with platinum nanoparticles. *Nanomedicine (Lond)*, 2009. **5**(1): p.51-64.
76. Gehrke, H., Pelka, J., Hartinger, C., Blank, H., Bleimund, F., Schneider, R., Gerthsen, D., Bräse, S., Crone, M., Türk, M., and Marko, D., Platinum nanoparticles and their cellular uptake and DNA platination at non-cytotoxic concentrations. *Archives of Toxicology*, 2011. **85**(7): p.799-812.
77. Ruthardt, N., Lamb, D.C., and Bräuchle, C., Single-particle tracking as a quantitative microscopy-based approach to unravel cell entry mechanisms of viruses and pharmaceutical nanoparticles. *Molecular Therapy*, 2011. **19**(7): p.1199-211.
78. de Bruin, K., Ruthardt, N., von Gersdorff, K., Bausinger, R., Wagner, E., Ogris, M., and Bräuchle, C., Cellular Dynamics of EGF Receptor-Targeted Synthetic Viruses. *Molecular Therapy*, 2007. **15**(7): p.1297-1305.
79. Sauer, A.M., de Bruin, K.G., Ruthardt, N., Mykhaylyk, O., Plank, C., and Bräuchle, C., Dynamics of magnetic lipoplexes studied by single particle tracking in living cells. *Journal of Controlled Release*, 2009. **137**(2): p.136-145.
80. Muller, J., Huaux, F., Moreau, N., Misson, P., Heilier, J.F., Delos, M., Arras, M., Fonseca, A., Nagy, J.B., and Lison, D., Respiratory toxicity of multi-wall carbon nanotubes. *Toxicology and Applied Pharmacology*, 2005. **207**(3): p.221-31.
81. Vinzents, P.S., Møller, P., Sørensen, M., Knudsen, L.E., Hertel, O., Jensen, F.P., Schibye, B., and Loft, S., Personal exposure to ultrafine particles and oxidative DNA damage. *Environmental Health Perspectives*, 2005. **113**(11): p.1485-90.
82. Gonzalez-Flecha, B., Oxidant mechanisms in response to ambient air particles. *Molecular Aspects of Medicine*, 2004. **25**(1-2): p.169-82.
83. Donaldson, K., Tran, L., Jimenez, L.A., Duffin, R., Newby, D.E., Mills, N., MacNee, W., and Stone, V., Combustion-derived nanoparticles: a review of their toxicology following inhalation exposure. *Particle and Fibre Toxicology*, 2005. **2**: p.10.
84. Rahman, I. and MacNee, W., Oxidative stress and regulation of glutathione in lung inflammation. *European Respiratory Journal*, 2000. **16**(3): p.534-54.
85. Brown, D.M., Donaldson, K., Borm, P.J., Schins, R.P., Dehnhardt, M., Gilmour, P., Jimenez, L.A., and Stone, V., Calcium and ROS-mediated activation of transcription factors and TNF-alpha cytokine gene expression in macrophages exposed to ultrafine particles. *American Journal of Physiology: Lung Cellular and Molecular Physiology*, 2004. **286**(2): p.L344-53.
86. Donaldson, K., Duffin, R., Langrish, J.P., Miller, M.R., Mills, N.L., Poland, C.A., Raftis, J., Shah, A., Shaw, C.A., and Newby, D.E., Nanoparticles and the cardiovascular system: a critical review. *Nanomedicine (Lond)*, 2013. **8**(3): p.403-423.
87. Pope, C.A., 3rd, Burnett, R.T., Thun, M.J., Calle, E.E., Krewski, D., Ito, K., and Thurston, G.D., Lung cancer, cardiopulmonary mortality, and long-term exposure to fine particulate air pollution. *The Journal of the American Medical Association*, 2002. **287**(9): p.1132-41.
88. Fröhlich, E., Samberger, C., Kueznik, T., Absenger, M., Roblegg, E., Zimmer, A., and Pieber, T.R., Cytotoxicity of nanoparticles independent from oxidative stress. *Journal of Toxicological Sciences*, 2009. **34**(4): p.363-75.
89. Lichtman, J.W. and Conchello, J.A., Fluorescence microscopy. *Nature Methods*, 2005. **2**(12): p.910-9.

90. Ettinger, A. and Wittmann, T., Fluorescence live cell imaging. *Methods in Cell Biology*, 2014. **123**: p.77-94.
91. Sung, M.H. and McNally, J.G., Live cell imaging and systems biology. *Wiley Interdisciplinary Reviews: Systems Biology and Medicine*, 2011. **3**(2): p.167-82.
92. Pawley, J.B., *Handbook of Biological Confocal Microscopy*. 3rd. ed. 2006: Springer Science & Business Media.
93. Stephens, D.J. and Allan, V.J., Light microscopy techniques for live cell imaging. *Science*, 2003. **300**(5616): p.82-6.
94. Fischer, R.S., Wu, Y., Kanchanawong, P., Shroff, H., and Waterman, C.M., Microscopy in 3D: a biologist's toolbox. *Trends in Cell Biology*, 2011. **21**(12): p.682-91.
95. Stender, A.S., Marchuk, K., Liu, C., Sander, S., Meyer, M.W., Smith, E.A., Neupane, B., Wang, G., Li, J., Cheng, J.-X., Huang, B., and Fang, N., Single Cell Optical Imaging and Spectroscopy. *Chemical Reviews*, 2013. **113**(4): p.2469-2527.
96. Naredi-Rainer, N., Prescher, J., Hartschuh, A., and Lamb, D.C., *Confocal Microscopy*, in *Fluorescence Microscopy*. 2013, Wiley-VCH Verlag GmbH & Co. KGaA. p.175-213.
97. Toomre, D.K., Langhorst, M.F., and Davidson, M. *Introduction to Spinning Disk Microscopy*. *Zeiss. Education in Microscopy and Digital Imaging*. Retrieved: June 11, 2015 from <http://zeiss-campus.magnet.fsu.edu/articles/spinningdisk/introduction.html>.
98. Hell, S.W., Microscopy and its focal switch. *Nature Methods*, 2009. **6**(1): p.24-32.
99. Betzig, E., Patterson, G.H., Sougrat, R., Lindwasser, O.W., Olenych, S., Bonifacino, J.S., Davidson, M.W., Lippincott-Schwartz, J., and Hess, H.F., Imaging Intracellular Fluorescent Proteins at Nanometer Resolution. *Science*, 2006. **313**(5793): p.1642-1645.
100. Rust, M.J., Bates, M., and Zhuang, X., Sub-diffraction-limit imaging by stochastic optical reconstruction microscopy (STORM). *Nature Methods*, 2006. **3**(10): p.793-5.
101. Möckl, L., Lamb, D.C., and Bräuchle, C., Super-resolved fluorescence microscopy: Nobel Prize in Chemistry 2014 for Eric Betzig, Stefan Hell, and William E. Moerner. *Angewandte Chemie International Edition*, 2014. **53**(51): p.13972-7.
102. Eliceiri, K.W., Berthold, M.R., Goldberg, I.G., Ibanez, L., Manjunath, B.S., Martone, M.E., Murphy, R.F., Peng, H., Plant, A.L., Roysam, B., Stuurman, N., Swedlow, J.R., Tomancak, P., and Carpenter, A.E., Biological imaging software tools. *Nature Methods*, 2012. **9**(7): p.697-710.
103. Waters, J.C., Accuracy and precision in quantitative fluorescence microscopy. *The Journal of Cell Biology*, 2009. **185**(7): p.1135-1148.
104. Bolte, S. and Cordelieres, F.P., A guided tour into subcellular colocalization analysis in light microscopy. *Journal of Microscopy*, 2006. **224**(Pt 3): p.213-32.
105. Chen, H., Puhl, H.L., 3rd, Koushik, S.V., Vogel, S.S., and Ikeda, S.R., Measurement of FRET efficiency and ratio of donor to acceptor concentration in living cells. *Biophysical Journal*, 2006. **91**(5): p.L39-41.
106. Sprague, B.L. and McNally, J.G., FRAP analysis of binding: proper and fitting. *Trends in Cell Biology*, 2005. **15**(2): p.84-91.
107. Schindelin, J., Arganda-Carreras, I., Frise, E., Kaynig, V., Longair, M., Pietzsch, T., Preibisch, S., Rueden, C., Saalfeld, S., Schmid, B., Tinevez, J.-Y., White, D.J., Hartenstein, V., Eliceiri, K., Tomancak, P., and Cardona, A., Fiji: an open-source platform for biological-image analysis. *Nature Methods*, 2012. **9**(7): p.676-682.
108. Asati, A., Santra, S., Kaittanis, C., and Perez, J.M., Surface-Charge-Dependent Cell Localization and Cytotoxicity of Cerium Oxide Nanoparticles. *ACS Nano*, 2010. **4**(9): p.5321-5331.
109. Yu, T., Hubbard, D., Ray, A., and Ghandehari, H., In vivo biodistribution and pharmacokinetics of silica nanoparticles as a function of geometry, porosity and surface characteristics. *Journal of Controlled Release*, 2012. **163**(1): p.46-54.

110. Oh, W.-K., Kim, S., Choi, M., Kim, C., Jeong, Y.S., Cho, B.-R., Hahn, J.-S., and Jang, J., Cellular Uptake, Cytotoxicity, and Innate Immune Response of Silica–Titania Hollow Nanoparticles Based on Size and Surface Functionality. *ACS Nano*, 2010. **4**(9): p.5301-5313.
111. Suzuki, H., Toyooka, T., and Ibuki, Y., Simple and Easy Method to Evaluate Uptake Potential of Nanoparticles in Mammalian Cells Using a Flow Cytometric Light Scatter Analysis. *Environmental Science & Technology*, 2007. **41**(8): p.3018-3024.
112. Bräuchle, C., Lamb, D., and Michaelis, J., *Single Particle Tracking and Single Molecule Energy Transfer*. 2009, Weinheim, Germany: Wiley-VCH Verlag GmbH & Co. KGaA.
113. Lu, F., Wu, S.-H., Hung, Y., and Mou, C.-Y., Size Effect on Cell Uptake in Well-Suspended, Uniform Mesoporous Silica Nanoparticles. *Small*, 2009. **5**(12): p.1408-1413.
114. Elsaesser, A., Taylor, A., de Yanes, G.S., McKerr, G., Kim, E.M., O'Hare, E., and Howard, C.V., Quantification of nanoparticle uptake by cells using microscopical and analytical techniques. *Nanomedicine (Lond)*, 2010. **5**(9): p.1447-57.
115. Brandenberger, C., Mühlfeld, C., Ali, Z., Lenz, A.-G., Schmid, O., Parak, W.J., Gehr, P., and Rothen-Rutishauser, B., Quantitative Evaluation of Cellular Uptake and Trafficking of Plain and Polyethylene Glycol-Coated Gold Nanoparticles. *Small*, 2010. **6**(15): p.1669-1678.
116. Mühlfeld, C., Mayhew, T.M., Gehr, P., and Rothen-Rutishauser, B., A novel quantitative method for analyzing the distributions of nanoparticles between different tissue and intracellular compartments. *Journal of Aerosol Medicine*, 2007. **20**(4): p.395-407.
117. Stark, W.J., Nanoparticles in biological systems. *Angewandte Chemie International Edition*, 2011. **50**(6): p.1242-58.
118. Schmid, B., Schindelin, J., Cardona, A., Longair, M., and Heisenberg, M., A high-level 3D visualization API for Java and ImageJ. *BMC Bioinformatics*, 2010. **11**(1): p.274.
119. Cho, E.C., Zhang, Q., and Xia, Y., The effect of sedimentation and diffusion on cellular uptake of gold nanoparticles. *Nature Nanotechnology*, 2011. **6**(6): p.385-391.
120. Osseforth, C., Moffitt, J.R., Schermelleh, L., and Michaelis, J., Simultaneous dual-color 3D STED microscopy. *Optics Express*, 2014. **22**(6): p.7028-39.
121. Nakajima, M., Takeda, M., Kobayashi, M., Suzuki, S., and Ohuchi, N., Nano-sized fluorescent particles as new tracers for sentinel node detection: Experimental model for decision of appropriate size and wavelength. *Cancer Science*, 2005. **96**(6): p.353-356.
122. *OECD: Synthetic amorphous silica and silicates - SIDS Initial Assessment Report for SIAM 19, in OECD SIDS, UNEP Publications; 2004*. Retrieved: June 11, 2015 from <http://www.chem.unep.ch/irptc/sids/oecdsids/Silicates.pdf>.
123. Merget, R., Bauer, T., Küpper, H., Philippou, S., Bauer, H., Breitstadt, R., and Bruening, T., Health hazards due to the inhalation of amorphous silica. *Archives of Toxicology*, 2002. **75**(11-12): p.625-634.
124. Yang, Y.-X., Song, Z.-M., Cheng, B., Xiang, K., Chen, X.-X., Liu, J.-H., Cao, A., Wang, Y., Liu, Y., and Wang, H., Evaluation of the toxicity of food additive silica nanoparticles on gastrointestinal cells. *Journal of Applied Toxicology*, 2014. **34**(4): p.424-435.
125. Mackowiak, S.A., Schmidt, A., Weiss, V., Argyo, C., von Schirnding, C., Bein, T., and Bräuchle, C., Targeted drug delivery in cancer cells with red-light photoactivated mesoporous silica nanoparticles. *Nano Letters*, 2013. **13**(6): p.2576-83.
126. Zhang, F.-F., Wan, Q., Li, C.-X., Wang, X.-L., Zhu, Z.-Q., Xian, Y.-Z., Jin, L.-T., and Yamamoto, K., Simultaneous assay of glucose, lactate, L-glutamate and hypoxanthine levels in a rat striatum using enzyme electrodes based on neutral red-doped silica nanoparticles. *Analytical and Bioanalytical Chemistry*, 2004. **380**(4): p.637-642.
127. Lin, W., Huang, Y.-w., Zhou, X.-D., and Ma, Y., In vitro toxicity of silica nanoparticles in human lung cancer cells. *Toxicology and Applied Pharmacology*, 2006. **217**(3): p.252-259.

128. Napierska, D., Thomassen, L.C.J., Rabolli, V., Lison, D., Gonzalez, L., Kirsch-Volders, M., Martens, J.A., and Hoet, P.H., Size-Dependent Cytotoxicity of Monodisperse Silica Nanoparticles in Human Endothelial Cells. *Small*, 2009. **5**(7): p.846-853.
129. Jin, Y., Kannan, S., Wu, M., and Zhao, J.X., Toxicity of Luminescent Silica Nanoparticles to Living Cells. *Chemical Research in Toxicology*, 2007. **20**(8): p.1126-1133.
130. Park, M.V.D.Z., Annema, W., Salvati, A., Lesniak, A., Elsaesser, A., Barnes, C., McKerr, G., Howard, C.V., Lynch, I., Dawson, K.A., Piersma, A.H., and de Jong, W.H., In vitro developmental toxicity test detects inhibition of stem cell differentiation by silica nanoparticles. *Toxicology and Applied Pharmacology*, 2009. **240**(1): p.108-116.
131. Lison, D. and Huaux, F., In vitro studies: Ups and downs of cellular uptake. *Nature Nanotechnology*, 2011. **6**(6): p.332-333.
132. Blechinger, J., Herrmann, R., Kiener, D., García-García, F.J., Scheu, C., Reller, A., and Bräuchle, C., Perylene-Labeled Silica Nanoparticles: Synthesis and Characterization of Three Novel Silica Nanoparticle Species for Live-Cell Imaging. *Small*, 2010. **6**(21): p.2427-2435.
133. Herrmann, R., Rennhak, M., and Reller, A., Synthesis and characterization of fluorescence-labelled silica core-shell and noble metal-decorated ceria nanoparticles. *Beilstein Journal of Nanotechnology*, 2014. **5**: p.2413-2423.
134. Bauer, A.T., Strozyk, E.A., Gorzelanny, C., Westerhausen, C., Desch, A., Schneider, M.F., and Schneider, S.W., Cytotoxicity of silica nanoparticles through exocytosis of von Willebrand factor and necrotic cell death in primary human endothelial cells. *Biomaterials*, 2011. **32**(33): p.8385-8393.
135. Bajaj, A., Miranda, O.R., Kim, I.-B., Phillips, R.L., Jerry, D.J., Bunz, U.H.F., and Rotello, V.M., Detection and differentiation of normal, cancerous, and metastatic cells using nanoparticle-polymer sensor arrays. *Proceedings of the National Academy of Sciences*, 2009. **106**(27): p.10912-10916.
136. Chang, J.-S., Chang, K.L.B., Hwang, D.-F., and Kong, Z.-L., In Vitro Cytotoxicity of Silica Nanoparticles at High Concentrations Strongly Depends on the Metabolic Activity Type of the Cell Line. *Environmental Science & Technology*, 2007. **41**(6): p.2064-2068.
137. Kim, J.A., Aberg, C., Salvati, A., and Dawson, K.A., Role of cell cycle on the cellular uptake and dilution of nanoparticles in a cell population. *Nature Nanotechnology*, 2012. **7**(1): p.62-68.
138. Yu, T., Malugin, A., and Ghandehari, H., Impact of Silica Nanoparticle Design on Cellular Toxicity and Hemolytic Activity. *ACS Nano*, 2011. **5**(7): p.5717-5728.
139. Jin, Y., Kannan, S., Wu, M., and Zhao, J.X., Toxicity of luminescent silica nanoparticles to living cells. *Chemical Research in Toxicology*, 2007. **20**(8): p.1126-33.
140. Popov, A.P., Lademann, J., Priezzhev, A.V., and Myllyla, R., Effect of size of TiO<sub>2</sub> nanoparticles embedded into stratum corneum on ultraviolet-A and ultraviolet-B sun-blocking properties of the skin. *Journal of Biomedical Optics*, 2005. **10**(6): p.064037 (pp 9).
141. Dunford, R., Salinaro, A., Cai, L., Serpone, N., Horikoshi, S., Hidaka, H., and Knowland, J., Chemical oxidation and DNA damage catalysed by inorganic sunscreen ingredients. *FEBS Letters*, 1997. **418**(1-2): p.87-90.
142. Wolf, R., Wolf, D., Morganti, P., and Ruocco, V., Sunscreens. *Clinics in Dermatology*, 2001. **19**(4): p.452-459.
143. Bolis, V., Busco, C., Ciarletta, M., Distasi, C., Erriquez, J., Fenoglio, I., Livraghi, S., and Morel, S., Hydrophilic/hydrophobic features of TiO<sub>2</sub> nanoparticles as a function of crystal phase, surface area and coating, in relation to their potential toxicity in peripheral nervous system. *Journal of Colloid and Interface Science*, 2012. **369**(1): p.28-39.
144. Rampaul, A., Parkin, I.P., and Cramer, L.P., Damaging and protective properties of inorganic components of sunscreens applied to cultured human skin cells. *Journal of Photochemistry and Photobiology A: Chemistry*, 2007. **191**(2-3): p.138-148.

145. Mo, S.-D. and Ching, W.Y., Electronic and optical properties of three phases of titanium dioxide: Rutile, anatase, and brookite. *Physical Review B*, 1995. **51**(19): p.13023-13032.
146. Prieto-Mahaney, O.-O., Murakami, N., Abe, R., and Ohtani, B., Correlation between Photocatalytic Activities and Structural and Physical Properties of Titanium(IV) Oxide Powders. *Chemistry Letters*, 2009. **38**(3): p.238-239.
147. Braydich-Stolle, L., Schaeublin, N., Murdock, R., Jiang, J., Biswas, P., Schlager, J., and Hussain, S., Crystal structure mediates mode of cell death in TiO<sub>2</sub> nanotoxicity. *Journal of Nanoparticle Research*, 2009. **11**(6): p.1361-1374.
148. Li, S.-Q., Zhu, R.-R., Zhu, H., Xue, M., Sun, X.-Y., Yao, S.-D., and Wang, S.-L., Nanotoxicity of TiO<sub>2</sub> nanoparticles to erythrocyte in vitro. *Food and Chemical Toxicology*, 2008. **46**(12): p.3626-3631.
149. Montiel-Dávalos, A., Ventura-Gallegos, J.L., Alfaro-Moreno, E., Soria-Castro, E., García-Latorre, E., Cabañas-Moreno, J.G., Ramos-Godinez, M.d.P., and López-Marure, R., TiO<sub>2</sub> Nanoparticles Induce Dysfunction and Activation of Human Endothelial Cells. *Chemical Research in Toxicology*, 2012. **25**(4): p.920-930.
150. Peters, K., Unger, R.E., Kirkpatrick, C.J., Gatti, A.M., and Monari, E., Effects of nano-scaled particles on endothelial cell function in vitro: studies on viability, proliferation and inflammation. *Journal of Materials Science: Materials in Medicine*, 2004. **15**(4): p.321-5.
151. Sayes, C.M., Wahi, R., Kurian, P.A., Liu, Y., West, J.L., Ausman, K.D., Warheit, D.B., and Colvin, V.L., Correlating Nanoscale Titania Structure with Toxicity: A Cytotoxicity and Inflammatory Response Study with Human Dermal Fibroblasts and Human Lung Epithelial Cells. *Toxicological Sciences*, 2006. **92**(1): p.174-185.
152. Iavicoli, I., Leso, V., Fontana, L., and Bergamaschi, A., Toxicological effects of titanium dioxide nanoparticles: a review of in vitro mammalian studies. *European Review for Medical and Pharmacological Sciences*, 2011. **15**(5): p.481-508
153. *Merck Performance Materials. Eusolex*. Retrieved: June 11, 2015 from <http://www.merck-performance-materials.com/en/cosmetics/eusolex/eusolex.html>.
154. *UL LCC. Prospector: Eusolex T-ECO*. Retrieved: June 11, 2015 from <http://www.ulprospector.com/en/eu/PersonalCare/Detail/824/34426/Eusolex-T-ECO>.
155. Allouni, Z.E., Cimpan, M.R., Høl, P.J., Skodvin, T., and Gjerdet, N.R., Agglomeration and sedimentation of TiO<sub>2</sub> nanoparticles in cell culture medium. *Colloids and Surfaces B: Biointerfaces*, 2009. **68**(1): p.83-87.
156. Torrado, G., Garcia-Arieta, A., de los Rios, F., Menendez, J.C., and Torrado, S., Quantitative determination of dimethicone in commercial tablets and capsules by Fourier transform infrared spectroscopy and antifoaming activity test. *Journal of Pharmaceutical and Biomedical Analysis*, 1999. **19**(3-4): p.285-92.
157. Brunauer, S., Emmett, P.H., and Teller, E., Adsorption of Gases in Multimolecular Layers. *Journal of the American Chemical Society*, 1938. **60**(2): p.309-319.
158. Ikeda, U., Matsui, K., Murakami, Y., and Shimada, K., Monocyte chemoattractant protein-1 and coronary artery disease. *Clinical Cardiology*, 2002. **25**(4): p.143-147.
159. Das, M., Patil, S., Bhargava, N., Kang, J.F., Riedel, L.M., Seal, S., and Hickman, J.J., Auto-catalytic ceria nanoparticles offer neuroprotection to adult rat spinal cord neurons. *Biomaterials*, 2007. **28**(10): p.1918-25.
160. Park, B., Martin, P., Harris, C., Guest, R., Whittingham, A., Jenkinson, P., and Handley, J., Initial in vitro screening approach to investigate the potential health and environmental hazards of Envirox™ - a nanoparticulate cerium oxide diesel fuel additive. *Particle and Fibre Toxicology*, 2007. **4**: p.10pp.
161. Tsunekawa, S., Sivamohan, R., Ohsuna, T., Takahashi, H., and Tohji, K., Ultraviolet Absorption Spectra of CeO<sub>2</sub> Nano-Particles. *Materials Science Forum*, 1999. **315-317**: p.439-445.

162. Yu, J.C., Zhang, L., and Lin, J., Direct sonochemical preparation of high-surface-area nanoporous ceria and ceria–zirconia solid solutions. *Journal of Colloid and Interface Science*, 2003. **260**(1): p.240-243.
163. Hirst, S.M., Karakoti, A.S., Tyler, R.D., Sriranganathan, N., Seal, S., and Reilly, C.M., Anti-inflammatory properties of cerium oxide nanoparticles. *Small*, 2009. **5**(24): p.2848-56.
164. Tarnuzzer, R.W., Colon, J., Patil, S., and Seal, S., Vacancy engineered ceria nanostructures for protection from radiation-induced cellular damage. *Nano Letters*, 2005. **5**(12): p.2573-7.
165. Xia, T., Kovochich, M., Liong, M., Mädler, L., Gilbert, B., Shi, H., Yeh, J.I., Zink, J.I., and Nel, A.E., Comparison of the mechanism of toxicity of zinc oxide and cerium oxide nanoparticles based on dissolution and oxidative stress properties. *ACS Nano*, 2008. **2**(10): p.2121-34.
166. Li, Y., He, X., Yin, J.J., Ma, Y., Zhang, P., Li, J., Ding, Y., Zhang, J., Zhao, Y., Chai, Z., and Zhang, Z., Acquired superoxide-scavenging ability of ceria nanoparticles. *Angewandte Chemie International Edition*, 2015. **54**(6): p.1832-5.
167. Lin, W., Huang, Y.W., Zhou, X.D., and Ma, Y., Toxicity of cerium oxide nanoparticles in human lung cancer cells. *International Journal of Toxicology*, 2006. **25**(6): p.451-7.
168. Strobel, C., Förster, M., and Hilger, I., Biocompatibility of cerium dioxide and silicon dioxide nanoparticles with endothelial cells. *Beilstein Journal of Nanotechnology*, 2014. **5**: p.1795-1807.
169. Tacker, D.H. and Okorodudu, A.O., Evidence for injurious effect of cocaethylene in human microvascular endothelial cells. *Clinica Chimica Acta*, 2004. **345**(1-2): p.69-77.
170. Strobel, C., Oehring, H., Herrmann, R., Förster, M., Reller, A., and Hilger, I., Fate of cerium dioxide nanoparticles in endothelial cells: exocytosis. *Journal of Nanoparticle Research*, 2015. **17**(5): p.1-14.
171. *United States Environmental Protection Agency (EPA). Six Common Air Pollutants*. Retrieved: June 11, 2015 from <http://www.epa.gov/airquality/urbanair/>.
172. Kumar, P., Robins, A., Vardoulakis, S., and Britter, R., A review of the characteristics of nanoparticles in the urban atmosphere and the prospects for developing regulatory controls. *Atmospheric Environment*, 2010. **44**(39): p.5035-5052.
173. Brook, R.D., Rajagopalan, S., Pope, C.A., 3rd, Brook, J.R., Bhatnagar, A., Diez-Roux, A.V., Holguin, F., Hong, Y., Luepker, R.V., Mittleman, M.A., Peters, A., Siscovick, D., Smith, S.C., Jr., Whitsel, L., and Kaufman, J.D., Particulate matter air pollution and cardiovascular disease: An update to the scientific statement from the American Heart Association. *Circulation*, 2010. **121**(21): p.2331-78.
174. Zanobetti, A., Dominici, F., Wang, Y., and Schwartz, J., A national case-crossover analysis of the short-term effect of PM<sub>2.5</sub> on hospitalizations and mortality in subjects with diabetes and neurological disorders. *Environmental Health*, 2014. **13**(1): p.38.
175. Loomis, D., Grosse, Y., Lauby-Secretan, B., Ghissassi, F.E., Bouvard, V., Benbrahim-Tallaa, L., Guha, N., Baan, R., Mattock, H., and Straif, K., The carcinogenicity of outdoor air pollution. *The Lancet Oncology*, 2013. **14**(13): p.1262-1263.
176. *International Agency for Research on Cancer (IARC). World Health Organization (WHO). Press Release N° 221 (17 October 2013). IARC: Outdoor air pollution a leading environmental cause of cancer deaths*. Retrieved: June 11, 2015 from [http://www.iarc.fr/en/media-centre/iarcnews/pdf/pr221\\_E.pdf](http://www.iarc.fr/en/media-centre/iarcnews/pdf/pr221_E.pdf).
177. *World Health Organization (WHO). Burden of disease from Household Air Pollution for 2012*. Retrieved: June 11, 2015 from [http://www.who.int/phe/health\\_topics/outdoorair/databases/FINAL\\_HAP\\_AAP\\_BoD\\_24Mar\\_ch2014.pdf](http://www.who.int/phe/health_topics/outdoorair/databases/FINAL_HAP_AAP_BoD_24Mar_ch2014.pdf).
178. Kumar, P., Morawska, L., Birmili, W., Paasonen, P., Hu, M., Kulmala, M., Harrison, R.M., Norford, L., and Britter, R., Ultrafine particles in cities. *Environment International*, 2014. **66**(0): p.1-10.

179. Qi, L., Zhou, M.-F., Zhao, Z., Hu, J., and Huang, Y., The characteristics of automobile catalyst-derived platinum group elements in road dusts and roadside soils: a case study in the Pearl River Delta region, South China. *Environmental Earth Sciences*, 2011. **64**(6): p.1683-1692.
180. Wichmann, H., Anquandah, G.A.K., Schmidt, C., Zachmann, D., and Bahadir, M.A., Increase of platinum group element concentrations in soils and airborne dust in an urban area in Germany. *Science of the Total Environment*, 2007. **388**(1–3): p.121-127.
181. Alt, F., Bambauer, A., Hopstock, K., Mergler, B., and Tölg, G., Platinum traces in airborne particulate matter. Determination of whole content, particle size distribution and soluble platinum. *Fresenius' Journal of Analytical Chemistry*, 1993. **346**(6-9): p.693-696.
182. Ek, K.H., Morrison, G.M., and Rauch, S., Environmental routes for platinum group elements to biological materials—a review. *Science of the Total Environment*, 2004. **334–335**(0): p.21-38.
183. Gómez, B., Gómez, M., Sanchez, J.L., Fernández, R., and Palacios, M.A., Platinum and rhodium distribution in airborne particulate matter and road dust. *Science of the Total Environment*, 2001. **269**(1–3): p.131-144.
184. Helmers, E., Elements accompanying platinum emitted from automobile catalyst's. *Chemosphere*, 1996. **33**(3): p.405-419.
185. Palacios, M.A., Gómez, M.M., Moldovan, M., Morrison, G., Rauch, S., McLeod, C., Ma, R., Laserna, J., Lucena, P., Caroli, S., Alimonti, A., Petrucci, F., Bocca, B., Schramel, P., Lustig, S., Zischka, M., Wass, U., Stenbom, B., Luna, M., Saenz, J.C., Santamaría, J., and Torrens, J.M., Platinum-group elements: quantification in collected exhaust fumes and studies of catalyst surfaces. *Science of the Total Environment*, 2000. **257**(1): p.1-15.
186. Rauch, S., Hemond, H.F., Barbante, C., Owari, M., Morrison, G.M., Peucker-Ehrenbrink, B., and Wass, U., Importance of Automobile Exhaust Catalyst Emissions for the Deposition of Platinum, Palladium, and Rhodium in the Northern Hemisphere. *Environmental Science & Technology*, 2005. **39**(21): p.8156-8162.
187. Tzamelis, I., The evolving role of mitochondria in metabolism. *Trends in Endocrinology and Metabolism*, 2012. **23**(9): p.417-419.
188. Green, D.R. and Reed, J.C., Mitochondria and Apoptosis. *Science*, 1998. **281**(5381): p.1309-1312.
189. Fulda, S., Galluzzi, L., and Kroemer, G., Targeting mitochondria for cancer therapy. *Nature Reviews: Drug Discovery*, 2010. **9**(6): p.447-464.
190. Marrache, S. and Dhar, S., Engineering of blended nanoparticle platform for delivery of mitochondria-acting therapeutics. *Proceedings of the National Academy of Sciences*, 2012. **109**(40): p.16288-16293.
191. Bantz, C., Koshkina, O., Lang, T., Galla, H.-J., Kirkpatrick, C.J., Stauber, R.H., and Maskos, M., The surface properties of nanoparticles determine the agglomeration state and the size of the particles under physiological conditions. *Beilstein Journal of Nanotechnology*, 2014. **5**: p.1774-1786.
192. Murphy, M.P., Targeting lipophilic cations to mitochondria. *Biochimica et Biophysica Acta (BBA) - Bioenergetics*, 2008. **1777**(7–8): p.1028-1031.
193. Kolmakov, K., Belov, V.N., Bierwagen, J., Ringemann, C., Müller, V., Eggeling, C., and Hell, S.W., Red-Emitting Rhodamine Dyes for Fluorescence Microscopy and Nanoscopy. *Chemistry – A European Journal*, 2010. **16**(1): p.158-166.
194. Vercauteren, D., Vandenbroucke, R.E., Jones, A.T., Rejman, J., Demeester, J., De Smedt, S.C., Sanders, N.N., and Braeckmans, K., The use of inhibitors to study endocytic pathways of gene carriers: optimization and pitfalls. *Molecular Therapy*, 2010. **18**(3): p.561-9.
195. Dausend, J., Musyanovych, A., Dass, M., Walther, P., Schrezenmeier, H., Landfester, K., and Mailänder, V., Uptake mechanism of oppositely charged fluorescent nanoparticles in HeLa cells. *Macromolecular Bioscience*, 2008. **8**(12): p.1135-43.

196. Leroueil, P.R., Hong, S., Mecke, A., Baker, J.R., Orr, B.G., and Banaszak Holl, M.M., Nanoparticle Interaction with Biological Membranes: Does Nanotechnology Present a Janus Face? *Accounts of Chemical Research*, 2007. **40**(5): p.335-342.
197. Li, Z., Barnes, J.C., Bosoy, A., Stoddart, J.F., and Zink, J.I., Mesoporous silica nanoparticles in biomedical applications. *Chemical Society Reviews*, 2012. **41**(7): p.2590-2605.
198. Rosenholm, J.M., Meinander, A., Peuhu, E., Niemi, R., Eriksson, J.E., Sahlgren, C., and Lindén, M., Targeting of Porous Hybrid Silica Nanoparticles to Cancer Cells. *ACS Nano*, 2008. **3**(1): p.197-206.
199. Tang, F., Li, L., and Chen, D., Mesoporous Silica Nanoparticles: Synthesis, Biocompatibility and Drug Delivery. *Advanced Materials*, 2012. **24**(12): p.1504-1534.
200. Sauer, A.M., Schlossbauer, A., Ruthardt, N., Cauda, V., Bein, T., and Bräuchle, C., Role of Endosomal Escape for Disulfide-Based Drug Delivery from Colloidal Mesoporous Silica Evaluated by Live-Cell Imaging. *Nano Letters*, 2010. **10**(9): p.3684-3691.
201. Ashley, C.E., Carnes, E.C., Phillips, G.K., Padilla, D., Durfee, P.N., Brown, P.A., Hanna, T.N., Liu, J., Phillips, B., Carter, M.B., Carroll, N.J., Jiang, X., Dunphy, D.R., Willman, C.L., Petsev, D.N., Evans, D.G., Parikh, A.N., Chackerian, B., Wharton, W., Peabody, D.S., and Brinker, C.J., The targeted delivery of multicomponent cargos to cancer cells by nanoporous particle-supported lipid bilayers. *Nature Materials*, 2011. **10**(5): p.389-97.
202. Lachelt, U., Kos, P., Mickler, F.M., Herrmann, A., Salcher, E.E., Rodl, W., Badgular, N., Bräuchle, C., and Wagner, E., Fine-tuning of proton sponges by precise diaminoethanes and histidines in pDNA polyplexes. *Nanomedicine: Nanotechnology, Biology, and Medicine*, 2014. **10**(1): p.35-44.
203. Varkouhi, A.K., Scholte, M., Storm, G., and Haisma, H.J., Endosomal escape pathways for delivery of biologicals. *Journal of Controlled Release*, 2011. **151**(3): p.220-228.
204. Behr, J.-P., The Proton Sponge: a Trick to Enter Cells the Viruses Did Not Exploit. *CHIMIA*, 1997. **51**(1-2): p.34-36.
205. Gruenberg, J. and Maxfield, F.R., Membrane transport in the endocytic pathway. *Current Opinion in Cell Biology*, 1995. **7**(4): p.552-563.
206. Wagner, E., Polymers for siRNA delivery: inspired by viruses to be targeted, dynamic, and precise. *Accounts of Chemical Research*, 2012. **45**(7): p.1005-13.
207. Albertazzi, L., Mickler, F.M., Pavan, G.M., Salomone, F., Bardi, G., Panniello, M., Amir, E., Kang, T., Killops, K.L., Brauchle, C., Amir, R.J., and Hawker, C.J., Enhanced bioactivity of internally functionalized cationic dendrimers with PEG cores. *Biomacromolecules*, 2012. **13**(12): p.4089-97.
208. Esfand, R. and Tomalia, D.A., Poly(amidoamine) (PAMAM) dendrimers: from biomimicry to drug delivery and biomedical applications. *Drug Discovery Today*, 2001. **6**(8): p.427-436.
209. Chambron, J.C. and Meyer, M., The ins and outs of proton complexation. *Chemical Society Reviews*, 2009. **38**(6): p.1663-73.
210. Cauda, V., Schlossbauer, A., Kecht, J., Zürner, A., and Bein, T., Multiple Core-Shell Functionalized Colloidal Mesoporous Silica Nanoparticles. *Journal of the American Chemical Society*, 2009. **131**(32): p.11361-11370.
211. Argyo, C. *Tailoring Properties of Multifunctional Mesoporous Silica Nanoparticles for Controlled Drug Delivery Applications*. (Ph.D. Thesis. Department of Chemistry, LMU Munich, Germany; 2014).
212. Mellman, I., Fuchs, R., and Helenius, A., Acidification of the endocytic and exocytic pathways. *Annual Review of Biochemistry*, 1986. **55**: p.663-700.
213. Pan, B.-F., Cui, D.-X., Xu, P., Chen, H., Liu, F.-T., Li, Q., Huang, T., You, X.-G., Shao, J., Bao, C.-C., Gao, F., He, R., Shu, M.-J., and Ma, Y.-J., Design of dendrimer modified carbon nanotubes for gene delivery. *Chinese Journal of Cancer Research*, 2007. **19**(1): p.1-6.



214. Knop, K., Hoogenboom, R., Fischer, D., and Schubert, U.S., Poly(ethylene glycol) in drug delivery: pros and cons as well as potential alternatives. *Angewandte Chemie, International Edition in English*, 2010. **49**(36): p.6288-308.
215. Barcellona, M.L., Cardiel, G., and Gratton, E., Time-resolved fluorescence of DAPI in solution and bound to polydeoxynucleotides. *Biochemical and Biophysical Research Communications*, 1990. **170**(1): p.270-280.
216. Morikawa, K. and Yanagida, M., Visualization of Individual DNA Molecules in Solution by Light Microscopy: DAPI Staining Method. *The Journal of Biochemistry*, 1981. **89**(2): p.693-696.
217. Go, Y.-M. and Jones, D.P., Redox compartmentalization in eukaryotic cells. *Biochimica et Biophysica Acta (BBA)*, 2008. **1780**(11): p.1273-1290.
218. Austin, C.D., Wen, X., Gazzard, L., Nelson, C., Scheller, R.H., and Scales, S.J., Oxidizing potential of endosomes and lysosomes limits intracellular cleavage of disulfide-based antibody–drug conjugates. *Proceedings of the National Academy of Sciences*, 2005. **102**(50): p. 17987-17992.
219. Molecular Probes. *DAPI Nucleic Acid Stain*. Retrieved: June 11, 2015 from <http://tools.lifetechnologies.com/content/sfs/manuals/mp01306.pdf>.
220. Schlossbauer, A., Sauer, A.M., Cauda, V., Schmidt, A., Engelke, H., Rothbauer, U., Zolghadr, K., Leonhardt, H., Bräuchle, C., and Bein, T., Cascaded photoinduced drug delivery to cells from multifunctional core-shell mesoporous silica. *Advanced Healthcare Materials*, 2012. **1**(3): p.316-20.
221. Skoufias, D.A. and Wilson, L., Mechanism of inhibition of microtubule polymerization by colchicine: inhibitory potencies of unliganded colchicine and tubulin-colchicine complexes. *Biochemistry*, 1992. **31**(3): p.738-746.
222. Cauda, V., Engelke, H., Sauer, A., Arcizet, D., Bräuchle, C., Rädler, J., and Bein, T., Colchicine-Loaded Lipid Bilayer-Coated 50 nm Mesoporous Nanoparticles Efficiently Induce Microtubule Depolymerization upon Cell Uptake. *Nano Letters*, 2010. **10**(7): p.2484-2492.
223. Nelson, P., *Biological Physics - Energy, Information, Life*. 2008, New York: W. H. Freeman.
224. Goldman, A.J., Cox, R.G., and Brenner, H., Slow viscous motion of a sphere parallel to a plane wall—II Couette flow. *Chemical Engineering Science*, 1967. **22**(4): p.653-660.
225. Bongrand, P., Ligand-receptor interactions. *Reports on Progress in Physics*, 1999. **62**(6): p.921-968.
226. Pierres, A., Benoliel, A.M., and Bongrand, P., Measuring the Lifetime of Bonds Made between Surface-linked Molecules. *Journal of Biological Chemistry*, 1995. **270**(44): p.26586-26592.
227. Silbernagl, S. and Lang, F., *Taschenatlas Pathophysiologie*. 2012, Stuttgart, Germany: Thieme.
228. Bai, K. and Wang, W., Shear stress-induced redistribution of the glycocalyx on endothelial cells in vitro. *Biomechanics and Modeling in Mechanobiology*, 2014. **13**(2): p.303-11.
229. Apodaca, G., Modulation of membrane traffic by mechanical stimuli. *American Journal of Physiology: Renal Physiology*, 2002. **282**(2): p.F179-90.
230. Davies, P.F., Dewey, C.F., Jr., Bussolari, S.R., Gordon, E.J., and Gimbrone, M.A., Jr., Influence of hemodynamic forces on vascular endothelial function. In vitro studies of shear stress and pinocytosis in bovine aortic cells. *Journal of Clinical Investigation*, 1984. **73**(4): p.1121-9.
231. Samuel, S.P., Jain, N., O'Dowd, F., Paul, T., Kashanin, D., Gerard, V.A., Gun'ko, Y.K., Prina-Mello, A., and Volkov, Y., Multifactorial determinants that govern nanoparticle uptake by human endothelial cells under flow. *International Journal of Nanomedicine*, 2012. **7**: p. 2943-56.
232. Friend, J. and Yeo, L.Y., Microscale acoustofluidics: Microfluidics driven via acoustics and ultrasonics. *Reviews of Modern Physics*, 2011. **83**(2): p.647-704.
233. Luong, T.D. and Nguyen, N.T., Surface Acoustic Wave Driven Microfluidics – A Review. *Micro and Nanosystems*, 2010. **2**(3): p.217-225.

234. Fillafer, C., Ratzinger, G., Neumann, J., Guttenberg, Z., Dissauer, S., Lichtscheidl, I.K., Wirth, M., Gabor, F., and Schneider, M.F., An acoustically-driven biochip - impact of flow on the cell-association of targeted drug carriers. *Lab on a Chip*, 2009. **9**(19): p.2782-8.
235. Hartmann, A., Stamp, M., Kmeth, R., Buchegger, S., Stritzker, B., Saldamli, B., Burgkart, R., Schneider, M.F., and Wixforth, A., A novel tool for dynamic cell adhesion studies--the De-Adhesion Number Investigator DANI. *Lab on a Chip*, 2014. **14**(3): p.542-6.
236. Wixforth, A., Acoustically driven planar microfluidics. *Superlattices and Microstructures*, 2003. **33**(5-6): p.389-396.
237. Lighthill, S.J., Acoustic streaming. *Journal of Sound and Vibration*, 1978. **61**(3): p.391-418.
238. Singh, R. and Bhethanabotla, V.R. *Enhancement in ultrasonic micro-transport using focused inter-digital transducers in a surface acoustic wave device: Fluid-structure interaction study*. in *Sensors, 2009 IEEE*. p.538-541.
239. Alghane, M., Chen, B.X., Fu, Y.Q., Li, Y., Luo, J.K., and Walton, A.J., Experimental and numerical investigation of acoustic streaming excited by using a surface acoustic wave device on a 128° YX-LiNbO<sub>3</sub> substrate. *Journal of Micromechanics and Microengineering*, 2011. **21**(1): p.015005 (11pp).
240. Sankaranarayanan, S.K.R.S. and Bhethanabotla, V.R., Design of efficient focused surface acoustic wave devices for potential microfluidic applications. *Journal of Applied Physics*, 2008. **103**(6): p.064518 (17pp).
241. Shilton, R., Tan, M.K., Yeo, L.Y., and Friend, J.R., Particle concentration and mixing in microdrops driven by focused surface acoustic waves. *Journal of Applied Physics*, 2008. **104**(1): p.014910 (9pp).
242. Wu, T.T., Tang, H.T., Chen, Y.Y., and Liu, P.L., Analysis and design of focused interdigital transducers. *IEEE Transactions on Ultrasonics, Ferroelectrics and Frequency Control*, 2005. **52**(8): p.1384-1392.
243. Sritharan, K., Strobl, C.J., Schneider, M.F., Wixforth, A., and Guttenberg, Z., Acoustic mixing at low Reynold's numbers. *Applied Physics Letters*, 2006. **88**(5): p.054102 (3pp).
244. Cauda, V., Argyo, C., and Bein, T., Impact of different PEGylation patterns on the long-term bio-stability of colloidal mesoporous silica nanoparticles. *Journal of Materials Chemistry*, 2010. **20**(39): p.8693-8699.
245. Denizot, F. and Lang, R., Rapid colorimetric assay for cell growth and survival. Modifications to the tetrazolium dye procedure giving improved sensitivity and reliability. *Journal of Immunological Methods*, 1986. **89**(2): p.271-7.
246. Haslam, G., Wyatt, D., and Kitos, P., Estimating the number of viable animal cells in multi-well cultures based on their lactate dehydrogenase activities. *Cytotechnology*, 2000. **32**(1): p.63-75.
247. Thielicke, W. *The Flapping Flight of Birds - Analysis and Application*. (Ph.D. Thesis. Rijksuniversiteit Groningen, 2014).
248. Thielicke, W. and Stamhuis, E. *PIVlab – Time-Resolved Digital Particle Image Velocimetry Tool for MATLAB*. Retrieved: June 11, 2015 from <http://dx.doi.org/10.6084/m9.figshare.1092508>.
249. Thielicke, W. and Stamhuis, E.J., PIVlab – Towards User-friendly, Affordable and Accurate Digital Particle Image Velocimetry in MATLAB. *Journal of Open Research Software*, 2014. **2**: p.e30.
250. French, C.S. and Young, V.K., The fluorescence spectra of red algae and the transfer of energy from phycoerythrin to phycocyanin and chlorophyll. *Journal of General Physiology*, 1952. **35**(6): p.873-90.

## List of abbreviations

AFM	atomic force microscopy
ATP	adenosine triphosphate
CCD	charge-coupled device
Col	colchicine
CP	chlorpromazine
DAPI	4',6-diamidino-2-phenylindole, dihydrochloride
DIC	differential interference contrast
DLS	dynamic light scattering
DNA	deoxyribonucleic acid
DTT	dithiothreitol
EA.hy926	endothelial cell line derived from HUVEC
EDX	energy-dispersive X-ray
EMCCD	electron-multiplying charge-coupled device
FA	folic acid
FACS	fluorescence-activated cell sorting
FBS	fetal bovine serum
FIDT	focusing interdigital transducer
FT-IR	Fourier transform infrared
GFP	green fluorescent protein
HeLa	cancer cell line derived from the cervix carcinoma
HMEC-1	human microvascular endothelial cells
HUVEC	human umbilical vein endothelial cells
IDT	interdigital transducer
IL-1 $\beta$	interleukin-1b
IntDens	integrated density, i.e., sum of all pixel intensities
KB	cervix carcinoma cells derived from HeLa
LDH	lactate dehydrogenase
MCP-1	monocyte chemoattractant protein-1

MSN	mesoporous silica nanoparticle
MTT	3-(4,5-dimethylthiazol-2-yl)-2,5-diphenyltetrazolium bromide
MTS-ROX	methanethiosulfonate 5(6)-carboxy-X-rhodamine
MTS-DAPI	DAPI derivatives with thiol-reactive methanethiosulfonate groups
NMR	nuclear magnetic resonance
NP	nanoparticle
PALM	photoactivated localization microscopy
PAMAM	poly(amidoamine)
PBS	phosphate buffered saline
PDI	polydispersivity index
PE-A	standard channel detection in flow cytometry. Phycoerythrin (PE) is a water-soluble protein commonly used as a fluorescent marker in flow cytometry. It has a peak emission at 578 nm [250]
PEG	polyethylene glycol
PI	pixel intensity
rATP	relative cellular ATP
rcDH	relative cellular dehydrogenase
ROI	region of interest
S1	segmentation strategy 1
S2	segmentation strategy 2
SAW	surface acoustic wave
SDCM	spinning disk confocal microscopy
SSA	specific surface area
STED	stimulated emission depletion (microscopy)
STORM	stochastic optical reconstruction microscopy
TEM	transmission electron microscopy
TIRF	total internal reflection fluorescence (microscopy)
WGA 488	wheat germ agglutinin Alexa Fluor® 488 conjugate

## Acknowledgements

I would like to express my deepest gratitude to many people who have contributed to make this dissertation possible.

First of all, I gratefully acknowledge Prof. Christoph Bräuchle for his guidance, extensive support, as well as for the opportunity to work with state-of-the-art research on an extremely interesting project.

My gratitude is extended to my second supervisor, Prof. Achim Wixforth, for his continuous encouragement and support since I first met him during my master's degree studies. Much appreciation is also given to Prof. Don Lamb and Prof. Jens Michaelis for close collaboration, scientific discussions, and the great working atmosphere while sharing the labs and during the Monday seminars. Many thanks also go to the reviewers of this thesis: Prof. Achim Hartschuh, Prof. Armin Reller, Prof. Regina de Vivie-Riedle, and Prof. Dina Fattakhova-Rohlfing.

It was a great privilege to take part and closely collaborate with colleagues in the SPP1313/NPBIOMEM research project. Many thanks go to Prof. Achim Wixforth, Prof. Armin Reller, Prof. Ingrid Hilger, Prof. Stefan W. Schneider, Prof. Matthias F. Schneider, as well as to Dr. Julia Blechinger, Dr. Rudolf Herrmann, Florian Strobl, Claudia Strobel, Dr. Alexander Bauer, Dr. Christoph Westerhausen, and Markus Rennhak. I wish to thank NPBIOMEM colleagues for many illuminating discussions – especially Dr. Julia Blechinger and Dr. Rudolf Herrmann for their wide-ranging support and helpful comments on the studies presented in this thesis. I am also grateful for the close collaboration with Prof. Thomas Bein and Dr. Christian Argyo.

It was a pleasure to discuss science and share everyday life with all members from AK Bräuchle, AK Lamb, and AK Michaelis. In particular, I would like to thank: Anna, Chris Osseforth, Ellen, Frauke, Julia, Leonhard, Viola, and Vroni, as well as Adam, Alvaro, Alexander, Anders, Aurélie, Bässem, Christophe Jung, Doro, Daniela, Fabian, Ganesh, Giulia, Ivo, Jelle, Jens, Korbi, Lena, Matthias, Meli, Nadia, Niko, Philipp, Robert, Sergey, Stephan, Sushi, and Waldi. Special thanks go to Julia, for introducing me to the field of live-cell microscopy and for extensive care and support. Furthermore, I thank Monika Franke and Jaroslava Obel for cell culture work. Another special thanks to Dr. Moritz Ehrl and to Silke Steger for helping me with many bureaucratic issues. Many thanks go also to my students Maria Hoyer, Christian Schmidt, and Christine Höls.

I thankfully acknowledge the German Research Foundation (DFG/SPP1313), the Center for NanoScience (CeNS), the Nanosystems Initiative Munich (NIM), and the Center for Integrated

Protein Science Munich (CIPS<sup>M</sup>) for financial support, for great conferences and workshops, and for the opportunity to meeting interdisciplinary researchers from all over the world.

Finally, I would like to express my deepest gratitude to my family and friends. Special thanks to my parents Claudete and Moacir for their continuous encouragement, optimism and care. Many thanks also go to my siblings Michele and Fabiano, and to my siblings-in-law Michele Rocha and Jefferson, as well as to my wife's family members. Above all, I thank Maike for her kindness and never-ending support in basically everything so as I could focus on the work involved in preparing this thesis. Warmhearted thanks to my daughter Eva and my son Lars for being so lovely and for understanding so well when they heard "Papai muss arbeiten".

## List of publications

### Publications included in this work

#### Peer-reviewed publications

- Torrano, A.A., Blechinger, J., Osseforth, C., Argyo, C., Reller, A., Bein, T., Michaelis, J., and Bräuchle, C., A fast analysis method to quantify nanoparticle uptake on a single cell level. *Nanomedicine (Lond)*, 2013. **8**(11): p. 1815-28. [\[link\]](#)
- Blechinger, J., Bauer, A.T., Torrano, A.A., Gorzelanny, C., Bräuchle, C., and Schneider, S.W., Uptake kinetics and nanotoxicity of silica nanoparticles are cell type dependent. *Small*, 2013. **9**(23): p. 3970-80, 3906. [\[link\]](#)
- Strobel, C., Torrano, A.A., Herrmann, R., Malissek, M., Bräuchle, C., Reller, A., Treuel, L., and Hilger, I., Effects of the physicochemical properties of titanium dioxide nanoparticles, commonly used as sun protection agents, on microvascular endothelial cells. *Journal of Nanoparticle Research*, 2014. **16**: p. 2130. [\[link\]](#)
- Torrano, A.A. and Bräuchle, C., Precise quantification of silica and ceria nanoparticle uptake revealed by 3D fluorescence microscopy. *Beilstein Journal of Nanotechnology*, 2014. **5**: p. 1616-24. [\[link\]](#)
- Strobl, F.G., Breyer, D., Link, P., Torrano, A.A., Bräuchle, C., Schneider, M.F., and Wixforth, A., A surface acoustic wave-driven micropump for particle uptake investigation under physiological flow conditions in very small volumes. *Beilstein Journal of Nanotechnology*, 2015. **6**: p. 414-9. [\[link\]](#)
- Weiss, V., Argyo, C., Torrano, A.A., Strobel, C., Mackowiak, S.A., Gatzemaier, T., Hilger, I., Bräuchle, C., and Bein, T., Dendronized mesoporous silica nanoparticles provide an internal endosomal escape mechanism for a successful cytosolic drug release. *Submitted*.

#### Book chapter

- Zellner, R., Blechinger, J., Bräuchle, C., Hilger, I., Janshoff, A., Lademann, J., Mailänder, V., Meinke, M.C., Nienhaus, G.U., Patzelt, A., Rancan, F., Rothen-Rutishauser, B., Stauber, R.H., Torrano, A.A., Treuel, L., and Vogt, A., *Biological Responses to Nanoparticles*, in *Safety Aspects of Engineered Nanomaterials*, W. Luther and A. Zweck, Editors. 2013, Pan Stanford Publishing. p. 157-218. [\[link\]](#)

### Publications not included in this work

#### Peer-reviewed publications

- Torrano, A.A., Pereira, A.S., Oliveira, O.N., and Barros-Timmons, A. Probing the interaction of oppositely charged gold nanoparticles with DPPG and DPPC Langmuir monolayers as cell membrane models. *Colloids and Surfaces B: Biointerfaces*, 2013. **108**: p. 120-6. [\[link\]](#)

- Strobl, F.G., Seitz, F., Westerhausen, C., Reller, A., Torrano, A.A., Bräuchle, C., Wixforth, A., and Schneider, M.F. Intake of silica nanoparticles by giant lipid vesicles: influence of particle size and thermodynamic membrane state. *Beilstein Journal of Nanotechnology*, 2014. **5**: p. 2468-78. [\[link\]](#)
- Prescher, J., Baumgartel, V., Ivanchenko, S., Torrano, A.A., Bräuchle, C., Muller, B., and Lamb, D.C. Super-resolution imaging of ESCRT-proteins at HIV-1 assembly sites. *PLoS Pathogens*, 2015. **11**(2): p. e1004677. [\[link\]](#)

## Conferences (selected presentations)

- International Meeting of the Physics of Living Systems Network – iPoLS. *Elucidating biological responses to nanoparticles by quantitative live-cell imaging* (poster). Munich, Germany, July 2014.
- Annual Meeting of the Center for Integrated Protein Science Munich – CiPSM. *Car exhaust nanoparticles are quickly internalized by cells and interact with mitochondria* (poster). Wildbad Kreuth, Germany, February 2014.
- Seminar Lecture in the Institute of Physics, University of Augsburg. *Investigation of nanoparticle-cell interactions via live-cell imaging* (talk). Augsburg, Germany, December 2013.
- 7<sup>th</sup> Thematic Workshop for the DFG Priority Programme SPP 1313-2: “Nanoparticle-cell interactions: Limitations, challenges and pitfalls”. *Interaction between nanoparticles generated by automobile catalytic converters and endothelial cells* (talk). Fribourg, Switzerland, June 2013.
- CeNS Workshop 2012 "Nanosciences: Soft, Solid, Alive and Kicking". *Detailed quantification of nanoparticle uptake by cells reveals that silica particles are more harmful to endothelial than to cancer cells* (poster). Venice, Italy, September 2012.
- NIM NanoDay: Deutsches Museum München – Zentrum für Neue Technologien. *Nanopartikel in der Medizin* (poster). Munich, Germany, September 2012.
- First Reporting Colloquium for the DFG Priority Programme SPP 1313-2: Biological Responses to Nanoscale Particles. *Kinetics of nanoparticle internalization by single cells* (talk). Fulda, Germany, February 2012.
- International Conference on “Biological Responses to Nanoscale Particles”. *Quantification and 3D reconstruction of nanoparticle uptake events at the single-cell level* (talk). Essen, Germany, September 2011.
- Kick-off Meeting for the DFG Priority Programme SPP 1313-2: Biological Responses to Nanoscale Particles. *Detailed characterization of nanoparticle-cell interactions* (talk). Fulda, Germany, March 2011.

## Awards

- CeNS Publication Award 2013 for the scientific article: *A fast analysis method to quantify nanoparticle uptake on a single cell level*. Torrano et al. *Nanomedicine*, 2013.
- Attocube Research Award 2012 for the master’s thesis: *Uptake behavior of nanoparticles into cells studied by scanning laser microscopy and quantitative digital image analysis*.



